



Title	High-Pressure Synthesis, Crystal Structures and Physical Properties of Perovskites in R <sub>2</sub> O <sub>3</sub> -Mn <sub>2</sub> O <sub>3</sub> Systems (R = Rare Earth Elements)
Author(s)	張, 墨
Citation	北海道大学. 博士(理学) 甲第13361号
Issue Date	2018-09-25
DOI	10.14943/doctoral.k13361
Doc URL	<a href="http://hdl.handle.net/2115/71985">http://hdl.handle.net/2115/71985</a>
Type	theses (doctoral)
File Information	ZHANG_Lei.pdf



[Instructions for use](#)

**High-Pressure Synthesis, Crystal Structures  
and Physical Properties of Perovskites in  
 $R_2O_3$ - $Mn_2O_3$  Systems ( $R$  = Rare Earth  
Elements)**

A Thesis

Submitted by

Lei ZHANG

In fulfillment for the award of the degree of

**Doctor of Science**

**Graduate School of Chemical Sciences and Engineering,**

**Hokkaido University**

**2018**



## Abstract

Perovskite-type manganese oxide has attracted enormous attention for decades because of its useful interplay between spin, charge, and orbital degrees of freedom. It led to discovery of colossal magnetoresistance, spin-driven multiferroics, and other interesting physical properties. In this study, I investigated the perovskite-type manganese oxide in chemical systems between  $R_2O_3$  ( $R$  = rare earth elements) and  $Mn_2O_3$ . Novel compositions were discovered by applying a high-pressure and high-temperature synthesis method, and those crystal structures and fundamental physical properties were clarified.

Chapter 1 introduces the general background, and chapter 2 explains the principal technologies used in this study. Chapters 3 to 5 consist of the main outcomes and the conclusion is drawn in chapter 6.

Chapter 3 describes unusual five-fold cation/charge ordering in high-pressure-synthesized  $RMnO_3$  perovskites of  $R = Gd-Tm$  and  $Y$  (at 6 GPa and 1673 K). The  $R^{3+}$ ,  $Mn^{2+}$ , and  $Mn^{3+}$  cations are ordered at the perovskite A site in two separate chains consisting of  $R^{3+}$  and alternating  $Mn^{2+}$  (in tetrahedral coordination) and  $Mn^{3+}$  (in square-planar coordination). Mixed-valent  $Mn^{3+}/Mn^{4+}$  cations are ordered in layers at the perovskite B site; the ordering can be described as  $[R^{3+}Mn^{2+}_{0.5}Mn^{3+}_{0.5}]_A[Mn^{3+}Mn^{3.5+}]_BO_6$ . The triple cation ordering observed at the A site is very rare, and the layered double B-site ordering is also scarcely seen.  $RMn_3O_6$  crystallizes in space group  $Pmmn$  with  $a = 7.2479(2)$  Å,  $b = 7.4525(3)$  Å, and  $c = 7.8022(2)$  Å for  $DyMn_3O_6$  (at 213 K), being structurally related to  $CaFeTi_2O_6$ . It appeared that they are non-stoichiometric and can be described as  $R_{1-\delta}Mn_3O_{6-1.5\delta}$  with  $\delta = -0.071$  to  $-0.059$  for  $R = Gd$ ,  $\delta = 0$  for  $Dy$ ,  $\delta = 0.05-0.1$  for  $Ho$  and  $Y$ , and  $\delta = 0.12$  for  $Er$  and  $Tm$ . All of them show complex magnetic behaviors with several transitions, and the magnetic properties are highly sensitive to the  $\delta$  values.

Chapter 4 introduces a quadruple perovskite  $\text{CeCuMn}_6\text{O}_{12}$  synthesized under high-pressure and high-temperature conditions at 6 GPa and about 1670 K.  $\text{CeCuMn}_6\text{O}_{12}$  crystallizes in space group  $Im-3$  above 297 K and  $R-3$  below the temperature with the 1:3 ( $\text{Mn}^{4+}:\text{Mn}^{3+}$ ) charge and orbital orders. Unusually compressed  $\text{Mn}^{3+}\text{O}_6$  octahedra found in  $\text{CeCuMn}_6\text{O}_{12}$  closely resembles what was found for the  $-Q_3$  Jahn-Teller distortion mode in  $\text{CaMn}_7\text{O}_{12}$ . Below approximately 90 K, structural instability results in a phase separation and appearance of competing phases; and below 70 K, two  $R-3$  phases coexist.  $\text{CeCuMn}_6\text{O}_{12}$  exhibits a ferrimagnetic-like transition below  $T_c$  of 140 K, and it is semiconducting with the magnetoresistance reaching -40 % (at 140 K and 70 kOe).

Chapter 5 reports orthorhombic rare-earth trivalent manganites  $\text{RMnO}_3$  ( $R = \text{Er} - \text{Lu}$ ), which were self-doped with Mn to form  $(\text{R}_{0.667}\text{Mn}_{0.333})\text{MnO}_3$  compositions. The series was synthesized by a high-pressure and high-temperature method at 6 GPa and about 1670 K from  $\text{R}_2\text{O}_3$  and  $\text{Mn}_2\text{O}_3$ . The average oxidation state of Mn is +3 in  $(\text{R}_{0.667}\text{Mn}_{0.333})\text{MnO}_3$ . However, Mn enters the A-site in the oxidation state of +2 creating the average oxidation state of +3.333 at the B site. The presence of  $\text{Mn}^{2+}$  was confirmed by hard X-ray photoelectron spectroscopy measurements. Crystal structures were studied by synchrotron X-ray powder diffraction.  $(\text{R}_{0.667}\text{Mn}_{0.333})\text{MnO}_3$  crystallizes in space group  $Pnma$  with  $a = 5.50348(2)$  Å,  $b = 7.37564(1)$  Å, and  $c = 5.18686(1)$  Å for  $(\text{Lu}_{0.667}\text{Mn}_{0.333})\text{MnO}_3$  at 293 K, and they are isostructural with the parent  $\text{RMnO}_3$  manganites. By comparing with  $\text{RMnO}_3$ ,  $(\text{R}_{0.667}\text{Mn}_{0.333})\text{MnO}_3$  exhibits enhanced Néel temperatures of about  $T_{\text{N1}} = 106\text{-}110$  K and canted antiferromagnetic properties. Compounds with  $R = \text{Er}$  and  $\text{Tm}$  show additional magnetic transitions at about  $T_{\text{N2}} = 10\text{-}15$  K.  $(\text{Tm}_{0.667}\text{Mn}_{0.333})\text{MnO}_3$  exhibits a magnetization reversal effect with the compensation temperature of 15 K.

Chapter 6 provides the general conclusion and future prospects.

**Keywords:** Perovskite, High-pressure synthesis, Crystal structure, Magnetic property.

## List of Abbreviations

MPMS	Magnetic property measurement system
PPMS	Physical property measurement system
XRPD	X-ray powder diffraction
SXRD	Synchrotron X-ray diffraction
FC	Field cooling
ZFC	Zero field cooling
$T_C$	Curie temperature
$T_N$	Neel temperature
AFM	Antiferromagnetic
FM	Ferromagnetic
$t$	Tolerance factor
$\theta$	Weiss temperature
$C$	Curie constant
$\mu_{\text{eff}}$	Effective magnetic moment
BVS	Bond valance sum
$C_p$	Heat capacity
NIMS	National Institute for Materials Science
$\chi$	Magnetic susceptibility
$\rho$	Electrical resistivity

# High-Pressure Synthesis, Crystal Structures and Physical Properties of Perovskites in $R_2O_3$ - $Mn_2O_3$ Systems (R = Rare Earth Elements)

## Contents

Chapter 1. Introduction .....	1
1.1. Crystal structure.....	1
1.1.1. Perovskite structure and perovskite oxide.....	1
1.1.2. Double-perovskite oxide.....	2
1.1.3. Quadruple-perovskite oxides.....	4
1.2. Electronic structure .....	5
1.2.1. Crystal field .....	5
1.2.2. The Jahn-Teller distortion.....	6
1.3. Magnetism.....	7
1.3.1. Origin of magnetism .....	7
1.3.2. Types of magnetic behaviors .....	8
1.3.3. Magnetic susceptibility and Curie-Weiss law .....	9
1.3.4. Canted antiferromagnetism or weak ferromagnetism .....	11
1.4. Magnetic interaction.....	13
1.4.1. Exchange interaction .....	13
1.4.2. Superexchange .....	14
1.4.3. Double exchange.....	14
1.5. Cation ordering in perovskites .....	15
1.5.1. Types of ordering in perovskites .....	15
1.5.2. B-site cation ordering in perovskite oxides .....	16
1.5.3. A-site cation ordering in perovskite oxides .....	17
1.6. Magnetoresistance .....	20
1.7. Ferroelectricity and Multiferroics .....	21
1.8. The perovskite manganites.....	23
1.8.1. $RMnO_3$ perovskites .....	23
1.8.2. $RMn_7O_{12}$ perovskites.....	25

1.9. Objectives of this thesis.....	28
References in chapter 1 .....	29
Chapter 2. Experimental methods .....	38
2.1. High pressure synthesis .....	38
2.2. X-ray diffraction.....	39
2.2.1. Powder X-ray diffraction.....	39
2.2.2. Synchrotron X-ray diffraction .....	40
2.3. Differential scanning calorimetry (DSC) .....	41
2.4. Magnetic properties measurement system (MPMS).....	42
2.5. Physical properties measurement system (PPMS) .....	44
References in chapter 2 .....	47
Chapter 3. Five-Fold Ordering in High-Pressure Perovskites $\text{RMn}_3\text{O}_6$ (R = Gd-Tm and Y) with Charge Disproportionation.....	48
3.1. Introduction.....	48
3.2. Experimental details of Chapter 3 .....	49
3.3. Results and discussion .....	51
3.3.1. Rare-Earth Stability Range, Chemical Compositions, and Thermal Stability of $\text{RMn}_3\text{O}_6$ .....	51
3.3.2. Crystal structures of $\text{RMn}_3\text{O}_6$ .....	57
3.3.3. Magnetic and other properties of $\text{RMn}_3\text{O}_6$ .....	62
3.4. Summary of Chapter 3 .....	76
References in chapter 3 .....	76
Chapter 4. Charge and orbital orders and structural instability in high-pressure quadruple perovskite $\text{CeCuMn}_6\text{O}_{12}$ .....	83
4.1 Introduction.....	83
4.2. Experimental details of Chapter 4 .....	84
4.3. Results and discussion .....	86
4.3.1. Structural phase transitions in $\text{CeCuMn}_6\text{O}_{12}$ .....	86
4.3.2 Crystal structures of $\text{CeCuMn}_6\text{O}_{12}$ .....	91
4.3.3. Magnetic and transport properties of $\text{CeCuMn}_6\text{O}_{12}$ .....	96
4.4. Summary of Chapter 4 .....	103
References in Chapter 4 .....	104
Chapter 5. Mn self-doping of orthorhombic $\text{RMnO}_3$ Perovskites: $(\text{R}_{0.667}\text{Mn}_{0.333})\text{MnO}_3$ with R = Er-Lu .....	109
5.1 Introduction.....	109
5.2. Experimental details of Chapter 5 .....	110

5.3. Results and discussion .....	113
5.3.1. Structural Properties of $(R_{0.667}Mn_{0.333})MnO_3$ and $(Er_{1-x}Mn_x)MnO_3$ .....	113
5.3.2 Magnetic Properties of $(R_{0.667}Mn_{0.333})MnO_3$ and $(Er_{1-x}Mn_x)MnO_3$ .....	121
5.4. Summary of Chapter 5 .....	139
References in Chapter 5 .....	139
Chapter 6. General conclusions and future prospects .....	145
6.1. General conclusions .....	145
6.2. Future prospects .....	146
References in chapter 6 .....	147
List of appended publications .....	148
Acknowledgement.....	150

# Chapter 1. Introduction

## 1.1. Crystal structure

### 1.1.1. Perovskite structure and perovskite oxide

Perovskite is a calcium titanium oxide mineral composed of calcium titanate ( $\text{CaTiO}_3$ ). It has been used to name the class of compounds which have the same type of crystal structure  $\text{ABX}_3$ . The ideal perovskite structure has  $Pm\bar{3}m$  space group symmetry [1], as shown in

**Figure 1.1.**

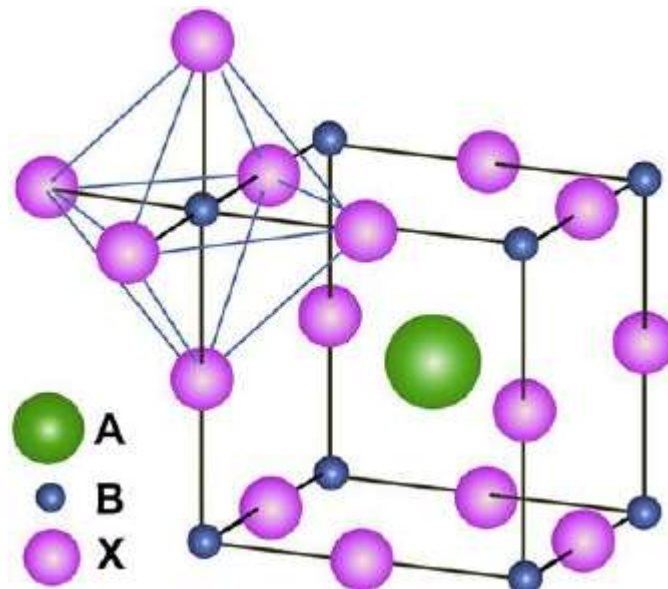


**Figure 1.1.**  $\text{ABX}_3$  ideal perovskite structure [2].

In this structure, A represents relatively large cations in the 12-coordinate cubo-octahedral cavities, such as alkaline metal, alkaline-earth metal, and lanthanide ions. Sometimes, A-site is able to accommodate organic cations, for instance  $\text{CH}_3\text{NH}_3^+$  [3,4] and  $\text{HC}(\text{NH}_2)_2^+$  [5,6]. B represents smaller transition-metal ions which are octahedrally coordinated by the X anions. If the tolerance factor  $t$  is in the range of 0.75-1.0, a lot of metallic elements are stable in the perovskite structure. The tolerance factor  $t$  of the perovskite structure is given by

$$t = \frac{r_A + r_X}{\sqrt{2}(r_B + r_X)}$$

where  $r_A$ ,  $r_B$ , and  $r_X$  are the ionic radii of A, B, and X site elements, respectively.

Due to their stable structure, perovskites, especially perovskite oxides ( $ABO_3$ ), are a very versatile material class being able to accommodate a number of elements [7]. The researchers have paid increasing attention to the unique properties of perovskite oxides and the application on many areas, such as capacitors [8,9], superconductors [10,11] and solar cell materials [5,12], as shown in **Table 1.1**.

**Table 1.1.** The properties of different perovskite materials [13].

Compound	Property
MgSiO <sub>3</sub>	Mantle mineral
CaTiO <sub>3</sub>	Dielectric
BaTiO <sub>3</sub>	Ferroelectric
PbZr <sub>1-x</sub> Ti <sub>x</sub> O <sub>3</sub>	Piezoelectric
Ba <sub>1-x</sub> La <sub>x</sub> TiO <sub>3</sub>	Semiconductor
Y <sub>0.33</sub> Ba <sub>0.66</sub> CuO <sub>3-δ</sub>	Superconductor
LnCoO <sub>3-δ</sub>	Mixed electronic ionic conductor
SrCeO <sub>3</sub>	Proton conductor
Li <sub>0.5-3x</sub> La <sub>0.5+x</sub> TiO <sub>3</sub>	Lithium ion conductor
La <sub>1-x</sub> Sr <sub>x</sub> GaO <sub>3-δ</sub>	Fast oxide ion conductor
BaInO <sub>2.5</sub>	Fast oxide ion conductor
KCaF <sub>3</sub>	Fast fluoride ion conductor
Na <sub>x</sub> WO <sub>3</sub>	Electrochromic
LaMnO <sub>3-δ</sub>	Colossal magnetoresistance
BaLiF <sub>3</sub>	Optical material

### 1.1.2. Double-perovskite oxide

In 1998, Kobayashi *et al* reported the half-metallicity and ferromagnetism ( $T_C \sim 400$  K) of

$\text{Sr}_2\text{FeMnO}_6$  [14]. Thus, more and more attention was drawn to the double perovskite whose general formula is  $\text{A}_2\text{BB}'\text{O}_6$ . Here, A-site accommodates alkaline earth or rare earth metal ions like those in simple perovskites. Different transition metals are in  $\text{BO}_6$  and  $\text{B}'\text{O}_6$  octahedra. The tolerance factor  $t$  of the double-perovskite oxide is given by

$$t = \frac{r_{\text{A}} + r_{\text{O}}}{\sqrt{2}(0.5r_{\text{B}} + 0.5r_{\text{B}'} + r_{\text{O}})}$$

where  $r_{\text{A}}$ ,  $r_{\text{B}}$ ,  $r_{\text{B}'}$ , and  $r_{\text{O}}$  are the ionic radii of A, B, B' site elements and Oxygen, respectively. The ideal double perovskite oxide structure (space group of  $Fm\bar{3}m$ ) when  $t = 1$ . However, monoclinic structure is usually observed when the tolerance factor is less than 1, as shown in **Figure 1.2**. Because A cation is small, there will be compressive stress on B-O and B'-O bonds and tensile stress on A-O bonds. It leads to the tilts of  $\text{BO}_6$  and  $\text{B}'\text{O}_6$  octahedra, which makes B-O-B' bond angles less than  $180^\circ$ . The structure with tilts results some unique properties, such as half-metallic ( $\text{Sr}_2\text{FeMnO}_6$ ) [14] and magnetodielectric ( $\text{Sc}_2\text{NiMnO}_6$  [15] and  $\text{Lu}_2\text{CoMnO}_6$  [16]) and therefore more and more interest has been focused on the double-perovskites.

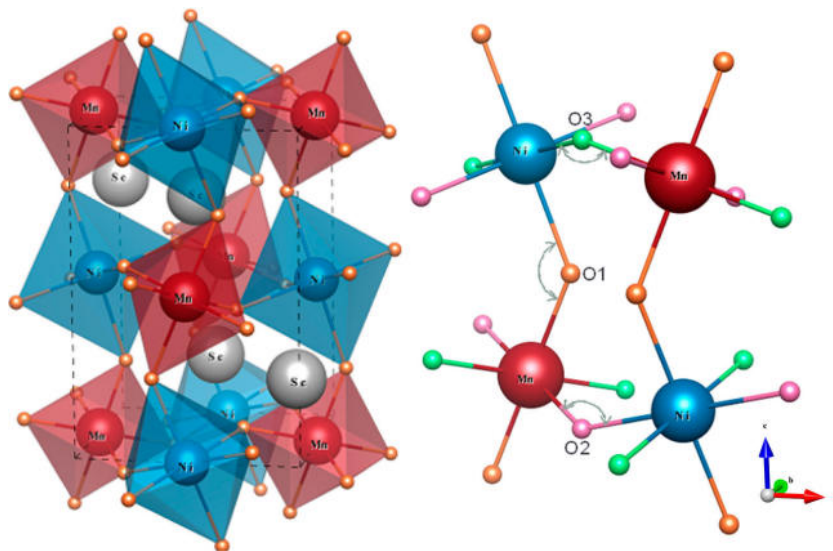


**Figure 1.2.** The lattice with tilts of  $\text{BO}_6$  and  $\text{B}'\text{O}_6$  octahedra in  $\text{Sc}_2\text{NiMnO}_6$  [15].

### 1.1.3. Quadruple-perovskite oxides

In 1973, Marezio *et al* reported a new compound  $\text{NaMn}_7\text{O}_{12}$  which is cubic, space group  $Im-3$  [18]. The general formula can be written as  $\text{AA}'_3\text{B}_4\text{O}_{12}$ , and its crystal structure is shown in **Figure 1.3**. Here, A and B still represent the larger cations and smaller transition-metal ions, respectively, like the simple perovskite  $\text{ABO}_3$ . A' represents small transition-metal cations. Jahn-Teller distorted cations such as  $\text{Cu}^{2+}$  and  $\text{Mn}^{3+}$  are representative ones accommodated at the A' site. In  $\text{AA}'_3\text{B}_4\text{O}_{12}$  perovskites, tilting of the  $\text{BO}_6$  octahedra and consequently  $\text{A}'\text{O}_4$  square-planar make the  $2a \times 2a \times 2a$  structure ( $a$  represents the simple perovskite unit cell). Because of their structures,  $\text{AA}'_3\text{B}_4\text{O}_{12}$  perovskites exhibit functional properties, such as a large dielectric constant in  $\text{CaCu}_3\text{Ti}_4\text{O}_{12}$  [19,20] and multiferroism in  $\text{RMn}_7\text{O}_{12}$  [21-24].

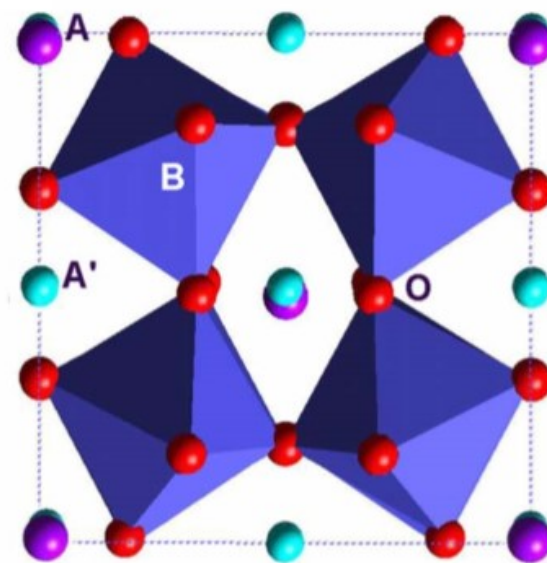


**Figure 1.3.** The structure of  $\text{BiMn}_7\text{O}_{12}$  [25].

When two different ions at B site, the quadruple perovskite oxide  $\text{AA}'_3\text{B}_2\text{B}'_2\text{O}_{12}$  can be obtained, as shown in **Figure 1.4**. In quadruple perovskite oxide, there are multiple interactions of cations, i.e., A'-A', A'-B, A'-B', B-B', and B'-B' interactions [26]. Due to the complex interactions, the quadruple perovskite oxides have unique properties, such as

ferrimagnetism with high transition temperature in  $\text{CaCu}_3\text{Fe}_2\text{Re}_2\text{O}_{12}$  [26].

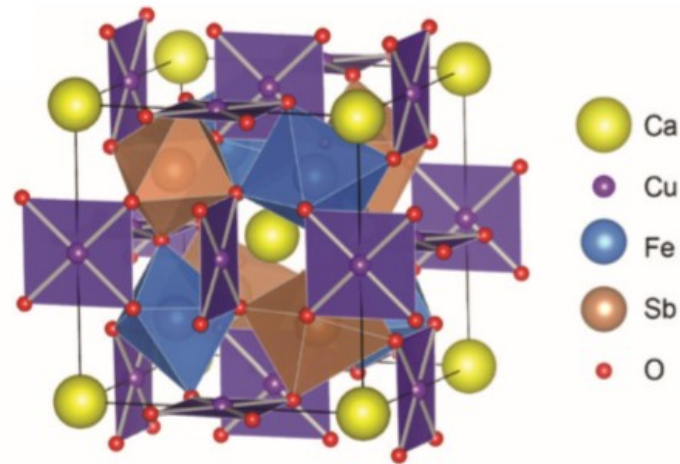


**Figure 1.4.** The structure of  $\text{AA}'_3\text{B}_2\text{B}'_2\text{O}_{12}$ -type compounds  $\text{CaCu}_3\text{Fe}_2\text{Sb}_2\text{O}_{12}$  [27].

## 1.2. Electronic structure

### 1.2.1. Crystal field

In 1930s, crystal field theory was developed by Hans Bethe and John Hasbrouck van Vleck [28] to describe the loss of degeneracy of electron orbital states, usually  $d$  orbitals in transition-metal ions, considering energy changes of the degenerate orbitals influenced by the charge of surrounding ligands.

The most common example is octahedral, where the transition-metal ion is surrounded by six ligands and the  $d$ -orbitals of the transition-metal ion split into two groups with an energy difference. Among them, the  $d_{xy}$ ,  $d_{xz}$ , and  $d_{yz}$  orbitals, which are directed between the ligands, have lower energy than in the steric field. These three orbitals are called  $t_{2g}$  orbitals. In opposite, the  $d_{x^2-y^2}$  and  $d_{z^2}$  orbitals have higher energy than in the steric field, called  $e_g$  orbitals. Thus, if the electrons occupying these orbitals, the metal ion is more stable compared with in the steric field.

The second most common type is tetrahedral, where four ligands surround the metal ion. The energy of  $e_g$  orbitals,  $d_{x^2-y^2}$  and  $d_{z^2}$ , will be lower and the higher energy orbitals will

be  $t_{2g}$  orbitals, i.e.  $d_{xy}$ ,  $d_{xz}$ , and  $d_{yz}$ .

Some ligands lead to a large gap due to the strong interactions between the ligands and the metal orbitals, called strong-field ligands. In this case, it is unfavourable to put electrons into high energy orbitals. Thus, the electrons are not able to occupy the higher energy orbitals until the lower ones are completely filled. It is named by "low spin" [29]. Other ligands, which weakly interact with the metal orbitals, named weak-field ligands. With these ligands, it is easier to put electrons into high energy orbitals. Thus the electrons are favourable to each of the orbitals than to put two into the same low-energy orbital according. It is named by "high spin".

### 1.2.2. The Jahn-Teller distortion

The Jahn-Teller distortion, sometimes also called as Jahn-Teller effect, was first reported by Hermann Arthur Jahn and Edward Teller in 1937 [30,31]. This theorem describes the geometrical distortion of ions and molecules, which is related to the electron configurations. If the nonlinear molecule with a degenerate electronic ground state, there will be spontaneous symmetry breaking by geometrical distortion in the molecule to remove the degeneracy since the distortion is able to make the overall energy decrease.

The Jahn-Teller distortion is most common in octahedra of the transition metals, especially in six-coordinate  $\text{Cu}^{2+}$  ion with  $d^9$  electronic configuration. In this ion, there are three electrons in  $e_g$  orbitals, leading to a degenerate electronic ground state. Thus, distortion along one the molecular fourfold axes (always  $z$  axis) occurs, which breaks the degeneracy and lower the overall energy. The Jahn-Teller distortion is also common in high-spin  $\text{Mn}^{3+}$  ion with  $d^4$  electronic configuration. In this ion, there are four electrons singly occupying one  $e_g$  orbital and three  $t_{2g}$  orbitals, respectively. The distortion occurs, splitting the  $e_g$  orbital and  $t_{2g}$  orbitals. The energy from lowering of the  $d_{yz}$  and  $d_{zx}$  orbitals is balanced by the raising of the  $d_{xy}$  orbital. The overall energy decreases because the low energy  $e_g$  orbital is singly occupied

and the high energy  $e_g$  orbital is empty, as shown in **Figure 1.7**.

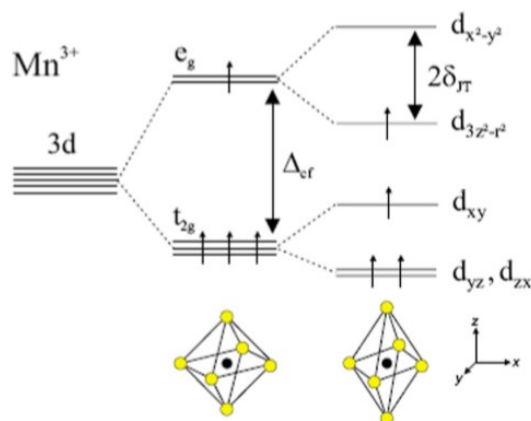


**Figure 1.5.** Diagram of electronic structure of  $Mn^{3+}$  with Jahn-Teller distortion [32].

The Jahn-Teller distortion is easily observed when an odd number of electrons occupy the  $e_g$  orbitals in octahedra, where there is a degeneracy due to the  $e_g$  orbitals. The distortion also appears when there is a degeneracy due to the  $t_{2g}$  orbitals, but it is much less noticeable than the former one.

### 1.3. Magnetism

#### 1.3.1. Origin of magnetism

Magnetism is a class of physical phenomena in an applied magnetic field. The solids exhibit magnetic effects because they have some unpaired electrons in their outer valence shells. The unpaired electrons have spin and orbital motion. Spin describes the intrinsic angular momentum of an electron. The spinning of electron on its axis is able to produce a magnetic moment like the gyromagnetic effect. And orbital motions of an electron will also generate a magnetic moment. Thus the magnetic properties of an individual atom or ion will be determined by the spin moments of the electrons and the orbital moments due to the motion of the electrons around the nucleus [33]. There is a convenient unit, Bohr magneton  $\mu_B$ , for describing the magnitude of atomic magnetic moments [34].

If the orbital motions are neglected, the magnetic moment resulting from the electron spins

alone is given by

$$\mu_S = g\sqrt{S(S+1)}\mu_B$$

where  $S$  is a sum of the spin angular momentum and  $g$  is the gyromagnetic ratio, also known as the  $g$ -factor, which is equal to 2.00023 for free electrons. If both the spinning and the orbital motions of electrons are considered, and when they fully contribute to the magnetic moments, the total magnetic moment is given by

$$\mu_{S+L} = \sqrt{4S(S+1) + L(L+1)}\mu_B$$

where  $L$  is a sum of the orbital angular momentum [33].

### 1.3.2. Types of magnetic behaviors

Because magnetic behavior occurs in the atom or ion with unpaired electrons, different types of magnetic states are associated with spin orientations of electrons in the material, as shown in **Figure 1.8**. If the unpaired electron spins are oriented at random directions on the different atoms in one material, it will be paramagnetic (a). When all of the unpaired electron spins align in parallel, the behavior is called ferromagnetic (b). In opposite, the spins are aligned antiparallel. If the moments balance completely resulting in zero overall magnetic moment, the material will be antiferromagnetic (c). Another type occurs in the materials where all of the spins are canted with respect to each other although they are equivalent. This leads to incomplete cancellation of magnetic moments, called canted antiferromagnetic or weak ferromagnetic (d). If the moments of the aligned and anti-aligned are unequal, there is a net magnetic moment and it is named by ferrimagnetic (e) [35].

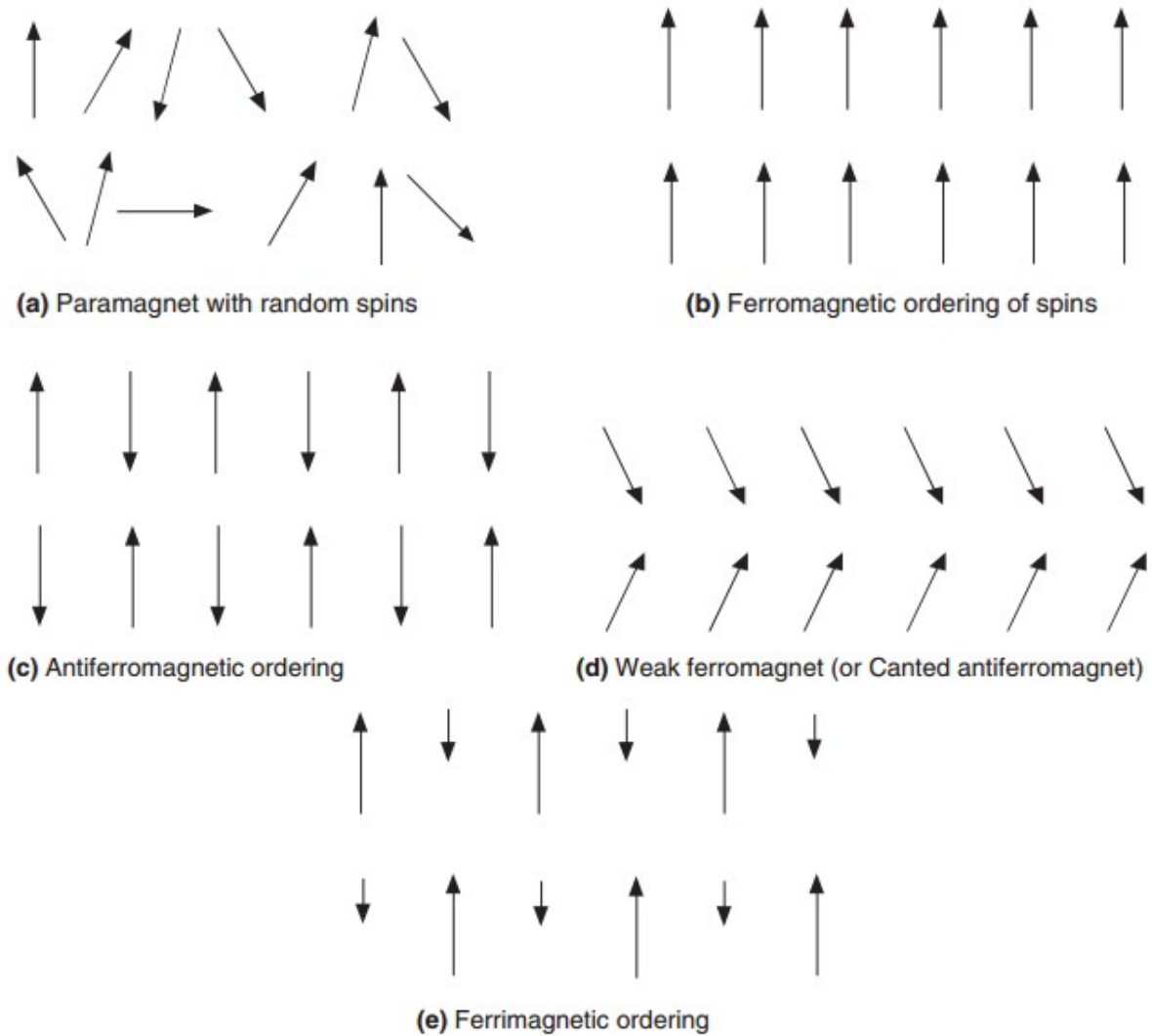


**Figure 1.6.** Schematic magnetic phenomena: (a) paramagnetism; (b) ferromagnetism; (c) antiferromagnetism; (d) canted antiferromagnetism or weak ferromagnetism, and (e) ferrimagnetism [36].

### 1.3.3. Magnetic susceptibility and Curie-Weiss law

For a material, there is no magnetization in free space (vacuum). When it is placed in magnetic field  $\mathbf{H}$ , a magnetization  $\mathbf{M}$  is induced in the material. The magnetization  $\mathbf{M}$  is linearly associated with the magnetic field  $\mathbf{H}$ , given by

$$\mathbf{M} = \chi \mathbf{H},$$

where  $\chi$  is a dimensionless quantity called the magnetic susceptibility. The values  $\chi$  of in

different materials are also different depending on the type of magnetism. In a diamagnetic material,  $\chi$  is very small and negative, indicating that it tends to exclude a magnetic field from its interior. Conversely,  $\chi$  is very small and positive in a paramagnetic one. For ferromagnetic materials,  $\chi > 1$  and such materials are strongly interacted with a magnetic field. If  $\chi$  is comparable to or somewhat less than that for paramagnetic substances, it reflects the antiferromagnetic property [37].

In all of the ferro-, ferri-, and antiferro-magnetic materials, the spins are ordered in some directions, not like the paramagnetic ones where the spins are ordered randomly. However, the spins of these ordered structures will become disordered and the materials will become paramagnetic, above a temperature known as either the Curie temperature,  $T_C$  (ferro- and ferri-magnets), or the Néel point,  $T_N$  (antiferro- and heli-magnets). **Figure 1.11** describes the schematic diagram of the temperature dependence of the magnetic susceptibility of different magnetic behaviors. It can be observed that in ferromagnetic materials,  $\chi$  is very large at low temperatures but decreases increasingly rapidly on heating towards  $T_C$ . Conversely antiferromagnetic substances show very small susceptibilities at low temperatures, which increase with increasing temperature and decrease after reaching a maximum at  $T_N$ .

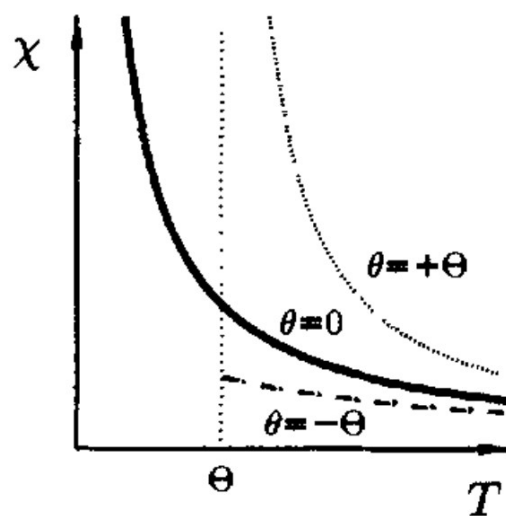
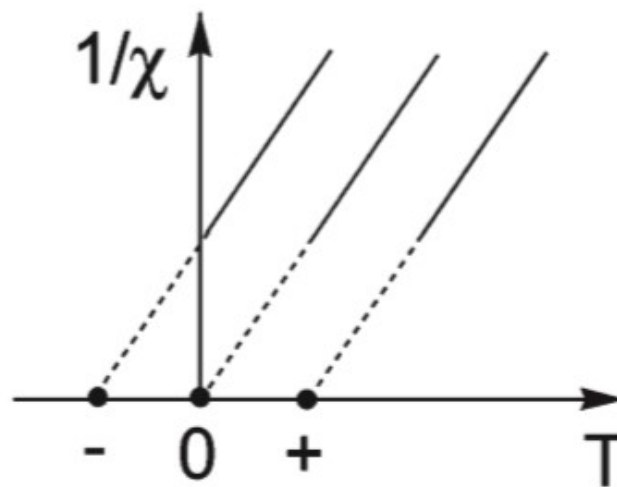


**Figure 1.7.** The temperature dependence of the magnetic susceptibility of paramagnetic, ferromagnetic and antiferromagnetic materials [38].

There is a better fit to the high-temperature behavior in the paramagnetic region often given by the Curie-Weiss law:

$$\chi = \frac{C}{T - \theta}$$

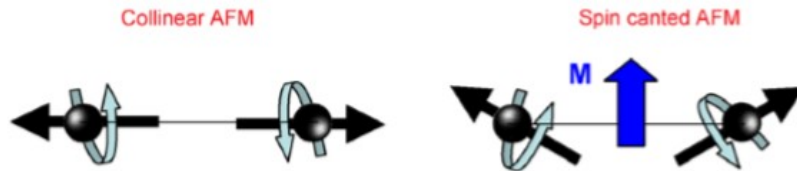
where  $C$  is the Curie constant and  $\theta$  is the Weiss constant. The different types of behavior are shown in **Figure 1.12**, in which  $\chi^{-1}$  is plotted against  $T$ . For paramagnetic materials which show no tendency to magnetic order, the plot extrapolates to 0 K. For the ones which show a tendency to ferromagnetic order,  $\chi$  is higher than the one for the simple paramagnetic case and becomes infinite at a positive value of  $\theta$ . If the paramagnetic substances show a tendency to antiferromagnetic order,  $\chi$  is lower than the one for the simple paramagnetic case and the extrapolated value of  $\theta$  is negative. Based on Curie-Weiss law, the effective moment  $\mu_{\text{eff}}$  can be calculated from the Curie constant by using the equation  $\mu_{\text{eff}} = 2.84\sqrt{\chi(T - \theta)} = 2.84\sqrt{C}$ .



**Figure 1.8.** Schematic diagrams of Curie's law and Curie-Weiss law [39].

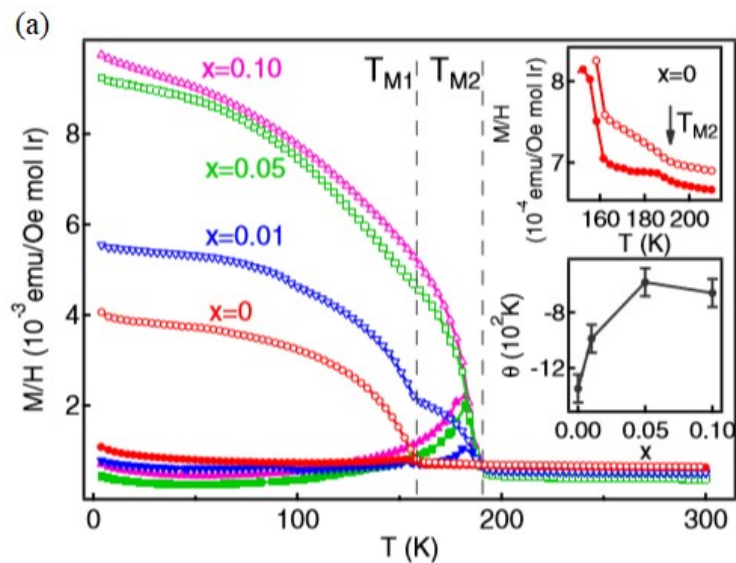
#### 1.3.4. Canted antiferromagnetism or weak ferromagnetism

In antiferromagnetic materials, the magnetic moments aligned antiparallel. Therefore the net magnetization is zero. If there is Dzyaloshinskii-Moriya interaction [40], it favours a slight canting of the magnetic moments, leading to a nonzero net magnetization, as shown in **Figure 1.9**.



**Figure 1.9.** The magnetic moments of antiferromagnetic and canted antiferromagnetic materials [41].

In the canted antiferromagnetic materials, there is always a large hysteresis difference between the zero field cooling (ZFC) and field cooling (FC) magnetic susceptibilities, as shown in **Figure 1.10(a)**. In the magnetization measurements as a function of applied field, there is a hysteresis which do not appear in common antiferromagnetic materials, even though the remanet magnetization is small, as shown in **Figure 1.10(b)**. It probably results from the changes in the domain boundaries or the freezing of free spins at the domain boundaries [42].



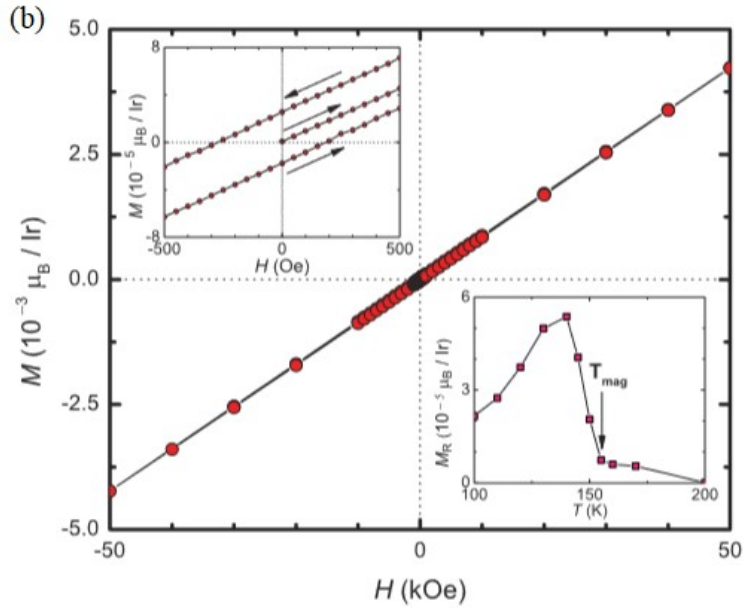


**Figure 1.10.** (a) Temperature dependence of ZFC and FC susceptibilities of  $(Y_{1-x}Ca_x)_2Ir_2O_7$  samples at 1 kOe [43] and (b) magnetization as a function of the applied magnetic field of  $Y_2Ir_2O_7$  at 100 K. Top-left inset: Expanded view of the low field. Bottom-right inset: Temperature dependence of the remanent magnetization. [42].

## 1.4. Magnetic interaction

### 1.4.1. Exchange interaction

Magnetic ordering results from the electrostatic interactions at a quantum mechanical level. The exchange interaction describes the magnetic moments interacted mutually through a quantum mechanical force.

If the electrons on neighbouring magnetic atoms interact directly by exchange interactions without the intermediary, it is known as direct exchange. However, direct exchange cannot be an important mechanism for the magnetic behavior because there is not sufficient direct overlap between the neighbouring magnetic orbitals. Thus some kinds of indirect exchange interactions are considered in many magnetic materials.

### 1.4.2. Superexchange

Superexchange, which is one type of indirect interactions, can be defined as an indirect exchange interaction between non-neighbouring magnetic ions. This interaction is mediated by a non-magnetic ion between the two magnetic ions. It occurs because there is a kinetic energy advantage for antiferromagnetism, as shown in **Figure 1.11**. In ferromagnetic substances, the moments of magnetic ions are aligned parallel. Thus the ground state is not able to mix with excited configurations which are prevented by the Pauli exclusion principle. Conversely, the moments of magnetic ions are aligned antiparallel in antiferromagnetic materials. The ground state can mix with excited configurations therefore lowering the kinetic energy.

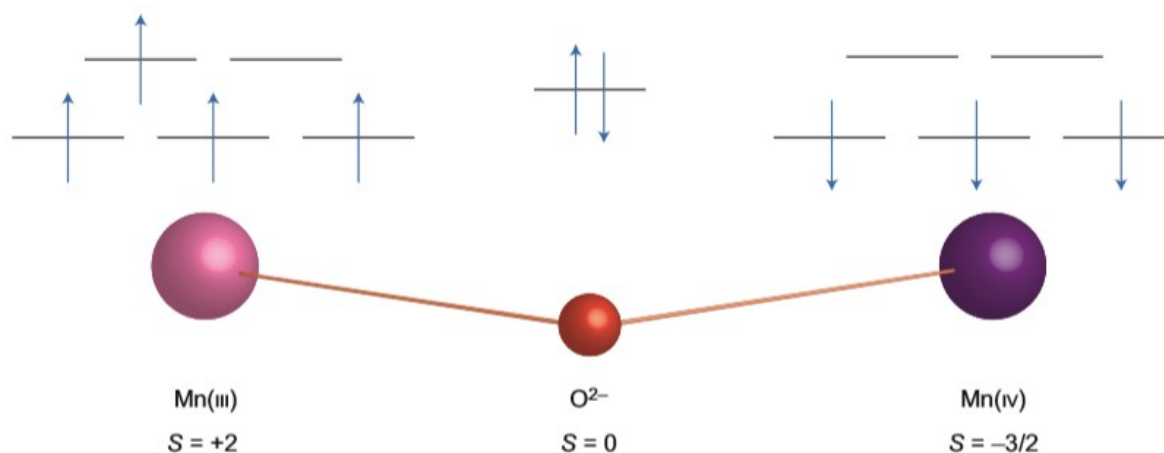


**Figure 1.11.** Schematic diagrams of superexchange in a magnetic oxide [44].

### 1.4.3. Double exchange

Besides superexchange, there is another interaction which occurs in some oxides because the magnetic ion can show mixed valency, known as double exchange [45]. **Figure 1.12** shows the process of double exchange in the oxide compound containing Mn<sup>3+</sup> and Mn<sup>4+</sup>. If oxygen ion gives up the spin-up electron to Mn<sup>4+</sup>, another spin-up will transfer from Mn<sup>3+</sup> to this oxygen ion and fill its vacant orbital. Because of the Hund's rules, it is not energetically favourable for an  $e_g$  electron transform to the neighbouring magnetic ion where the  $t_{2g}$  spins

are antiparallel to the  $e_g$  electron. Ferromagnetic alignment of the neighbouring ions is required in order to reduce the overall energy.

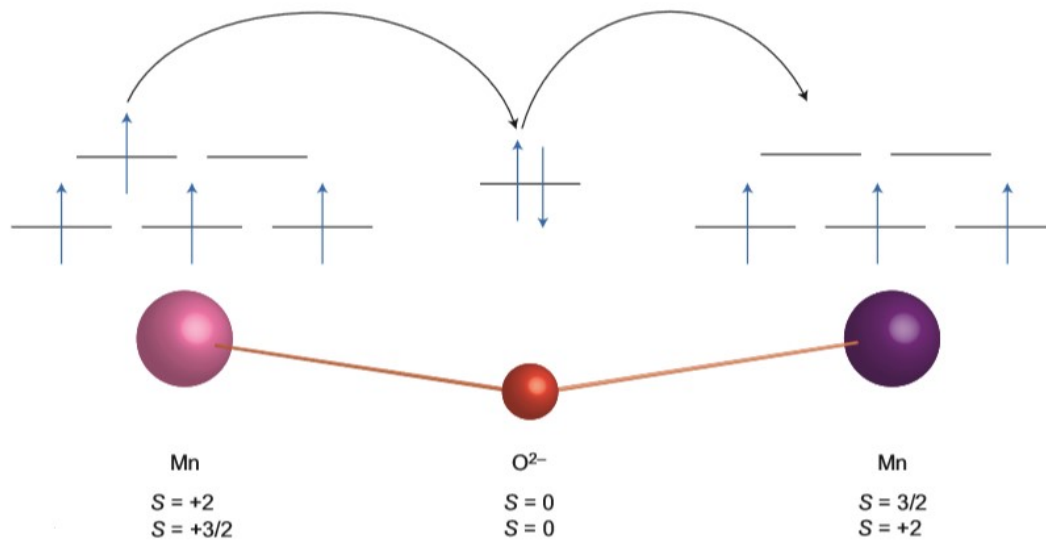


**Figure 1.12.** Schematic diagram of double exchange [44].

## 1.5. Cation ordering in perovskites

### 1.5.1. Types of ordering in perovskites

There are three simple types of ordering in perovskites, namely (111) rock salt, (110) columnar, and (100) layered arrangements. All of the three types have been observed in double perovskites, as shown in **Figure 1.13**. The most symmetric one is called rock salt ordering because the arrangement of B and B' (or A and A') cations is similar with the positions in the rock salt structure. And it can be thought of as 0D since each  $BX_6$  octahedra (or A cation) is isolated from all other  $B'X_6$  octahedra (or A' cation) by  $BX_6$  octahedra (or A cation). Columnar ordering corresponds to 1D ordering because the  $BX_6$  octahedra (or A cation) is allowed to connect with other  $BX_6$  octahedra (or A cation) in one dimension. Layered ordering can be thought of as 2D ordering because it allows for connectivity of the  $BX_6$  octahedra (or A cation) in two dimensions, thereby forming layers of the ordering.

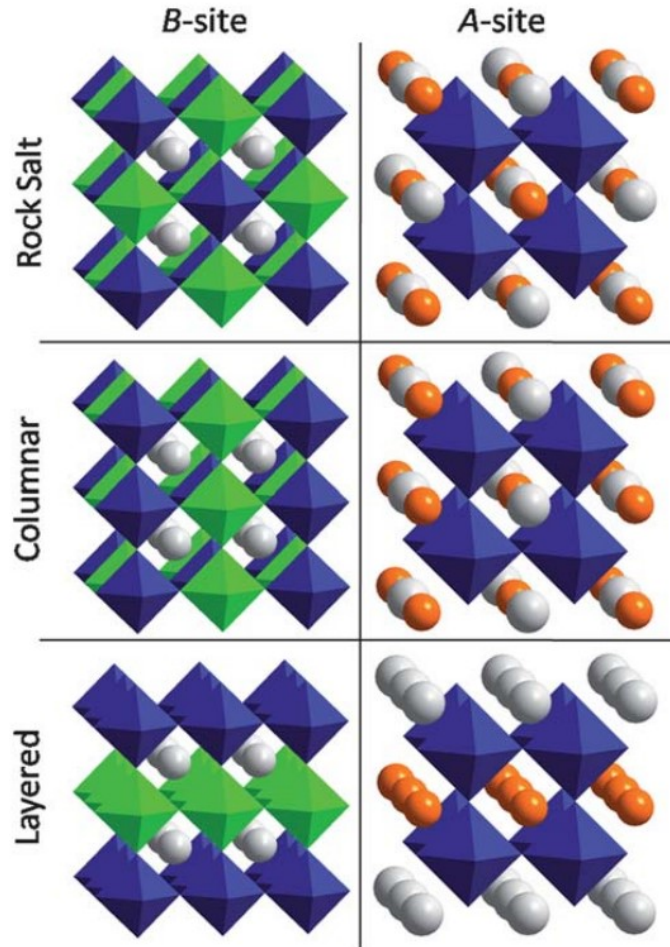


**Figure 1.13.** Cation ordering schemes in perovskites. From top to bottom 0D (rock salt), 1D (columnar ordering) and 2D (layered ordering) are shown for B-site ordering in  $A_2BB'X_6$  perovskites (left) and for A-site ordering in  $AA'B_2X_6$  perovskites (right) [1].

### 1.5.2. B-site cation ordering in perovskite oxides

Large numbers of B-site-ordered perovskite oxides have researched [17,46]. In a simple  $ABO_3$  perovskites, the B-B interaction contributes predominantly to the physical properties. For instance,  $Cr^{3+}(d^3)-O-Cr^{3+}(d^3)$  and  $Fe^{3+}(d^5)-O-Fe^{3+}(d^5)$  superexchange interactions lead to the antiferromagnetic properties of  $LaCrO_3$  and  $LaFeO_3$ , respectively [47-49]. In double perovskite oxides  $A_2BB'O_6$ , B-B' interactions have an effect on the properties, instead of the B-B interaction in  $ABO_3$  compounds. This can be understood via the Goodenough-Kanamori rules [50,51]. For example, in  $La_2CrFeO_6$  show ferromagnetism attributed to  $Cr^{3+}(d^3)-O-Fe^{3+}(d^5)$  superexchange interaction [52]. There are four factors which control B-cation

arrangement, that is the charge, ionic radius, and electron coordination of the B-cations, and the A/B size ratio [17].

The rock salt ordering is the most favourable for B-B' interaction because each B cation is surrounded by six B' cations [1]. In columnar ordering, each B cation has four B and two B' neighbours, so it is the next best arrangement, for example  $\text{LnCaMn}^{3+}\text{Mn}^{4+}\text{O}_6$  [53] and  $\text{NaSrMn}^{3+}\text{Mn}^{4+}\text{O}_6$  [54], where Jahn-Teller distortions of the B cations (e.g.  $\text{Mn}^{3+}$ ) stabilize the ordering. Layered ordering is the most unfavourable because each B cation has only two B cations as its nearest neighbours, such as  $\text{La}_2\text{CuZrO}_6$  [55] and  $\text{La}_2\text{CuSnO}_6$  [56] whose unusual layered ordering is stabilized by Jahn-Teller distortion of the  $\text{Cu}^{2+}$  cations.

### 1.5.3. A-site cation ordering in perovskite oxides

In perovskite oxides  $\text{AA}'_3\text{B}_4\text{O}_{12}$ , there is a unusual-ordered arrangement of the A'-site ions, which is much less common than B-site cation ordering. It always occurs when Jahn-Teller distorted ions occupy the A'-site such as  $\text{Cu}^{2+}$  and  $\text{Mn}^{3+}$  form square-coordinated units which align perpendicularly to each other, as shown in **Figure 1.14**. In the cubic perovskite structure, there is significant tilting of the corner-sharing  $\text{BO}_6$  octahedra. In most cases the tilting does not remove the crystallographic equivalence of the A-site cations. However, they create holes of different size within the corner sharing  $\text{BO}_3$  network in order to stabilize A-site ordering. The  $a^+a^+a^+$  tilting is the most common, making the cubic symmetry intact and doubling the length of the cell edge [1]. Although the A'A' interaction contribute to the properties of A-site ordered  $\text{AA}'_3\text{B}_4\text{O}_{12}$ , this interaction is not only determined by the intrinsic properties of A' cations, but also influenced by the B-site cations, no matter whether they are magnetic ions or not [57].

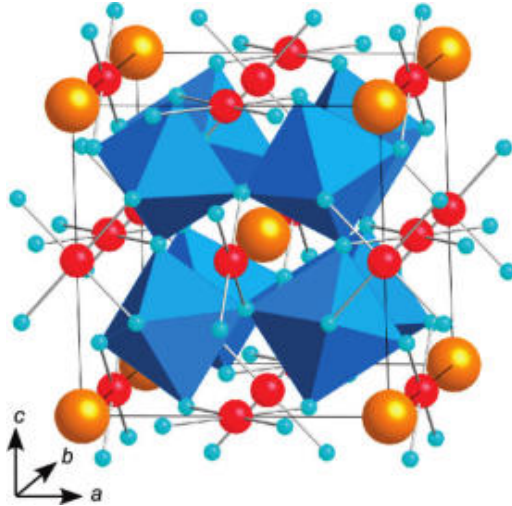


**Figure 1.14.** Crystal structure of  $AA_3B_4O_{12}$ . The A cation (large sphere) and A' cation (middle sphere) are ordered at the A site at a ratio of 1:3, and the B-site cations form  $BO_6$  octahedra in a cubic  $ABO_3$  perovskite structure [57].

Unlike B-site cations which favour rock salt ordering, layered ordering is the most favourable for A-site cations. In rock salt ordering perovskites, each anion is surrounded by two A and two A' cations in a *trans* configuration, as shown in **Figure 1.15a**. There will be a topological argument that the anion is not able to shift in response to an A/A' size differential. However in layered ordering perovskites, two A and two A' cations coordinate the anion in *cis* configuration, and therefore the anion is free to displace if A and A' have different radii, as shown in **Figure 1.15b** [1].

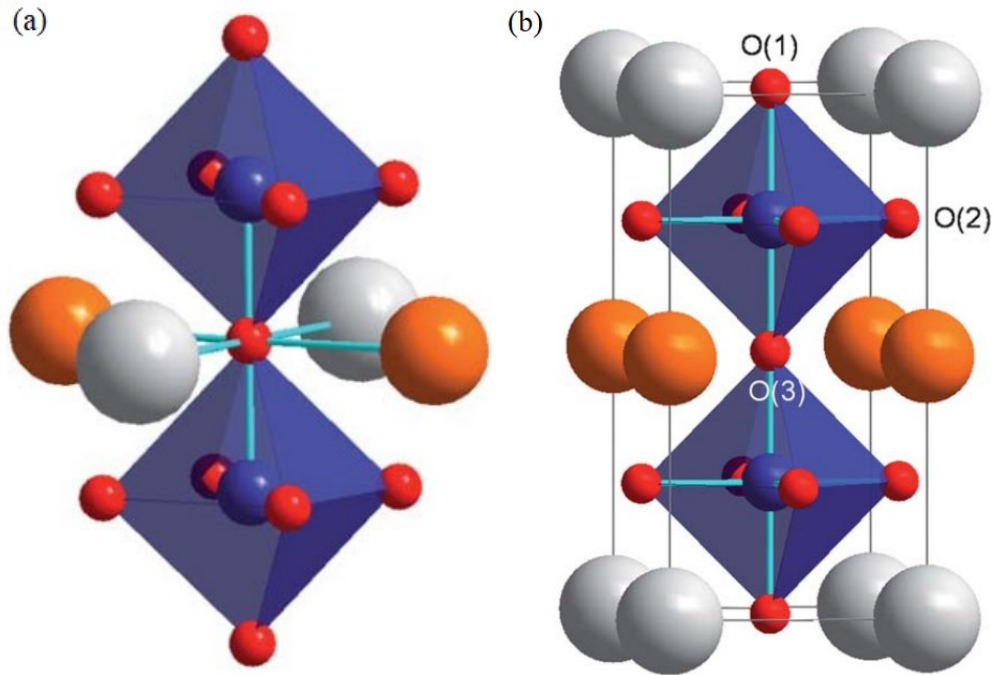


**Figure 1.15.** The anion environment in a rock salt ordered (a) and layered ordered (b)  $AA'B_2O_6$  perovskites. The color scheme for the ions is grey (A), orange (A'), blue (B), and red(O) [1].

In quadruple perovskite  $AA'_3B_2B'_2O_{12}$ , body centered A/A' ordering and rocksalt B/B' ordering occur simultaneously, indicating that it combines the advantages of an A-site-ordered  $AA'_3B_4O_{12}$  perovskite and a B-site-ordered  $A_2BB'O_6$  double perovskite (shown in **Figure 1.16**). Because of the rock salt B-site ordering, the symmetry is reduced to  $Pn\bar{3}$ . Because there are multiple magnetic interactions of A', B, and B' cations (A'-A', A'-B, A'-B', B-B, B-B', and B'-B'), the properties of quadruple perovskite  $AA'_3B_2B'_2O_{12}$  are affected by some factors.

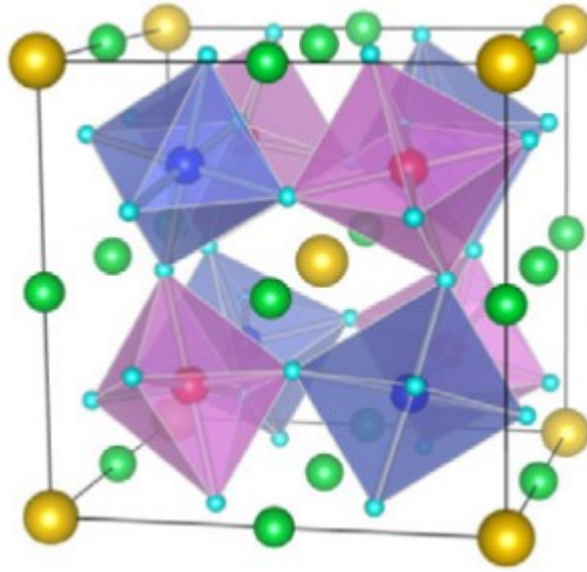


**Figure 1.16.** Crystal structures of A- and B-site-ordered quadruple perovskite with the formula of  $AA'_3B_2B'_2O_{12}$ . A-site ions (yellow spheres) and A'-site ions (green spheres) are ordered at the ratio of 1:3. B-site ions (blue spheres) and B'-site ions (red spheres) form  $BO_6$  and  $B'O_6$  octahedra and the octahedra are arranged in a rock salt type [26].

## 1.6. Magnetoresistance

Magnetoresistance is the tendency of a substance to change the electric resistance in response to an applied magnetic field. Some occur in the non-magnetic metals and semiconductors, such as geometrical magnetoresistance [58]. Other occur in magnetic metals, such as anisotropic magnetoresistance [59].

There is a further example of the diversity of MR phenomena, called colossal magnetoresistance, CMR. It is observed in complex perovskites such as  $(Pr_{0.7}Ca_{0.3})MnO_3$  [60], as shown in **Figure 1.17**. It is related to a metal-insulator transition which appears under high applied fields near the Curie temperature,  $T_C$ . In **Figure 1.17**, the resistivity of  $(Pr_{0.7}Ca_{0.3})MnO_3$  is measured at 4.2 K. In the range 3-6 T,  $(Pr_{0.7}Ca_{0.3})MnO_3$  has a transition from an insulating antiferromagnet to a metallic ferromagnet.

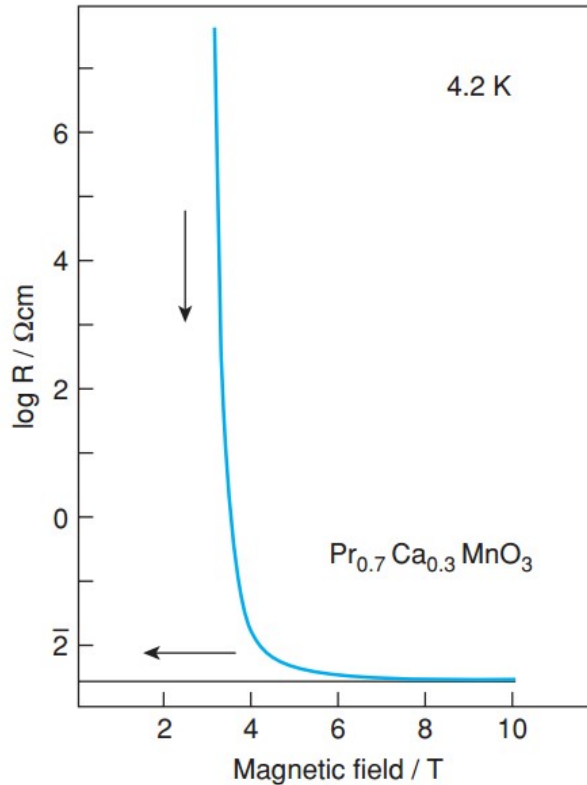


**Figure 1.17.** Dramatic decrease in resistivity of  $(\text{Pr}_{0.7}\text{Ca}_{0.3})\text{MnO}_3$  in response to an applied magnetic field [60].

## 1.7. Ferroelectricity and Multiferroics

If a substance has a spontaneous electric polarization which can be reversed by the applied electric field, it exhibits a ferroelectric property. The ferroelectric materials have high permittivities, the reversibility of the polarisation under the action of an applied reverse electric field, and the possibility of retaining electrical polarisation after an applied electric field switching. These characteristics give rise to a polarisation,  $P$ , vs the electric field,  $V$ , hysteresis loop, as shown in **Figure 1.18a**. Like ferromagnetic, the ferroelectric state is always a low-temperature condition and transform into paraelectric state above a certain temperature, ferroelectric Curie temperature  $T_C$ . The curve of dielectric constants  $\epsilon'$  vs  $T$  is shown in **Figure 1.18b**. Above  $T_C$ ,  $\epsilon'$  is given by the Curie-Weiss law:

$$\epsilon' = C/(T - \theta)$$

where  $C$  is the Curie constant and  $\theta$  is the Curie-Weiss temperature, as shown in **Figure 1.18c**.

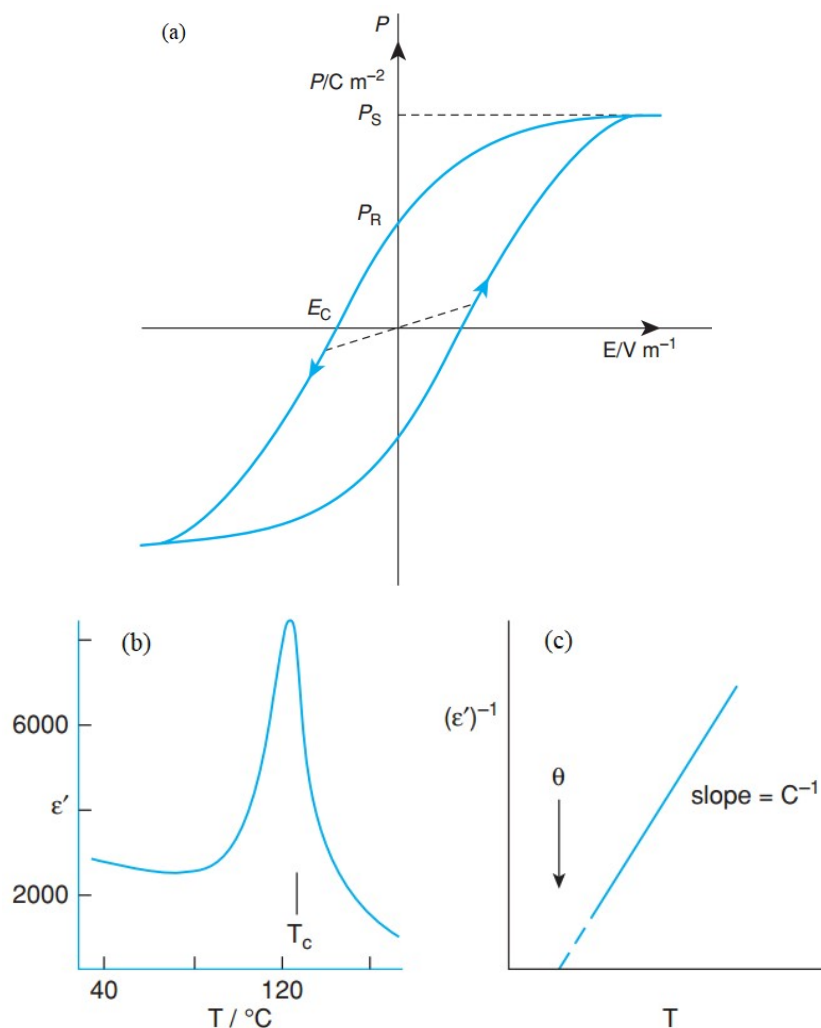


**Figure 1.18.** (a) Hysteresis loop of a ferroelectric. (b) Dielectric constant of  $\text{BaTiO}_3$ . (c) Curie-Weiss plot [35].

Multiferroics are materials which exhibit more than one type of ferroic order, including ferromagnetic, ferroelectric, and ferroelastic. The materials, which ferromagnetic and ferroelectric at the same time, and in particular if there is coupling between the two properties, are paid most attention to. However, ferroelectricity occurs only in non-centrosymmetric structures whereas a centrosymmetric environment is favorable for magnetic ions. Thus, ferroelectricity and magnetism are difficult to coexist [61]. Some multiferroic materials have

been researched, such as BiFeO<sub>3</sub> [62,63] and TbMnO<sub>3</sub> [64,65].

## 1.8. The perovskite manganites

Mn<sup>3+</sup> cation has the  $e_g^1 t_{2g}^3$  electronic configuration, and degenerates  $e_g$  orbitals in the cubic crystal field. Thus, it always exhibits the Jahn-Teller distorted driven polarization of the two relevant  $e_g$   $d_{x^2-y^2}$  or  $d_{3z^2-r^2}$  orbitals in the MnO<sub>6</sub> octahedra [25,66]. Mn<sup>3+</sup> cation has been widely used for B-site in ABO<sub>3</sub> [64,65] and A<sub>2</sub>BB'O<sub>6</sub> [15], and even A-site in AA'B<sub>4</sub>O<sub>12</sub> [67-69], as shown in **Figure 1.19**.

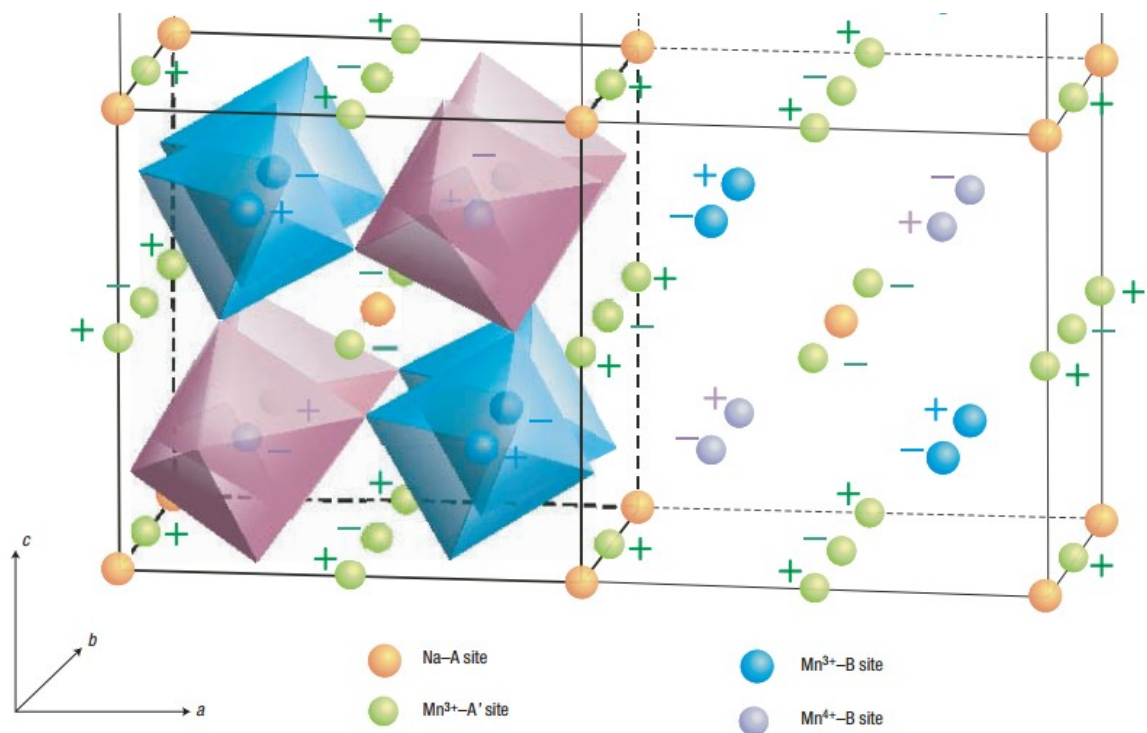


**Figure 1.19.** Crystal structure of (NaMn<sub>3</sub>)Mn<sub>4</sub>O<sub>12</sub> [67].

### 1.8.1. RMnO<sub>3</sub> perovskites

RMnO<sub>3</sub> perovskites have been paid attention to because they exhibit a variety of unusual states. They have the orthorhombic structure (space group *Pbnm*), for example LaMnO<sub>3</sub> (**Figure 1.20**). The Jahn-Teller distortion of the MnO<sub>6</sub> octahedra has a strong effect on the distortion from the ideal cubic structure in RMnO<sub>3</sub> perovskites [70]. Besides that, the

mismatch of the  $R$ -O and Mn-O equilibrium bond lengths is also able to influence the structure distortion because there will be a cooperative rotation of the  $MnO_6$  octahedra in the lattice for the mismatch. And increasing ionic radius of  $R$  will decrease the rotation or tilting [71].

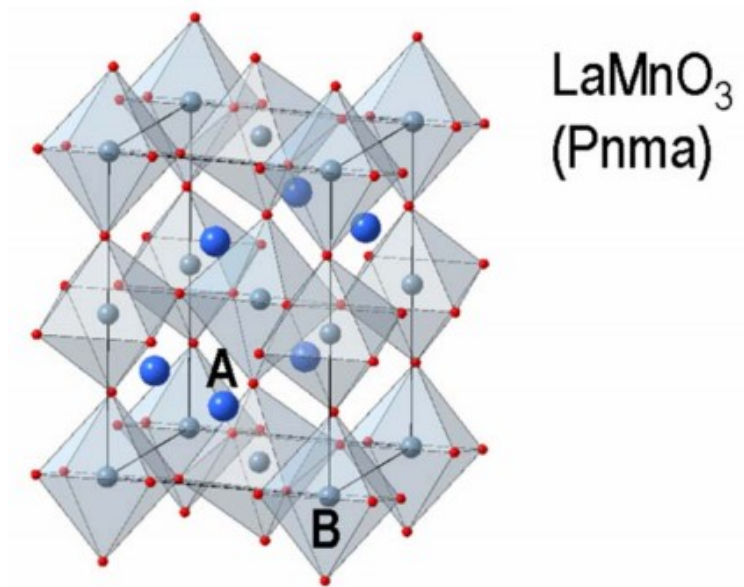


**Figure 1.20.** The structure of  $LaMnO_3$  [72].

Recently, multiferroicity has been found in  $TbMnO_3$  [64] and  $DyMnO_3$  [73]. For example,  $TbMnO_3$  also has orthorhombic structure at room temperature. But there are not 6s lone pairs, which produce a polar structure in ferroelectric materials  $BiMnO_3$  and  $BiFeO_3$  [64]. In  $TbMnO_3$ , the magnetoelastically induced lattice modulation accompanies the modulated magnetic structure, leading to the magnetoelectric and magnetocapacitance effects. In addition, magnetoresistance has been found in some manganese-based perovskite oxides, for example  $R_{1-x}M_xMnO_3$  [74,75], where  $R$  is a trivalent lanthanide cation and  $M$  is a divalent cation, as shown in **Figure 1.21**. The possible mechanism is the double-exchange interaction between heterovalent  $Mn^{3+}$ ,  $Mn^{4+}$  neighbours [74].

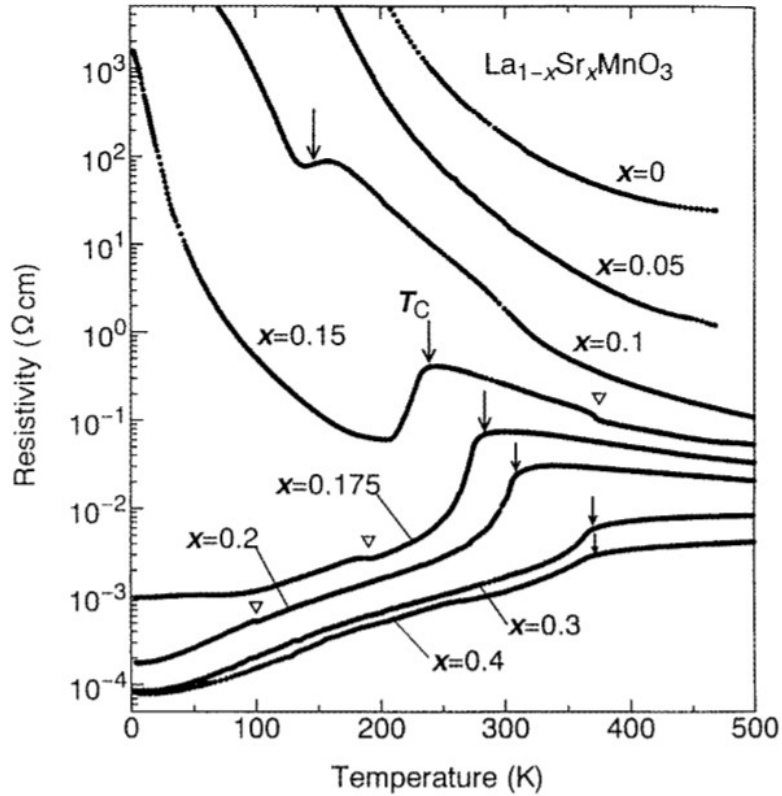


**Figure 1.21.** Resistivity against  $T$  for  $\text{La}_{1-x}\text{Sr}_x\text{MnO}_3$  [74].

### 1.8.2. $\text{RMn}_7\text{O}_{12}$ perovskites

Recently,  $\text{LaMn}_7\text{O}_{12}$  has been found since there is an unusual magnetic C-type structure which is composed of ferromagnetically coupled antiferromagnetic planes [72]. In this pseudocubic  $\text{LaMn}_7\text{O}_{12}$ , there is a network of corner-sharing  $\text{MnO}_6$  tilted octahedra, with the Jahn-Teller stom  $\text{Mn}^{3+}$ . The octahedral  $\text{Mn}^{3+}$  ions results in the unique magnetic structure of  $\text{LaMn}_7\text{O}_{12}$ , as shown in **Figure 1.22**.

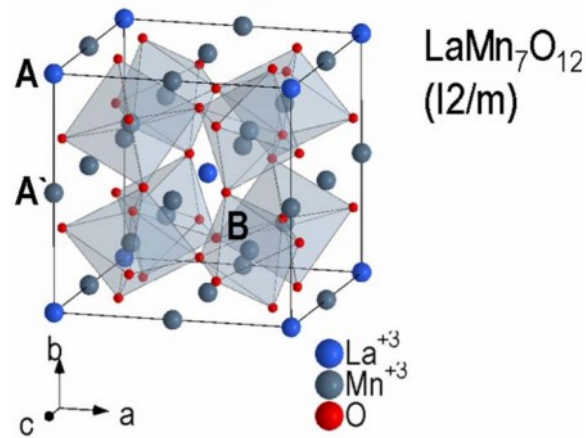


**Figure 1.22.** The structure of  $\text{AA}'_3\text{B}_4\text{O}_{12}$ -type compounds  $\text{LaMn}_7\text{O}_{12}$  [72].

After adding some other cations in  $\text{RMn}_7\text{O}_{12}$ , for instance  $\text{La}(\text{Cu}_{3-x}\text{Mn}_x)\text{Mn}_4\text{O}_{12}$  ( $x = 1, 2$ ) [76], there will be some interesting phenomena. The structure changed from  $I2/m$  for  $\text{LaMn}_7\text{O}_{12}$  to  $Im-3$  for  $\text{La}(\text{Cu}_{3-x}\text{Mn}_x)\text{Mn}_4\text{O}_{12}$ , as shown in **Figure 1.23a**. The neutron diffraction data of  $\text{La}(\text{Cu}_{3-x}\text{Mn}_x)\text{Mn}_4\text{O}_{12}$  indicated there is a globally ferromagnetic structure, as shown in **Figure 1.23b**. Moreover, the transition temperature  $\text{La}(\text{Cu}_{3-x}\text{Mn}_x)\text{Mn}_4\text{O}_{12}$  also depends the value of  $x$  ( $T_C = 310$  K for  $x = 1$  and  $T_C = 150$  K for  $x = 2$ ). Recently, Alexei et al [66] have found quadruple perovskite  $\text{BiCuMn}_6\text{O}_{12}$  of which the structure will change with decreasing the temperature, as shown in **Figure 1.24**. These results reveal that doped perovskites may exhibit some unique properties.

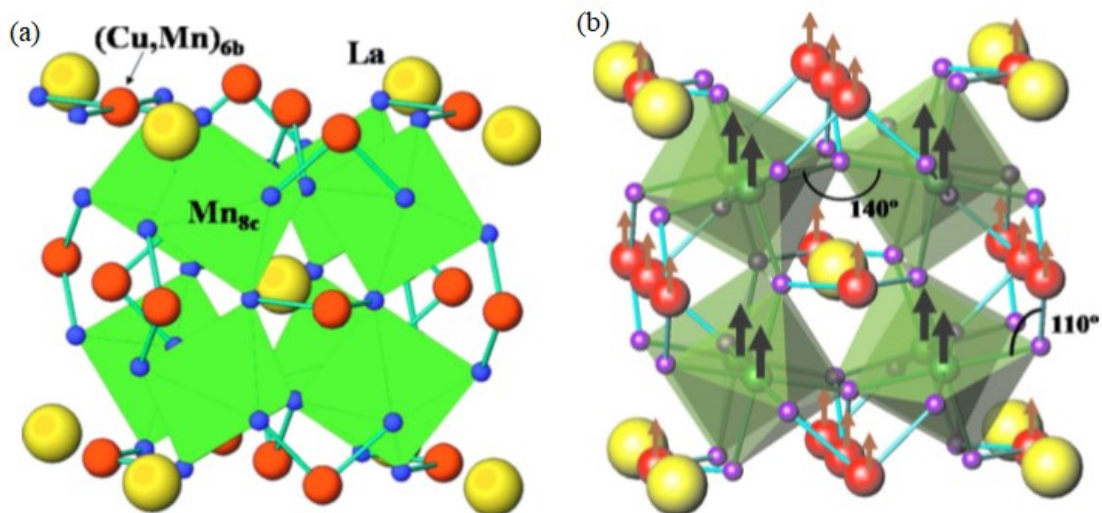


**Figure 1.23.** The view of the crystallographic (a) and magnetic (b) structure of  $\text{La}(\text{Cu}_{3-x}\text{Mn}_x)\text{Mn}_4\text{O}_{12}$  ( $x = 1, 2$ ) [76].

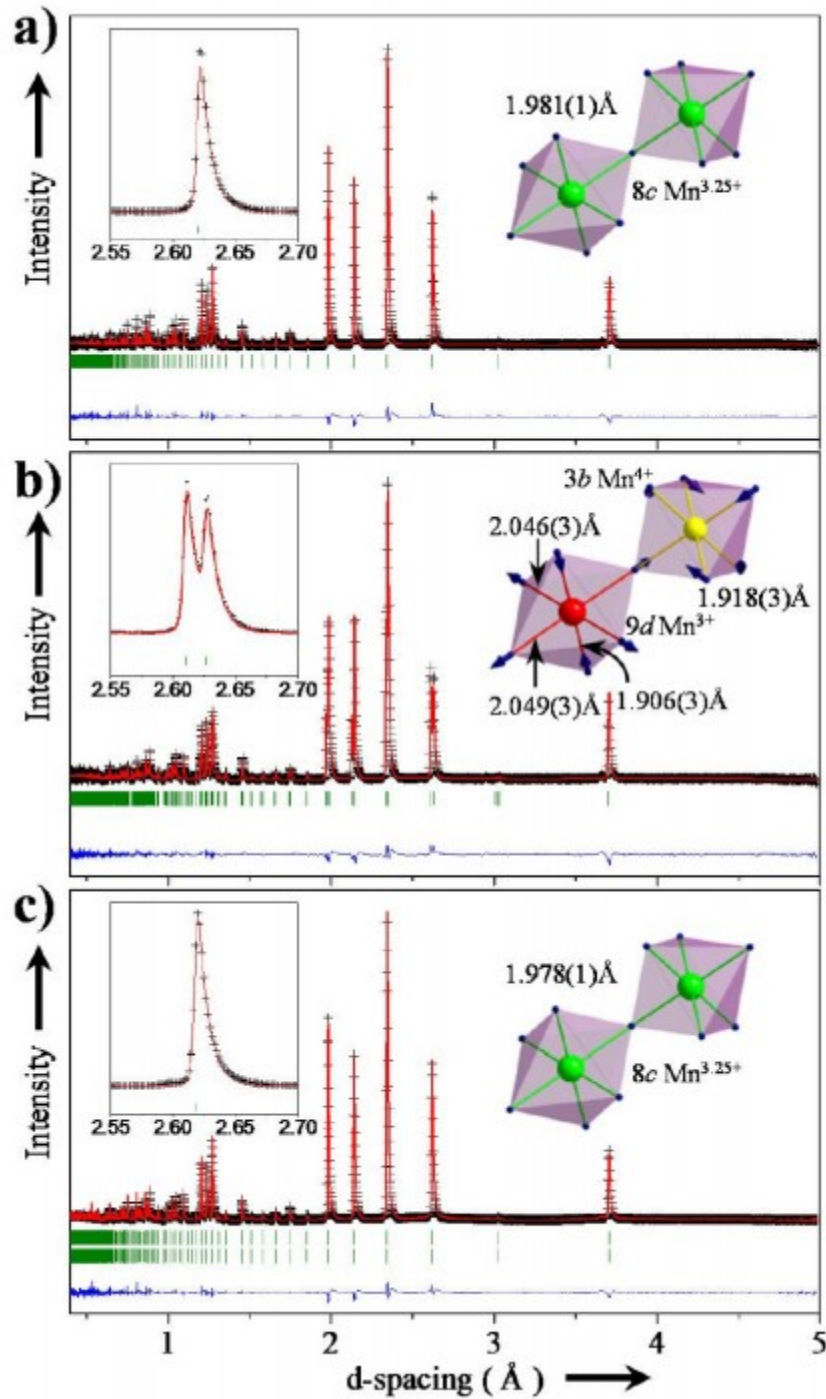


**Figure 1.24.** The neutron diffraction data of  $\text{BiCuMn}_6\text{O}_{12}$  at (a)  $T = 317 \text{ K}$ , (b)  $T = 248 \text{ K}$ , and (c)  $T = 1.5 \text{ K}$  [66].

## 1.9. Objectives of this thesis

In this thesis,  $\text{Mn}_2\text{O}_3$  and the oxide of rare earth element or  $\text{Y}_2\text{O}_3$  were used for fabrication of the new perovskite oxides.

### (i) Crystal structure and physical properties of new $\text{RMn}_3\text{O}_6$ perovskites.

$\text{R}_2\text{O}_3 - \text{Mn}_2\text{O}_3$  (R = rare earth elements) system has been widely researched. There has been two classical series:  $\text{RMnO}_3$  and  $\text{RMn}_7\text{O}_{12}$ , as shown in **Figure 1.19**. In  $\text{RMnO}_3$ ,  $\text{Mn}^{3+}$  cations occupy B-site by the formation of  $\text{MnO}_6$  octahedra. In  $\text{RMn}_7\text{O}_{12}$ ,  $\text{Mn}^{3+}$  cations occupy both A-site and B-site in the sublattice. In this thesis,  $\text{R}_2\text{O}_3$  and  $\text{Mn}_2\text{O}_3$  were used for the reactions by the ratio of 1:3. And the crystal structure and physical properties were investigated. The detailed study will be discussed in **Chapter 3**.

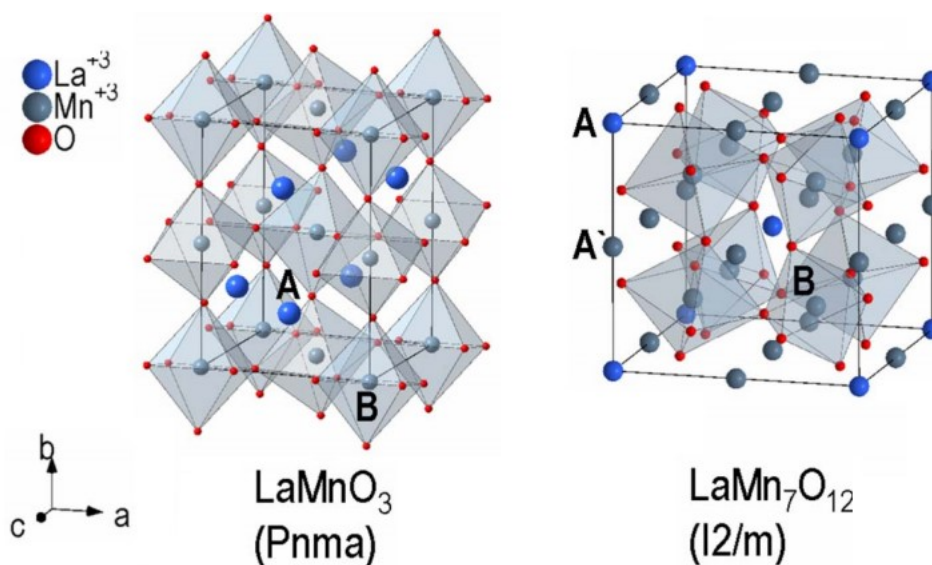


**Figure 1.25.** Nuclear structure of  $\text{LaMnO}_3$  and  $\text{LaMn}_7\text{O}_{12}$  [72].

### (ii) Crystal structure and physical properties of Cu-doped $\text{RMn}_7\text{O}_{12}$ perovskites.

$\text{Cu}^{2+}$  cation has the  $d^9$  electronic configuration, and also degenerates  $e_g$  orbitals in the cubic crystal field. Like  $\text{Mn}^{3+}$ , it usually exhibits the Jahn-Teller distorted environment, too [66]. For  $\text{CaMn}_7\text{O}_{12}$ , the average oxidation state of the B cation is +3.25 because  $\text{A} = \text{Ca}^{2+}$  and  $\text{A}' = \text{Mn}^{3+}$ . There is a charge-order transition between  $[\text{Ca}^{2+}\text{Mn}^{3+}_3]_{\text{A}}[\text{Mn}^{4+}\text{Mn}^{3+}_3]_{\text{B}}\text{O}_{12}$  (space group  $R-3$ ) and  $[\text{Ca}^{2+}\text{Mn}^{3+}_3]_{\text{A}}[\text{Mn}^{3.25+}_4]_{\text{B}}\text{O}_{12}$  (space group  $\text{Im}-3$ ), with an unusual Jahn-Teller

distortion appearing at the B-site [77]. In this thesis, CuO was used for doping  $\text{CeMn}_7\text{O}_{12}$ . And the crystal structure, charge-order transition, and physical properties were investigated. The detailed study will be discussed in **Chapter 4**.

### **(iii) Crystal structure and physical properties of Mn-doped $\text{RMnO}_3$ perovskites.**

$\text{RMnO}_3$  perovskites exhibit some unique properties, such as colossal magnetoresistance [60] and multiferroicity [64,65]. Because of the electronic configuration of  $\text{Mn}^{3+}$  cation, it can occupy A-site in some perovskites, such as  $\text{RMn}_7\text{O}_{12}$  [25,24]. In this thesis,  $\text{Mn}_2\text{O}_3$  was used for doping  $\text{RMnO}_3$ . And the crystal structure and physical properties were investigated. The detailed study will be discussed in **Chapter 5**.

## **References in chapter 1**

- [1] King, G.; Woodward, P. M. Cation ordering in perovskite. *J. Mater. Chem.* **2010**, *20*, 5785-5796.
- [2] Zhao, X.; Park, N.-G. Stability issues on perovskite solar cells. *Photonics* **2015**, *2*(4), 1139-1151.
- [3] Kojima, A.; Teshima, K.; Shirai, Y.; Miyasaka, T. Organometal halide perovskite as visible-light sensitizers for photovoltaic cells. *J. Am. Chem. Soc.* **2009**, *131*(17), 6050-6051.
- [4] Wang, H.; Lin, H.; Piao, X.; Tian, P.; Fang, M.; An, X.; Luo, C.; Qi, R.; Chen, Y.; Peng, H. Organometal halide perovskite nanocrystals embedded in silicone resins with bright luminescence and ultrastability. *J. Mater. Chem. C* **2017**, *5*, 12044-12049.
- [5] Lee, J.-W.; Seol, D.-J.; Cho, A.-N.; Park, N.-G. High-efficiency perovskite solar cells based on the black polymorph of  $\text{HC}(\text{NH}_2)_2\text{PbI}_3$ . *Adv. Mater.* **2014**, *26*, 4991-4998.
- [6] Sekimoto, T.; Suzuka, M.; Yokoyama, T.; Uchida, R.; Machida, S.; Sekiguchi, T.; Kawano,

K. Energy level diagram of  $\text{HC}(\text{NH}_2)_2\text{PbI}_3$  single crystal evaluated by electrical and optical analyses. *Phys. Chem. Chem. Phys.* **2018**, *20*, 1373-1380.

[7] Kubicek, M.; Bork, A. H.; Rupp, J. L. M. Perovskite oxides - a review on a versatile material class for solar-to-fuel conversion processes. *J. Mater. Chem. A* **2017**, *5*, 11983-12000.

[8] Desgardin, H. M. G.; Raveau, B. Improved Lead Perovskite Compounds (PFn-PFt) for  $\text{Z}_5\text{UCapacitor}$  Applications. *Adv. Ceramic Mater.* **1988**, *3*(1), 32-37.

[9] Zhou, S.; Li, L.; Yu, H.; Chen, J.; Wong, C.-P.; Zhao, N. Thin film electrochemical capacitors based on organolead triiodide perovskite. *Adv. Elec. Mater.* **2016**, *2*(7), 1600114.

[10] Wang, Y. S.; Bennema, P.; Zheng, M. N.; Fu, C. M.; van der Linden, P. A mechanism of high- $T_c$  superconductivity relating to perovskite crystal structure. *Cryst. Res. Technol.* **1993**, *28*(7), 1015-1020.

[11] Raveau, B.; Maignan, A.; Martin, C.; Hervieu, M. Ru doping of perovskite manganites: an effective route to ferromagnetism, metallicity, and CMR. *Journal of Superconductivity* **2001**, *14*(2), 217-229.

[12] Gupta, S.; Bendikov, T.; Hodes, G.; Cahen, D.  $\text{CsSnBr}_3$ , a lead-free halide perovskite for long-term solar cell application: insights on  $\text{SnF}_2$  addition. *Acs Energy Letters* **2016**, *1*(5), 1028-1033.

[13] Stølen, S.; Bakken, E.; Mohn, C. E. Oxygen-deficient perovskites: linking structure, energetics and ion transport. *Phys. Chem. Chem. Phys.* **2006**, *8*, 429-447.

[14] Kobayashi, K.-I.; Kimura, T.; Sawada, H.; Terakura, K.; Tokura, Y. Room-temperature magnetoresistance in an oxide material with an ordered double-perovskite structure. *Nature*

1998, 395, 677-680.

[15] Yi, W.; Princep, A. J.; Guo, Y.; Johnson, R. D.; Khalyavin, D.; Manuel, P.; Senyshyn, A.; Presniakov, I. A.; Sobolev, A. V.; Matsushita, Y.; Tanaka, M.; Belik, A. A.; Boothroyd, A. T.  $\text{Sc}_2\text{NiMnO}_6$ : a double-perovskite with a magnetodielectric response driven by multiple magnetic orders. *Inorg. Chem.* **2015**, *54*, 8012-8021.

[16] Lee, N.; Choi, H. Y.; Jo, Y. J.; Seo, M. S.; Park, S. Y.; Choi, Y. J. Strong ferromagnetic-dielectric coupling in multiferroic  $\text{Lu}_2\text{CoMnO}_6$  single crystals. *App. Phys. Lett.* **2014**, *104*, 112907.

[17] Anderson, M. T.; Greenwood, K. B.; Taylor, G. A.; Peoppelmeier, K. R. B-cation arrangements in double perovskites. *Prog. Solid St. Chem.* **1993**, *22*, 197-233.

[18] Marezio, M.; Dernier, P. D.; Chenavas, J.; Joubert, J. C. High pressure synthesis and crystal structure of  $\text{NaMn}_7\text{O}_{12}$ . *J. Solid State Chem.* **1973**, *6*, 16-20.

[19] Subramanian, M. A.; Li, D.; Duan, N.; Reisner, B. A.; Sleight, A. W. High dielectric constant in  $\text{ACuTi}_4\text{O}_{12}$  and  $\text{ACu}_3\text{Ti}_3\text{FeO}_{12}$  phases. *J. Solid State Chem.* **2000**, *151*(2), 323-325.

[20] Homes, C. C.; Vogt, T.; Shapiro, S. M.; Wakimoto, S.; Ramirez, A. P. Optical response of high-dielectric-constant perovskite-related oxide. *Science* **2001**, *293*, 673-676.

[21] Mezzadri, F.; Calestani, G.; Calicchio, M.; Gilioli, E.; Bolzoni, F.; Cabassi, R.; Marezio, M.; Migliori, A. Synthesis and characterization of multiferroic  $\text{BiMn}_7\text{O}_{12}$ . *Phys. Rev. B* **2009**, *79*, 100106.

[22] Zhang, G.; Dong, S.; Yan, Z.; Guo, Y.; Zhang, Q.; Yunoki, S.; Dagotto, E.; Liu, J.-M. Multiferroic properties of  $\text{CaMn}_7\text{O}_{12}$ . *Phys. Rev. B* **2011**, *84*, 174413.

- [23] Belik, A. A.; Glazkova, Y. S.; Terada, N.; Matsushita, Y.; Sobolev, A. V.; Presniakov, I. A.; Tsujii, N.; Nimori, S.; Takehana, K.; Imanaka, Y. Spin-driven multiferroic properties of  $\text{PbMn}_7\text{O}_{12}$  perovskite. *Inorg. Chem.* **2016**, *55*, 6169-6177.
- [24] Glazkova, Y. S.; Terada, N.; Matsushita, Y.; Katsuya, Y.; Tanaka, M.; Sobolev, A. V.; Presniakov, I. A.; Belik, A. A. High-pressure synthesis, crystal structures, and properties of  $\text{CdMn}_7\text{O}_{12}$  and  $\text{SrMn}_7\text{O}_{12}$  perovskites. *Inorg. Chem.* **2015**, *54*, 9081-9091.
- [25] Mezzadri, F.; Calestani, G.; Calicchio, M.; Gilioli, E.; Bolzoni, F.; Cabassi, R.; Marezio, M.; Migliori, A. Synthesis and characterization of multiferroic  $\text{BiMn}_7\text{O}_{12}$ . *Phys. Rev. B* **2009**, *79*, 100106.
- [26] Shimakawa, Y.; Mizumaki, M. Multiple magnetic interactions in A-site-ordered perovskite-structure oxide. *J. Phys.: Condens. Matter* **2014**, *26*, 473203.
- [27] Chen, W.-T.; Mizumaki, M.; Saito, T.; Shimakawa, Y. Frustration relieved ferrimagnetism in novel A- and B-site-ordered quadruple perovskite. *Dalton Trans.* **2013**, *42*, 10116-10120.
- [28] van Vleck, J. H. Theory of the variations in paramagnetic anisotropy among different salts of the iron group. *Phys. Rev.* **1932**, *41*, 208.
- [29] Miessler, G. L.; Tarr, D. A. *Inorganic Chemistry* **2004**, Pearson Education.
- [30] Jahn, H. A.; Teller, E. Stability of polyatomic molecules in degenerate electronic states - I--Orbital degeneracy. *Proc. Roy. Soc.* **1937**, *161*, 220.
- [31] Jahn, H. A. Stability of polyatomic molecules in degenerate electronic states - II--Orbital degeneracy. *Proc. Roy. Soc.* **1937**, *164*, 117.
- [32] Siwach, P. K.; Singh, H. K.; Srivastava, O. N. Low field magnetotransport in manganites.

*J. Phys.: Condens. Matter* **2008**, *20*, 273201.

[33] Cotton, F. A.; Wilkinson, G.; Murillo, C.A.; Bochmann, M.; Grimes, R. *Advanced inorganic chemistry* **1988**, *5*: Wiley New York.

[34] Handley, O.; Robert, C. *Modern Magnetic Materials: Principles and Applications*. **2000**, New York, USA: Wiley.

[35] West, A. R. *Solid State Chemistry and its Application*. **2014**, University of Sheffield, UK: Wiley.

[36] Miller, J. S. Organic- and molecule-based magnets. *Materials Today* **2014**, *17*, 224-235.

[37] West, A. R. *Solid State Chemistry and its Application*. **2014**, University of Sheffield, UK: Wiley.

[38] Blundell, S. *Magnetism in Condensed Matter*. **2001**: Oxford University Press, UK.

[39] Xiang, H.; Lee, C.; Koo, H.-J.; Gong, X.; Whangbo, M.-H. Magnetic properties and energy-mapping analysis. *Dalton Trans.* **2013**, *42*, 823-853.

[40] Dzyaloshinsky, I. A thermodynamic theory of "weak" ferromagnetism of antiferromagnetics. *J. Phys. Chem. Solids* **1958**, *4*, 241-255.

[41] Ederer, C.; Fennie, C. J. Electric-field switchable magnetization via the Dzyaloshinskii-Moriya interaction: FeTiO<sub>3</sub> versus BiFeO<sub>3</sub>. *J. Phys.: Condens. Matter* **2008**, *20*, 434219.

[42] Shapiro, M. C.; Riggs, S. C.; Stone, M. B.; de la Cruz, C. R.; Chi, S.; Podlesnyak, A. A.; Fisher, I. R. Structure and magnetic properties of the pyrochlore iridate Y<sub>2</sub>Ir<sub>2</sub>O<sub>7</sub>. *Phys. Rev. B* **2012**, *85*, 214434.

- [43] Zhu, W. K.; Wang, M.; Seradjeh, B.; Yang, F.; Zhang, S. X. Enhanced weak ferromagnetism and conductivity in hole-doped pyrochlore iridate  $\text{Y}_2\text{Ir}_2\text{O}_7$ . *Phys. Rev. B* **2014**, *90*, 054419.
- [44] Powell, A. K. Molecular magnetism: A bridge to higher ground. *Nature Chem.* **2010**, *2*, 351-352.
- [45] Anderson, P. W.; Hasegawa, H. Considerations on Double Exchange. *Phys. Rev.* **1955**, *100*(2), 675-681.
- [46] Howard, C. J.; Kennedy, B. J.; Woodward, P. M. Ordered double perovskites - a group-theoretical analysis. *Acta Crystallogr. B* **2003**, *59*, 463-471.
- [47] Aleonard, R.; Pauthenet, R.; Rebouillat, J. P.; Veyret, C. Interpretation of the magnetic properties of the rare earth chromites and the rare earth manganites. *J. Appl. Phys.* **1968**, *39*, 379.
- [48] Koehler, W. C.; Wollan, E. O.; Wilkinson, M. K. Neutron diffraction study of the magnetic properties of rare-earth-iron perovskites. *Phys. Rev.* **1960**, *118*, 58.
- [49] Treves, D. Studies on orthoferrites at the Weizmann institute of science. *J. Appl. Phys.* **1965**, *36*, 1033.
- [50] Goodenough, J. B. Theory of the role of convalence in the perovskite-type manganites [La, M(II)] $\text{MnO}_3$ . *Phys. Rev.* **1955**, *100*, 564.
- [51] Kanamori, J. Superexchange interaction and symmetry properties of electron orbitals. *J. Phys. Chem. Solids* **1959**, *10*, 87.
- [52] Ueda, K.; Tabata, H.; Kawai, T. Ferromagnetism in  $\text{LaFeO}_3$ - $\text{LaCrO}_3$  superlattices. *Science* **1998**, *280*, 1064.

- [53] Radaelli, P. G.; Cox, D. E.; Marezio, M.; Cheong, S.-W. Charge, orbital, and magnetic ordering in  $\text{La}_{0.5}\text{Ca}_{0.5}\text{O}_3\text{s}$ . *Phys. Rev. B* **1997**, *55*, 3015-3023.
- [54] Caignaert, V.; Millange, F.; Hervieu, M.; Suard, E.; Raveau, B. The Manganite  $\text{Nd}_{0.5}\text{Sr}_{0.5}\text{MnO}_3$ : A rare distortion of the perovskite. *Solid State Commun.* **1996**, *99*(3), 173-177.
- [55] Azuma, M.; Kaimori, S.; Takano, M. High-pressure synthesis and magnetic properties of layered double perovskites  $\text{Ln}_2\text{CuMO}_6$  (Ln = La, Pr, Nd, and Sm; M = Sn and Zr). *Chem. Mater.* **1988**, *10*(10), 3124-3130.
- [56] Anderson, M. T.; Poeppelmeier, K. R. Lanthanum copper tin oxide ( $\text{La}_2\text{CuSnO}_6$ ): a new perovskite-related compound with an unusual arrangement of B cations. *Chem. Mater.* **1991**, *3*(3), 476-482.
- [57] Shimakawa, Y. A-Site-Ordered Perovskites with Intriguing Physical Properties. *Inorg. Chem.* **2008**, *47*, 8562-8570.
- [58] Solin, S. A.; Thio, T.; Hines, D. R.; Heremans, J. J. Enhanced Room-Temperature Geometric Magnetoresistance in Inhomogeneous Narrow-Gap Semiconductors. *Science* **2000**, *289*, 1530-1532.
- [59] McGuire, T. R.; Potter, R. I. Anisotropic Magnetoresistance in Ferromagnetic 3d Alloys. *IEEE Transactions on Magnetism* **1975**, *4*, 1018-1038.
- [60] Yoshizawa, H.; Kawano, H.; Tomioka, Y.; Tokura, Y. Neutron-diffraction study of the magnetic-field-induced metal-insulator transition in  $\text{Pr}_{0.7}\text{Ca}_{0.3}\text{MnO}_3$ . *Phys. Rev. B* **1995**, *52*, R13145.
- [61] Alonso, J. A. Multiferroicity in In-Containing Perovskites. *ChemPhysChem* **2010**, *11*,

58-60.

[62] Wang, J.; Neaton, J. B.; Zheng, H.; Nagarajan, V.; Ogale, S. B.; Liu, B.; Viehland, D.; Vaithyanathan, V.; Schlom, D. G.; Waghmare, U. V.; Spaldin, N. A.; Rabe, K. M.; Wuttig, M.; Ramesh, R. Epitaxial BiFeO<sub>3</sub> Multiferroic Thin Film Heterostructures. *Science* **2003**, *299*, 1719-1722.

[63] Kuo, C.-Y.; Hu, Z.; Yang, J. C.; Liao, S.-C.; Huang, Y. L.; Vasudevan, R. K.; Okatan, M. B.; Jsse, S.; Kalinin, S. V.; Li, L.; Liu, H. J.; Lai, C.-H.; Pi, T. W.; Agrestini, S.; Chen, K.; Ohresser, P.; Tanaka, A.; Tjeng, L. H.; Chu, Y. H. Single-domain multiferroic BiFeO<sub>3</sub> films. *Nature Commun.* **2016**, 12712.

[64] Matsubara, M.; Manz, S.; Mochizuki, M.; Kubacka, T.; Iyama, A.; Aliouane, N.; Kimura, T.; Johnson, S. L.; Meier, D.; Fiebig, M. Magnetoelectric domain control in multiferroic TbMnO<sub>3</sub>. *Science* **2015**, *348*, 1112-1115.

[65] Staruch, M.; Violette, D.; Jain, M. Structural and magnetic properties of multiferroic bulk TbMnO<sub>3</sub>. *Mater. Chem. Phys.* **2013**, *139*, 897-900.

[66] Belik, A. A.; Matsushita, Y.; Khalyavin, D. D. Reentrant Structural Transitions and Collapse of Charge and Orbital Orders in Quadruple Perovskites. *Angew. Chem. Int. Ed.* **2017**, *56*, 10423-10427.

[67] Prodi, A.; Gilioli, E.; Gauzzi, A.; Licci, F.; Marezio, M.; Bolzoni, F.; Huang, Q.; Santoro, A.; Lynn, J. W. Charge, orbital and spin ordering phenomena in the mixed valence manganite (NaMn<sup>3+</sup>)<sub>3</sub>(Mn<sup>3+</sup><sub>2</sub>Mn<sup>4+</sup><sub>2</sub>)O<sub>12</sub>. *Nature Mater.* **2004**, *3*, 48-52.

[68] Bochu, B.; Chenavas, J.; Joubert, J. C.; Marezio, M. High pressure synthesis and crystal structure of a new series of perovskite-like compounds CMn<sub>7</sub>O<sub>12</sub> (C = Na, Ca, Cd, Sr, La,

Nd). *J. Solid State Chem.* **1974**, *11*, 88-93.

[69] Mezzadri, F.; Calicchio, M.; Gilioli, E.; Cabassi, R.; Bolzoni, F.; Calestani, G.; Bissoli, F. High-pressure synthesis and characterization of  $\text{PrMn}_7\text{O}_{12}$  polymorphs. *Phys. Rev. B* **2009**, *79*, 014420.

[70] Kanamori, J. Crystal Distortion in Magnetic Compounds. *J. Appl. Phys.* **1960**, *31*, S14.

[71] Zhou, J.-S.; Goodenough, J. B. Universal Octahedral-Site Distortion in Orthorhombic Perovskite Oxides. *Phys. Rev. B* **2005**, *94*, 065501.

[72] Prodi, A.; Gilioli, E.; Cabassi, R.; Bolzoni, F.; Licci, F.; Huang, Q.; Lynn, J. W.; Affronte, M.; Gauzzi, A.; Marezio, M. Magnetic structure of the high-density single-valent  $e_g$  Jahn-Teller system  $\text{LaMn}_7\text{O}_{12}$ . *Phys. Rev. B* **2009**, *79*, 085105.

[73] Kimura, T.; Goto, T.; Shintani, H.; Ishizaka, K.; Arima, T.; Tokura, Y. Magnetic control of ferroelectric polarization. *Nature* **2003**, *426*, 55.

[74] Ramirez, A. P. Colossal magnetoresistance. *J. Phys.: Condens. Matter* **1997**, *9*, 8171-8199.

[75] Rodriguez-Martinez, L. M.; Attfield, J. P. Cation disorder and size effects in magnetoresistive manganese oxide perovskites. *Phys. Rev. B* **1996**, *54*, 622.

[76] Muñoz, A.; Martínez-Lope, M. J.; Retuerto, M.; Falcón, H.; Alonso, A. Ferromagnetic behavior in  $\text{La}(\text{Cu}_{3-x}\text{Mn}_x)\text{Mn}_4\text{O}_{12}$  ( $x = 1, 2$ ) perovskites. *J. Appl. Phys.* **2008**, *104*, 083911.

[77] Bochu, B.; Buevoz, J. L.; Chenavas, J.; Collomb, A.; Joubert, J. C.; Marezio, M. Bond lengths in  $\text{'CaMn}_3\text{'(Mn}_4\text{)O}_{12}$ : A new Jahn-Teller distortion of  $\text{Mn}^{3+}$  octahedra. *Solid State Commun.* **1980**, *36*, 133-138.

## Chapter 2. Experimental methods

High-pressure synthesis is a very effective method to fabricate materials with perovskite structures because it is able to shorten the synthesis time and stabilize dense structure, and is good for forming the ordered structure. Therefore, in this thesis, all of the samples were synthesized under high-pressure and high-temperature. The crystal structures and physical properties of the samples were characterized by some systems, such as X-ray diffraction (XRD), differential scanning calorimetry (DSC), magnetic property measurement system (MPMS), and physical property measurement system (PPMS).

### 2.1. High pressure synthesis

In this thesis, all of the samples were prepared by a belt-type high-pressure apparatus (Kobe Steel, Ltd.) which can press to 8 GPa and heat to 2000 °C, respectively. The pyrophyllite cell is used for obtaining quasi-hydrostatic conditions during the reaction [1]. The graphite is applied to heat the samples as the heating furnace. The NaCl sleeve and cylindrical pieces block the contact of the capsule and graphite in order to insulate them.

Before the reaction,  $R_2O_3$  powders (R = rare earth elements and Y) have been annealed in order to remove water. Stoichiometric amounts of starting materials were mixed together and ground thoroughly. The mixtures were added into the Pt capsule which was then sealed and pressed by using hand press. The sealed Pt capsules, graphite, NaCl sleeve and cylindrical pieces were pressed into the cell, as shown in **Figure 2.1**. The prepared sample cell was put into high-pressure apparatus where pressure increased slowly to the target pressure. After the pressure became stable, it can be hold by manual operation. Then the heating control panel can be turned on samples and temperature increased to the target temperature. After kept heating for certain time, the samples were quenched to room temperature and then the pressure was released slowly.

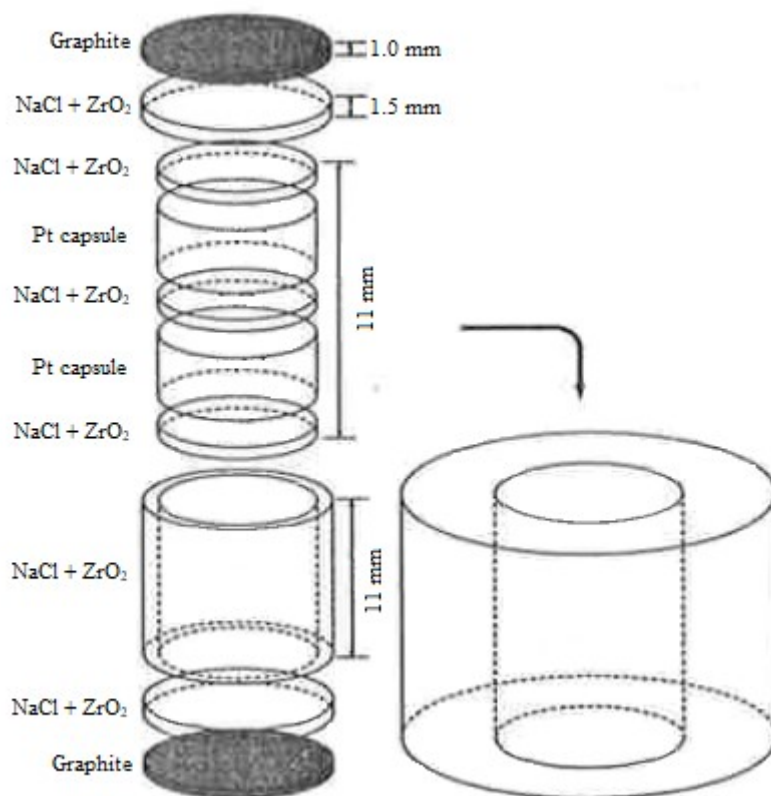


**Figure 2.1.** The schematic diagram of the capsule and sample container.

## 2.2. X-ray diffraction

### 2.2.1. Powder X-ray diffraction

Powder X-ray diffraction (XRD) is an effective method for preliminary characterizations such as phase identification and structure determination. In this thesis, room temperature powder XRD data were measured by using a Desktop X-ray Diffractometer MiniFlex600 (Rigaku) equipped with Cu K $\alpha$  radiation ( $\lambda = 1.5418 \text{ \AA}$ ), as shown in **Figure 2.2**.



**Figure 2.2.** The picture of Powder XRD apparatus in NIMS.

The X-rays which are used in the laboratory-based diffraction experiments are emitted from Cu. In this process, the Cu 1s electrons are ionised by the strike from a beam of electrons and then the electron in an outer orbital drops down, leading to the energy released in the transition appears as X-radiation.

XRD measurement is based on the Bragg's law:  $n\lambda = 2d\sin\theta$ , where  $n$  is any integer,  $\lambda$  is the wavelength of the incident wave,  $d$  is the perpendicular distance between pairs of adjacent planes, and  $\theta$  is the scattering angle [2]. In this law, crystals are considered as a semi-transparent mirror off which some of the X-ray are reflected with an angle equal to  $\theta$ . Some crystal information can be obtained by recording the reflections.

### **2.2.2. Synchrotron X-ray diffraction**

Synchrotron radiation is generated when charged particles, such as electrons, are accelerated radially, first observed in 1947. Electrons pass through a storage ring by a bending magnet and are accelerated to the speed close to light. And then they produce streams of synchrotron radiation which is tangent to the electron path, as shown in **Figure 2.3**. The intensities of synchrotron radiation X-ray are several orders of magnitude higher than

that of the best X-ray laboratory source, so it is a very powerful technique to analyze unknown materials.

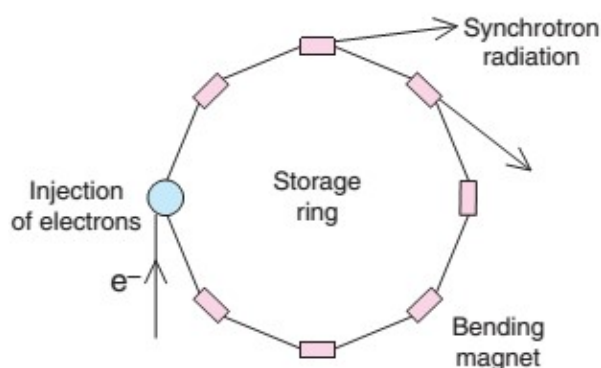


**Figure 2.3.** Schematic diagram of a synchrotron storage ring [3].

In this thesis, the synchrotron X-ray diffraction (SXR) data were measured in the BL15XU beam line ( $\lambda = 0.65298 \text{ \AA}$ ) of the SPring-8 synchrotron radiation facility in Japan. The large Debye-Scherrer camera was used for this SXR facility [4]. The obtained data were analyzed by using the program RIETAN-FP [5,6].

### **2.3. Differential scanning calorimetry (DSC)**

Differential scanning calorimetry is a thermoanalytical technique, used to detect the phase transitions of samples. While the measurement, the sample and reference are maintained at the same temperature. It is necessary to choose a reference which has a well-defined heat capacity over the range of scanning temperatures. When the samples undergo a phase transition, there will be more or less energy required for the transformation than the reference. The difference in the amount of heat required to increase the temperature of the sample and reference is measured as a function of temperature.

In this thesis, a Mettler Toledo DSC1 STAR<sup>e</sup> system was used for measuring the DSC curves, as shown in **Figure 2.4**.



**Figure 2.4.** The photo of the Mettler Toledo DSC1 STAR<sup>c</sup> system (NIMS).

## **2.4. Magnetic properties measurement system (MPMS)**

The dc magnetic properties of all the samples were measured by using MPMS-7T (Quantum Design) as shown in **Figure 2.5**. The temperature dependent dc magnetic susceptibilities ( $\chi$ ) were measured under both field-cooling and zero-field-cooling conditions in a temperature range 2-400 K under an applied magnetic field of 10 kOe. The field dependence isothermal magnetizations were measured in a range between +70 kOe and -70 kOe at different temperatures. The ac susceptibility were measured by using MPMS-1T. The real parts ( $\chi'$ ) and imaginary parts ( $\chi''$ ) were measured at different frequencies ( $f$ ) and different applied oscillating magnetic fields ( $H_{ac}$ ).

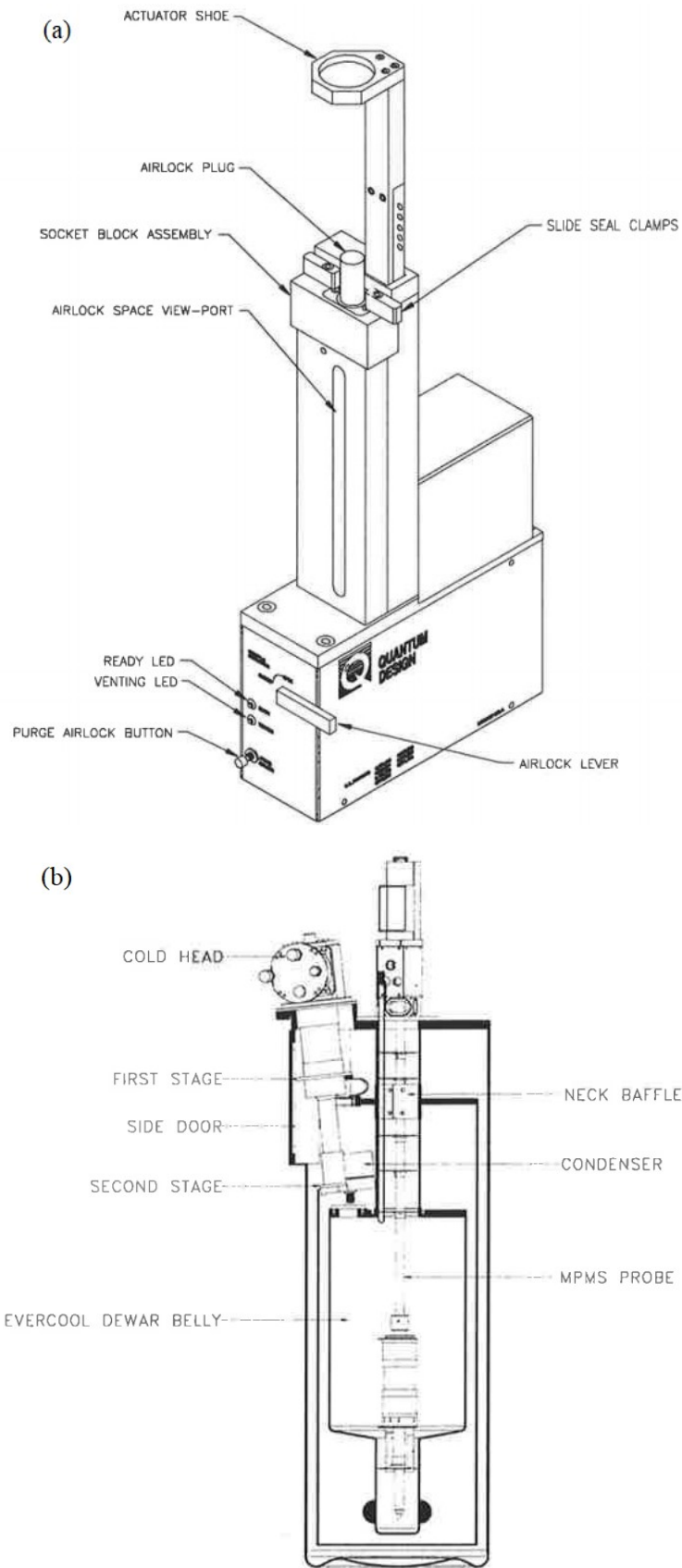


**Figure 2.5.** Sample transport (a) and measurement system (b) of MPMS XL in NIMS Namiki-site.

MPMS uses the SQUID (Superconducting QUantum Interference Device) detection system, comprising the sensing loops, a superconducting transformer, and the SQUID sensor, to detect the magnetic information of the samples. During the measurement, there is a magnetic field applied to the sample. The change in flux is resulted only from the change of the magnetic moment of the sample responding to the applied field. The magnetic flux from the sample is trapped by a superconducting pickup coil which is a part of a closed superconducting circuit inductively coupled to the Superconducting QUantum Interference Device (SQUID).

In this measurement, a persistent current in the five tesla superconducting magnet is used for the magnetic field on the sample. It is because MPMS does not use superconducting shield to trap the magnetic field over the sample volume. Power supply is turned on first and delivers the current to the next desired field. Then the 1822 controller will overshoot the desired value in order to reduce relaxation in the magnet following a field change.

MPMS utilizes Temperature Control Module (TCM) to control the temperature. This system uses a third order Proportional-Integral-Differential (PID) feedback technique to minimize temperature variations by maximize response to temperature changes.

## **2.5. Physical properties measurement system (PPMS)**

PPMS provides a flexible, automated workstation that can perform a variety of experiments requiring precise thermal control. It can be used for execute magnetic, electro-transport, or thermo-electric measurements. **Figure 2.6** illustrates the PPMS probe that control temperature. The outer layer of the probe is between the liquid-helium bath and cooling annulus to minimize thermal exchange. The cooling annulus filled helium is important to control the temperature. A platinum resistance thermometer is used to monitor the temperature of the sample. PPMS uses Magnet Controller to change the magnetic field. While the measurement, a superconducting magnet wire is heated by another resistive wire.

After it becomes non-superconducting, it will switch the Magnet Controller which drives the magnet to the current for the new field.

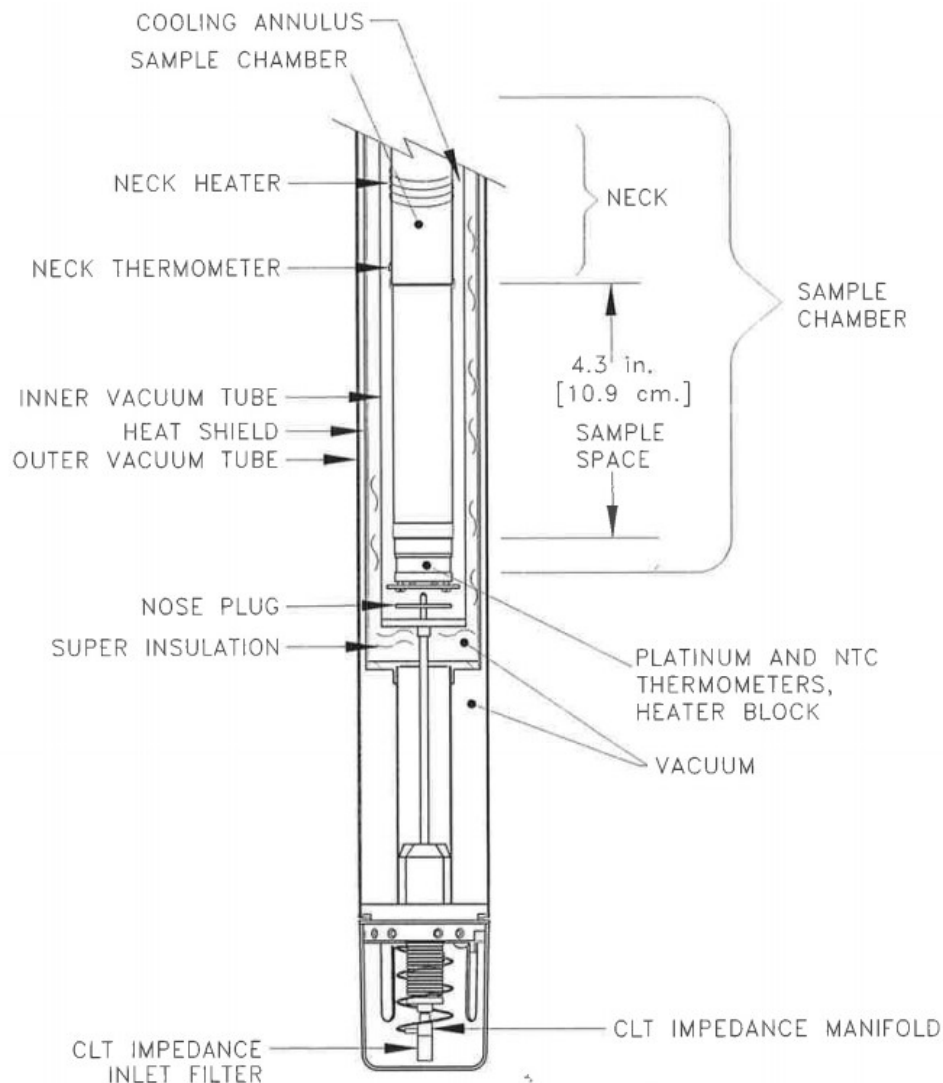


**Figure 2.6.** PPMS probe and the temperature-control components.

Heat capacity can provide some information about the lattice, electronic, and even magnetic properties of materials. The calorimeter puck containing sample-mounting platform is necessary for the measurement (**Figure 2.7**). And there are puck wires providing thermal link to sample platform. While the measurement, the Heat Capacity option fits the entire temperature response of the sample platform to a model that accounts for both the thermal relaxation of the sample platform to the bath temperature and the relaxation between the sample platform and the sample itself.

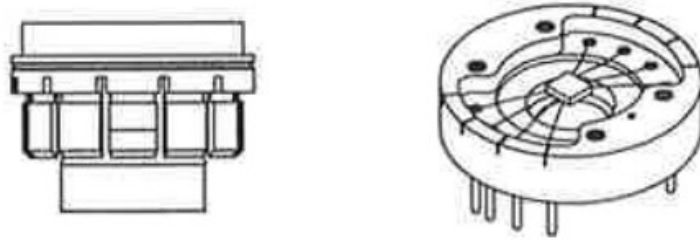


**Figure 2.7.** Calorimeter puck (left) and the sample platform (right) for heat capacity measurement.

In this thesis, heat capacity is a measurable physical quantity which refers to the energy, required to heat up or cool down of an object for a certain temperature change. Heat capacity measurements were carried out at 0 Oe, 70 kOe, and 90 kOe using a relaxation technique with a Physical Property Measurement System (PPMS, Quantum Design), A polished pellet of the sample was mounted on an aluminum plate with Apiezon N-Grease for better thermal contact.

In PPMS, four-wire resistance measurements are used to obtain the resistivity of the sample. Resistivity sample puck (**Figure 2.8**) is necessary. There are four contacts in the puck, where one positive and one negative contact are for current and voltage. And the resistivity option can measure three samples at one time.

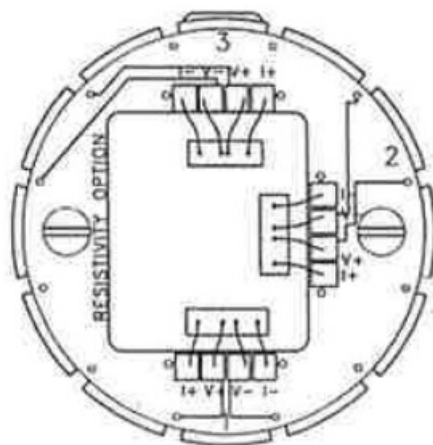


**Figure 2.8.** Resistivity sample puck with three samples mounted for four-wire resistance measurements.

## References in chapter 2

- [1] Fernández-Sanjulián, J.; E. Morán; Alario-Franco, M. Á. Synthesis, stability range and characterization of  $\text{Pr}_2\text{Cu}_2\text{O}_5$ . *High Pressure Research* **2010**, *30*(1), 159-166.
- [2] Baskaran, S. Structure and Regulation of Yeast Glycogen Synthase. **2010**, University of California, Berkeley.
- [3] West, A. R. Solid State Chemistry and its Application. **2014**, University of Sheffield, UK: Wiley.
- [4] Tanaka, M.; Katsuya, Y.; Yamamoto, A. A new large radius imaging plate camera for high-resolution and high-throughput synchrotron X-ray powder diffraction by multiexposure method. *Rev. Sci. Instrum.* **2008**, *79*(7), 075106.
- [5] Izumi, F.; Momma, K. Three-Dimensional Visualization in Powder Diffraction. *Solid State Phenomena* **2007**, *130*, 15-20.
- [6] Izumi, F.; Asano, H.; Murata, H.; Watanabe, N. Rietveld analysis of powder patterns obtained by TOF neutron diffraction using cold neutron sources. *J. Appl. Cryst.* **1987**, *20*, 411-418.

## Chapter 3. Five-Fold Ordering in High-Pressure Perovskites

### $RMn_3O_6$ ( $R = \text{Gd-Tm and Y}$ ) with Charge Disproportionation

#### 3.1. Introduction

$ABO_3$  perovskite-type compounds with "exotic" cations at the A site, such as, magnetic and small  $Mn^{2+}$  ( $r^{VIII} = 0.96 \text{ \AA}$ ) [1] or quite small  $Sc^{3+}$  ( $r^{VIII} = 0.87 \text{ \AA}$ ) and  $In^{3+}$  ( $r^{VIII} = 0.92 \text{ \AA}$ ), were briefly examined in the 1960s and 1970s [2,3]. In the last decade, they have been paid some attention to [4] because it was realized that many unique physical and chemical properties might emerge in such perovskites. For example,  $MnVO_3$  [5] and  $Mn_2FeSbO_6$  [6] have incommensurate antiferromagnetic  $Mn^{2+}$  spin orders.  $Mn_2MnReO_6$  has competing antiferromagnetic orders [7].  $Mn_2O_3$  crystallizes in the so-called 134 quadruple perovskite structure [8].  $Mn_2FeReO_6$  had a high ferrimagnetic transition temperature and a giant and switchable magnetoresistance [9,10]. Small  $Mn^{2+}$  cations are located in a large 12-coordinated site in  $MnCu_3V_4O_{12}$  [11]. Independent spin orders of 3d transition metals ( $Ni^{2+}$  and  $Mn^{4+}$ ) at the B site were suggested in  $Sc_2NiMnO_6$  [12]. The C-type magnetic order of  $Cr^{3+}$  spins takes place in  $ScCrO_3$  [13]. Tolerance factors of such perovskites are quite small; therefore, the perovskite-type structure often competes with other related structures, such as,  $LiNbO_3$  [14],  $Ni_3TeO_6$  [15], and others.

In  $R_2O_3$ - $Mn_2O_3$  systems with  $R =$  rare earth elements, two perovskite-type structures have been researched,  $RMnO_3$  and  $RMn_7O_{12}$ . Classical  $RMnO_3$  perovskites have been a playground of materials physicists and chemists for decades due to the existence of an interplay among the lattice, spin, and orbital degrees of freedom [16-18].  $RMnO_3$  exhibits spin-driven multiferroic properties for  $R = \text{Tb-Lu}$  [17].  $RMnO_3$  is known for all  $R$  from La to Lu, but  $RMnO_3$  perovskites with  $R = \text{Dy-Lu}$  and Y can only be prepared under high-pressure (HP) high-temperature (HT) conditions in a bulk form [18].  $RMn_7O_{12}$  perovskites discovered

in the 1970s [19]; they can only be prepared under HP, HT conditions, and compounds with  $R = \text{La, Pr, and Nd}$  have been reported [20,21].  $\text{RMn}_7\text{O}_{12}$  has the 134 quadruple perovskite structure,  $[\text{R}^{3+}\text{Mn}^{3+}_3]_{\text{A}}[\text{Mn}^{3+}_4]_{\text{B}}\text{O}_{12}$ , where a 1:3 cation order at the A site is realized because of quite different nature of  $\text{R}^{3+}$  and  $\text{Mn}^{3+}$  cations. Small  $\text{Mn}^{3+}$  cations at the A site have a square-planar environment [22].

Cation and anion orders play important roles in the properties of perovskite materials [23,24]. There always should be driving forces for ordered arrangements, for example, quite different sizes, oxidation states, and preferred coordination of cations and/or anions. In recent years, perovskites with double order at the A site and double order at the B site have drawn a great deal of attention, for example,  $\text{NaLaMgWO}_6$ ,  $\text{NaLaScNbO}_6$ ,  $\text{NaLaFeWO}_6$ , etc., [24-28] and  $\text{MnRMnSbO}_6$  ( $R = \text{La-Sm}$ ) [29].

In this work, I discovered new perovskites in the  $\text{R}_2\text{O}_3\text{-Mn}_2\text{O}_3$  systems with compositions of  $\text{RMn}_3\text{O}_6$  (an ideal composition) and  $\text{R}_{1-\delta}\text{Mn}_3\text{O}_{6-1.5\delta}$  for  $R = \text{Gd-Tm and Y}$  using HP and HT. Rare-earth (formally) trivalent manganites were extended beyond the 1:1  $\text{RMnO}_3$  and 1:7  $\text{RMn}_7\text{O}_{12}$  families. The charge distribution can be presented like  $[\text{R}^{3+}\text{Mn}^{2+}_{0.5}\text{Mn}^{3+}_{0.5}]_{\text{A}}[\text{Mn}^{3+}\text{Mn}^{3.5+}]_{\text{B}}\text{O}_6$ , while the average oxidation state of manganese is +3. There are triple chain-like ordering at the A site and double layered ordering at B site resulting in unusual 5-fold cation ordering in  $\text{RMn}_3\text{O}_6$ .

### 3.2. Experimental details of Chapter 3

$\text{R}_{1-\delta}\text{Mn}_3\text{O}_{6-1.5\delta}$  samples with  $R = \text{Sm-Lu and Y}$  (except Tb) were prepared from stoichiometric mixtures of  $\text{Mn}_2\text{O}_3$  and  $\text{R}_2\text{O}_3$  (99.9 %); and  $\text{TbMn}_3\text{O}_6$  was prepared from a stoichiometric mixture of  $\text{Mn}_2\text{O}_3$ ,  $\text{Mn}_3\text{O}_4$  (99.99 %), and  $\text{Tb}_4\text{O}_7$  (99.9 %). Single-phase  $\text{Mn}_2\text{O}_3$  was prepared from commercial  $\text{MnO}_2$  (99.99 %) by being heated in air at 923 K for 24 h. The mixtures were placed in Pt capsules and treated at 6 GPa and  $\sim 1673$  K for 2 h (the time needed to heat the sample to the desired temperature was 10 min) in a belt-type

high-pressure apparatus. After the heat treatments, the samples were quenched to room temperature (RT), and the pressure was slowly released. All the samples obtained were black pellets (quite loose in some cases). The temperature of our high-pressure apparatus is controlled by the heating power with a calibrated relationship between power and temperature.

X-ray powder diffraction (XRPD) data were collected at RT on a Rigaku MiniFlex600 diffractometer using  $\text{CuK}\alpha$  radiation ( $2\theta$  range of  $10\text{-}85^\circ$ , step width of  $0.02^\circ$ , and scan speed of  $1^\circ \text{min}^{-1}$ ). Rietveld analysis was performed with RIETAN-2000 [30]. Structural parameters of  $\text{DyMn}_3\text{O}_6$  (this work),  $\text{LaMn}_7\text{O}_{12}$  [20], and  $\text{RMnO}_3$  [16] were used as initial ones to fit the XRPD data. The refined scale factors were used to estimate (by RIETAN-2000) the amounts of impurities. The X-ray intensity measurements for the crystal structure analysis of a  $\text{DyMn}_3\text{O}_6$  single crystal ( $0.034 \text{ mm} \times 0.033 \text{ mm} \times 0.031 \text{ mm}$  in size) were taken using a Rigaku Saturn CCD diffractometer equipped with a VariMax confocal optics for  $\text{MoK}\alpha$  radiation ( $\lambda = 0.71073 \text{ \AA}$ ). Prior to the diffraction experiment, the crystal was flash-cooled to 213 K (at a sample position) in a stream of cold  $\text{N}_2$  gas. Cell refinement and data reduction were carried out using the program d\*trek package in Crystal Clear software suite [31]. Preliminary structures were determined using SHELXT [32] and refined by full-matrix least squares on  $F^2$  using the SHELXL-2014/7 [33] in WinGX program package [34].

Magnetic measurements were performed on a SQUID magnetometer (Quantum Design, MPMS-XL-7T) between 2 and 400 K in different applied fields under both zero-field-cooled (ZFC) and field-cooled on cooling (FCC) conditions. Isothermal magnetization measurements were performed between -70 and 70 kOe at different temperatures. Frequency-dependent ac susceptibility measurements were taken with a Quantum Design MPMS-1T instrument at different frequencies ( $f$ ) and different applied oscillating magnetic fields ( $H_{ac}$ ). The specific heat,  $C_p$ , at magnetic fields of 0 and 90 kOe was recorded between 2 and 300 K upon cooling (in most cases) by a pulse relaxation method using a commercial

calorimeter (Quantum Design PPMS). Dielectric properties were measured using a NOVOCONTROL Alpha-A High Performance Frequency Analyzer between 5 and 300 K upon cooling and heating in the frequency range of 100 Hz and 2 MHz and at 0 and 90 kOe. Pieces of pellets of single-phase samples were used in magnetic, specific heat, and dielectric measurements.

Differential scanning calorimetry (DSC) curves were recorded on a Mettler Toledo DSC1 STAR<sup>c</sup> system at a heating/cooling rate of 10 K min<sup>-1</sup> under N<sub>2</sub> flow between 150 K and 873 K in open Al capsules. Three DSC runs were performed to check the reproducibility.

Electron probe microanalysis (EPMA) of TmMn<sub>3</sub>O<sub>6</sub> was performed on a JEOL JXA-8900F instrument at 15 kV. The surface of pellet samples was polished on a fine (0.3 μm) alumina coated film before measurements. MnO and TmP<sub>5</sub>O<sub>14</sub> were used as standard samples for Mn and Tm, respectively.

The density of powder samples was measured using the Archimedes method using CCl<sub>4</sub> with the density of 1.587 g cm<sup>-3</sup>.

To determine the oxygen content of DyMn<sub>3</sub>O<sub>6</sub>, we reduced the sample in the flow of 10% H<sub>2</sub> and 90% Ar at 1273 K for 1 h in a usual furnace and weighed the powdered sample before and after the reduction. The sample decomposed to a mixture of Dy<sub>2</sub>O<sub>3</sub> and MnO, and the calculated oxygen content was DyMn<sub>3</sub>O<sub>6.00(1)</sub>.

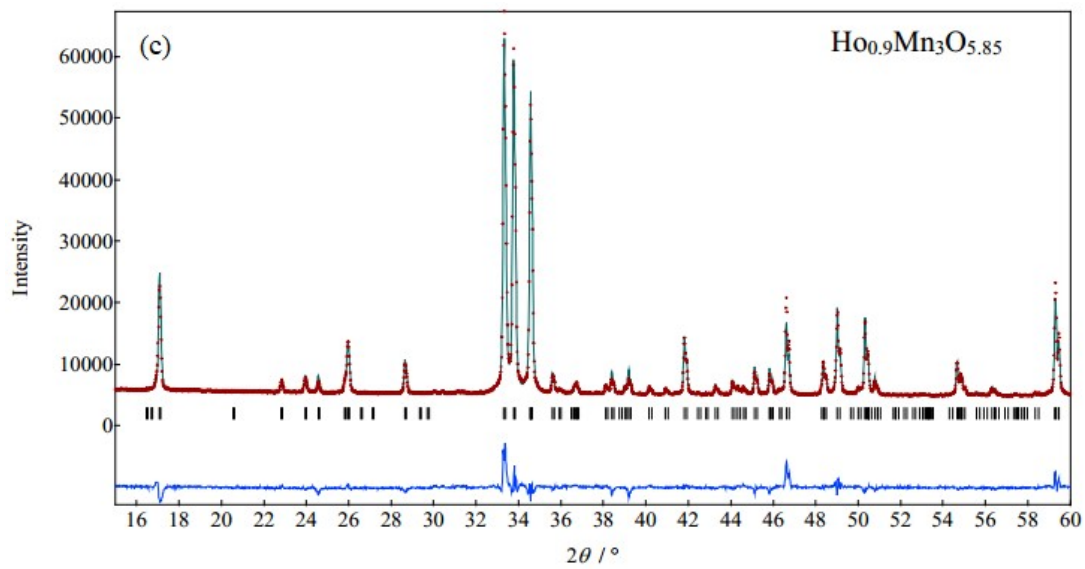
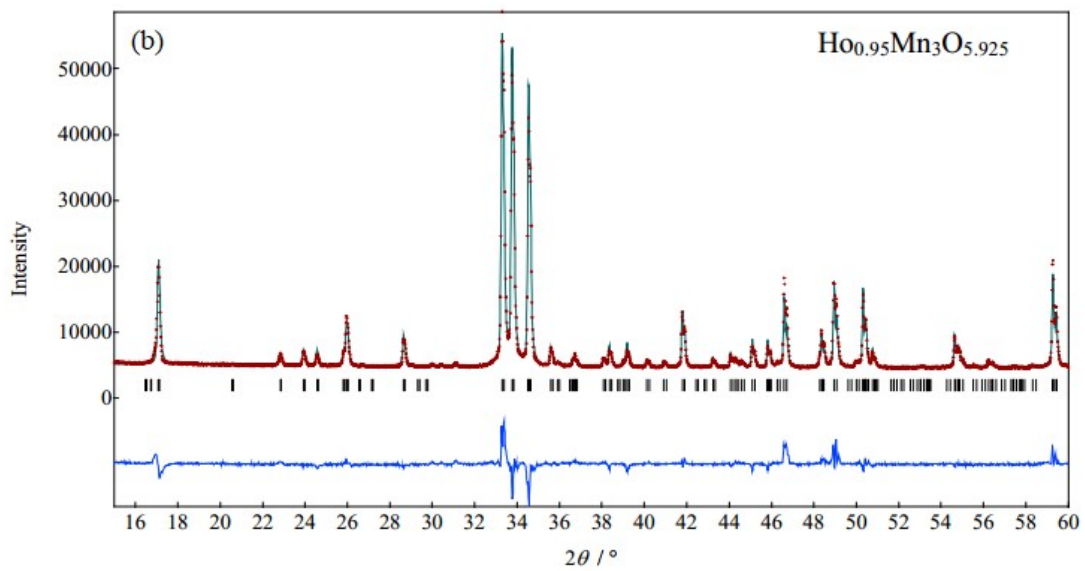
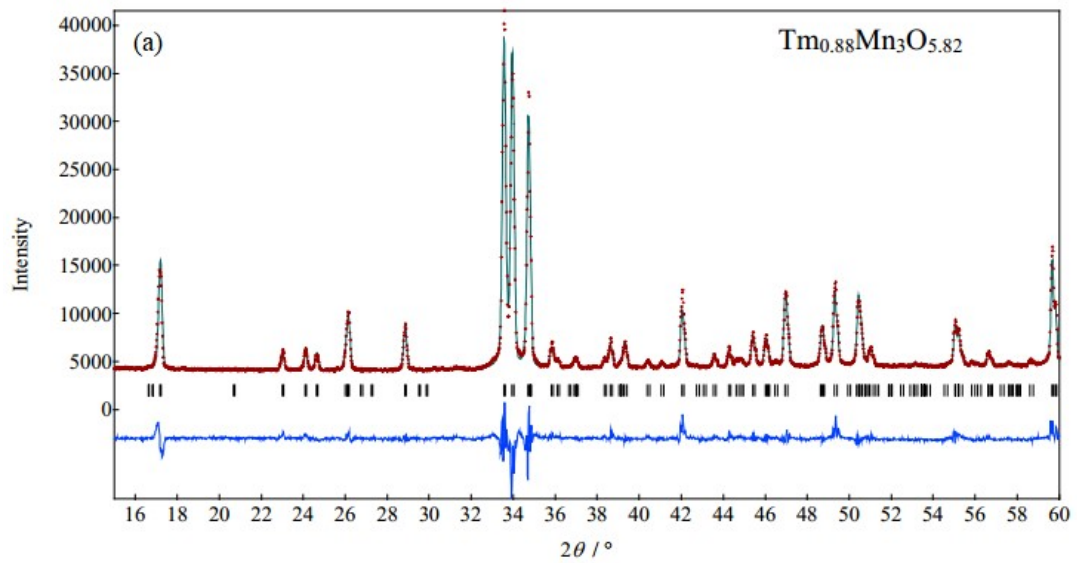
### **3.3. Results and discussion**

#### **3.3.1. Rare-Earth Stability Range, Chemical Compositions, and Thermal Stability of RMn<sub>3</sub>O<sub>6</sub>**

The formation of a new phase was found in samples with  $R = \text{Sm-Tm}$  and Y. However, the RMn<sub>3</sub>O<sub>6</sub> samples with  $R = \text{Ho, Er, Tm, and Y}$  contained an impurity of (R<sub>1-x</sub>Mn<sub>x</sub>)MnO<sub>3</sub>, a next perovskite phase, suggesting that the composition of the main phase is shifted to the Mn-rich side, R<sub>1-δ</sub>Mn<sub>3</sub>O<sub>6-1.5δ</sub>. EPMA of a sample with the total composition of TmMn<sub>3</sub>O<sub>6</sub>

showed that the compositions of the phases were  $\text{Tm}_{0.881(8)}\text{Mn}_{3.00(3)}\text{O}_{5.99(3)}$  and  $\text{Tm}_{0.636(11)}\text{Mn}_{1.343(13)}\text{O}_{3.000(14)}$ . The oxygen content by the EPMA method should be taken with care. Indeed, when I tried to prepare samples with the total chemical compositions of  $\text{Er}_{0.88}\text{Mn}_3\text{O}_6$  and  $\text{Tm}_{0.88}\text{Mn}_3\text{O}_6$  with an average oxidation state of manganese of +3.12 (by adding stoichiometric amounts of  $\text{MnO}_2$ ), a mixture of an  $\text{RMn}_3\text{O}_6$ -type phase and  $\text{RMn}_2\text{O}_5$  was obtained. This fact shows that the excess of oxygen accumulates in the  $\text{RMn}_2\text{O}_5$  impurity, and the average oxidation state of manganese should be kept as +3 to obtain single-phase samples. I note that the total chemical composition (including the oxygen content) is usually kept constant during a high-pressure synthesis in sealed capsules.

Single-phase samples with the total compositions of  $\text{Ho}_{0.95}\text{Mn}_3\text{O}_{5.925}$ ,  $\text{Ho}_{0.9}\text{Mn}_3\text{O}_{5.85}$ ,  $\text{Y}_{0.95}\text{Mn}_3\text{O}_{5.925}$ ,  $\text{Y}_{0.9}\text{Mn}_3\text{O}_{5.85}$ ,  $\text{Er}_{0.88}\text{Mn}_3\text{O}_{5.82}$ , and  $\text{Tm}_{0.88}\text{Mn}_3\text{O}_{5.82}$  were synthesized.  $\text{Ho}_{0.88}\text{Mn}_3\text{O}_{5.82}$  and  $\text{Y}_{0.88}\text{Mn}_3\text{O}_{5.82}$  already contained an impurity of  $\text{R}_{1-\delta}\text{Mn}_7\text{O}_{12-1.5\delta}$  (~2 wt %). (Note that I showed in a separate study that  $\text{RMn}_7\text{O}_{12}$  perovskites are formed as  $\text{R}_{1-\delta}\text{Mn}_7\text{O}_{12-1.5\delta}$  for  $R = \text{Tb-Er}$  and  $\text{Y}$ .)  $\text{TbMn}_3\text{O}_6$  contained a  $\text{TbMn}_2\text{O}_5$  impurity (~13 wt %) and a  $\text{Tb}_{1-\delta}\text{Mn}_7\text{O}_{12-1.5\delta}$  impurity (~7 wt %); the appearance of  $\text{TbMn}_2\text{O}_5$  could be caused by a nonstoichiometry of  $\text{Tb}_4\text{O}_7$  because  $\text{TbMn}_2\text{O}_5$  has an excess of oxygen (or 50 % of  $\text{Mn}^{4+}$ ) in comparison with  $\text{TbMn}_3\text{O}_6$ .  $\text{GdMn}_3\text{O}_6$  contained a  $\text{GdMn}_7\text{O}_{12}$  impurity (~9 wt %). The appearance of  $\text{GdMn}_7\text{O}_{12}$ , a next perovskite phase, suggests that the composition of the main phase is shifted to the Gd-rich side,  $\text{GdMn}_{3-y}\text{O}_{6-1.5y}$ , and single-phase samples were prepared for  $y$  values of 0.167, 0.2, and 0.25. Only stoichiometric  $\text{DyMn}_3\text{O}_6$  was prepared in a single-phase form. Some XRPD patterns of  $\text{R}_{1-\delta}\text{Mn}_3\text{O}_{6-1.5\delta}$  are shown in **Figure 3.1**, and numerical values are summarized in **Table 3.1**.



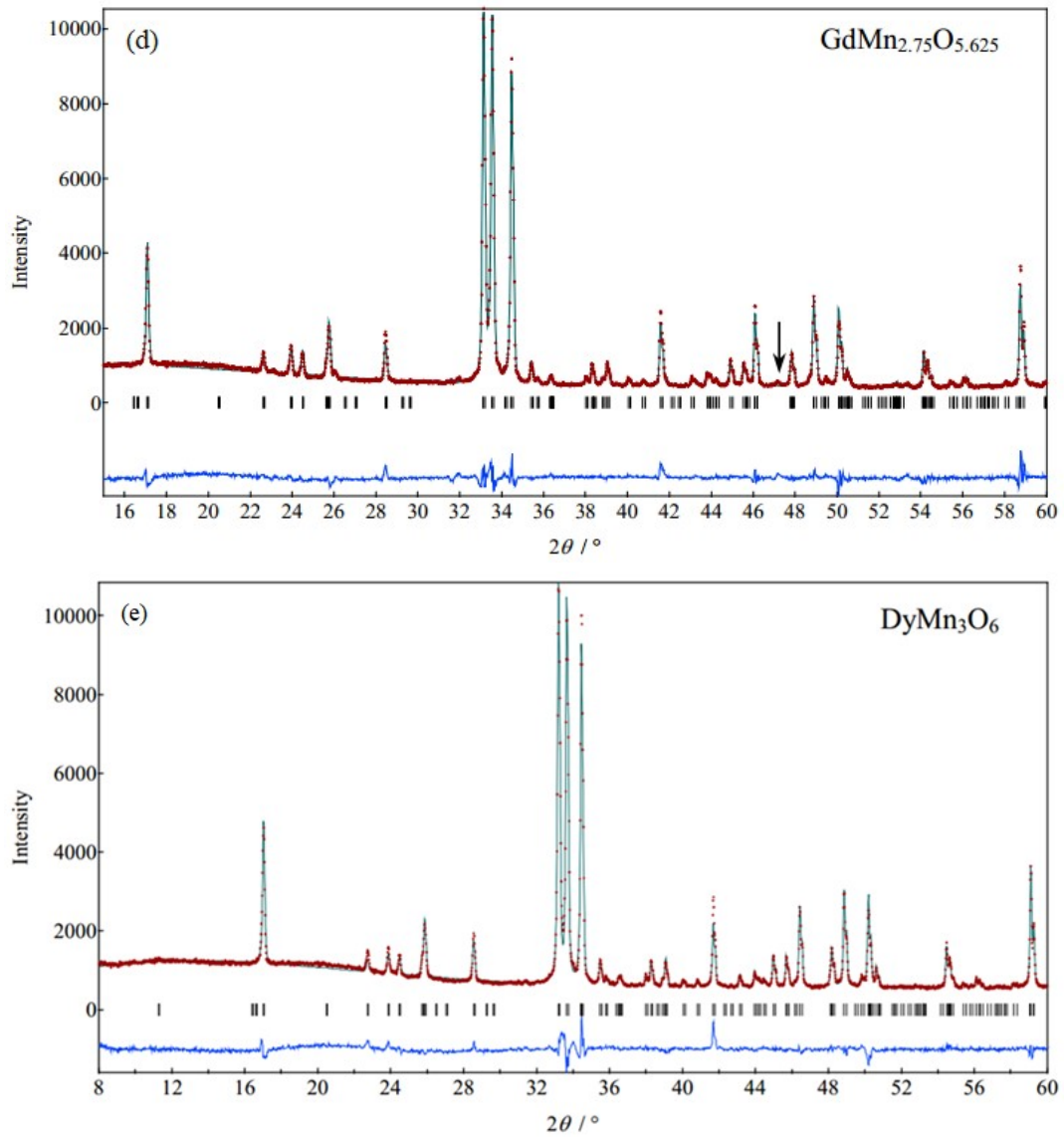


**Figure 3.1.** Fragments of experimental laboratory X-ray powder diffraction patterns measured at room temperature (brown crosses) with fitting results for samples with the total compositions of  $\text{Tm}_{0.88}\text{Mn}_3\text{O}_{5.82}$  (a),  $\text{Ho}_{0.95}\text{Mn}_3\text{O}_{5.925}$  (b),  $\text{Ho}_{0.9}\text{Mn}_3\text{O}_{5.85}$  (c),  $\text{GdMn}_{2.75}\text{O}_{5.625}$  (d), and  $\text{DyMn}_3\text{O}_6$  (e).

**Table 3.1.** Lattice parameters ( $a$ ,  $b$ , and  $c$ ) refined from laboratory XRPD and impurities in  $\text{R}_{1-\delta}\text{Mn}_7\text{O}_{12-1.5\delta}$  and  $\text{GdMn}_{3-\gamma}\text{O}_{6-1.5\gamma}$  (prepared at 6 GPa and 1673 K for 2 h).

Composition	<i>a</i> (Å)	<i>b</i> (Å)	<i>c</i> (Å)	Impurity	Weight fraction of impurity *
LuMn <sub>3</sub>	-	-	-	(Lu <sub>1-x</sub> Mn <sub>x</sub> )MnO <sub>3</sub>	82 %
				Mn <sub>2</sub> O <sub>3</sub>	18 %
YbMn <sub>3</sub>	-	-	-	(Yb <sub>1-x</sub> Mn <sub>x</sub> )MnO <sub>3</sub>	80 %
				Mn <sub>2</sub> O <sub>3</sub>	20 %
Tm <sub>0.88</sub> Mn <sub>3</sub>	7.2305	7.3872	7.7347	-	
TmMn <sub>3</sub>	7.2381	7.4081	7.7412	(Tm <sub>1-x</sub> Mn <sub>x</sub> )MnO <sub>3</sub>	28 %
Ho <sub>0.88</sub> Mn <sub>3</sub>	7.2483	7.4263	7.7896	Ho <sub>1-δ</sub> Mn <sub>7</sub> O <sub>12-1.5δ</sub>	2 %
Ho <sub>0.9</sub> Mn <sub>3</sub>	7.2461	7.4266	7.7872	-	
Ho <sub>0.95</sub> Mn <sub>3</sub>	7.2464	7.4353	7.7887	-	
HoMn <sub>3</sub>	7.2501	7.4430	7.7933	(Ho <sub>1-x</sub> Mn <sub>x</sub> )MnO <sub>3</sub>	3.9 %
Y <sub>0.88</sub> Mn <sub>3</sub>	7.2406	7.4183	7.7811	Y <sub>1-δ</sub> Mn <sub>7</sub> O <sub>12-1.5δ</sub>	1.5 %
Y <sub>0.9</sub> Mn <sub>3</sub>	7.2400	7.4212	7.7816	-	
Y <sub>0.95</sub> Mn <sub>3</sub>	7.2409	7.4308	7.7836	-	
DyMn <sub>3</sub>	7.2576	7.4475	7.8124	-	
TbMn <sub>3</sub>	7.2649	7.4493	7.8392	TbMn <sub>2</sub> O <sub>5</sub>	13 %
				Tb <sub>1-δ</sub> Mn <sub>7</sub> O <sub>12-1.5δ</sub>	7 %
GdMn <sub>3</sub>	7.2864	7.4542	7.8817	GdMn <sub>7</sub> O <sub>12</sub>	9.3 %
GdMn <sub>2.833</sub>	7.2846	7.4513	7.8799	-	
GdMn <sub>2.8</sub>	7.2857	7.4510	7.8800	-	
GdMn <sub>2.75</sub>	7.2862	7.4521	7.8807	-	
GdMn <sub>2.70</sub>	7.2836	7.4494	7.8775	(Gd <sub>1-x</sub> Mn <sub>x</sub> )MnO <sub>3</sub>	Few percent**
EuMn <sub>3</sub>	7.2914	7.4608	7.9021	EuMn <sub>7</sub> O <sub>12</sub>	46 %
				(Eu <sub>1-x</sub> Mn <sub>x</sub> )MnO <sub>3</sub>	30 %
SmMn <sub>3</sub>	7.2852	7.4591	7.9286	SmMn <sub>7</sub> O <sub>12</sub>	50 %
				(Sm <sub>1-x</sub> Mn <sub>x</sub> )MnO <sub>3</sub>	38 %

\*The weight fraction was estimated from the refined scale factors during the Rietveld fitting.

\*\*Because of its small amount, it was difficult to find/catch the lattice parameters of (Gd<sub>1-x</sub>Mn<sub>x</sub>)MnO<sub>3</sub> impurity during the Rietveld fitting; therefore, the weight fraction of this impurity could not be estimated from the Rietveld fitting.

The RMn<sub>3</sub>O<sub>6</sub>-type phase appeared as a minority phase in samples with the total compositions of SmMn<sub>3</sub>O<sub>6</sub> [SmMn<sub>7</sub>O<sub>12</sub>, 50 %; (Sm<sub>1-x</sub>Mn<sub>x</sub>)MnO<sub>3</sub>, 38 %; SmMn<sub>3-y</sub>O<sub>6-1.5y</sub>, 12 %] and EuMn<sub>3</sub>O<sub>6</sub> [EuMn<sub>7</sub>O<sub>12</sub>, 46 %; (Eu<sub>1-x</sub>Mn<sub>x</sub>)MnO<sub>3</sub>, 30 %; EuMn<sub>3-y</sub>O<sub>6-1.5y</sub>, 24 %]. The

appearance of three perovskite phases in the quasi-binary  $R_2O_3$ - $Mn_2O_3$  system shows a nonequilibrium state and suggests that  $RMn_3O_6$  phases (partially) decompose during temperature quenching and/or pressure release. No  $RMn_3O_6$ -type phase was found in samples with the total compositions of  $YbMn_3O_6$  and  $LuMn_3O_6$  [ $(Lu_{2/3}Mn_{1/3})MnO_3$ , 82 %;  $Mn_2O_3$ , 18 %].

The aforementioned facts show that at 6 GPa, the  $RMn_3O_6$ -type structure can be considered stable for  $R = Gd-Tm$  and  $Y$ . However, the appearance of an  $RMn_3O_6$ -type phase in  $SmMn_3O_6$  and  $EuMn_3O_6$  suggests that  $RMn_{3-y}O_{6-1.5y}$  ( $R = Sm$  and  $Eu$ ) can be stabilized at higher pressure. The samples are nonstoichiometric, and the general total composition can be expressed as  $R_{1-\delta}Mn_3O_{6-1.5\delta}$ . Nonstoichiometry varies from  $\delta = -0.071$  to  $-0.059$  for  $R = Gd$ , to  $\delta = 0$  for  $R = Dy$  to  $\delta = 0.05-0.1$  for  $R = Ho$  and  $Y$  to  $\delta = 0.12$  for  $R = Er$  and  $Tm$ . The smaller the size of  $R^{3+}$  cations, the larger the  $R^{3+}$  deficiency in  $R_{1-\delta}Mn_3O_{6-1.5\delta}$ .

No DSC anomalies were found in  $DyMn_3O_6$  and  $Ho_{0.95}Mn_3O_{5.925}$  between 150 and 873 K. This fact suggests the absence of any charge-disordered transitions at the B site. No weight change was detected (measured before and after DSC experiments), and XRPD data showed no change in the phase composition after DSC experiments. These facts indicate that  $DyMn_3O_6$  and  $Ho_{0.95}Mn_3O_{5.925}$  are thermally stable at least up to 873 K. This is a remarkable thermal stability for high-pressure phases.  $DyMn_3O_6$  was partially decomposed after being heated to 1173 K in air with the appearance of a  $DyMn_3O_6$  impurity, as shown in **Figure 3.2**.

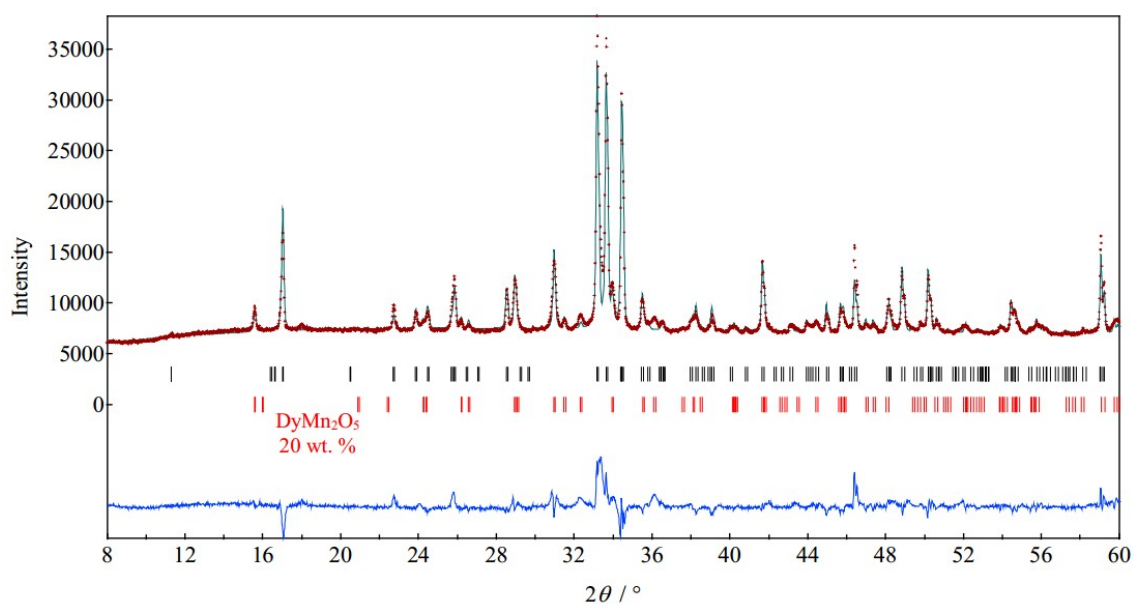


**Figure 3.2.** Fragments of experimental laboratory X-ray powder diffraction patterns measured at room temperature (brown crosses) with fitting results for samples with the total compositions of  $\text{DyMn}_3\text{O}_6$  after a TG-DTA experiment performed up to 1173 K (heating-cooling rate was 10 K/min) in air on a Mettler Toledo instrument.

### 3.3.2. Crystal structures of $\text{RMn}_3\text{O}_6$

The crystal structure of stoichiometric  $\text{DyMn}_3\text{O}_6$  was determined through the single-crystal X-ray analysis. The refinement results are summarized in Table 3.2 and bond-lengths, Mn-O-Mn bond angles, and bond valence sums (BVS) [35] in Table 3.3. Figure 3.3 shows the structure of  $\text{DyMn}_3\text{O}_6$ .

**Table 3.2.** Structural parameters of  $\text{DyMn}_3\text{O}_6$  at 213 K<sup>a</sup>.

Site	Wyckoff position	$x$	$y$	$z$	$U_{\text{eq}} (\text{\AA}^2)$
Dy1	2a	0.25	0.25	0.77911(4)	0.00559(8)
Dy2	2a	0.25	0.25	0.28309(4)	0.00610(8)
Mn1	2b	0.75	0.25	0.71992(16)	0.00623(18)
Mn2	2b	0.75	0.25	0.23984(13)	0.00223(15)
Mn3	4c	0.5	0	0	0.00381(12)
Mn4	4d	0	0.5	0.5	0.00361(12)
O1	8g	0.4362(4)	-0.0685(4)	0.2676(3)	0.0065(4)
O2	4f	0.0569(6)	0.25	0.0403(5)	0.0060(6)

O3	4e	0.25	0.5292(6)	0.9231(5)	0.0050(5)
O4	4f	0.5398(6)	0.25	0.4157(5)	0.0116(8)
O5	4e	0.25	0.4329(6)	0.5392(5)	0.0053(6)

<sup>a</sup>The occupancies of all the sites are unity ( $g = 1.0$ ). Space group  $Pm\bar{m}n$  (No. 59, origin choice 2) with  $a = 7.2479(2)$  Å,  $b = 7.4525(3)$  Å,  $c = 7.8022(2)$  Å,  $V = 421.44(2)$  Å<sup>3</sup>,  $Z = 4$ ,  $\rho_{\text{cal}} = 6.672$  g cm<sup>-3</sup>, and  $\rho_{\text{exp}} = 6.56(2)$  g cm<sup>-3</sup>. Final reliabilities:  $R_1(\text{all}) = 5.64\%$ ,  $R_1[I > 2\sigma(I)] = 4.62\%$ ,  $wR_2(\text{all}) = 10.63\%$ ,  $wR_2[I > 2\sigma(I)] = 10.11\%$ , and goodness of fit = 1.151.

**Table 3.3** Selected bond lengths ( $l < 3.2$  Å), Mn-O-Mn bond angles (degree), bond valence sums (BVS), and distortion parameters of MnO<sub>6</sub> [ $\Delta(\text{Mn})$ ] in DyMn<sub>3</sub>O<sub>6</sub> at 213 K<sup>a</sup>.

Dy1-O5 (×2)	2.315(4)	Dy2-O4 (×2)	2.341(5)
Dy1-O3 (×2)	2.365(4)	Dy2-O2 (×2)	2.355(4)
Dy1-O2 (×2)	2.472(4)	Dy2-O5 (×2)	2.419(4)
Dy1-O1 (×4)	2.671(3)	Dy2-O1 (×4)	2.733(3)
BVS (Dy1 <sup>3+</sup> )	3.10	BVS (Dy2 <sup>3+</sup> )	3.04
Mn1-O1 (×4)	1.913(3)	Mn2-O4 (×2)	2.050(5)
Mn1-O4 (×2)	2.820(3)	Mn2-O3 (×2)	2.079(4)
Mn1-O5 (×2)	3.110(3)	Mn2-O2 (×2)	2.715(4)
BVS (Mn1 <sup>3+</sup> )	2.81	Mn2-O5 (×2)	2.925(4)
		BVS (Mn2 <sup>2+</sup> O <sub>4</sub> )	1.91
		BVS (Mn2 <sup>2+</sup> O <sub>8</sub> )	2.16
Mn3-O3 (×2)	1.9212(13)	Mn4-O5 (×2)	1.9044(13)
Mn3-O2 (×2)	1.9340(11)	Mn4-O1 (×2)	1.940(3)
Mn3-O1 (×2)	2.199(3)	Mn4-O4 (×2)	1.9967(16)
BVS (Mn3 <sup>3+</sup> )	3.15	BVS (Mn4 <sup>3+</sup> )	3.64
$\Delta(\text{Mn3})$	$40.3 \times 10^{-4}$	$\Delta(\text{Mn4})$	$3.8 \times 10^{-4}$
Mn3-O1-Mn4	140.9(2)	Mn4-O4-Mn4	137.8(2)
Mn3-O2-Mn3	148.9(2)	Mn4-O5-Mn4	144.1(2)
Mn3-O3-Mn3	141.2(2)		

<sup>a</sup> BVS =  $\sum_{i=1}^N v_i$ , where  $v_i = \exp[(R_0 - l_i)/B]$ ,  $N$  is the coordination number,  $B = 0.37$ ,  $R_0(\text{Dy}^{3+}) = 2.036$ ,  $R_0(\text{Mn}^{2+}) = 1.79$ , and  $R_0(\text{Mn}^{3+}) = 1.76$  [35].  $\Delta = (1/N)\sum_{i=1}^N [(l_i - l_{\text{av}})/l_{\text{av}}]^2$ , where  $l_{\text{av}} = (1/N)\sum_{i=1}^N l_i$  is the average Mn-O distance and  $N$  is the coordination number.

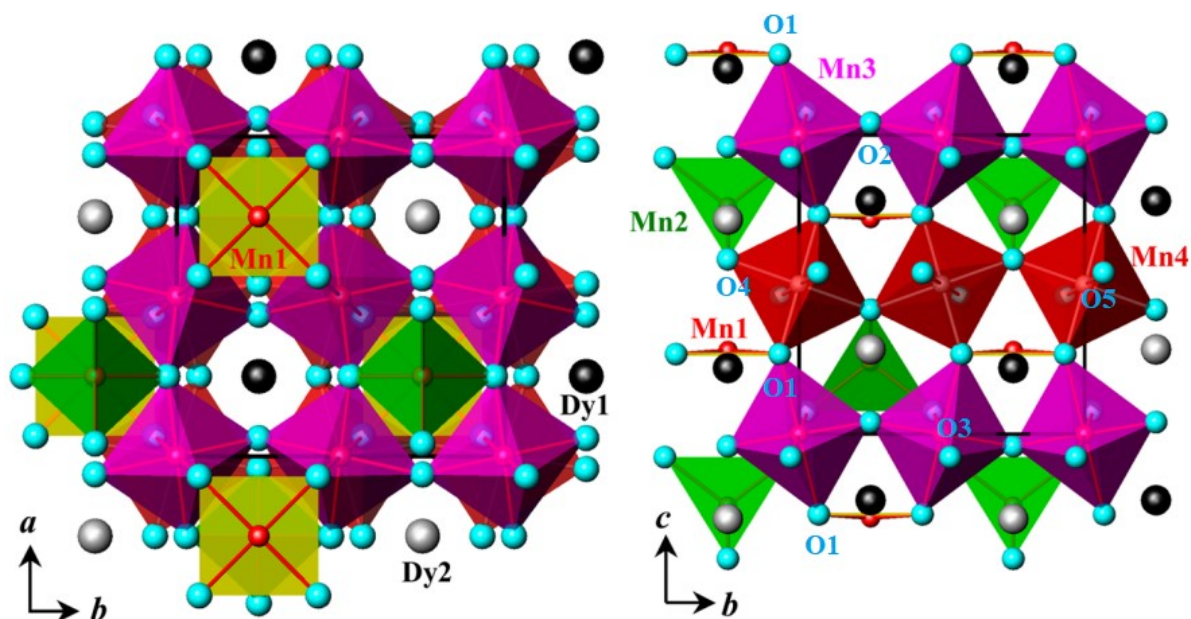


**Figure 3.3.** Projections of the crystal structure of  $\text{DyMn}_3\text{O}_6$  along the  $c$  axis (left) and  $a$  axis (right).  $\text{MnO}_n$  polyhedra are plotted, while Dy atoms are shown as black and gray spheres. Cyan spheres are oxygen atoms.

There are four sites for A-type cations: Dy1, Dy2, Mn1, and Mn2. The Mn2 site has a tetrahedral environment, and its BVS value is close to +2.  $\text{Mn}^{3+}$  is a Jahn-Teller cation, which highly prefers an octahedral coordination (square-pyramidal and square-planar environments are also possible). Therefore, manganese at the Mn2 site cannot have an oxidation state of +3, the average oxidation state of Mn in  $\text{RMn}_3\text{O}_6$ , and this is supported by its BVS value. To form this structure, manganese can enter the Mn2 site only in the +2 oxidation state. The Mn1 site has a square-planar environment, which is allowed for  $\text{Mn}^{3+}$ . The Mn1-O1 bond lengths (1.913 Å) are very close to Mn-O bond lengths for the square-planar  $\text{Mn}^{3+}$  cations in A-site ordered  $\text{AA}'_3\text{B}_4\text{O}_{12}$ -type compounds:  $\text{AMn}_7\text{O}_{12}$  ( $A = \text{Cd}, \text{Ca}, \text{Sr}, \text{and Pb}$ ) [36,37],  $\text{LaMn}_7\text{O}_{12}$  [20,38], and  $\text{BiMn}_7\text{O}_{12}$  [38]; they are quite different from Mn-O bond lengths (2.091 Å) for the square-planar  $\text{Mn}^{2+}$  cations in  $\text{MnRMnSbO}_6$  [29]. The BVS value of Mn1 supports the +3 oxidation state.  $\text{Dy}^{3+}$  cations have 10-fold coordination with the BVS values of +3.10 and +3.04, in the agreement with the expected oxidation state. Therefore, triple ordering of

cations is realized at the A site of  $\text{DyMn}_3\text{O}_6$ :  $[\text{Dy}^{3+}\text{Mn}^{2+}_{0.5}\text{Mn}^{3+}_{0.5}]_{\text{A}}$ . The cations are ordered in chains running along the  $c$  axis: one chain consists of  $\text{Dy}^{3+}$  cations, and another chain consists of alternating  $\text{Mn}^{2+}$  and  $\text{Mn}^{3+}$  cations (Figure 3.3). Triple cation ordering in perovskites is very rare. It was found, for example, at the B sites of  $\text{Ca}_4\text{GaNbO}_8$  ( $= [\text{Ca}^{2+}_3]_{\text{A}}[\text{Ca}^{2+}\text{Ga}^{3+}\text{Nb}^{5+}]_{\text{B}}\text{O}_{9-\delta}$ ) [39]; however, the triple ordering was realized because ordered oxygen vacancies create tetrahedral coordination for  $\text{Ga}^{3+}$ . The crystal structure of  $\text{Ca}_2\text{FeOsO}_6$  is shown in **Figure 3.2**, based on the experimental solution, showing that Fe and Os ions alternate to occupy the octahedral like a checker board. Bond angles of the inter-octahedral Fe-O-Os are  $151^\circ$  and  $154^\circ$ , which are far from  $180^\circ$ , indicating significant buckling of the octahedral connection. **Figure 3.2** shows alternate rotations of the octahedra along and perpendicular to the  $c$  axis, respectively. The Glazer's notation is  $a^-a^-b^+$ , where the superscripts indicate that neighbor octahedra rotated in the same ( $^+$ ) and opposite ( $^-$ ) direction [39]. The degree of distortion is clearly more enhanced than that of  $\text{Sr}_2\text{FeOsO}_6$ , where the inter-octahedral Fe-O-Os are  $180^\circ$  and  $165^\circ$  [35].

There are two sites for B-type cations: Mn3 and Mn4. The Mn3 site has an octahedral environment and a strong elongated Jahn-Teller distortion with a typical (for  $\text{Mn}^{3+}$ ) octahedral distortion parameter,  $\Delta(\text{Mn})$ , of  $40.3 \times 10^{-4}$ . The BVS value of +3.15 supports the +3 oxidation state for Mn. Therefore, the Mn3 site should be solely occupied by  $\text{Mn}^{3+}$ . The Mn4 site also has an octahedral environment, but with a significantly reduced  $\Delta(\text{Mn})$  parameter of  $3.8 \times 10^{-4}$ , and with a BVS value of +3.64. These facts suggest that the Mn4 site cannot have sole Jahn-Teller  $\text{Mn}^{3+}$  cations, and it should contain a mixture of  $\text{Mn}^{3+}$  and  $\text{Mn}^{4+}$  cations. Therefore, double ordering of cations is realized at the B site of  $\text{DyMn}_3\text{O}_6$ :  $[\text{Mn}^{3+}\text{Mn}^{3.5+}]_{\text{B}}$ . It has been mentioned that unusual layered ordering of  $\text{Mn}^{3+}$  and  $\text{Mn}^{3.5+}$  takes place in  $\text{RMn}_3\text{O}_6$  in contrast with the usually observed rock-salt ordering at B sites. One of the conditions for layered ordering is the presence of cations with a pronounced Jahn-Teller

effect (e.g., in  $\text{La}_2\text{CuSnO}_6$  [23]) ; and this condition is fulfilled in  $\text{RMn}_3\text{O}_6$ . Another empirical condition (that the charge difference between B-type cations should be +2) [23] for layered ordering is not realized. Ordering of manganese in different oxidation states at the B site was also found in  $\text{In}_{2/3}\text{Mn}_{4/3}\text{O}_3$  ( $= [\text{In}^{3+}_{4/3}\text{Mn}^{2+}_{2/3}]_{\text{A}}[\text{Mn}^{3+}\text{Mn}^{3.667+}]_{\text{B}}\text{O}_6$  [40]). The ratio of  $\text{Mn}^{3+}$  and  $\text{Mn}^{4+}$  cations at the Mn4 site could vary in principle; this could be one of the origin of nonstoichiometry of other  $R_{1-\delta}\text{Mn}_3\text{O}_{6-1.5\delta}$  compounds with  $R = \text{Y, Ho, Er, and Tm}$ .

New  $\text{RMn}_3\text{O}_6$  perovskites are structurally related with  $\text{CaFeTi}_2\text{O}_6$  [41],  $\text{CaMnTi}_2\text{O}_6$  [42], and recently discovered  $\text{MnRMnSbO}_6$  ( $R = \text{La-Sm}$ ) [29] and  $\text{RMnGaTiO}_6$  ( $R = \text{Sm and Gd}$ ) [43] perovskites. In  $\text{MnRMnSbO}_6$  ( $R = \text{La-Sm}$ ), the oxidation states of +3 for R and +5 for Sb determine the oxidation state of Mn as +2; this oxidation state of Mn in all the sites was supported by BVS values and other methods. For this reason,  $\text{MnRMnSbO}_6$  ( $R = \text{La-Sm}$ ) compounds were described as perovskites with double order at the A site and double order at the B site,  $[\text{R}^{3+}\text{Mn}^{2+}]_{\text{A}}[\text{Mn}^{2+}\text{Sb}^{5+}]_{\text{B}}\text{O}_6$ .  $\text{MnRMnSbO}_6$  is stabilized for larger rare-earth elements ( $R = \text{La-Sm}$ ), while  $\text{RMn}_3\text{O}_6$  is stabilized for intermediate rare-earth elements ( $R = \text{Gd-Tm and Y}$ ).  $\text{MnRMnSbO}_6$  with  $R = \text{Eu and Gd}$  crystallizes in the B-site ordered structure with a disordered distribution of  $\text{Mn}^{2+}$  and  $\text{R}^{3+}$  cations at the A site (similar to  $\text{In}_{2/3}\text{Mn}_{4/3}\text{O}_3$ ); and no information is reported about the behavior of such compounds with  $R = \text{Tb-Lu and Y}$  [29].  $\text{RMn}_3\text{O}_6$  perovskites do not form for  $R = \text{La-Eu, Yb, and Lu}$  (at 6 GPa).  $\text{MnRMnSbO}_6$  crystallizes in tetragonal space group  $P4_2/n$ , while  $\text{RMn}_3\text{O}_6$  crystallizes in orthorhombic space group  $Pmmn$ . There are no direct group-subgroup relations between  $P4_2/n$  and  $Pmmn$ , but they are both subgroups of  $P4_2/nmc$  (No. 137), which can be considered as a parent model for both  $\text{MnRMnSbO}_6$  and  $\text{RMn}_3\text{O}_6$  perovskites.  $\text{CaFeTi}_2\text{O}_6$  [41] and  $\text{RMnGaTiO}_6$  ( $R = \text{Sm and Gd}$ ) [43] adopt this parent structure. The parent structure is tetragonal with  $a = b$  and with the rare  $a^+ a^+ c^-$  tilt system [23]. To form the layered B-site ordering, and orthorhombic distortion is needed, and the noticeable contraction of the cell along the  $a$  axis can be explained by a

stronger octahedral tilt (Mn3-O3-Mn3) along this axis in comparison with the *b* axis (Mn3-O2-Mn3). Ten GPa was needed to synthesize  $\text{MnRMnSbO}_6$  ( $R = \text{La-Sm}$ ), while  $\text{RMn}_3\text{O}_6$  ( $R = \text{Gd-Tm and Y}$ ) could be prepared at 6 GPa. As mentioned above, layered ordering of  $\text{Mn}^{3+}$  and  $\text{Mn}^{3.5+}$  takes place in  $\text{RMn}_3\text{O}_6$  in comparison with the rock-salt ordering of  $\text{Mn}^{2+}$  and  $\text{Sb}^{5+}$  in  $\text{MnRMnSbO}_6$ . Therefore, unique structural properties take place in the  $\text{RMn}_3\text{O}_6$  family of perovskite materials.

Because of very specific coordination environments of cations at the A site, it is difficult to expect any charge-disordered transitions associated with the A site with a random distribution of  $\text{Mn}^{2+}$  and  $\text{Mn}^{3+}$  cations between the Mn1 and Mn2 site. On the other hand, a charge-disordered transition associated with the B site is possible when the Mn3 and Mn4 sites will become equivalent with a random distribution of  $\text{Mn}^{3+}$  and  $\text{Mn}^{4+}$  cations. However, there is no evidence for such a transition up to 873 K, indicating that B-site cation ordering is quite robust.

### 3.3.3. Magnetic and other properties of $\text{RMn}_3\text{O}_6$

**Figure 3.4** presents dc magnetic susceptibilities of  $\text{Er}_{0.88}\text{Mn}_3\text{O}_{5.82}$ , and  $\text{Tm}_{0.88}\text{Mn}_3\text{O}_{5.82}$ . They show two magnetic transitions at  $T_{N1} = 75$  K and  $T_{N2} = 20$  K for  $\text{Tm}_{0.88}\text{Mn}_3\text{O}_{5.82}$ , and  $T_{N1} = 68$  K and  $T_{N2} = 21$  K for  $\text{Er}_{0.88}\text{Mn}_3\text{O}_{5.82}$ . Specific heat measurements of  $\text{Tm}_{0.88}\text{Mn}_3\text{O}_{5.82}$  confirm transitions at  $T_{N1}$  and  $T_{N2}$  and show an additional anomaly near 3 K, which could originate from magnetism of  $\text{Tm}^{3+}$ , as shown in **Figure 3.5**.

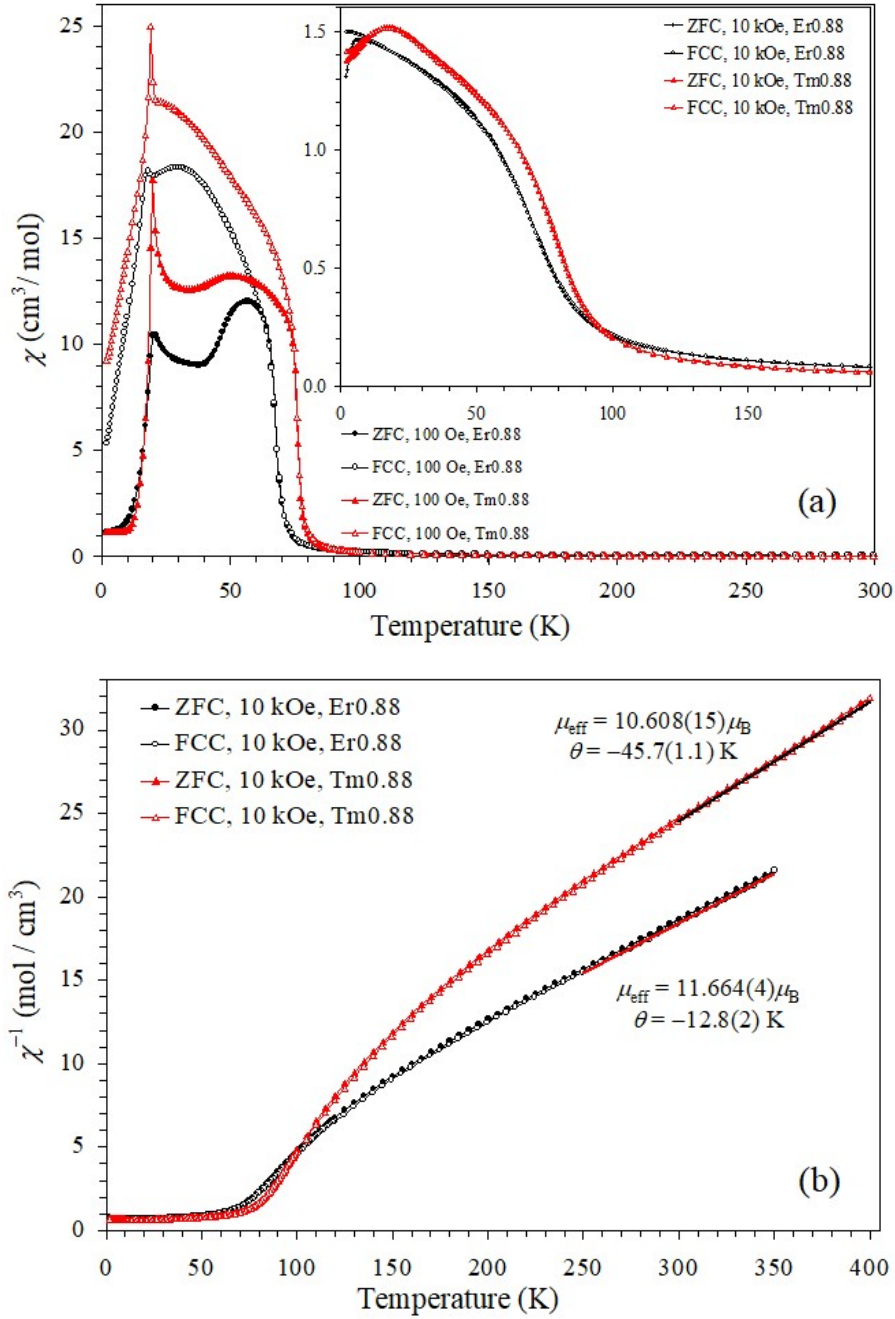


**Figure 3.4.** (a) ZFC (filled symbols) and FCC (empty symbols) dc magnetic susceptibility ( $\chi = M/H$ ) curves of  $\text{Er}_{0.88}\text{Mn}_3\text{O}_{5.82}$  and  $\text{Tm}_{0.88}\text{Mn}_3\text{O}_{5.82}$  at 100 Oe. The inset in (a) shows the  $\chi$  vs  $T$  curves at 10 kOe. (b)  $\chi^{-1}$  vs  $T$  curves of  $\text{Er}_{0.88}\text{Mn}_3\text{O}_{5.82}$  and  $\text{Tm}_{0.88}\text{Mn}_3\text{O}_{5.82}$  at 10 kOe with the Curie-Weiss fits.

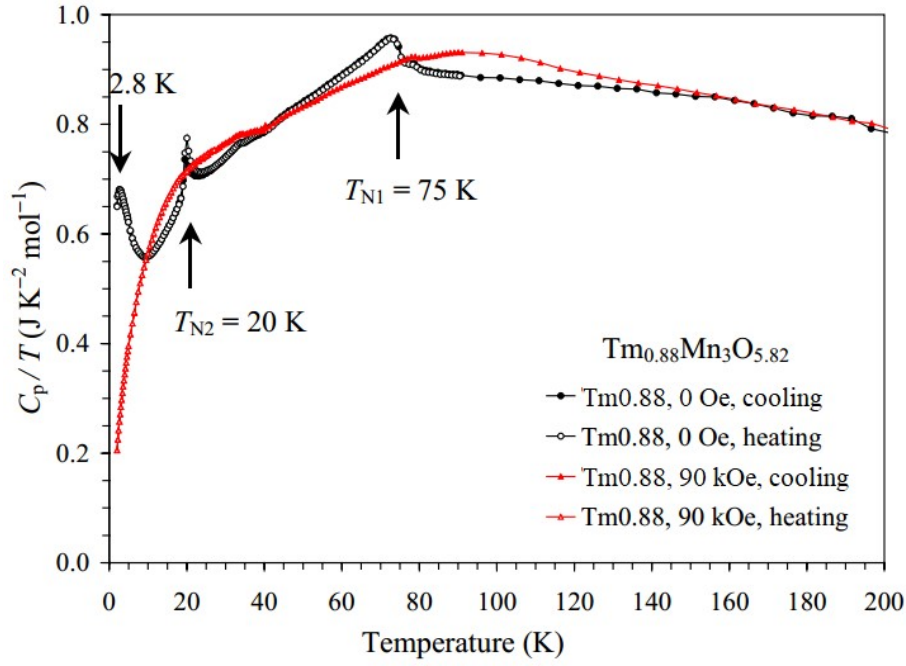
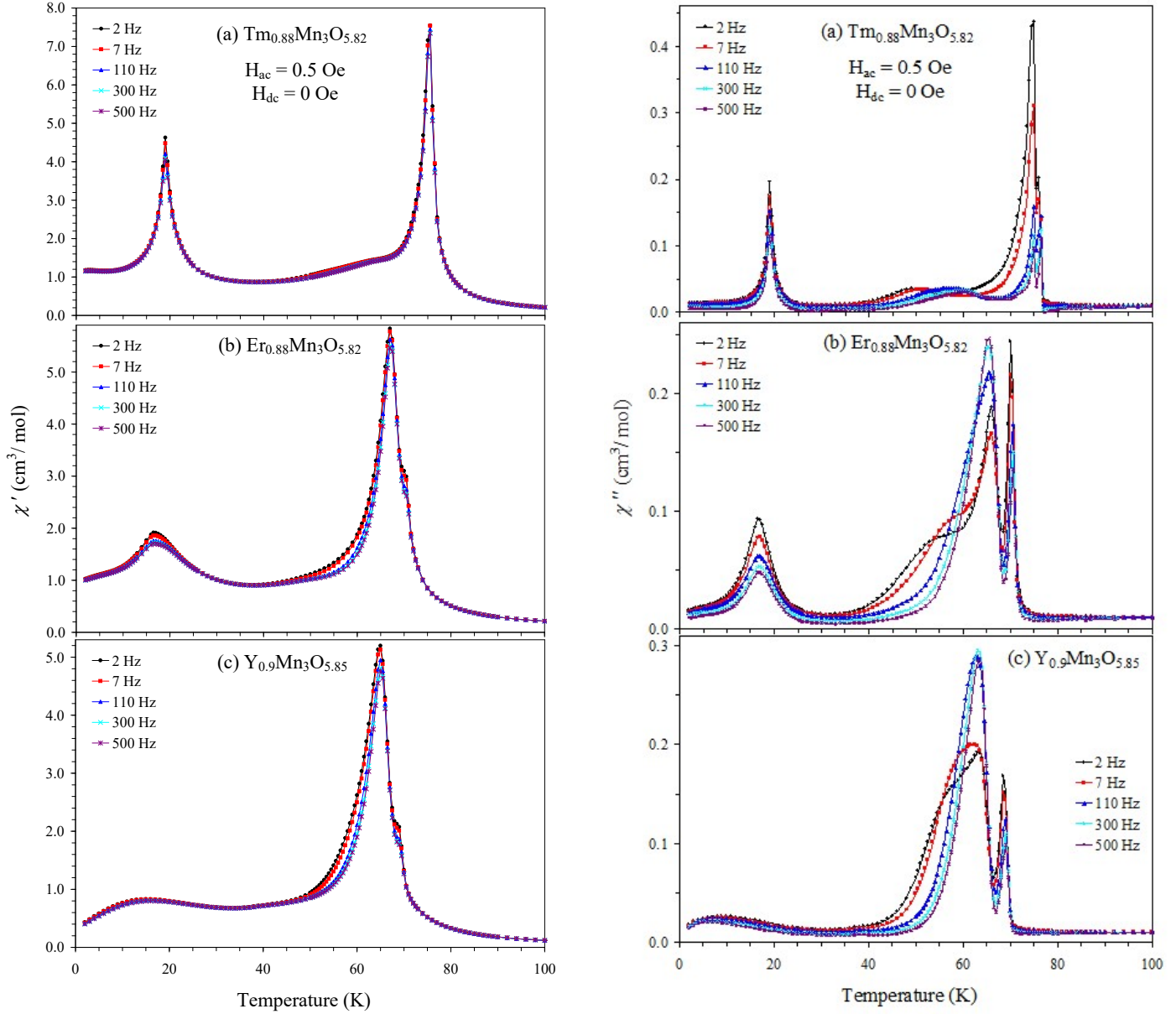


**Figure 3.5** Specific heat of  $\text{Tm}_{0.88}\text{Mn}_3\text{O}_{5.82}$  (plotted as  $C_p/T$  vs  $T$ ) measured at  $H = 0$  Oe and 90 kOe on cooling and heating.

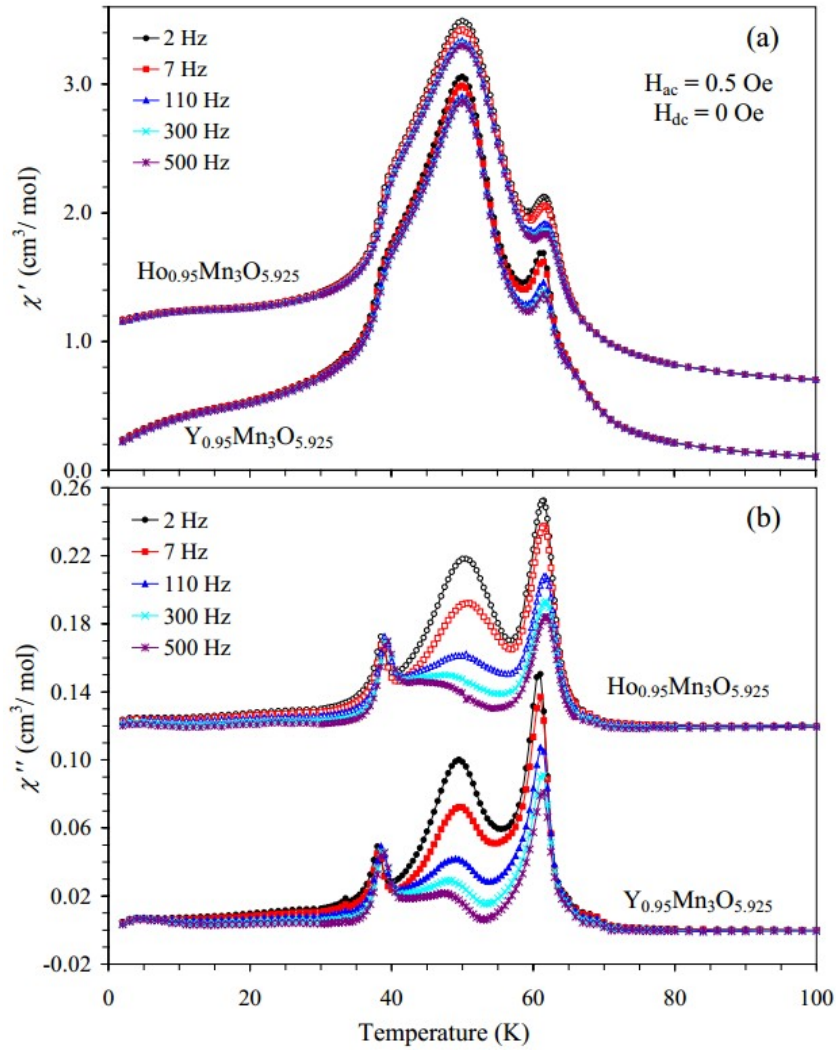
**Figure 3.6** present the real parts and imaginary parts of ac magnetic susceptibilities of  $\text{Er}_{0.88}\text{Mn}_3\text{O}_{5.82}$ ,  $\text{Tm}_{0.88}\text{Mn}_3\text{O}_{5.82}$  and  $\text{Y}_{0.9}\text{Mn}_3\text{O}_{5.85}$ . They show more complex behavior with split anomalies near  $T_{N1}$ :  $T_{N1a} = 77$  K and  $T_{N1b} = 75$  K for  $\text{Tm}_{0.88}\text{Mn}_3\text{O}_{5.82}$ , and  $T_{N1a} = 70$  K and  $T_{N1b} = 67$  K for  $\text{Er}_{0.88}\text{Mn}_3\text{O}_{5.82}$ . The splitting near  $T_{N1}$  is enhanced in  $\text{Ho}_{0.9}\text{Mn}_3\text{O}_{5.85}$  ( $T_{N1a} = 69$  K, and  $T_{N1b} = 65$  K) and  $\text{Y}_{0.9}\text{Mn}_3\text{O}_{5.85}$  ( $T_{N1a} = 69$  K and  $T_{N1b} = 65$  K). The ac anomalies near  $T_{N2}$  are sharp in  $\text{Tm}_{0.88}\text{Mn}_3\text{O}_{5.82}$ ; they become broader in  $\text{Er}_{0.88}\text{Mn}_3\text{O}_{5.82}$ , and they almost completely vanish in  $\text{Ho}_{0.9}\text{Mn}_3\text{O}_{5.85}$  and  $\text{Y}_{0.9}\text{Mn}_3\text{O}_{5.85}$ .

Significant effects of the composition on magnetic properties have been found. For example, magnetic anomalies on ac susceptibilities are observed at  $T_{N1} = 61$  K,  $T_{N2} = 50$  K, and  $T_{N3} = 39$  K in  $\text{Ho}_{0.95}\text{Mn}_3\text{O}_{5.925}$  and  $\text{Y}_{0.95}\text{Mn}_3\text{O}_{5.925}$  (shown in **Figure 3.7**) and near  $T_{N1a} = 69$  K and  $T_{N1b} = 65$  K in  $\text{Ho}_{0.9}\text{Mn}_3\text{O}_{5.85}$  and  $\text{Y}_{0.9}\text{Mn}_3\text{O}_{5.85}$  (shown in **Figure 3.8**). And magnetic properties of  $\text{Ho}_{0.95}\text{Mn}_3\text{O}_{5.925}$  and  $\text{Y}_{0.95}\text{Mn}_3\text{O}_{5.925}$  are almost identical (and those of  $\text{Ho}_{0.9}\text{Mn}_3\text{O}_{5.85}$  and  $\text{Y}_{0.9}\text{Mn}_3\text{O}_{5.85}$  are, too). This fact shows that their properties are determined

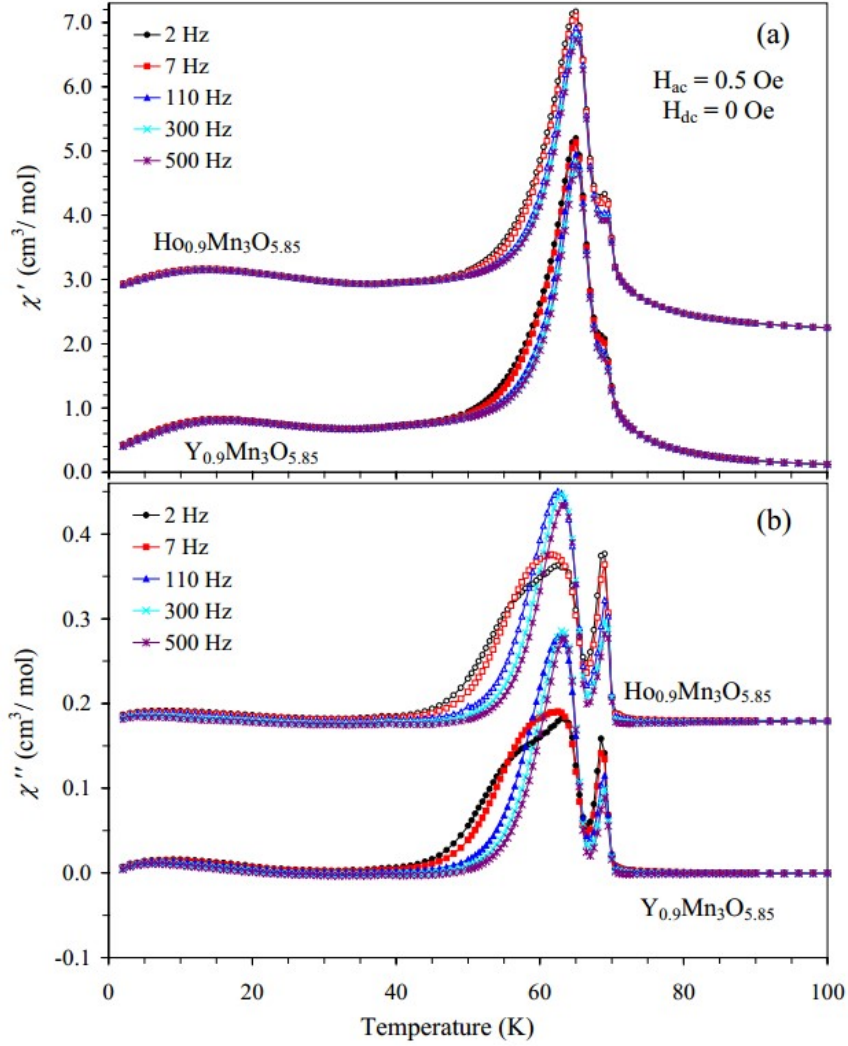
by the stoichiometry and size of  $R^{3+}$  cations [ $\text{Ho}^{3+}$  ( $r^{\text{VIII}} = 1.015 \text{ \AA}$ ) is very close to  $\text{Y}^{3+}$  ( $r^{\text{VIII}} = 1.019 \text{ \AA}$ )] [1].



**Figure 3.6.** Real parts ( $\chi'$  vs  $T$ ) and imaginary parts ( $\chi''$  vs  $T$ ) of the ac susceptibilities of (a)  $\text{Tm}_{0.88}\text{Mn}_3\text{O}_{5.82}$ , (b)  $\text{Er}_{0.88}\text{Mn}_3\text{O}_{5.82}$ , and (c)  $\text{Y}_{0.9}\text{Mn}_3\text{O}_{5.85}$ . Measurements were performed on cooling from 100 K to 2 K at a zero static magnetic field using an ac field with the amplitude  $H_{\text{ac}} = 0.5$  Oe and different frequencies.

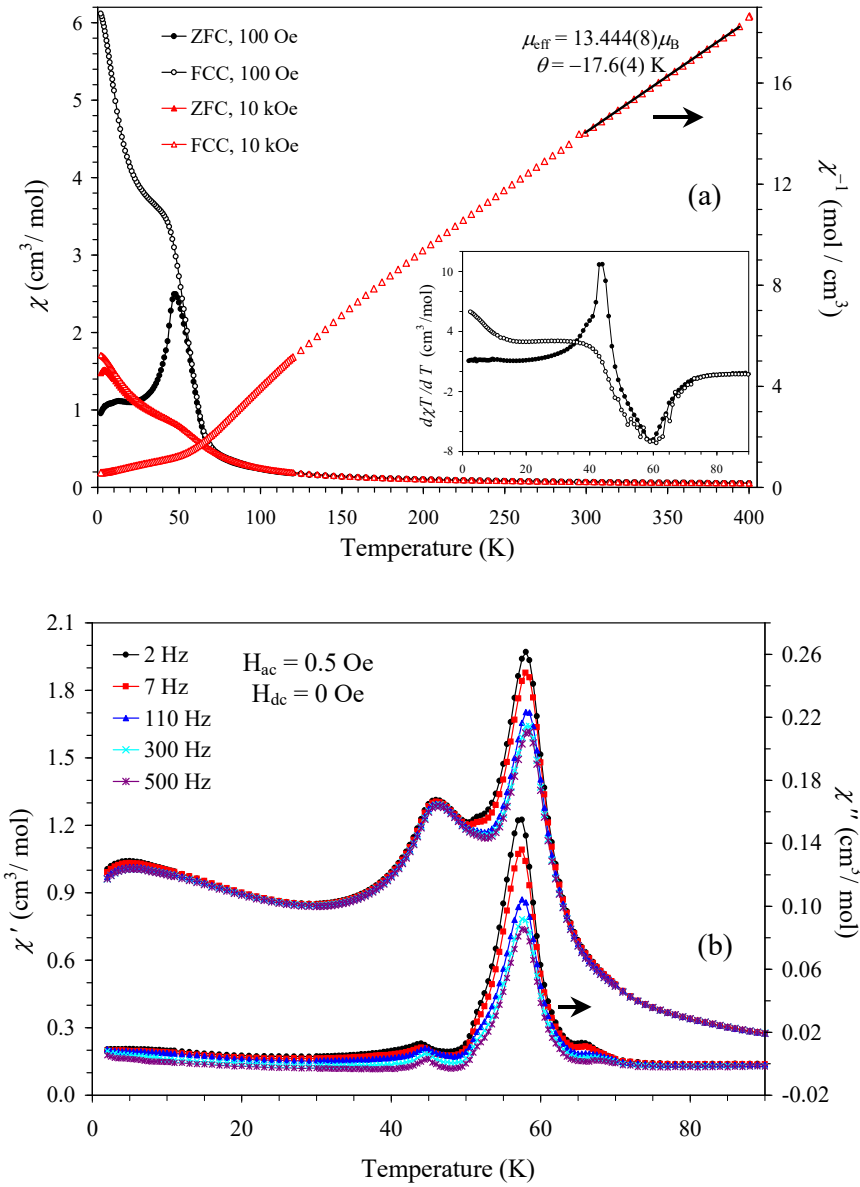


**Figure 3.7.** (a) Real parts of the ac susceptibilities ( $\chi'$  vs  $T$ ) of  $\text{Ho}_{0.95}\text{Mn}_3\text{O}_{5.925}$  and  $\text{Y}_{0.95}\text{Mn}_3\text{O}_{5.925}$  (the curves for  $\text{Ho}_{0.95}\text{Mn}_3\text{O}_{5.925}$  are shifted by +0.5 for the clarity). (b) Imaginary parts of the ac susceptibilities ( $\chi''$  vs  $T$ ) of  $\text{Ho}_{0.95}\text{Mn}_3\text{O}_{5.925}$  and  $\text{Y}_{0.95}\text{Mn}_3\text{O}_{5.925}$  (the curves for  $\text{Ho}_{0.95}\text{Mn}_3\text{O}_{5.925}$  are shifted by +0.12 for the clarity).

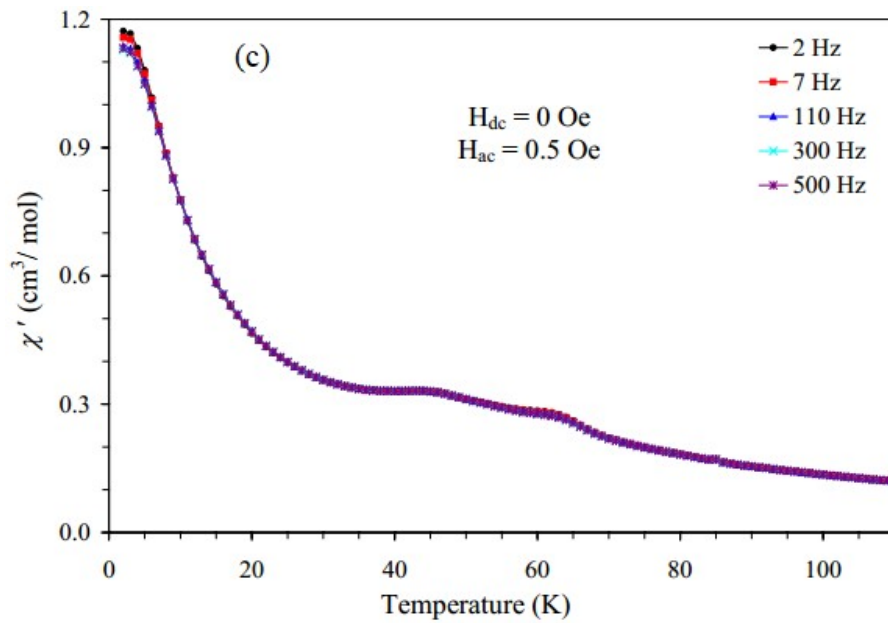
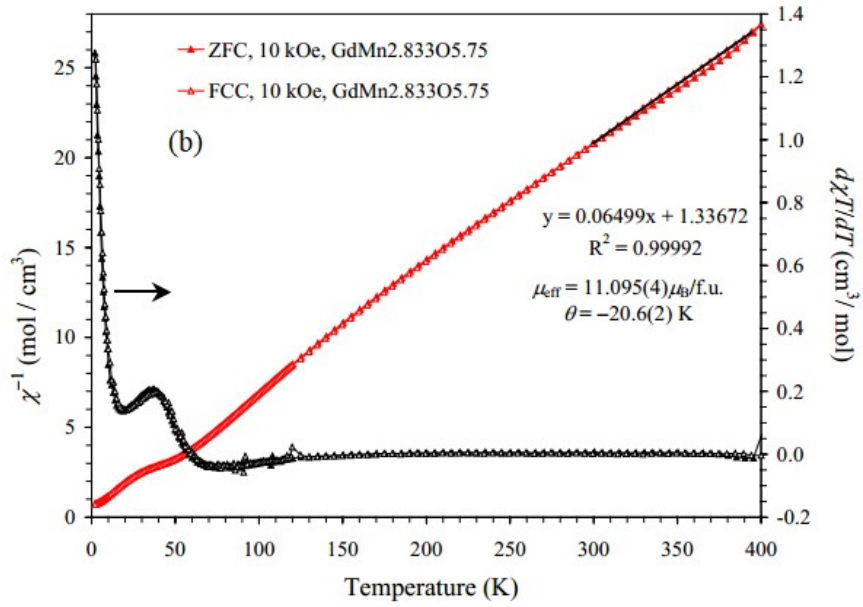
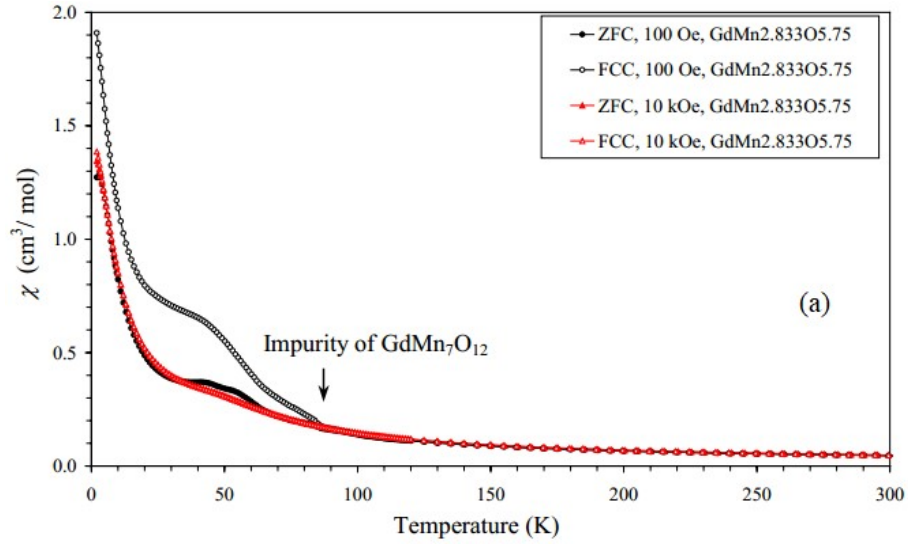


**Figure 3.8.** (a) Real parts of the ac susceptibilities ( $\chi'$  vs  $T$ ) of  $\text{Ho}_{0.9}\text{Mn}_3\text{O}_{5.85}$  and  $\text{Y}_{0.9}\text{Mn}_3\text{O}_{5.85}$  (the curves for  $\text{Ho}_{0.9}\text{Mn}_3\text{O}_{5.85}$  are shifted by +2 for the clarity). (b) Imaginary parts of the ac susceptibilities ( $\chi''$  vs  $T$ ) of  $\text{Ho}_{0.9}\text{Mn}_3\text{O}_{5.85}$  and  $\text{Y}_{0.9}\text{Mn}_3\text{O}_{5.85}$  (the curves for  $\text{Ho}_{0.9}\text{Mn}_3\text{O}_{5.85}$  are shifted by +0.18 for the clarity).

Magnetic properties of  $\text{DyMn}_3\text{O}_6$  change again in comparison with some those of the  $\text{Ho}_{1-\delta}\text{Mn}_3\text{O}_{6-1.5\delta}$  system with some anomalies on  $d\chi T/dT$  vs  $T$ ,  $\chi'$  vs  $T$ , and  $\chi''$  vs  $T$  curves at  $T_{N1} = 58$  K and  $T_{N2} = 46$  K (shown in **Figure 3.9**). No clearly defined anomalies are detected in  $\text{GdMn}_{2.833}\text{O}_{5.75}$  on dc susceptibilities, but  $d\chi T/dT$  vs  $T$ ,  $\chi'$  vs  $T$ , or  $\chi''$  vs  $T$  curves show some anomalies near 63, 37, and 3 K (shown in **Figure 3.10**).



**Figure 3.9.** (a, left-hand axis) ZFC (filled symbols) and FCC (empty symbols) dc magnetic susceptibility curves of  $\text{DyMn}_3\text{O}_6$  at 100 Oe and 10 kOe. (a, right-hand axis) FCC  $\chi^{-1}$  vs  $T$  curve of  $\text{DyMn}_3\text{O}_6$  at 10 kOe with the Curie-Weiss fit. The inset in (a) shows the  $d\chi T/dT$  vs  $T$  curves at 100 Oe. (b) Real parts ( $\chi'$  vs  $T$ ) and imaginary parts ( $\chi''$  vs  $T$ ) of the ac susceptibilities of  $\text{DyMn}_3\text{O}_6$  ( $H_{ac} = 0.5$  Oe).



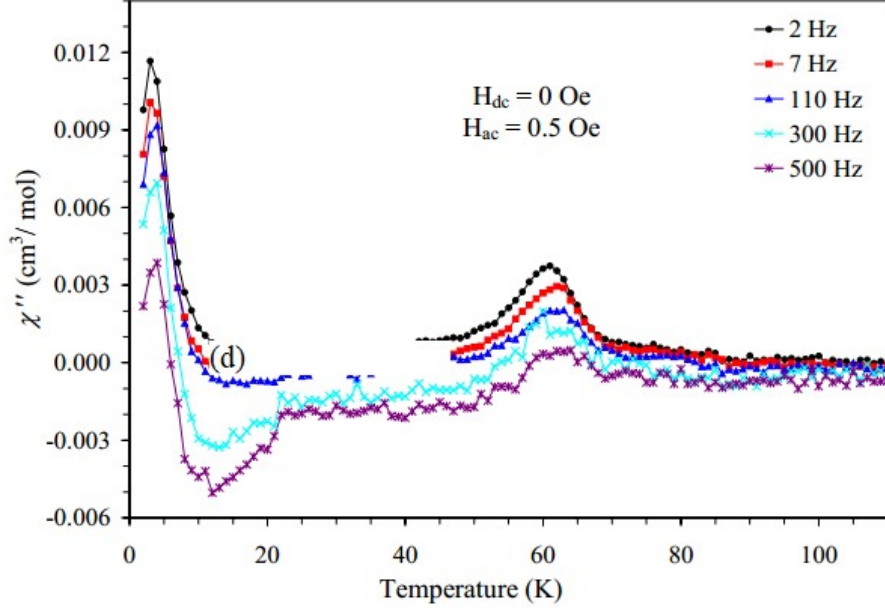


**Figure 3.10.** (a) ZFC and FCC dc magnetic susceptibility curves of  $\text{GdMn}_{2.833}\text{O}_{5.75}$  at 100 Oe and 10 kOe. (b, left-hand axis) ZFC and FCC  $\chi^{-1}$  vs  $T$  curve of  $\text{GdMn}_{2.833}\text{O}_{5.75}$  at 10 kOe with the Curie-Weiss fit. (b, right-hand axis) The  $d\chi T/dT$  vs  $T$  curves of  $\text{GdMn}_{2.833}\text{O}_{5.75}$  at 100 Oe. (c) Real parts and (d) imaginary parts of the ac susceptibilities of  $\text{GdMn}_{2.833}\text{O}_{5.75}$ .

The inverse magnetic susceptibilities follow the Curie-Weiss law, but only at high temperatures. Below  $\sim 250$  K, which is much higher than  $T_N$ , significant deviations from the Curie-Weiss behavior are observed (shown in **Figure 3.4b**). This deviation is also observed in  $\text{Y}_{0.9}\text{Mn}_3\text{O}_{5.85}$  and  $\text{Y}_{0.95}\text{Mn}_3\text{O}_{5.925}$  without magnetic  $R^{3+}$  cations (shown in **Figure 3.11**). This fact indicates that the deviation should originate from short-range magnetic interactions among manganese cations. Between 300 and 395 K, the inverse magnetic susceptibilities (measured at 10 kOe in the FCC mode) are fit by the Curie-Weiss equation

$$\chi(T) = \mu_{\text{eff}}^2 N [3k_B(T - \theta)]^{-1}$$

where  $\mu_{\text{eff}}$  is an effective magnetic moment,  $N$  is Avogadro's number,  $k_B$  is Boltzmann's constant, and  $\theta$  is the Curie-Weiss temperature. The fitting parameters are summarized in **Table 3.4**. The  $\mu_{\text{eff}}$  values are in good agreement with the theoretical values. The negative

Curie-Weiss temperatures show that the strongest exchange interactions are antiferromagnetic in nature.

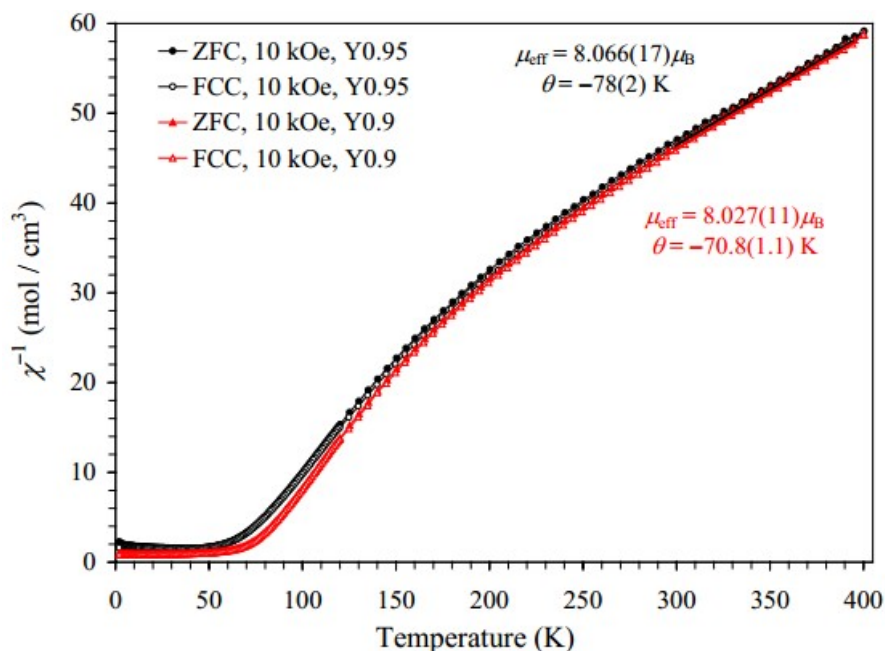


**Figure 3.11.** ZFC and FCC dc  $\chi^{-1}$  vs T curves of at  $\text{Y}_{0.9}\text{Mn}_3\text{O}_{5.85}$  and  $\text{Y}_{0.95}\text{Mn}_3\text{O}_{5.925}$  10 kOe with the Curie-Weiss fits.

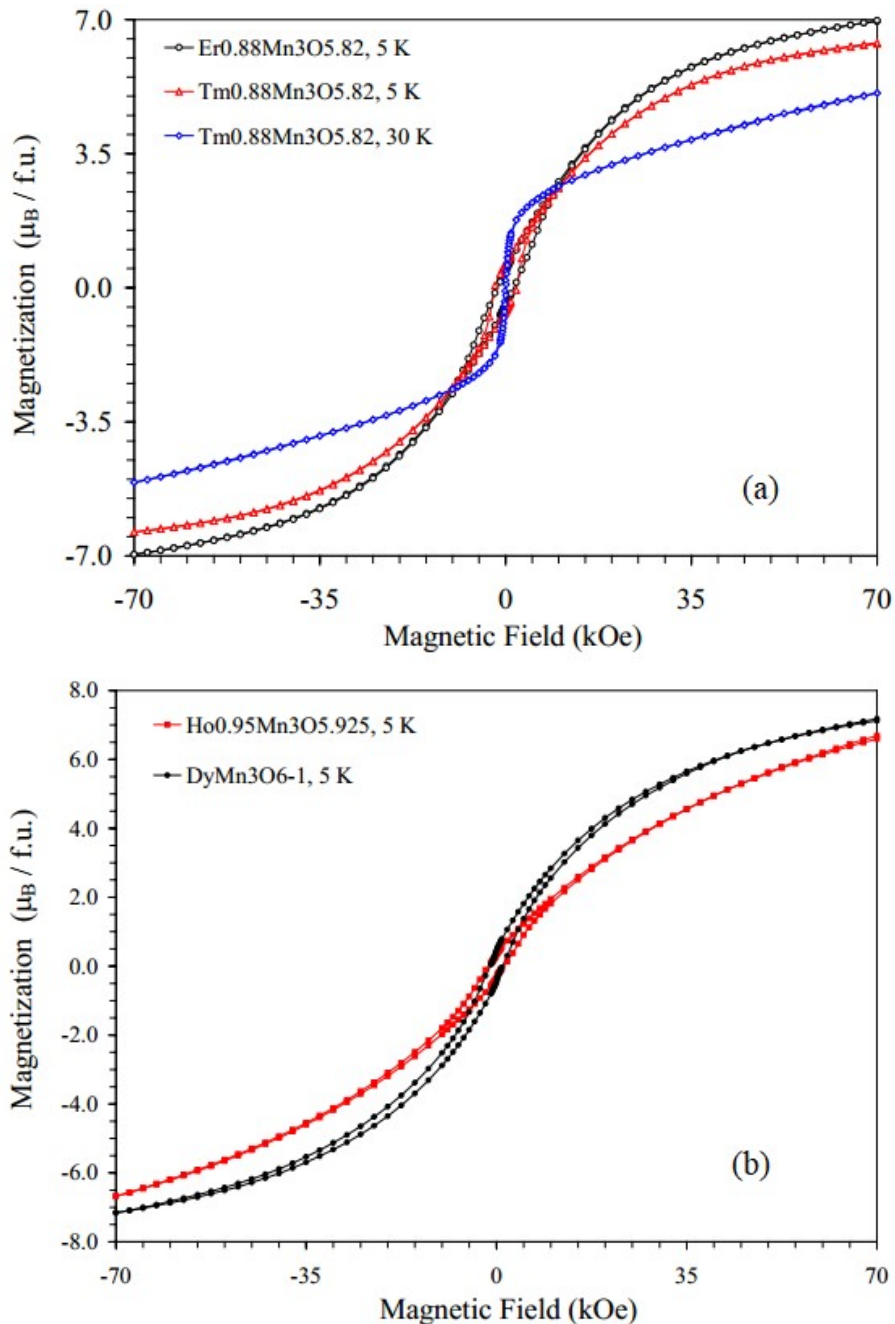
**Table 3.4** Temperatures of magnetic anomalies, parameters of the Curie-Weiss fits, and saturation magnetization of  $\text{R}_{1-\delta}\text{Mn}_3\text{O}_{6-1.5\delta}$  and  $\text{GdMn}_{3-y}\text{O}_{6-1.5y}$ .<sup>a</sup>

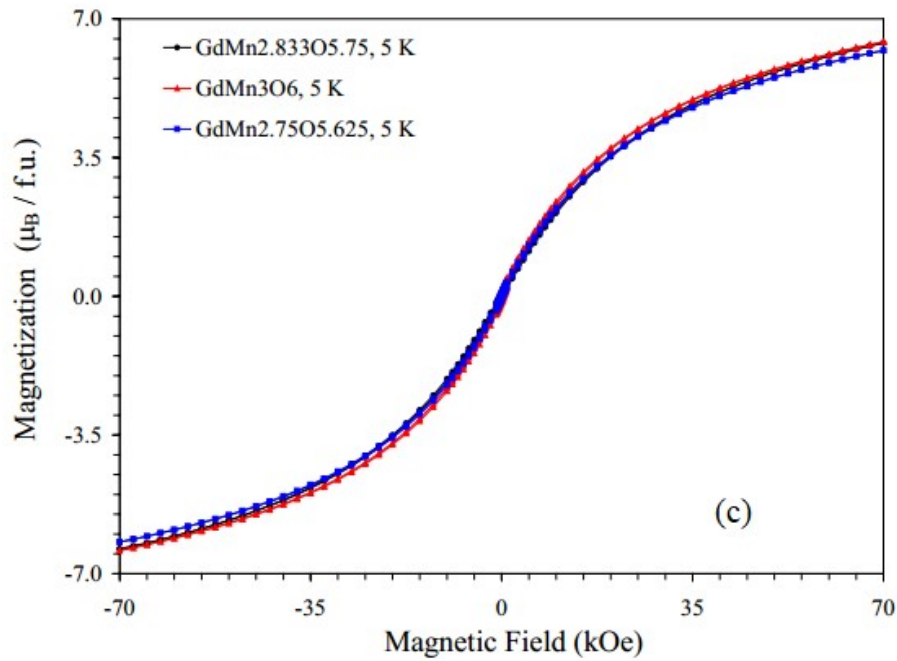
composition	$T$ (K)	$\mu_{\text{eff}}$ ( $\mu_B/\text{f.u.}$ )	$M_{\text{calc}}$ ( $\mu_B/\text{f.u.}$ )	$\theta$ (K)	$M_s$ ( $\mu_B/\text{f.u.}$ )
$\text{Tm}_{0.88}\text{Mn}_3$	3, 20, 75, 77	10.608(15)	11.110	-45.7(1.1)	6.40
$\text{Er}_{0.88}\text{Mn}_3$	21, 67, 70	12.318(16)	12.407	-46.7(1.0)	6.97
$\text{Ho}_{0.9}\text{Mn}_3$	65, 69	12.917(9)	13.200	-24.7(5)	6.89
$\text{Ho}_{0.95}\text{Mn}_3$	39, 50, 61	13.244(14)	13.407	-31.0(8)	6.69
$\text{Y}_{0.9}\text{Mn}_3$	65, 69	8.027(11)	8.544	-70.8(1.1)	3.05
$\text{Y}_{0.95}\text{Mn}_3$	39, 49, 61	8.066(17)	8.544	-78(2)	2.26
$\text{DyMn}_3$	46, 58	13.444(8)	13.638	-17.6(4)	7.18
$\text{GdMn}_{2.833}$	3, 37, 63	11.095(11)	11.447	-20.6(8)	6.39
$\text{GdMn}_{2.75}$	4, 36, 61	11.073(8)	11.360	-32.9(5)	6.13

<sup>a</sup> The Curie-Weiss fits are performed between 300 and 395 K for the FCC data at 10 kOe.  $M_s$  is the magnetization value at 5 K and 70 kOe.  $\mu_{\text{calc}}$  is calculated assuming  $\text{R}^{3+}_{1-\delta}\text{Mn}^{2+}_{0.5}\text{Mn}^{3+}_2\text{Mn}^{4+}_{0.5}$  for R = Dy-Tm and Y {with calculated values of magnetic

moments for  $R^{3+}$ ,  $g[J(J+1)]^{0.5}$  and  $Gd^{3+}Mn^{3+}_{3-y}$  because the charge distribution is difficult to assign in  $GaMn_{3-y}O_{6-1.5y}$ , and the average oxidation state of Mn is used.

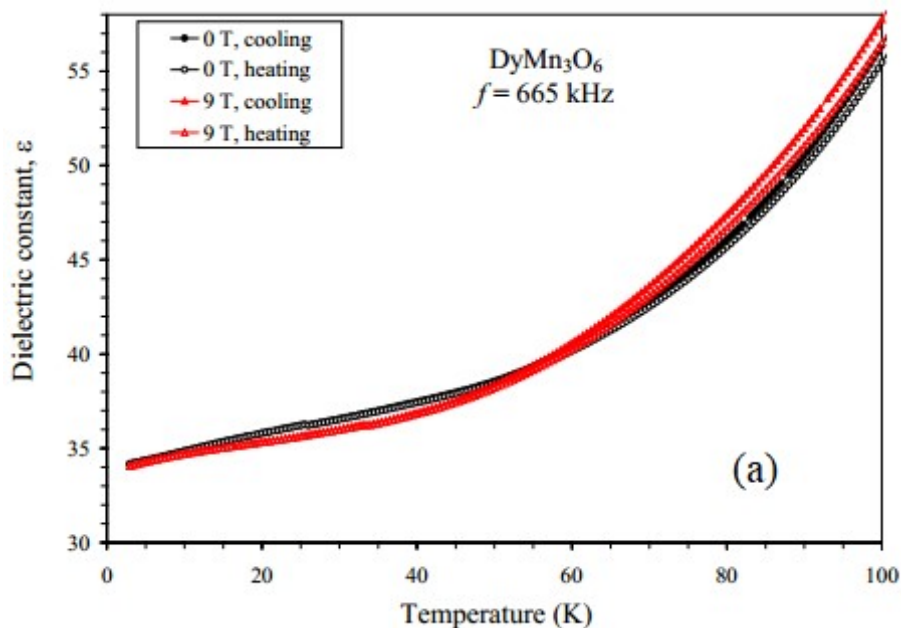
Isothermal field-dependent M-H curves are reported on the insets of **Figures 3.12**, and the magnetization values at 5 K and 70 kOe ( $M_S$ ) are reported in **Table 3.4**. The presence of hysteresis loops indicates that  $R_{1-\delta}Mn_3O_{6-1.5\delta}$  compounds are canted antiferromagnets or ferrimagnets.





**Figure 3.12.** (a) M-H curves of  $\text{Tm}_{0.88}\text{Mn}_3\text{O}_{5.82}$  at 5 K and 30 K and  $\text{Er}_{0.88}\text{Mn}_3\text{O}_{5.82}$  at 5 K. (b) M-H curves of  $\text{DyMn}_3\text{O}_6$  and  $\text{Ho}_{0.95}\text{Mn}_3\text{O}_{5.925}$  at 5 K. (c) M-H curves of  $\text{GdMn}_3\text{O}_6$ ,  $\text{GdMn}_{2.833}\text{O}_{5.75}$ , and  $\text{GdMn}_{2.75}\text{O}_{5.625}$  at 5 K.

No dielectric anomalies are observed at the magnetic transition temperatures in  $\text{DyMn}_3\text{O}_6$  (shown in Figure 3.13) and  $\text{Tm}_{0.88}\text{Mn}_3\text{O}_{5.82}$  (shown in Figure 3.14) and the magnetodielectric effect is negligible. These facts indicate that  $\text{R}_{1-\delta}\text{Mn}_3\text{O}_{6-1.5\delta}$  compounds are not (spin-driven) multiferroics.



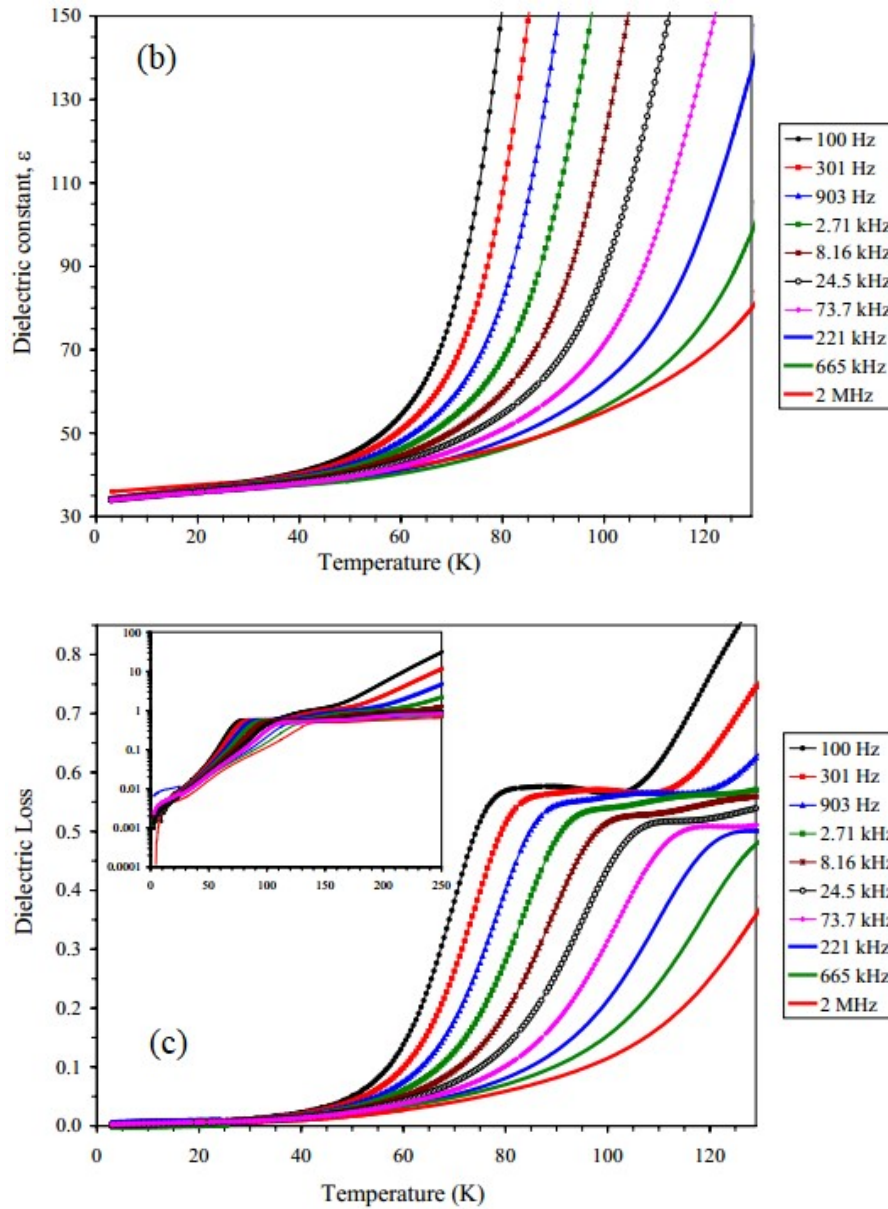


**Figure 3.13.** (a) Temperature dependence of dielectric constant of DyMn<sub>3</sub>O<sub>6</sub> on cooling and heating at 0 and 90 kOe at a frequency of 665 kHz. Temperature dependence of dielectric constant (b) and loss tangent (c) of DyMn<sub>3</sub>O<sub>6</sub> at different frequencies measured on cooling at a zero magnetic field.

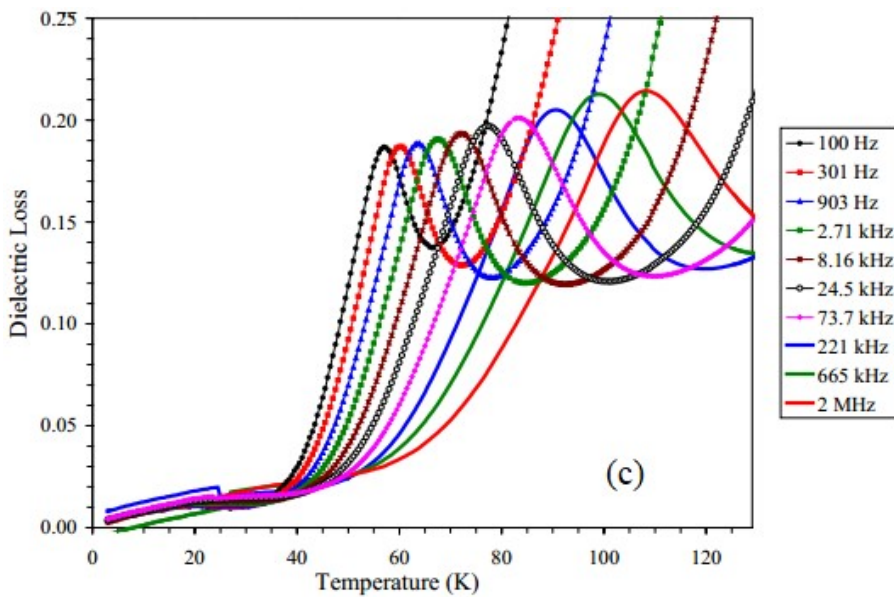
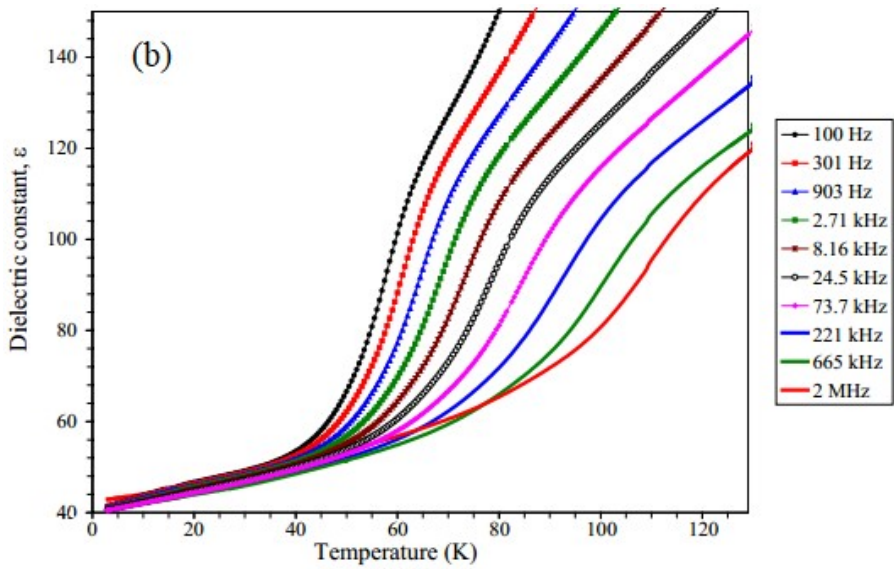
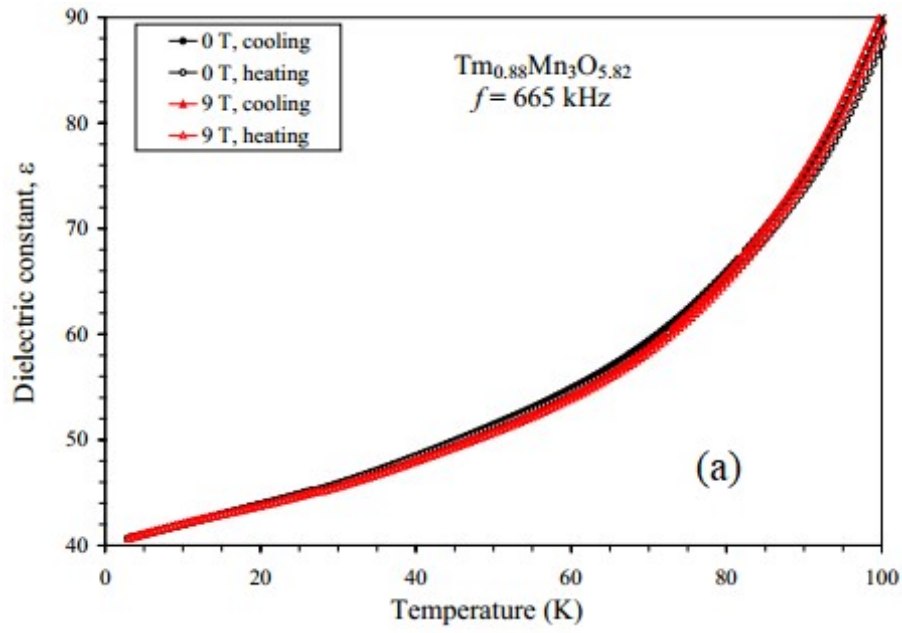


**Figure 3.14** (a) Temperature dependence of dielectric constant of  $\text{Tm}_{0.88}\text{Mn}_3\text{O}_{5.82}$  on cooling and heating at 0 and 90 kOe at a frequency of 665 kHz. Temperature dependence of dielectric constant (b) and loss tangent (c) of  $\text{Tm}_{0.88}\text{Mn}_3\text{O}_{5.82}$  at different frequencies measured on cooling at a zero magnetic field.

$R_{1-\delta}\text{Mn}_3\text{O}_{6-1.5\delta}$  compounds exhibit complex and interesting magnetic properties, and magnetic properties are highly sensitive to the  $\delta$  values. To fully understand the magnetic behavior, information about their magnetic structures is essential.

### 3.4. Summary of Chapter 3

I found a new family of perovskite materials in the  $R_2\text{O}_3\text{-Mn}_2\text{O}_3$  systems with  $R = \text{Gd-Tm}$  and  $\text{Y}$  having an idealized composition of  $\text{RMn}_3\text{O}_6$ . Unusual five-fold cation ordering is realized in them with charge disproportionation on manganese:  $[\text{R}^{3+}\text{Mn}^{2+}_{0.5}\text{Mn}^{3+}_{0.5}]_{\text{A}}\text{-}[\text{Mn}^{3+}\text{Mn}^{3.5+}]_{\text{B}}\text{O}_6$ . At the A site, cations are ordered in two separate chains consisting of  $\text{R}^{3+}$  and alternating  $\text{Mn}^{2+}$  (in tetrahedral coordination) and  $\text{Mn}^{3+}$  (in square-planar coordination). At the B site,  $\text{Mn}^{3+}$  and mixed-valent  $\text{Mn}^{3+}/\text{Mn}^{4+}$  cations are ordered in layers.  $\text{RMn}_3\text{O}_6$  compounds show complex magnetic behaviors with several transition temperatures, and magnetic properties are highly sensitive to the non-stoichiometry.

### References in chapter 3

[1] Shannon, R. D. Revised Effective Ionic Radii and Systematic Studies of Interatomic Distances in Halides and Chalcogenides. *Acta Crystallogr., Sec. A: Cryst. Phys., Diffr., Theor. Gen. Crystallogr.* **1976**, *32*, 751-767.

[2] Shannon, R. D. Synthesis of Some New Perovskites Containing Indium and Thallium. *Inorg. Chem.* **1967**, *6*, 1474-1478.

[3] Syono, Y.; Akimoto, S.; Endoh, Y. High Pressure Synthesis of Ilmenite and Perovskite

Type  $\text{MnVO}_3$  and Their Magnetic Properties. *J. Phys. Chem. Solid.* **1971**, *32*, 243-249.

[4] Belik, A. A.; Yi, W. High-pressure synthesis, crystal chemistry and physical properties of perovskite with small cations at the A site. *J. Phys.: Condens. Matter* **2014**, *26*, 163201.

[5] Markkula, M.; Arevalo-Lopez, A. M.; Kusmartseva, A.; Rodgers, J. A.; Ritter, C.; Wu, H.; Attfield, J. P. Incommensurate Spin Order in the Metallic Perovskite  $\text{MnVO}_3$ . *Phys. Rev. B: Condens. Matter Mater. Phys.* **2011**, *84*, 094450.

[6] Dos Santos-Garcia, A. J.; Ritter, C.; Solana-Madruga, E.; Saez-Puche, R. Magnetic and Crystal Structure Determination of  $\text{Mn}_2\text{FeSbO}_6$  Double Perovskite. *J. Phys. Condens. Matter* **2013**, *25*, 206004.

[7] Arevalo-Lopez, A. M.; Stegemann, F.; Attfield, J. P. Competing Antiferromagnetic Orders in the Double Perovskite  $\text{Mn}_2\text{MnReO}_6$  ( $\text{Mn}_3\text{ReO}_6$ ). *Chem. Commun.* **2016**, *52*, 5558-5560.

[8] Ovsyannikov, S. V.; Abakumov, A. M.; Tsirlin, A. A.; Schnelle, W.; Egoavil, R.; Verbeeck, J.; Van Tendeloo, G.; Glazyrin, K. V.; Hanfland, M.; Dubrovinsky, L. Perovskite-like  $\text{Mn}_2\text{O}_3$ : a path to new manganites. *Angew. Chem., Int. Ed.* **2013**, *52*, 1494-1498.

[9] Li, M.-R.; Retuerto, M.; Deng, Z.; Stephens, P. W.; Croft, M.; Huang, Q.; Wu, H.; Deng, X.; Kotliar, G.; Sánchez-Benítez, J.; Hadermann, J.; Walker, D.; Greenblatt, M. Giant magnetoresistance in the half-metallic double-perovskite ferrimagnet  $\text{Mn}_2\text{FeReO}_6$ . *Angew. Chem., Int. Ed.* **2015**, *54*, 12069-12073.

[10] Arévalo-López, A. M.; McNally, G. M.; Attfield, J. P. Large Magnetization and Frustration Switching of Magnetoresistance in the Double-Perovskite Ferrimagnet  $\text{Mn}_2\text{FeReO}_6$ . *Angew. Chem., Int. Ed.* **2015**, *54*, 12074–12077.

[11] Akizuki, Y.; Yamada, I.; Fujita, K.; Nishiyama, N.; Irifune, T.; Yajima, T.; Kageyama, H.;

Tanaka, K. A-site-ordered perovskite  $\text{MnCu}_3\text{V}_4\text{O}_{12}$  with a 12-coordinated manganese (II). *Inorg. Chem.* **2013**, *52*, 11538-11543.

[12] Yi, W.; Princep, A. J.; Guo, Y.; Johnson, R. D.; Khalyavin, D.; Manuel, P.; Senyshyn, A.; Presniakov, I. A.; Sobolev, A. V.; Matsushita, Y.; Tanaka, M.; Belik, A. A.; Boothroyd, A. T.  $\text{Sc}_2\text{NiMnO}_6$ : A Double-Perovskite with a Magnetodielectric Response Driven by Multiple Magnetic Orders. *Inorg. Chem.* **2015**, *54*, 8012–8021.

[13] Ding, L.; Manuel, P.; Khalyavin, D. D.; Orlandi, F.; Kumagai, Y.; Oba, F.; Yi, W.; Belik, A. A. Unusual magnetic structure of the high-pressure synthesized perovskites  $\text{ACrO}_3$  (A = Sc, In, Tl). *Phys. Rev. B: Condens. Matter Mater. Phys.* **2017**, *95*, 054432.

[14] Li, M.-R.; Walker, D.; Retuerto, M.; Sarkar, T.; Hadermann, J.; Stephens, P. W.; Croft, M.; Ignatov, A.; Grams, C. P.; Hemberger, J.; Nowik, I.; Halasyamani, P. S.; Tran, T. T.; Mukherjee, S.; Dasgupta, T. S.; Greenblatt, M. Polar and Magnetic  $\text{Mn}_2\text{FeMO}_6$  (M = Nb, Ta) with  $\text{LiNbO}_3$ -type Structure: High-Pressure Synthesis. *Angew. Chem., Int. Ed.* **2013**, *52*, 8406–8410.

[15] Li, M.-R.; Retuerto, M.; Walker, D.; Sarkar, T.; Stephens, P. W.; Mukherjee, S.; Dasgupta, T. S.; Hodges, J. P.; Croft, M.; Grams, C. P.; Hemberger, J.; Sánchez-Benítez, J.; Huq, A.; Saouma, F. O.; Jang, J. I.; Greenblatt, M. Magnetic-Structure-Stabilized Polarization in an Above-Room-Temperature Ferrimagnet. *Angew. Chem., Int. Ed.* **2014**, *53*, 10774–10778.

[16] Tachibana, M.; Shimoyama, T.; Kawaji, H.; Atake, T.; Takayama-Muromachi, E. Jahn-Teller Distortion and Magnetic Transitions in Perovskite  $\text{RMnO}_3$  (R = Ho, Er, Tm, Yb, and Lu). *Phys. Rev. B: Condens. Matter Mater. Phys.* **2007**, *75*, 144425.

[17] Kimura, T.; Goto, T.; Shintani, H.; Ishizaka, K.; Arima, T.; Tokura, Y. Magnetic Control

of Ferroelectric Polarization. *Nature (London, U. K.)* **2003**, *426*, 55-58.

[18] Uusi-Esko, K.; Malm, J.; Imamura, N.; Yamauchi, H.; Karppinen, M. Characterization of  $\text{RMnO}_3$  (R = Sc, Y, Dy-Lu): High-Pressure Synthesized Metastable Perovskites and Their Hexagonal Precursor Phases. *Mater. Chem. Phys.* **2008**, *112*, 1029-1034.

[19] Bochu, B.; Chenavas, J.; Joubert, J. C.; Marezio, M. High Pressure Synthesis and Crystal Structure of a New Series of Perovskite-Like Compounds  $\text{CMn}_7\text{O}_{12}$  (C = Na; Ca; Cd; Sr; La; Nd). *J. Solid State Chem.* **1974**, *11*, 88-93.

[20] Prodi, A.; Gilioli, E.; Cabassi, R.; Bolzoni, F.; Licci, F.; Huang, Q.; Lynn, J. W.; Affronte, M.; Gauzzi, A.; Marezio, M. Magnetic Structure of the High-Density Single-Valent eg Jahn-Teller System  $\text{LaMn}_7\text{O}_{12}$ . *Phys. Rev. B: Condens. Matter Mater. Phys.* **2009**, *79*, 085105.

[21] Mezzadri, F.; Calicchio, M.; Gilioli, E.; Cabassi, R.; Bolzoni, F.; Calestani, G.; Bissoli, F. High-Pressure Synthesis and Characterization of  $\text{PrMn}_7\text{O}_{12}$  Polymorphs. *Phys. Rev. B: Condens. Matter Mater. Phys.* **2009**, *79*, 014420.

[22] Vasil'ev, A. N.; Volkova, O. S. New Functional Materials  $\text{AC}_3\text{B}_4\text{O}_{12}$  (Review). *Low Temp. Phys.* **2007**, *33*, 895-914.

[23] Abakumov, A. M.; Tsirlin, A. A.; Antipov, E. V. Transition-Metal Perovskites, *Comprehensive Inorganic Chemistry II. Reference Module in Chemistry, Molecular Sciences and Chemical Engineering.* **2013**, *2*, 1-40.

[24] Attfield, J. P. Principles and Applications of Anion Order in Solid Oxynitrides. *Cryst. Growth Des.* **2013**, *13*, 4623-4629.

[25] Sharits, A. R.; Khoury, J. F.; Woodward, P. M. Evaluating  $\text{NaREMgWO}_6$  (RE = La, Gd,

Y) doubly ordered double perovskites as  $\text{Eu}^{3+}$  phosphor hosts. *Inorg. Chem.* **2016**, *55*, 12383-12390.

[26] King, G.; Garcia-Martin, S.; Woodward, P. M. Octahedral tilt twinning and compositional modulation in  $\text{NaLaMgWO}_6$ . *Acta Crystallogr., Sect. B: Struct. Sci.* **2009**, *65*, 676-683.

[27] Knapp, M. C.; Woodward, P. M. A-site Cation Ordering in  $\text{AA}'\text{BB}'\text{O}_6$  Perovskites. *J. Solid State Chem.* **2006**, *179*, 1076-1085.

[28] Retuerto, M.; Li, M. R.; Ignatov, A.; Croft, M.; Ramanujachary, K. V.; Chi, S.; Hodges, J. P.; Dachraoui, W.; Hadermann, J.; Tran, T. T.; Halasyamani, P. S.; Grams, C. P.; Hemberger, J.; Greenblatt, M. Polar and Magnetic Layered A-Site and Rock Salt B-Site-Ordered  $\text{NaLnFeWO}_6$  ( $\text{Ln} = \text{La}, \text{Nd}$ ) Perovskites. *Inorg. Chem.* **2013**, *52*, 12482-12491.

[29] Solana-Madruga, E.; Arevalo-Lopez, A. M.; Dos Santos-Garcia, A. J.; Urones-Garrote, E.; Avila-Brandé, D.; Saez-Puche, R.; Attfield, J. P. Double Double Cation Order in the High-Pressure Perovskites  $\text{MnRMnSbO}_6$ . *Angew. Chem. Int. Ed.* **2016**, *55*, 9340-9344.

[30] Izumi, F.; Ikeda, T. Rietveld-analysis program RIETAM-98 and its applications to zeolites. *Mater. Sci. Forum* **2000**, *321-324*, 198-205.

[31] *CrystalClear*; Rigaku Corporation, Tokyo, 2005.

[32] Sheldrick G. M. SHELXT – Integrated Space-Group and Crystal-Structure Determination. *Acta Crystallogr., Sec. A: Found. Adv.* **2015**, *71*, 3-8.

[33] Sheldrick G. M. Crystal Structure Refinement with SHELXL. *Acta Crystallogr., Sec. C: Struct. Chem.* **2015**, *71*, 3-8.

[34] Farrugia, L. J. WinGX Suite for Small-Molecule Single-Crystal Crystallography. *J. Appl.*

*Crystallogr.* **1999**, *32*, 837-838.

[35] Brese, N. E.; O'Keeffe, M. Bond-Valence Parameters for Solids. *Acta Crystallogr., Sect. B: Struct. Sci.* **1991**, *47*, 192-197.

[36] Glazkova, Y. S.; Terada, N.; Matsushita, Y.; Katsuya, Y.; Tanaka, M.; Sobolev, A. V.; Presniakov, I. A.; Belik, A. A. High-Pressure Synthesis, Crystal Structures, and Properties of  $\text{CdMn}_7\text{O}_{12}$  and  $\text{SrMn}_7\text{O}_{12}$  Perovskites. *Inorg. Chem.* **2015**, *54*, 9081-9091.

[37] Belik, A. A.; Glazkova, Y. S.; Katsuya, Y.; Tanaka, M.; Sobolev, A. V.; Presniakov, I. A. Low-Temperature Structural Modulations in  $\text{CdMn}_7\text{O}_{12}$ ,  $\text{CaMn}_7\text{O}_{12}$ ,  $\text{SrMn}_7\text{O}_{12}$ , and  $\text{PbMn}_7\text{O}_{12}$  Perovskites Studied by Synchrotron X-ray Powder Diffraction and Mossbauer Spectroscopy. *J. Phys. Chem. C* **2016**, *120*, 8278–8288.

[38] Okamoto, H.; Imamura, N.; Karppinen, M.; Yamauchi, H.; Fjellvag, H. Square Coordinated  $\text{MnO}_2$ -Units in  $\text{BiMn}_7\text{O}_{12}$ . *Inorg. Chem.* **2010**, *49*, 8709-8712.

[39] Yang, T.; Claridge, J. B.; Rosseinsky, M. J. 1:1:1 Triple-Cation B-Site-Ordered and Oxygen-Deficient Perovskite  $\text{Ca}_4\text{GaNbO}_8$ : A Member of a Family of Anion-Vacancy-Based Cation-Ordered Complex Perovskites. *Inorg. Chem.* **2013**, *52*, 3795–3802.

[40] Belik, A. A.; Matsushita, Y.; Tanaka, M.; Takayama-Muromachi, E.  $(\text{In}_{1-y}\text{Mn}_y)\text{MnO}_3$  ( $1/9 \leq y \leq 1/3$ ): Unusual Perovskites with Unusual Properties. *Angew. Chem. Inter. Ed.* **2010**, *49*, 7723–7727.

[41] Leinenweber, K.; Parise, J. High-Pressure Synthesis and Crystal Structure of  $\text{CaFeTi}_2\text{O}_6$ , a New Perovskite Structure Type. *J. Solid State Chem.* **1995**, *114*, 277-281.

[42] Aimi, A.; Mori, D.; Hiraki, K.; Takahashi, T.; Shan, Y. J.; Shirako, Y.; Zhou, J. S.; Inaguma, Y. High-Pressure Synthesis of A-Site Ordered Double Perovskite  $\text{CaMnTi}_2\text{O}_6$  and

Ferroelectricity Driven by Coupling of A-Site Ordering and the Second-Order Jahn–Teller Effect. *Chem. Mater.* **2014**, *26*, 2601–2608.

[43] Shimura, G.; Niwa, K.; Shirako, Y.; Hasegawa, M. High-Pressure Synthesis and Magnetic Behavior of A-site Columnar-Ordered Double Perovskites,  $\text{LnMn}(\text{Ga}_{0.5}\text{Ti}_{0.5})_2\text{O}_6$  (Ln = Sm, Gd). *Eur. J. Inorg. Chem.* **2017**, *2017*, 835-839.

# Chapter 4. Charge and orbital orders and structural instability in high-pressure quadruple perovskite $\text{CeCuMn}_6\text{O}_{12}$

## 4.1 Introduction

A-site-ordered quadruple perovskites with the  $\text{AA}'_3\text{B}_4\text{O}_{12}$  stoichiometry and the parent symmetry of  $Im\bar{3}$  [1,2] are a special class of the  $\text{ABO}_3$  perovskite family. They are formed from  $\text{ABO}_3$  by in-phase, very large  $\text{BO}_6$  octahedral tilts along all crystallographic directions with B-O-B tilt angles reaching about  $140^\circ$ . The tilt system is  $a^+a^+a^+$  in terms of the Glazer notations [3]. The strong tilts create a twelve-fold coordinated A site and a square-planar coordinated A' site with the 1:3 ratio. These distortions are primarily determined by the cation stoichiometry and the cation nature. In other words, to cause such distortions the A' site should be occupied by small cations that allow a square-planar coordination. In most cases,  $\text{Cu}^{2+}$  and  $\text{Mn}^{3+}$  cations with a pronounced Jahn-Teller effect are located at the A' site [1]. However, with high enough synthesis pressure, other cations can also be forced into the A' site, such as,  $\text{Fe}^{2+}$  [4],  $\text{Co}^{2+}$  [5],  $\text{Pd}^{2+}$  [6],  $\text{Pb}^{4+}$  [7] and  $\text{Mn}^{2+}$  [8]. The B site of  $\text{AA}'_3\text{B}_4\text{O}_{12}$  can be occupied by all typical B-site cations for perovskites including manganese.

Therefore, when  $\text{A}' = \text{B} = \text{Mn}$ , quadruple manganites with the  $\text{AMn}_3\text{Mn}_4\text{O}_{12}$  or  $\text{AMn}_7\text{O}_{12}$  stoichiometry are formed [9-20]. Quadruple  $\text{AMn}_7\text{O}_{12}$  manganites show very rich structural and physical properties from the interplay among lattice, charge, spin and orbital degrees of freedom, as do simple  $\text{AMnO}_3$  perovskite manganites [21]. When  $\text{A} = \text{R}^{3+}$  (R = rare-earths) or  $\text{Bi}^{3+}$  and  $\text{A}' = \text{Mn}^{3+}$ , the average oxidation state of manganese at the B site is +3, and there is no charge degree of freedom.  $\text{LaMn}_7\text{O}_{12}$  [10, 11] and  $\text{BiMn}_7\text{O}_{12}$  [12-14] show orbital order transitions from  $Im\bar{3}$  to  $I2/m$  at 650 K and 608 K, respectively, and spin order transitions (at  $T_{\text{N1}} = 21$  and  $T_{\text{N2}} = 78$  K for  $\text{LaMn}_7\text{O}_{12}$  and at  $T_{\text{N1}} = 28$  and  $T_{\text{N2}} = 59$  K for  $\text{BiMn}_7\text{O}_{12}$ ).  $\text{BiMn}_7\text{O}_{12}$  additionally exhibits polar distortions from  $I2/m$  to  $Im$  to  $P1$  due to the effect of the

lone electron pair of  $\text{Bi}^{3+}$  [14]. When  $A = \text{Cd}^{2+}$ ,  $\text{Ca}^{2+}$ ,  $\text{Sr}^{2+}$  and  $\text{Pb}^{2+}$  and  $A' = \text{Mn}^{3+}$ , the average oxidation state of manganese at the B site is +3.25, and there exists charge degree of freedom.  $A^{2+}\text{Mn}_7\text{O}_{12}$  manganites show charge order (CO) transitions from  $Im-3$  to  $R-3$  at high temperatures ( $T_{\text{CO}} = 397\text{-}493$  K) together with orbital orders and spin order transitions at much lower temperatures (below 90 K) [15-19]. A very unusual  $-Q_3$  Jahn-Teller distortion mode [21] is realized in  $A^{2+}\text{Mn}_7\text{O}_{12}$  with compressed  $\text{Mn}^{3+}\text{O}_6$  octahedra along one direction [15]. As a result,  $A^{2+}\text{Mn}_7\text{O}_{12}$  compounds show different orbital modulation transitions at 254-294 K [16-18].

The average oxidation state of +3.25 for manganese at the B site can also be reached with  $A = R^{3+}$  and  $A' = 2/3\text{Mn}^{3+} + 1/3\text{Cu}^{2+}$  in  $\text{RCuMn}_6\text{O}_{12}$  compositions. A number of such  $\text{RCuMn}_6\text{O}_{12}$  compounds with the cubic  $Im-3$  structure have been investigated in the literature [22-25]. However, no phase transitions were found for  $R = \text{La}$  [23],  $\text{Nd}$  [24] and  $\text{Pr}$  [24], probably because real chemical compositions were different from target compositions. But a charge order transition ( $Im-3 \rightarrow R-3$ ) was found in  $\text{PrCuMn}_6\text{O}_{12}$  at 267 K in another work [25]. Very unusual reentrant structural transitions in  $\text{BiCuMn}_6\text{O}_{12}$  have been discovered, where the symmetry changes as  $Im-3 \rightarrow R-3 \rightarrow Im-3$  on cooling, and charge and orbital orders collapse [25]. Therefore, I performed detailed studies of other  $\text{RCuMn}_6\text{O}_{12}$  compounds with  $R = \text{La-Lu}$  in wide temperature ranges. This paper is focused on  $\text{CeCuMn}_6\text{O}_{12}$  because Ce can have the +3 and +4 oxidation states in comparison with most other rare earth elements, and quadruple perovskites with Ce often show distinct properties, for example,  $\text{CeCu}_3\text{Mn}_4\text{O}_{12}$  [27] and  $\text{CeCu}_3\text{Fe}_4\text{O}_{12}$  [28]. It has been showed that  $\text{CeCuMn}_6\text{O}_{12}$  exhibits the  $Im-3 \rightarrow R-3$  charge order transition at 297 K, and it shows structural instability below 90 K. Ce has the oxidation state +3 in  $\text{CeCuMn}_6\text{O}_{12}$ .

## 4.2. Experimental details of Chapter 4

$\text{CeCuMn}_6\text{O}_{12}$  was prepared from stoichiometric mixtures of  $\text{CeO}_2$  (99.9 %),  $\text{CuO}$

(99.99 %) and  $\text{Mn}_2\text{O}_3$ . Single-phase  $\text{Mn}_2\text{O}_3$  was prepared from commercial  $\text{MnO}_2$  (99.99 %) by heating in air at 923 K for 24 h. The mixtures were placed in Pt capsules and treated at 6 GPa and about 1670 K for 2 h (heating time to the desired temperature was 10 min) in a belt-type high-pressure apparatus. After the heat treatments, the samples were quenched to room temperature (RT), and the pressure was slowly released. All the samples obtained were black pellets. The temperature of our high-pressure apparatus is controlled by the heating power with a calibrated relationship between power and temperature.

X-ray powder diffraction (XRPD) data were collected at RT on a RIGAKU MiniFlex600 diffractometer using  $\text{CuK}\alpha$  radiation ( $2\theta$  range of 8-140°, a step width of 0.02°, and scan speed of 1° min<sup>-1</sup>). Low-temperature XRPD data from 10 K to 300 K (that is, on heating) were measured on a RIGAKU SmartLab using  $\text{CuK}\alpha_1$  radiation (45 kV, 200 mA; 2° range of 10-110°, a step width of 0.02°, and scan speed of 2° min<sup>-1</sup>) with a cryostat system. XRPD patterns were analysed and lattice parameters were obtained by the Rietveld method using RIETAN-2000 [29]. Synchrotron XRPD data were measured at 113 and 380 K on a large Debye-Scherrer camera at the BL15XU beam line of SPring-8 [30,31], where cooling and heating were performed by a nitrogen-gas gun. The intensity data were collected between 3° and about 59° at 0.003° intervals in  $2\theta$ ; the incident beam was monochromatized at  $\lambda = 0.65298$  Å. The sample was packed into a Lindemann glass capillary (inner diameter: 0.1 mm), which was rotated during the measurement. The absorption coefficient was also measured. The Rietveld analysis was performed using the RIETAN-2000 program [29]. The sample contained about 1.3 wt. % of  $\text{CeO}_2$  impurity (the weight fraction was estimated by RIETAN-2000 from the refined scale factors). At 113 K, reflections from ice were observed because ice was accumulated on the outer surface of the capillary; ice was introduced as the third phase during the refinement.

Magnetic measurements were performed on a SQUID magnetometer (Quantum Design, MPMS-XL-7T) between 2 and 400 K in different applied fields under both zero-field-cooled

(ZFC) and field-cooled on cooling (FCC) conditions. Isothermal magnetization measurements were performed between -70 and 70 kOe at 2 K. Frequency dependent ac susceptibility measurements were performed with a Quantum Design MPMS-1T instrument at different frequencies ( $f$ ) and different applied oscillating magnetic fields ( $H_{ac}$ ). Specific heat,  $C_p$ , at magnetic fields of 0 and 70 kOe was recorded between 2 and 300 K on cooling by a pulse relaxation method using a commercial calorimeter (Quantum Design PPMS). dc electrical resistivity was measured between 400 K and 10 K by the conventional four-probe method using a Quantum Design PPMS with the excitation current of 1  $\mu$ A; resistivity became too high to be measured with our system below 125 K. Pieces of pellets were used in all magnetic, specific heat and resistivity measurements.

Differential scanning calorimetry (DSC) curves were recorded on a Mettler Toledo DSC1 STAR<sup>e</sup> system at a heating/cooling rate of 10 K min<sup>-1</sup> under N<sub>2</sub> flow between 123 K and 423 K in sealed Al capsules. Three DSC runs were performed to check the reproducibility.

## 4.3. Results and discussion

### 4.3.1. Structural phase transitions in CeCuMn<sub>6</sub>O<sub>12</sub>

**Figure 4.1** depicts DSC curves of CeCuMn<sub>6</sub>O<sub>12</sub> between 180 and 410 K. Sharp peaks were observed at  $T_{CO} = 297$  K (CO: charge order) on heating and 290 K on cooling indicating a structural phase transition of the first order. The peak area was about 8.5 J g<sup>-1</sup> (on heating). The peak positions (near 300 K) and areas were well reproduced on cycling.

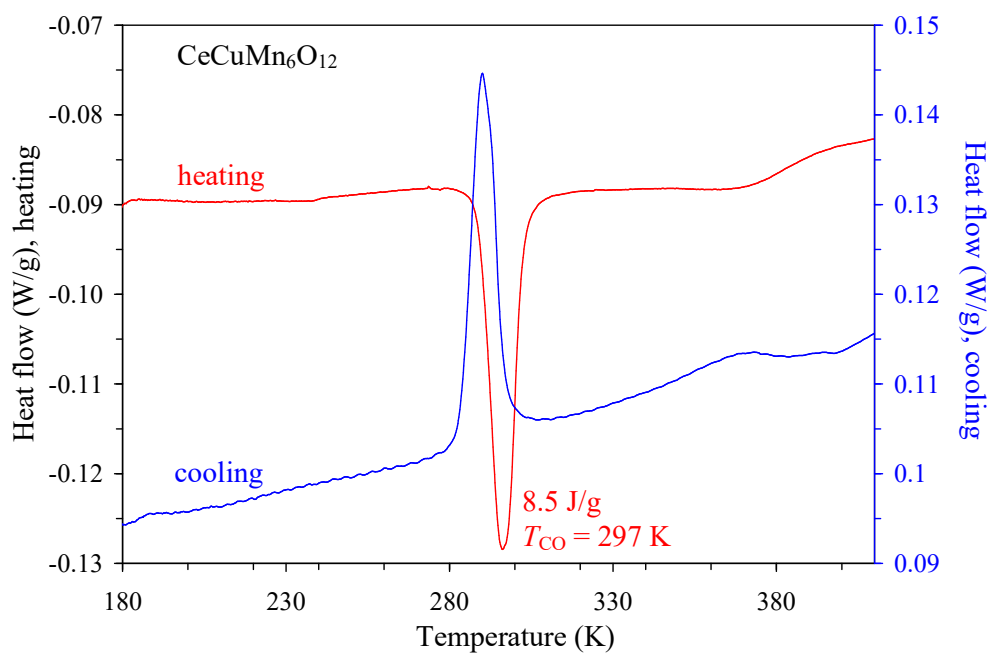


**Figure 4.1.** Differential scanning calorimetry (DSC) curves of CeCuMn<sub>6</sub>O<sub>12</sub> between 180 and 410 K on heating and cooling with 10 K min<sup>-1</sup>.

**Figure 4.2** shows the evolution of XRPD patterns of CeCuMn<sub>6</sub>O<sub>12</sub> from 10 K to 300 K. At 300 K, the main phase was the cubic *Im-3* one with traces of the *R-3* phase. At 290 K, the main phase was the *R-3* one with traces of the *Im-3* phase. These features are in agreement with the DSC results, which give the structural phase transition temperature as 297 K, and with the first-order nature of the phase transition. Between 100 K and 280 K, the sample was single-phase and contained only the *R-3* phase. At 80 and 90 K, some reflections showed broadening, and shoulders appeared on some reflections (e.g, near 34.24°, shown in **Figure 4.2b**). These features could be interpreted as the appearance of traces of a cubic phase. However at 70 K and below, these features disappeared, and other reflections showed splitting (new reflections could not be assigned to a cubic phase). This splitting was reduced gradually with decreasing temperature, but it was still visible even at 10 K (e.g., near 61.60° for the 024 reflection in *R-3*, shown in **Figure 4.2a**).

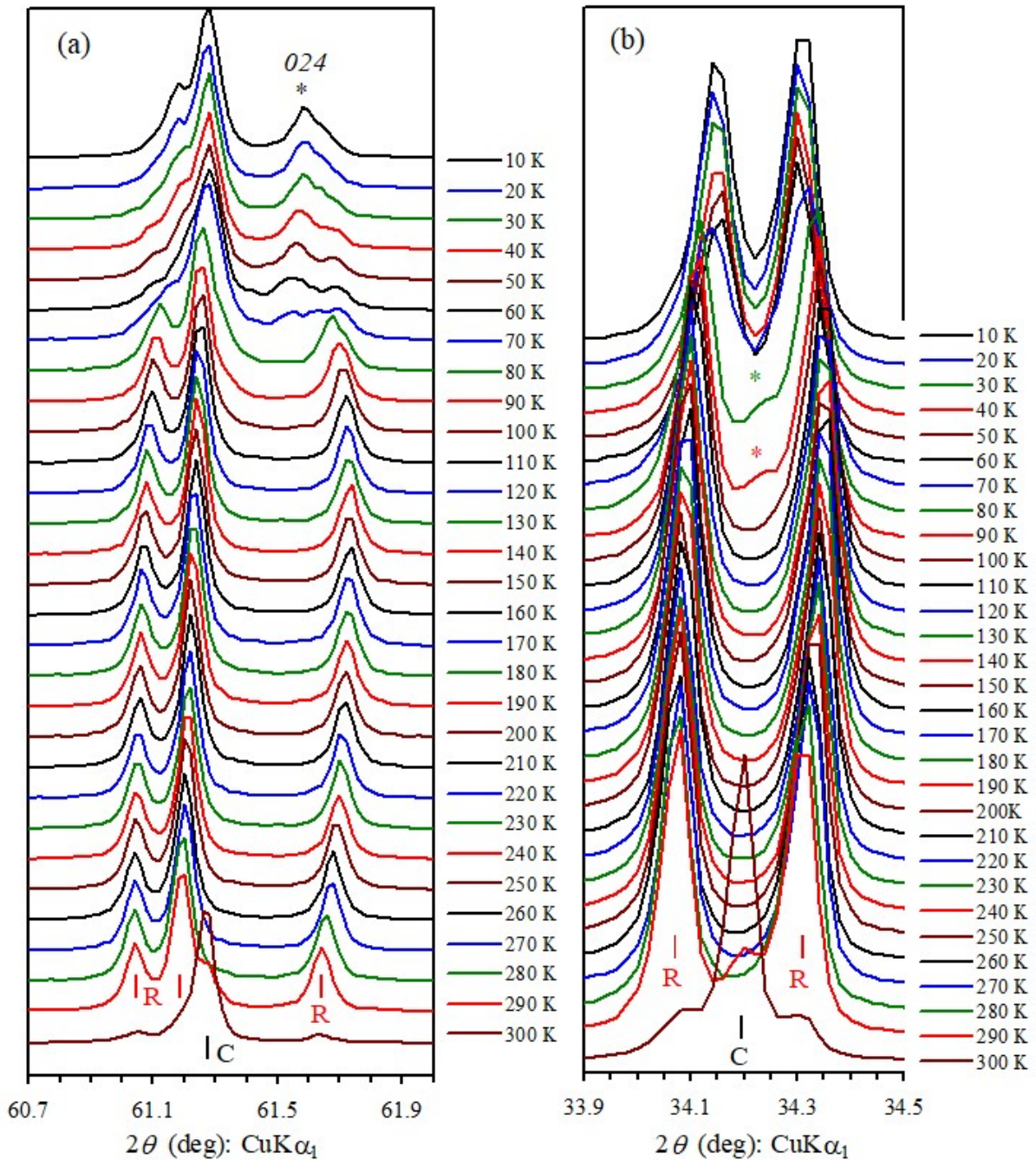


**Figure 4.2.** (a) Fragments of low-temperature laboratory X-ray powder diffraction patterns of  $\text{CeCuMn}_6\text{O}_{12}$  between  $60.7^\circ$  and  $62.0^\circ$ . Bragg reflections of the cubic (C)  $Im\bar{3}$  phase and the  $R\bar{3}$  (R) phase are given. The 024 reflection of the  $R\bar{3}$  phase is marked by an asterisk; it shows a shoulder from the right side at 10 K. (b) Fragments of low-temperature laboratory X-ray powder diffraction patterns of  $\text{CeCuMn}_6\text{O}_{12}$  near the strongest reflections between  $33.9^\circ$  and  $34.5^\circ$ . Asterisks show shoulders, which can be assigned to a cubic phase, from the

left side at 80 and 90 K.

I performed some attempts to index and fit the splitting reflections using different superstructure models. However, all attempts to explain the splitting by a single-phase model failed. It could be explained the splitting assuming the presence of two  $R-3$  phases with slightly different lattice parameters, as shown in **Figure 4.3**, and the refined (by the Rietveld method) ratio of two phases was almost the same between 10 and 60 K (30-35 wt.% for one  $R-3$  phase). The temperature dependence of the lattice parameters is given on **Figure 4.4**. The  $c$  lattice parameter of the  $R-3$  phase starts increasing with decreasing temperature below the magnetic transition temperature of  $T_C = 140$  K. And below 80 K, both  $a$  and  $c$  lattice parameters have sharp changes. These results demonstrate that the  $R-3$  phase becomes unstable on decreasing temperature, and different competing phases exist at low temperatures. However,  $\text{CeCuMn}_6\text{O}_{12}$  does not exhibit a reentrant structural transition to the high-temperature  $Im-3$  phase in comparison with  $\text{BiCuMn}_6\text{O}_{12}$  [26]. Instead, another  $R-3$  phase appears, but two  $R-3$  phases coexist in a wide temperature range. High-resolution structural studies below 10 K are necessary to understand the difference between the low-temperature phase and the intermediate-temperature (stable between 100 and 280 K)  $R-3$  phase.

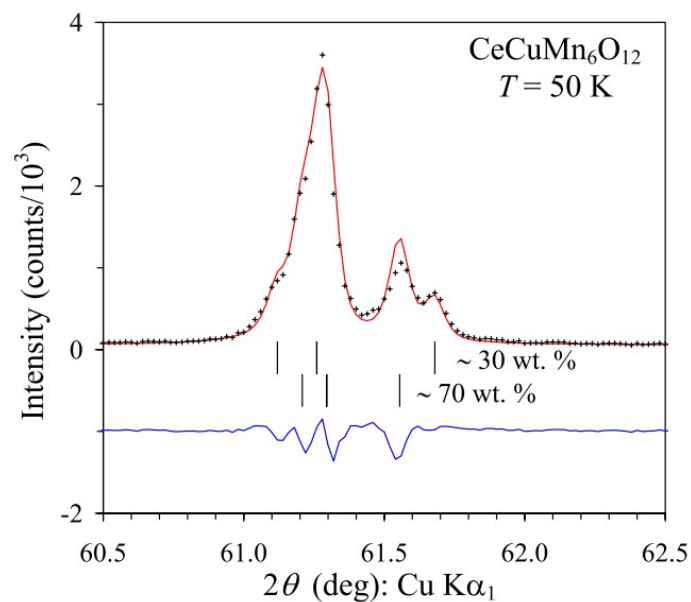


**Figure 4.3.** Fragments (between 60.5° and 62.5°) of experimental (black crosses), calculated (red line) and difference (blue line) laboratory XRPD patterns of CeCuMn<sub>6</sub>O<sub>12</sub> at  $T = 50$  K.

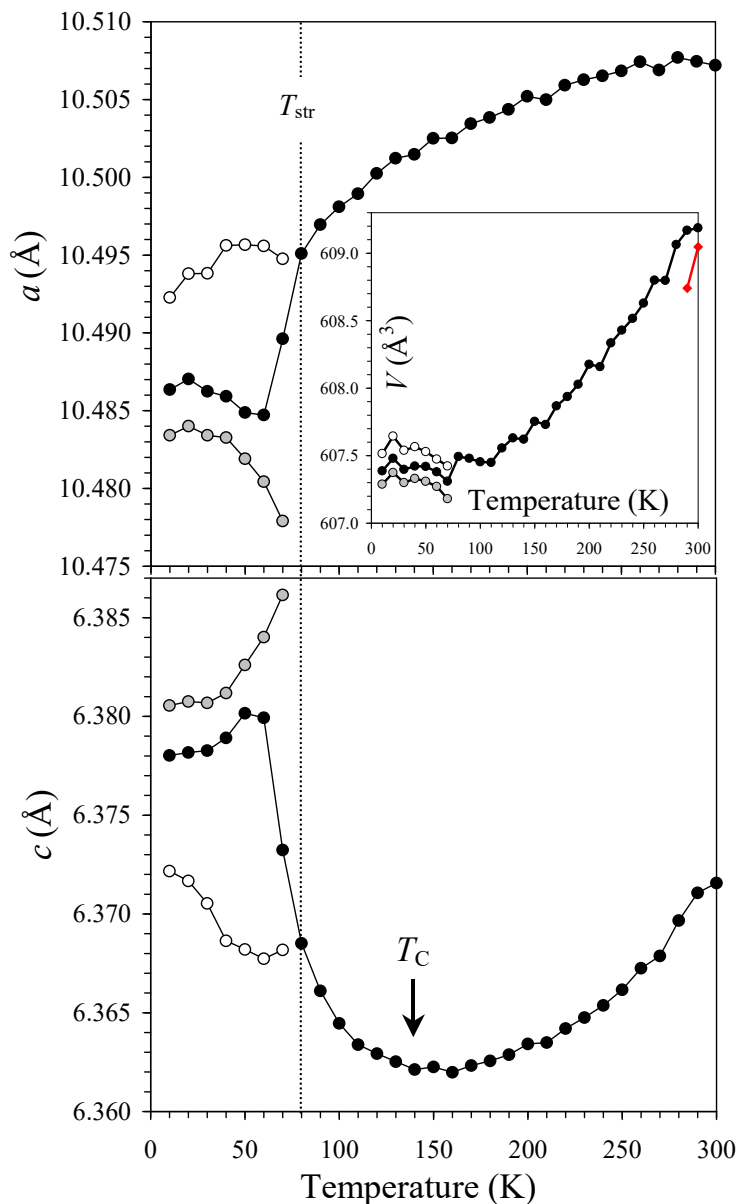


**Figure 4.4.** Temperature dependence of the lattice parameters in CeCuMn<sub>6</sub>O<sub>12</sub>. The lattice parameters were obtained assuming one  $R-3$  phase (black symbols) between 10 and 300 K or two  $R-3$  phases (white and gray symbols) between 10 and 70 K. The inset shows temperature dependence of the unit cell volume ( $V$ ), where red diamonds show the  $1.5V$  values for the cubic phase.

### 4.3.2 Crystal structures of CeCuMn6O12

The crystal structures were refined in the *Im*-3 model at 380 K and in the *R*-3 model at 113 K. The refinement results are summarized in **Table 4.1**, and bond-lengths, Mn-O-Mn bond angles and bond valence sums (BVS) [32] in **Table 4.2**.

**Table 4.1** Structure parameters of CeCuMn6O12 at 113 K and 380 K from synchrotron X-ray powder diffraction data<sup>a</sup>.

Site	WP	<i>g</i>	<i>x</i>	<i>y</i>	<i>z</i>	<i>B</i> (Å <sup>2</sup> )
<i>T</i> = 113 K, space group <i>R</i> -3						
Ce	3 <i>a</i>	1	0	0	0	0.180(7)
Mn1	9 <i>e</i>	2/3	0.5	0	0	0.293(8)
Cu1	9 <i>e</i>	1/3	0.5	0	0	= <i>B</i> (Mn1)
Mn2	9 <i>d</i>	1	0.5	0	0.5	0.171(9)
Mn3	3 <i>b</i>	1	0	0	0.5	0.144(17)
O1	18 <i>f</i>	1	0.2191(2)	0.2688(2)	0.0820(3)	0.10(4)
O2	18 <i>f</i>	1	0.3438(2)	0.5220(2)	0.3465(4)	0.09(4)
<i>T</i> = 380 K, space group <i>Im</i> -3						
Ce	2 <i>a</i>	1	0	0	0	0.385(5)
Mn1	6 <i>b</i>	2/3	0	0.5	0.5	0.698(7)
Cu1	6 <i>b</i>	1/3	0	0.5	0.5	= <i>B</i> (Mn1)
Mn2	8 <i>c</i>	1	0.25	0.25	0.25	0.212(6)
O	24 <i>g</i>	1	0	0.30597(14)	0.17520(15)	0.20(2)

<sup>a</sup> WP represents Wyckoff position. At 113 K: Space group *R*-3 (No. 148, hexagonal axes) with *a* = 10.48971(2) Å, *c* = 6.36403(1) Å, and *V* = 606.4427(18) Å<sup>3</sup>; *Z* = 3,  $\rho_{\text{cal}} = 5.958 \text{ g cm}^{-3}$ ; *R*<sub>wp</sub> = 4.87%, *R*<sub>P</sub> = 3.13%, *R*<sub>B</sub> = 2.56% and *R*<sub>F</sub> = 2.23%. At 380 K: Space group *Im*-3 (No. 204) with *a* = 7.40712(1) Å and *V* = 606.4427(18) Å<sup>3</sup>; *Z* = 2,  $\rho_{\text{cal}} = 5.927 \text{ g cm}^{-3}$ ; *R*<sub>wp</sub> = 4.56%, *R*<sub>P</sub> = 3.17%, *R*<sub>B</sub> = 4.75% and *R*<sub>F</sub> = 4.25%.

**Table 4.2** Selected bond lengths (*l* < 3.0 Å), bond angles (degree), bond valence sums (BVS), and distortion parameter of MnO<sub>6</sub> [ $\Delta$ (Mn)] in CeCuMn<sub>6</sub>O<sub>12</sub> at 113 K and 380 K.

$T = 113 \text{ K, space group } R-3$			
Ce-O2 ( $\times 6$ )	2.575(2)	Mn1-O1 ( $\times 2$ )	1.921(2)
Ce-O1 ( $\times 6$ )	2.650(2)	Mn1-O2 ( $\times 2$ )	1.924(2)
		Mn1-O1 ( $\times 2$ )	2.774(2)
BVS(Ce <sup>3+</sup> ) <sup>a</sup>	3.47	Mn1-O2 ( $\times 2$ )	2.825(2)
BVS(Ce <sup>4+</sup> ) <sup>a</sup>	2.49		
BVS(Ce <sup>3+</sup> ) <sup>b</sup>	3.20	BVS(Mn1 <sup>3+</sup> )	2.82
BVS(Ce <sup>4+</sup> ) <sup>b</sup>	2.77	BVS(Cu1 <sup>2+</sup> )	2.27
BVS(Ce <sup>n+</sup> ) <sup>b</sup>	2.97		
Mn2-O1 ( $\times 2$ )	1.907(2)	Mn3-O2 ( $\times 6$ )	1.947(2)
Mn2-O2 ( $\times 2$ )	2.017(2)	BVS(Mn3 <sup>4+</sup> )	3.55
Mn2-O1 ( $\times 2$ )	2.039(2)		
BVS(Mn2 <sup>3+</sup> )	3.28	Mn2-O1-Mn2 ( $\times 4$ )	139.04(5)
$\Delta(\text{Mn2})$	$8.4 \times 10^{-4}$	Mn2-O2-Mn3 ( $\times 2$ )	137.68(5)
$T = 380 \text{ K, space group } Im-3$			
Ce-O ( $\times 12$ )	2.6116(11)	Mn1-O1 ( $\times 4$ )	1.9364(10)
		Mn1-O1 ( $\times 4$ )	2.8024(11)
BVS(Ce <sup>3+</sup> ) <sup>a</sup>	3.46	BVS(Mn1 <sup>3+</sup> )	2.72
BVS(Ce <sup>4+</sup> ) <sup>a</sup>	2.48	BVS(Cu1 <sup>2+</sup> )	2.19
BVS(Ce <sup>3+</sup> ) <sup>b</sup>	3.19		
BVS(Ce <sup>4+</sup> ) <sup>b</sup>	2.76	Mn2-O ( $\times 6$ )	1.9769(4)
BVS(Ce <sup>n+</sup> ) <sup>b</sup>	2.96	BVS(Mn2 <sup>3+</sup> )	3.34
		Mn2-O-Mn2 ( $\times 6$ )	139.02(3)

<sup>a</sup> BVS =  $\sum_{i=1}^N v_i$ ,  $v_i = \exp[(R_0 - l_i)/B]$ ,  $N$  is the coordination number,  $B = 0.37$ ,  $R_0(\text{Ce}^{3+}) = 2.151$ ,  $R_0(\text{Ce}^{4+}) = 2.028$ ,  $R_0(\text{Cu}^{2+}) = 1.679$ ,  $R_0(\text{Mn}^{4+}) = 1.753$ , and  $R_0(\text{Mn}^{3+}) = 1.76$  [32].

<sup>b</sup> Updated values of  $R_0(\text{Ce}^{3+}) = 2.121$ ,  $R_0(\text{Ce}^{4+}) = 2.068$ , and  $R_0(\text{Ce}^{n+}) = 2.094$  were used [34].  $\Delta = (1/N)\sum_{i=1}^N [(l_i - l_{\text{av}})/l_{\text{av}}]^2$ , where  $l_{\text{av}} = (1/N)\sum_{i=1}^N l_i$  is the average Mn-O distance and  $N$  is the coordination number.

In the  $Im-3$  phase, there is one B site with the Mn2-O bond lengths of 1.9769 Å. In the  $R-3$  phase, there are two B sites (3b and 9d in the Wyckoff notations) with the 1:3 ratio. This distortion suggests a charge order similar to  $A^{2+}\text{Mn}_7\text{O}_{12}$  ( $A = \text{Cd, Ca, Sr and Pb}$ ) [15-17,19]. One site (Mn3) has an undistorted octahedron with the Mn3-O bond lengths of 1.947 Å and

should be occupied by  $\text{Mn}^{4+}$ . Another site (Mn2) has a very unusual Jahn-Teller distortion, namely, the  $\text{Mn}_2\text{O}_6$  octahedron is strongly compressed along one direction. It is the so-called  $-Q_3$  Jahn-Teller distortion mode of  $\text{Mn}^{3+}$  cations. Therefore, the Mn2 site should be occupied by  $\text{Mn}^{3+}$ . The same mode is realized in other 1:3 charge-ordered quadruple perovskites:  $\text{CdMn}_7\text{O}_{12}$  [19],  $\text{CaMn}_7\text{O}_{12}$  [15-17],  $\text{SrMn}_7\text{O}_{12}$  [19],  $\text{PbMn}_7\text{O}_{12}$  [17] and  $\text{BiCuMn}_6\text{O}_{12}$  [26]. This distortion mode is energetically unfavourable [20], and it is realized in these compounds because the orbital order is driven by the primary charge order. This could be a reason for an orbital modulation transition in  $\text{CaMn}_7\text{O}_{12}$  [16] and a reentrant structural transition back to the high-temperature cubic phase in  $\text{BiCuMn}_6\text{O}_{12}$  [26].  $\text{CeCuMn}_6\text{O}_{12}$  also shows structural instabilities, probably due to the same reason. But  $\text{CeCuMn}_6\text{O}_{12}$  remains multi-phase between 10 and 90 K. It means that different phases compete each other. Tiny compositional inhomogeneity could be a reason for the phase coexistence in a wide temperature range. Some evidence for the compositional inhomogeneity could be seen from the shape of reflections on high-resolution synchrotron XPRD patterns of the cubic  $Im\bar{3}$  phase: reflections in the high  $2\theta$  region (e.g. near  $2\theta = 57.744^\circ$  or  $d = 0.6762 \text{ \AA}$ , as shown in the inset of **Figure 4.5**) were not symmetrical and had small tails from the right side.

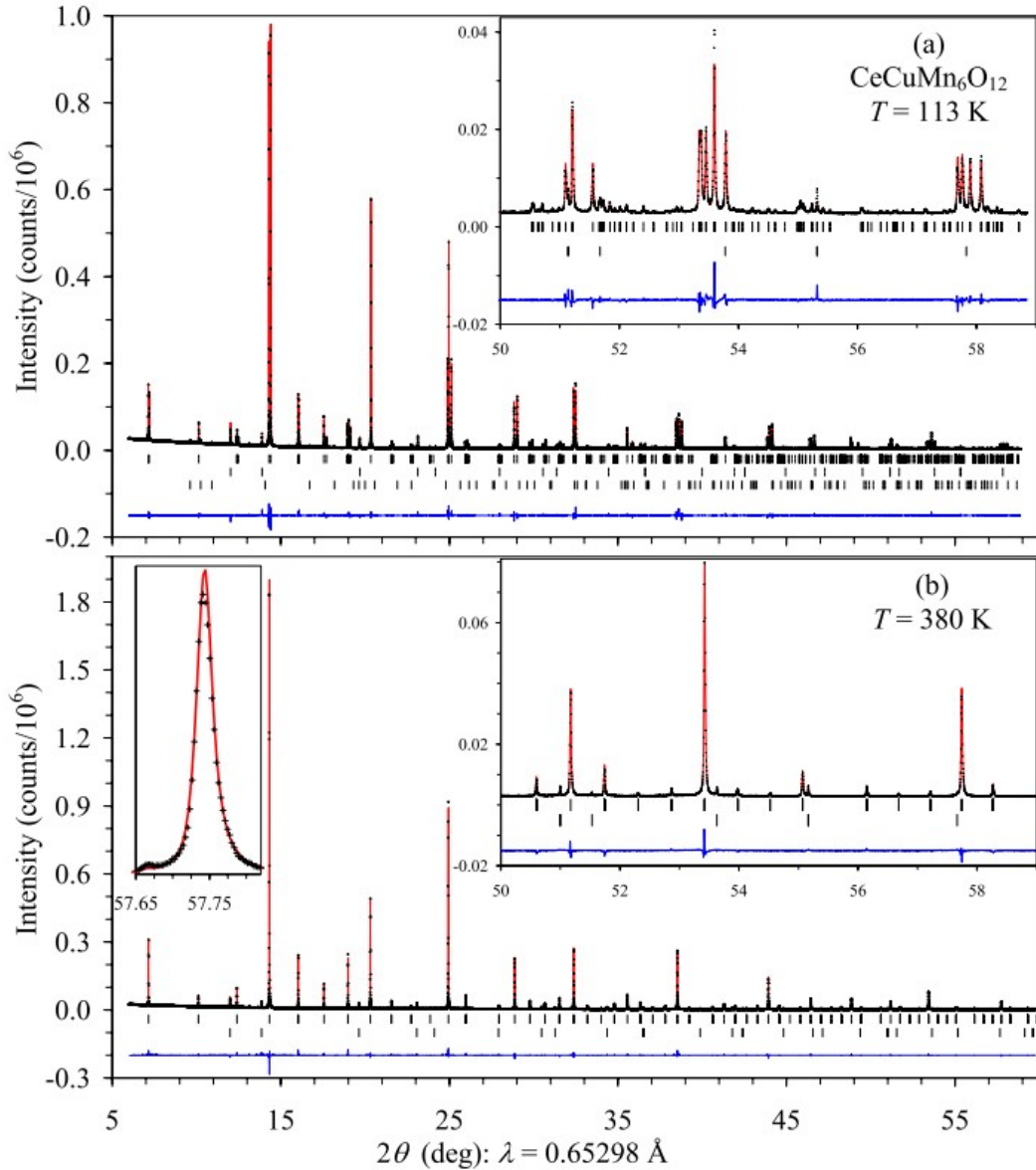


**Figure 4.5.** Experimental (black crosses), calculated (red line) and difference (blue line) synchrotron XPRD patterns of  $\text{CeCuMn}_6\text{O}_{12}$  at (a)  $T = 113$  K and (b)  $T = 380$  K. The tick marks show possible Bragg reflection positions for the main phase (the first line) and  $\text{CeO}_2$  impurity (the second line); at 113 K, the third line of Bragg reflections is for ice. The insets show details between  $50^\circ$  and  $59^\circ$  (Bragg reflections from ice are omitted). The left inset on panel (b) emphasizes the shape of single reflection of the cubic phase in the high  $2\theta$  region.

The valence state of Ce can be +3 or +4. Unfortunately, the BVS values of Ce, calculated with the  $R_0$  values from [32], are not reliable (probably because of a misprint or a mistake in

[32] for  $\text{Ce}^{4+}$ ) and do not allow assigning the valence state, for example,  $\text{BVS} = +2.49$  (with the  $R_0$  value for  $\text{Ce}^{4+}$ ) was completely unreliable, and  $\text{BVS} = +3.46$  (with the  $R_0$  value for  $\text{Ce}^{3+}$ ). The similar strange BVS values for Ce were observed in  $\text{CeCu}_3\text{Mn}_4\text{O}_{12}$  [27] and  $\text{CeCu}_3\text{Fe}_4\text{O}_{12}$  [28]. An intermediate valence between +3 and +4 was suggested in  $\text{CeCu}_3\text{Mn}_4\text{O}_{12}$  [27], while the valence was argued to be +4 in  $\text{CeCu}_3\text{Fe}_4\text{O}_{12}$  [28]. I believe that the valence of Ce should be +3 in  $\text{CeCuMn}_6\text{O}_{12}$ . First, the lattice parameters of  $\text{CeCuMn}_6\text{O}_{12}$  are in agreement with other members of the  $\text{RCuMn}_6\text{O}_{12}$  series ( $R$  = rare-earth elements) [33]. Second, the existence of the charge-order transition in  $\text{CeCuMn}_6\text{O}_{12}$  (at almost the same temperature with other members of the  $\text{RCuMn}_6\text{O}_{12}$  series [33]) suggests the  $\text{Ce}^{3+}(\text{Cu}^{2+}\text{Mn}^{3+}_2)(\text{Mn}^{3+}_3\text{Mn}^{4+})\text{O}_{12}$  charge distribution in the charge-ordered  $R$ -3 phase and  $\text{Ce}^{3+}(\text{Cu}^{2+}\text{Mn}^{3+}_2)(\text{Mn}^{3.25+}_4)\text{O}_{12}$  in the charge-disordered  $Im$ -3 phase. In  $\text{Ce}^{4+}(\text{Cu}^{2+}\text{Mn}^{3+}_2)(\text{Mn}^{3+}_4)\text{O}_{12}$ , no charge-order transitions associated with the B site would be expected. Moreover,  $\text{Ce}^{3+}\text{Mn}_7\text{O}_{12}$ , with all structural and physical properties being similar to those of  $\text{R}^{3+}\text{Mn}_7\text{O}_{12}$ , could be prepared, while  $\text{Ce}^{4+}_{0.75}\text{Mn}_7\text{O}_{12}$  could not be prepared at all (there was no reaction between  $\text{Mn}_2\text{O}_3$  and  $\text{CeO}_2$  at 6 GPa and 1570 K) [33]. Using the updated  $R_0$  values for Ce and especially the recommended  $R_0 = 2.094$  for the estimation of oxidation states of Ce [34], the obtained  $\text{BVS}(\text{Ce}^{n+})$  values were very close to +3 (**Table 4.2**). Therefore, the updated BVS parameters also support the +3 oxidation state of Ce in  $\text{CeCuMn}_6\text{O}_{12}$ . The crystal structures in the  $R$ -3 and  $Im$ -3 phases are illustrated on **Figure 4.6**.

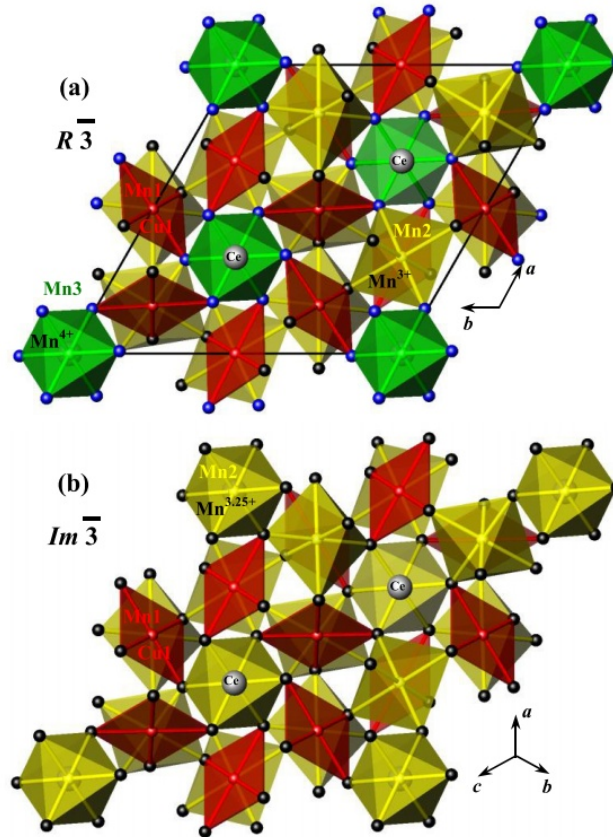


**Figure 4.6** (a) Projection of the crystal structure of  $\text{CeCuMn}_6\text{O}_{12}$  at  $T = 113$  K (space group  $R\bar{3}$ ) along the  $c$  axis. (b) The similar projection of the crystal structure of  $\text{CeCuMn}_6\text{O}_{12}$  at  $T = 380$  K (space group  $Im\bar{3}$ ).

### 4.3.3. Magnetic and transport properties of $\text{CeCuMn}_6\text{O}_{12}$

**Figures 4.7** presents dc magnetic susceptibilities of  $\text{CeCuMn}_6\text{O}_{12}$ . ZFC and FCC dc susceptibilities at 100 Oe diverge below about 95 K and show large upturn with the maximum on the  $d\chi T/dT$  vs  $T$  curves at  $T_C = 140$  K. The temperature of the ZFC and FCC curve divergence is very close to 90 K, where the structural instability takes place. However, this coincidence is probably accidental because very similar ZFC and FCC curve divergence was observed in some other  $RCuMn_6O_{12}$  compounds, which do not show structural instability [33], and also in  $\text{CaCuMn}_6\text{O}_{12}$  [35]. Similar ZFC and FCC curve divergence was also observed in other members of  $\text{CeCu}_x\text{Mn}_{7-x}\text{O}_{12}$  solid solutions, which do not show structural instability [33]. In other words, the divergence of the ZFC and FCC curves near 95 K at 100

Oe in CeCuMn<sub>6</sub>O<sub>12</sub> is caused by an additional intrinsic magnetic transition, not by a structural transition. The ZFC and FCC curves almost coincide with each other when measured at 10 kOe (**Figure 4.7b**). And in this case, the structural instability transition could be seen as small anomalies on the  $d\chi T/dT$  vs  $T$  curves with hysteresis. At 10 kOe, the maximum on the  $d\chi T/dT$  vs  $T$  curves due to the magnetic transition moves to about 148 K.

The inverse magnetic susceptibilities (measured at 10 kOe in the FCC mode) are fit by the Curie-Weiss equation

$$\chi(T) = \mu_{\text{eff}}^2 N [3k_B(T - \theta)]^{-1}$$

where  $\mu_{\text{eff}}$  is an effective magnetic moment,  $N$  is Avogadro's number,  $k_B$  is Boltzmann's constant, and  $\theta$  is the Curie-Weiss temperature. The fitting parameters are  $\mu_{\text{eff}} = 10.420(19)$   $\mu_B/\text{f.u.}$  and  $\theta = 203.9(5)$  K (between 305 and 395 K) and  $\mu_{\text{eff}} = 10.931(15)$   $\mu_B/\text{f.u.}$  and  $\theta = 172.8(2)$  K (between 235 and 280 K). The  $\mu_{\text{eff}}$  values are slightly lower than the theoretical value of 12.02  $\mu_B/\text{f.u.}$  (calculated using  $\mu(\text{Ce}^{3+}) = 2.54 \mu_B$ ). The positive Curie-Weiss temperature indicates that dominant exchange interactions are ferromagnetic in nature.

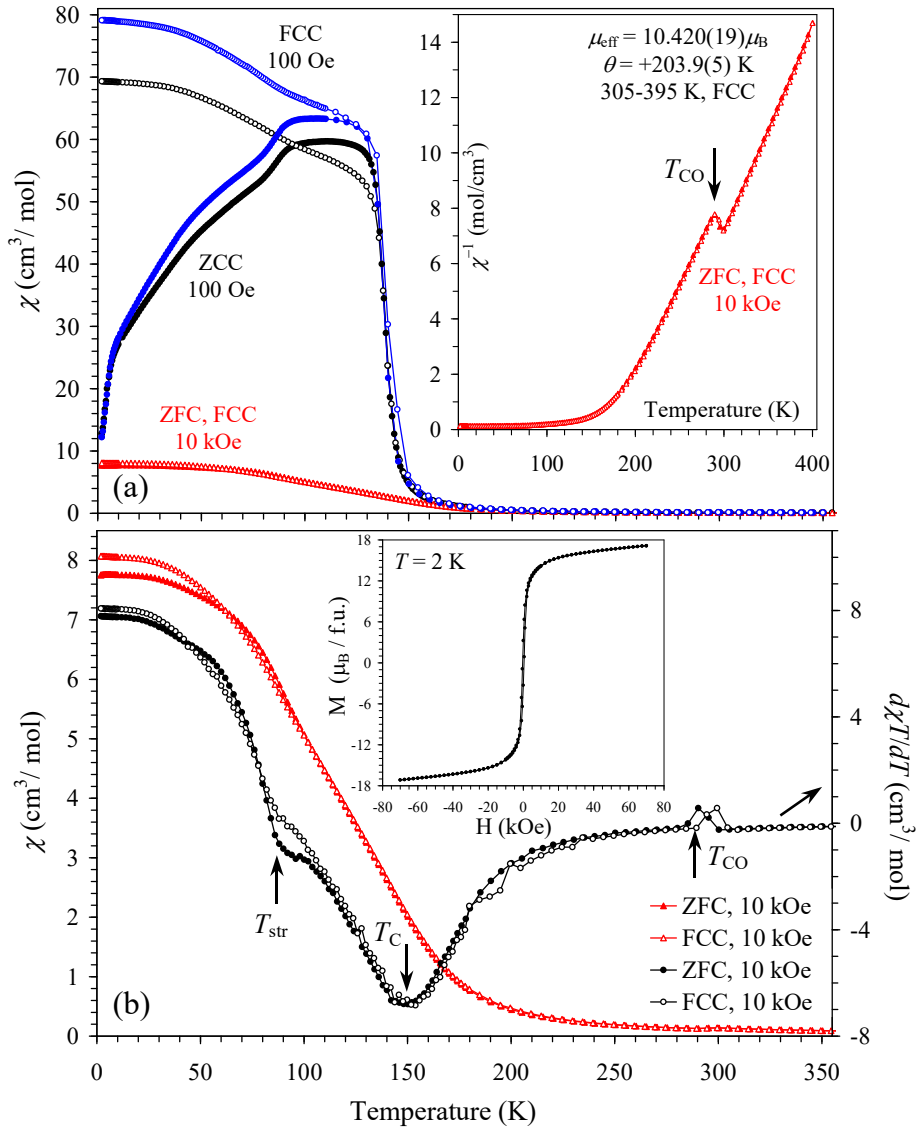


**Figure 4.7.** (a) ZFC (filled symbols) and FCC (empty symbols) dc magnetic susceptibility ( $\chi = M/H$ ) curves of  $\text{CeCuMn}_6\text{O}_{12}$  at 100 Oe (two runs for the same sample) and at 10 kOe. The inset shows the  $\chi^{-1}$  vs  $T$  curves at 10 kOe with the Curie-Weiss fit results. (b) ZFC (filled symbols) and FCC (empty symbols)  $\chi$  vs  $T$  (left-hand axis) and  $d\chi T/dT$  vs  $T$  (right-hand axis) curves at 10 kOe. Arrows emphasize different anomalies. The inset shows the  $M$  vs  $H$  curves at  $T = 2$  K.

The  $M$  vs  $H$  curve of  $\text{CeCuMn}_6\text{O}_{12}$  at 2 K is shown on the inset of **Figure 4.7b**. The curve is typical for soft ferromagnets with tiny hysteresis and fast saturation. However,

magnetization does not saturate completely at high magnetic fields, but increases gradually (e.g., from 15.37  $\mu_B$ /f.u. at 20 kOe to 17.16  $\mu_B$ /f.u. at 70 kOe). This behavior could be partially caused by the contribution of paramagnetic  $Ce^{3+}$  cations. However, unsaturated behavior of  $M$  vs  $H$  curves was also observed in  $LaCuMn_6O_{12}$  [23] and  $CaCuMn_6O_{12}$  [35] without magnetic A cations. Ferromagnetic ordering between  $(Cu^{2+}, Mn^{3+})$  at the A' site and  $(Mn^{3+}, Mn^{4+})$  at the B site was found in  $RCuMn_6O_{12}$  ( $R = La$  [23], Pr [24] and Nd [24]) and  $BiCuMn_6O_{12}$  [26] by neutron powder diffraction, but with strongly reduced ordered magnetic moments. On the other hand, ferrimagnetic ordering between  $Cu^{2+}$  at the A' site and  $(Mn^{3+}, Mn^{4+})$  at the B site takes place in  $RCu_3Mn_4O_{12}$  [27]. By analogy with  $RCuMn_6O_{12}$ , it can be assumed that the primary magnetic order is ferromagnetic in  $CeCuMn_6O_{12}$ , but  $M$  vs  $H$  curves suggest an antiferromagnetic contribution. Neutron diffraction studies are needed to confirm this assumption.

The ac susceptibility curves,  $\chi'$  vs  $T$  and  $\chi''$  vs  $T$ , as functions of frequency and ac magnetic field are given on **Figures 4.8** and **Figure 4.9**. The ac field dependence shows interactions of ac field with ferromagnetic-like domain structures. Below  $T_C = 140$  K, noticeable frequency dependence was also observed: near 90-120 K on both  $\chi'$  vs  $T$  and  $\chi''$  vs  $T$  curves and near 50 K on the  $\chi''$  vs  $T$  curves. At 6 K, frequency independent and ac field independent sharp peaks are present on the  $\chi''$  vs  $T$  curves, while the  $\chi'$  vs  $T$  curves demonstrate sharp downturn. All these features give evidence for complex magnetic behaviors of  $CeCuMn_6O_{12}$  below  $T_C$ , but the origin of such behaviors is not clear at the moment. I just emphasize that similar behaviors were observed in  $CeCu_xMn_{7-x}O_{12}$  and  $BiCu_xMn_{7-x}O_{12}$  solid solutions [33],  $RCuMn_6O_{12}$  compounds [33] and  $CaCuMn_6O_{12}$  [35].

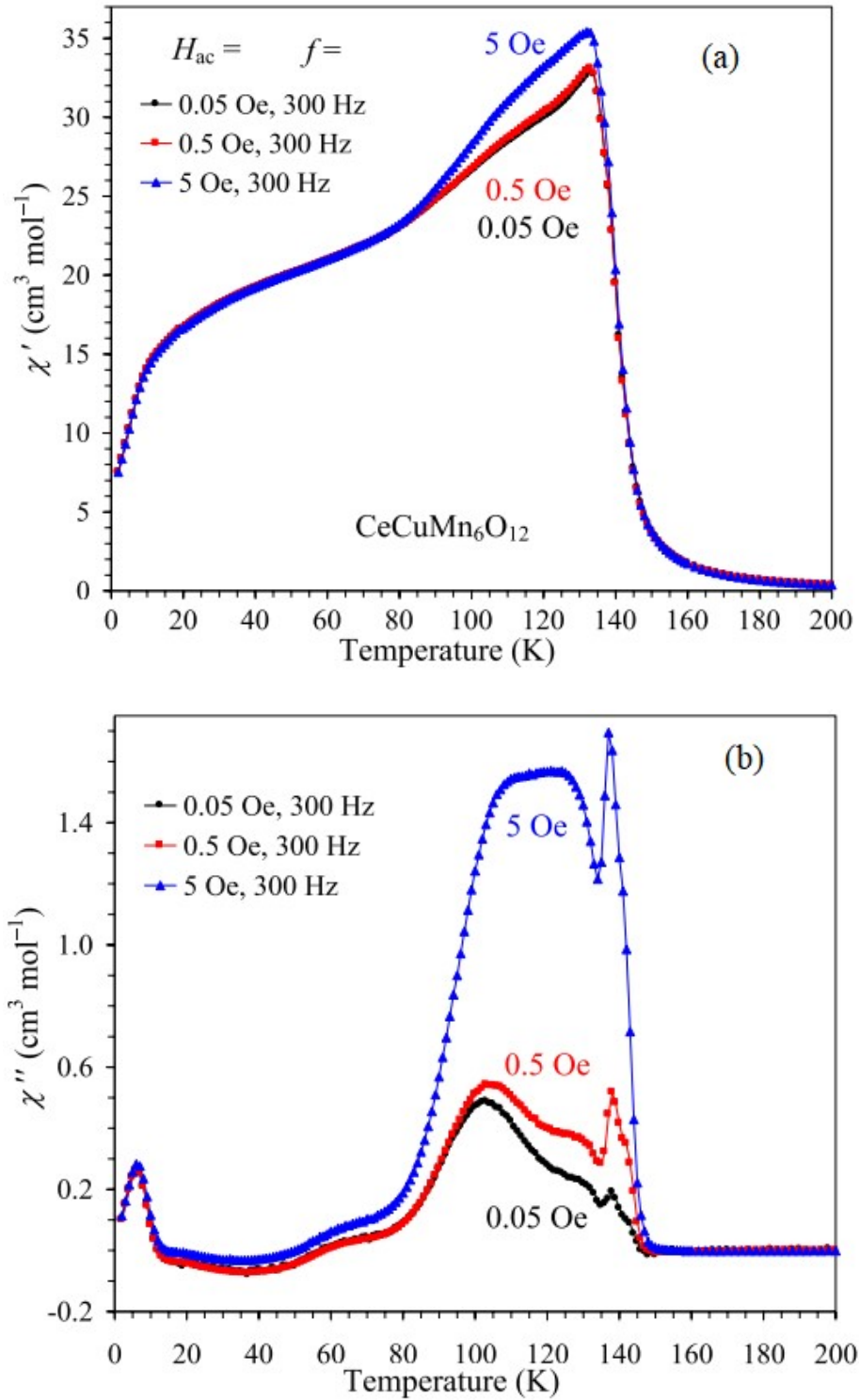


**Figure 4.8.** (a) Real parts of the ac susceptibilities ( $\chi'$  vs  $T$ ) and (b) imaginary parts ( $\chi''$  vs  $T$ ) for  $\text{CeCuMn}_6\text{O}_{12}$  ( $\chi' = M/H_{ac}$  and  $\chi'' = M''/H_{ac}$ ). Measurements were performed on cooling from 200 K to 2 K at a zero static magnetic field using ac fields with the amplitudes of  $H_{ac} = 0.05, 0.5$  and 5 Oe and one frequency of 300 Hz.

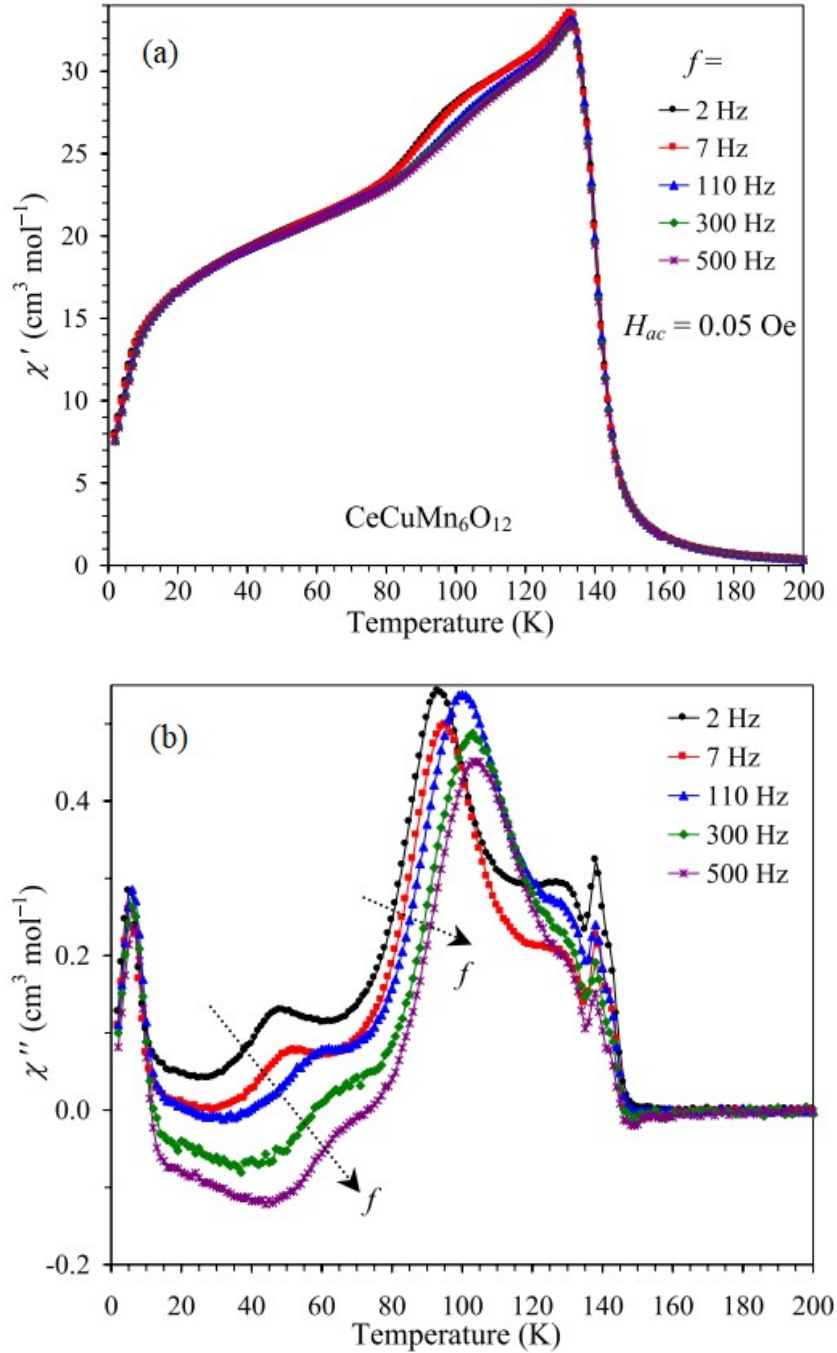


**Figure 4.9.** (a) Real parts of the ac susceptibilities ( $\chi'$  vs  $T$ ) and (b) imaginary parts ( $\chi''$  vs  $T$ ) for  $\text{CeCuMn}_6\text{O}_{12}$ . Measurements were performed on cooling from 200 K to 2 K at a zero static magnetic field using an ac field with the amplitudes of  $H_{ac} = 0.05$  Oe and different frequencies ( $f = 2, 7, 110, 300,$  and  $500$  Hz).

Specific heat of  $\text{CeCuMn}_6\text{O}_{12}$  between 2 and 300 K and at  $H = 0$  and 70 kOe is given on **Figure 4.10**. Anomalies near  $T_{CO} = 297$  K could be clearly detected. Almost no anomalies

were found near  $T_C = 140$  K – only a very tiny increase was visible.

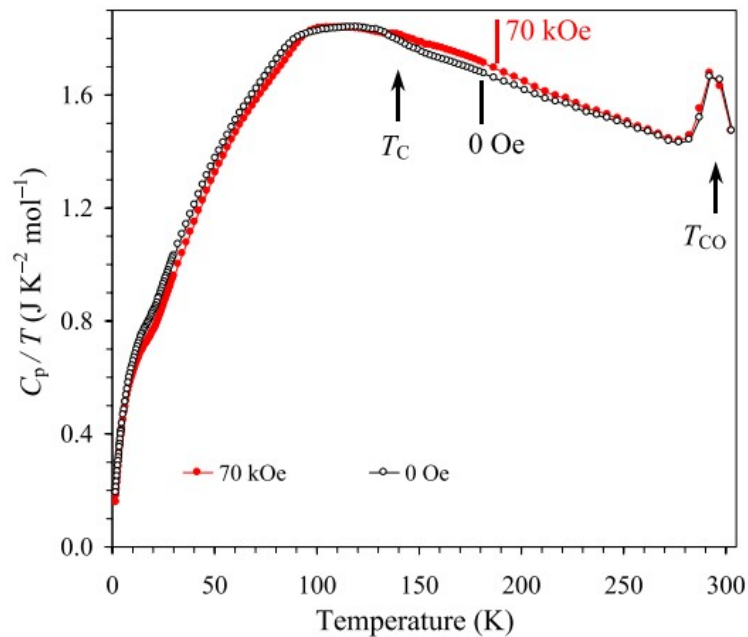


**Figure 4.10.** Specific heat of  $\text{CeCuMn}_6\text{O}_{12}$  at 0 and 70 kOe plotted as  $C_p/T$  vs  $T$ , measured on cooling. Anomalies near 20 K are instrumental artifacts.

$\text{CeCuMn}_6\text{O}_{12}$  shows semiconducting behavior (**Figure 4.11a**). Between 320 and 400 K in the high-temperature cubic  $Im\bar{3}$  phase, the temperature dependence of resistivity follows the activation law with the activation energy of about 0.14 eV. The similar activation energy of about 0.20 eV was observed in the high-temperature cubic  $Im\bar{3}$  phase of  $\text{BiCuMn}_6\text{O}_{12}$  [26]. Resistivity sharply increases in the charge-ordered  $R\bar{3}$  phase – the same was observed in  $\text{BiCuMn}_6\text{O}_{12}$  [26] and  $\text{PrCuMn}_6\text{O}_{12}$  [25]. Below about 125 K, resistivity of  $\text{CeCuMn}_6\text{O}_{12}$  was too high to be measured with our system. Magnetoresistance of  $\text{CeCuMn}_6\text{O}_{12}$  was about -40% at 140 K and 70 kOe (**Figure 4.11b**).

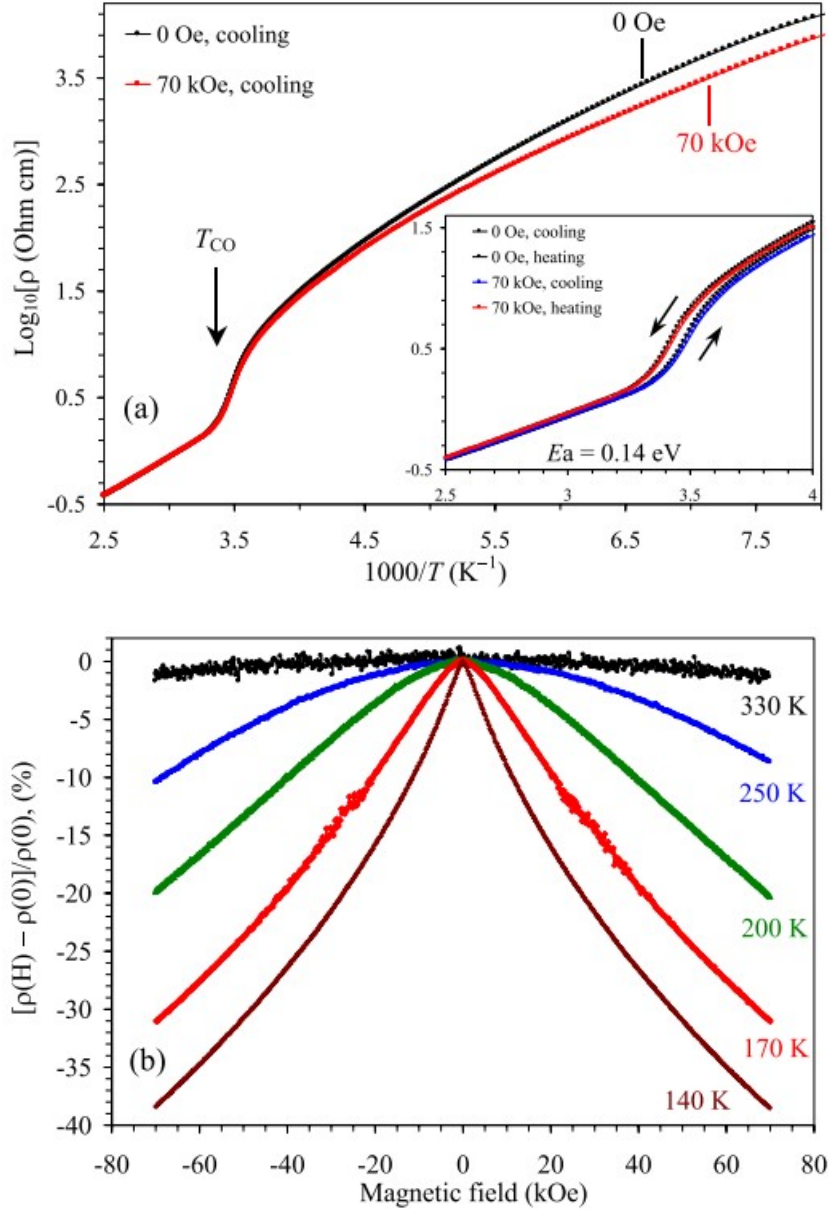


**Figure 4.11.** (a) Resistivity curves of  $\text{CeCuMn}_6\text{O}_{12}$  at  $H = 0$  and 70 kOe on cooling measured by the four-probe method, plotted as  $\log_{10}\rho$  vs  $1000/T$ . The inset shows details on heating and cooling near  $T_{\text{CO}} = 297$  K. (b) Magnetoresistance of  $\text{CeCuMn}_6\text{O}_{12}$  at different temperatures.

#### 4.4. Summary of Chapter 4

I prepared a quadruple perovskite  $\text{CeCuMn}_6\text{O}_{12}$  and observed a charge-order transition ( $Im-3 \rightarrow R-3$ ) below 297 K. There is a structure instability in  $\text{CeCuMn}_6\text{O}_{12}$  below 90 K of different nature in comparison with a reentrant structural transition found in  $\text{BiCuMn}_6\text{O}_{12}$ .  $\text{CeCuMn}_6\text{O}_{12}$  exhibits a ferromagnetic-like transition below  $T_C = 140$  K, and it is a

semiconductor with the magnetoresistance reaching about -40% at 140 K and 70 kOe. The valence of Ce is +3 in CeCuMn<sub>6</sub>O<sub>12</sub>.

## References in Chapter 4

[1] Vasil'ev, A. N.; Volkova, O. S. New functional materials. *Low Temp. Phys.* **2007**, *33*, 895–914.

[2] Yamada, I. High-pressure synthesis, electronic states, and structure-property relationships of perovskite oxides, ACu<sub>3</sub>Fe<sub>4</sub>O<sub>12</sub> (A: divalent alkaline earth or trivalent rare-earth ion). *J. Ceram. Soc. Jpn.* **2014**, *122*, 846–851.

[3] Glazer, A. M. Simple ways of determining perovskite structures. *Acta Crystallogr. Sect. A* **1975**, *31*, 756–762.

[4] Leinenweber, K.; Linton, J.; Navrotsky, A.; Fei, Y.; Parise, J. B. Highpressure perovskites on the join CaTiO<sub>3</sub>-FeTiO<sub>3</sub>. *Phys. Chem. Miner.* **1995**, *22*, 251–258.

[5] Ovsyannikov, S. V.; Zainulin, Y. G.; Kadyrova, N. I.; Tyutyunnik, A. P.; Semenova, A. S.; Kasinathan, D.; Tsirlin, A. A.; Miyajima, N.; Karkin, A. E. New Antiferromagnetic Perovskite CaCo<sub>3</sub>V<sub>4</sub>O<sub>12</sub> Prepared at High-Pressure and High-Temperature Conditions. *Inorg. Chem.* **2013**, *52*, 11703–11710.

[6] Shiro, K.; Yamada, I.; Ikeda, N.; Ohgushi, K.; Mizumaki, M.; Takahashi, R.; Nishiyama, N.; Inoue, T.; Irifune, T. Pd<sup>2+</sup>-Incorporated Perovskite CaPd<sub>3</sub>B<sub>4</sub>O<sub>12</sub> (B = Ti, V). *Inorg. Chem.* **2013**, *52*, 1604–1609.

[7] Sakai, Y.; Yang, J.; Yu, R.; Hojo, H.; Yamada, I.; Miao, P.; Lee, S.; Torii, S.; Kamiyama, T.; Ležaić, M.; Bihlmayer, G.; Mizumaki, M.; Komiyama, J.; Mizokawa, T.; Yamamoto, H.;

Nishikubo, T.; Hattori, Y.; Oka, K.; Yin, Y.; Dai, J.; Li, W.; Ueda, S.; Aimi, A.; Mori, D.; Inaguma, Y.; Hu, Y.; Uozumi, T.; Jin, C.; Long, Y.; Azuma, M. A-site and B-site Charge Orderings in an *s-d* Level Controlled Perovskite Oxide  $\text{PbCoO}_3$ . *J. Am. Chem. Soc.* **2017**, *139*, 4574–4581.

[8] Shimura, G.; Shirako, Y.; Niwa, K.; Hasegawa, M. High-pressure synthesis and relationship between A-site ordering and local structure of multicomponent perovskites  $(\text{Ln}_{0.25}\text{Mn}_{0.75})(\text{Al}_{0.25}\text{Ti}_{0.75})\text{O}_3$ , Ln = La, Pr, Nd, Sm, Gd, Tb, Dy, Y. *J. Solid State Chem.* **2016**, *242*, 55–62.

[9] Bochu, B.; Chenavas, J.; Joubert, J. C.; Marezio, M. High pressure synthesis and crystal structure of a new series of perovskite-like compounds  $\text{CMn}_7\text{O}_{12}$  (C = Na, Ca, Cd, Sr, La, Nd). *J. Solid State Chem.* **1974**, *11*, 88-93.

[10] Prodi, A.; Gilioli, E.; Cabassi, R.; Bolzoni, F.; Licci, F.; Huang, Q.; Lynn, J. W.; Affronte, M.; Gauzzi, A.; Marezio, M. Magnetic structure of the high-density single-valent eg Jahn-Teller system  $\text{LaMn}_7\text{O}_{12}$ . *Phys. Rev. B: Condens. Matter Mater. Phys.* **2009**, *79*, 085105.

[11] Okamoto, H.; Karppinen, M.; Yamauchi, H.; Fjellvag, H. High-temperature synchrotron X-ray diffraction study of  $\text{LaMn}_7\text{O}_{12}$ . *Solid State Sci.* **2009**, *11*, 1211–1215.

[12] Imamura, N.; Karppinen, M.; Motohashi, T.; Fu, D.; Itoh, M.; Yamauchi, H. Positive and Negative Magnetodielectric Effects in A-site Ordered  $(\text{BiMn}_3)\text{Mn}_4\text{O}_{12}$  Perovskite. *J. Am. Chem. Soc.* **2008**, *130*, 14948.

[13] Mezzadri, F.; Calestani, G.; Calicchio, M.; Gilioli, E.; Bolzoni, F.; Cabassi, R.; Marezio, M.; Migliori, A. Synthesis and characterization of multiferroic  $\text{BiMn}_7\text{O}_{12}$ . *Phys. Rev. B* **2009**, *79*, 100106.

- [14] Belik, A. A.; Matsushita, Y.; Kumagai, Y.; Katsuya, Y.; Tanaka, M.; Stefanovich, S. Y.; Lazoryak, B. I.; Oba, F.; Yamaura, K. Complex Structural Behavior of BiMn<sub>7</sub>O<sub>12</sub> Quadruple Perovskite. *Inorg. Chem.* **2017**, *56*, 12272–12281.
- [15] Bochu, B.; Buevoz, J. L.; Chenavas, J.; Collomb, A.; Joubert, J. C.; Marezio, M. Bond lengths in 'CaMn<sub>3</sub>(Mn<sub>4</sub>)O<sub>12</sub>': A new Jahn-Teller distortion of Mn<sup>3+</sup> octahedra. *Solid State Commun.* **1980**, *36*, 133-138.
- [16] Perks, N. J.; Johnson, R. D.; Martin, C.; Chapon, L. C.; Radaelli, P. G. Magneto-orbital helices as a route to coupling magnetism and ferroelectricity in multiferroic CaMn<sub>7</sub>O<sub>12</sub>. *Nat. Commun.* **2012**, *3*, 1277.
- [17] Belik, A. A.; Glazkova, Y. S.; Katsuya, Y.; Tanaka, M.; Sobolev, A. V.; I. Presniakov, A. Low-Temperature Structural Modulations in CdMn<sub>7</sub>O<sub>12</sub>, CaMn<sub>7</sub>O<sub>12</sub>, SrMn<sub>7</sub>O<sub>12</sub>, and PbMn<sub>7</sub>O<sub>12</sub> Perovskites Studied by Synchrotron X-ray Powder Diffraction and Mössbauer Spectroscopy. *J. Phys. Chem. C* **2016**, *120*, 8278–8288.
- [18] Johnson, R. D.; Khalyavin, D. D.; Manuel, P.; Radaelli, P. G.; Glazkova, I. S.; Terada, N.; Belik, A. A. Magneto-orbital ordering in the divalent A-site quadruple perovskite manganites AMn<sub>7</sub>O<sub>12</sub> (A = Sr, Cd, and Pb). *Phys. Rev. B* **2017**, *96*, 054448.
- [19] Glazkova, Y. S.; Terada, N.; Matsushita, Y.; Katsuya, Y.; Tanaka, M.; Sobolev, A. V.; Presniakov, I. A.; Belik, A. A. High-Pressure Synthesis, Crystal Structures, and Properties of CdMn<sub>7</sub>O<sub>12</sub> and SrMn<sub>7</sub>O<sub>12</sub> Perovskites. *Inorg. Chem.* **2015**, *54*, 9081-9091.
- [20] Streltsov, S. V.; Khomskii, D. I. Jahn-Teller distortion and charge, orbital, and magnetic order in NaMn<sub>7</sub>O<sub>12</sub>. *Phys. Rev. B* **2014**, *89*, 201115.
- [21] Salamon, M. B.; Jaime, M. The physics of manganites: Structure and transport. *Rev. Mod.*

*Phys.* **2001**, *73*, 583-628.

[22] Troyanchuk, I. O.; Balyko, L. V.; Bashkirov, L. A.; Crystal Structure Phase Transitions in the Perovskites  $A(\text{Cu}_{1-x}\text{Mn}_x)\text{Mn}_4\text{O}_{12}$  ( $A = \text{Na}^+, \text{Ca}^{2+}, \text{Y}^{3+}, \text{La}^{3+}$ ). *Cryst. Res. Technol.* **1986**, *21*, 705-710.

[23] Muñoz, A.; Martínez-Lope, M. J.; Retuerto, M.; Falcón, H.; Alonso, A. Ferromagnetic behavior in  $\text{La}(\text{Cu}_{3-x}\text{Mn}_x)\text{Mn}_4\text{O}_{12}$  ( $x = 1, 2$ ) perovskites. *J. Appl. Phys.* **2008**, *104*, 083911.

[24] Retuerto, M.; Martínez-Lope, M. J.; Sánchez-Benítez, J.; García-Hernández, M.; Fernández-Díza, M. T.; Alonso, A. Synthesis, magnetic properties, and neutron diffraction study of the complex perovskites  $\text{R}(\text{Cu}_{3-x}\text{Mn}_x)\text{Mn}_4\text{O}_{12}$  ( $\text{R} = \text{Pr}, \text{Nd}$  and  $x = 1, 2$ ). *J. Appl. Phys.* **2010**, *108*, 083905.

[25] Zhang, W.; Yao, L. D.; Yang, L. X.; Liu, Z. X.; Jin, C. Q.; Yu, R. C. Charge ordering in  $\text{PrCuMn}_6\text{O}_{12}$  and its behavior under pressure. *J. Appl. Phys.* **2010**, *107*, 023914.

[26] Belik, A. A.; Matsushita, Y.; Khalyavin, D. D. Reentrant Structural Transitions and Collapse of Charge and Orbital Orders in Quadruple Perovskites. *Angew. Chem. Int. Ed.* **2017**, *56*, 10423–10427.

[27] Sánchez-Benítez, J.; Martínez-Lope, M. J.; Alonso, A. Preparation at moderate pressures, crystal and magnetic structure and magnetotransport of the ferrimagnetic  $\text{CeCu}_3\text{Mn}_4\text{O}_{12}$  perovskite. *J. Appl. Phys.* **2010**, *107*, 103904.

[28] Yamada, I.; Etani, H.; Murakami, M.; Hayashi, N.; Kawakami, T.; Mizumaki, M.; Ueda, S.; Abe, H.; Liss, K.-D.; Studer, A. J.; Ozaki, T.; Mori, S.; Takahashi, R.; Irifune, T. Charge-Order Melting in Charge- Disproportionated Perovskite  $\text{CeCu}_3\text{Fe}_4\text{O}_{12}$ . *Inorg. Chem.* **2014**, *53*, 11794-11801.

- [29] Izumi, F.; Ikeda, T. A Rietveld-Analysis Programm RIETAN-98 and its Applications to Zeolites. *Mater. Sci. Forum* **2000**, 321-324, 198-205.
- [30] Tanaka, M.; Katsuya, Y.; Yamamoto, A. A New Large Radius Imaging Plate Camera for High-Resolution and High-Throughput Synchrotron X-Ray Powder Diffraction by Multiexposure Method. *Rev. Sci. Instrum.* **2008**, 79, 075106.
- [31] Tanaka, M.; Katsuya, Y.; Matsushita, Y.; Sakata, O. Development of a Synchrotron Powder Diffractometer with a One-Dimensional X-Ray Detector for Analysis of Advanced Materials. *J. Ceram. Soc. Jpn.* **2013**, 121, 287-290.
- [32] Brese, N. E.; O'Keeffe, M. Bond-Valence Parameters for Solids. *Acta Crystallogr., Sect. B* **1991**, 47, 192-197.
- [33] Zhang, L.; Matsushita, Y.; Yamaura, K.; Belik, A. A. unpublished results.
- [34] Roulhac, P. L.; Palenik, G. J. Bond Valence Sums in Coordination Chemistry. The Calculation of the Oxidation State of Cerium in Complexes Containing Cerium Bonded Only to Oxygen. *Inorg. Chem.* **2003**, 42(1), 118-121.
- [35] Zhang, Q.; Bréard, Y.; Guillou, F.; Hardy, V. Investigation of the magnetocaloric effect in double distorted perovskites  $\text{Ca}(\text{Cu}_{3-x}\text{Mn}_x)\text{Mn}_4\text{O}_{12}$  ( $1 \leq x \leq 2$ ): From standard ferrimagnetism to glassy ferrimagnetism. *Phys. Rev. B* **2011**, 84, 224430.

## Chapter 5. Mn self-doping of orthorhombic $RMnO_3$ Perovskites:

### $(R_{0.667}Mn_{0.333})MnO_3$ with $R = \text{Er-Lu}$

#### 5.1 Introduction

Rare-earth trivalent manganites, belonging to  $R_2O_3$ - $Mn_2O_3$  systems with  $R =$  rare-earth elements, have been a playground for solid-state and materials chemists and physicists for decades [1-7]. The most studied compounds have a 1:1 ratio and an  $RMnO_3$  stoichiometry, and two modifications of  $RMnO_3$  exist: an orthorhombic perovskite modification with space group  $Pnma$  and a nonperovskite hexagonal modification with space group  $P6_3cm$  (which is still often referred to as the hexagonal "perovskite" because of the same stoichiometry) [8]. The perovskite modification is known for all  $R$  from La to Lu, even though the preparation of  $RMnO_3$  with  $R = \text{Ho-Lu}$  and Y in the bulk form requires high-pressure (HP) and high-temperature (HT) conditions.  $RMnO_3$  with  $R = \text{Ho-Lu}$  and Y adopts the hexagonal modification when synthesized at ambient pressure [8].

Distortions of  $RMnO_3$  perovskites increase with a decrease in the size of the  $R^{3+}$  cations, and it is reflected in the increased magnitude of octahedral tilts, which, in turn, affect the transition metal-oxygen angles and the ground-state magnetic ordering [2-4]. A-type antiferromagnetic (AFM) ordering with spin canting is observed for  $R = \text{La-Gd}$ , spin spirals are realized for  $R = \text{Tb}$  and Dy, and collinear and noncollinear E-type AFM ordering without spin canting takes place for  $R = \text{Ho-Lu}$  [5,6]. The last two spin ordering (spirals and E-type) give rise to spin-induced multiferroic properties[1,5,6].

The  $R_2O_3$ - $Mn_2O_3$  systems also have compounds with a 1:7 ratio and an idealized  $RMn_7O_{12}$  stoichiometry and the A-site-ordered  $AA_3B_4O_{12}$  quadruple perovskite structure [9-16]. The ideal stoichiometry is realized for large rare-earth elements (e.g.,  $R = \text{La-Gd}$ ), while such compounds with small rare-earth elements (e.g.,  $R = \text{Dy-Er}$  and Y) have  $(R_{1-x}Mn_x)Mn_7O_{12}$

compositions.  $RMn_7O_{12}$  can be prepared only at HP and HT conditions. All Mn cations located at the A' and B sites have the oxidation state of 3+ (in the ideal stoichiometry).  $Mn^{3+}$  at the A' site has an unusual square-planar coordination environment, while  $Mn^{3+}$  at the B site has a typical Jahn-Teller-distorted octahedral environment.

The perovskites with a 1:3 ratio have been discovered and an idealized  $RMn_3O_6$  stoichiometry under HP and HT conditions [16]. They belong to the A-site columnar-ordered  $A_2A'A''B_4O_{12}$  quadruple perovskite family [17], and the charge distribution in  $RMn_3O_6$  can be presented as  $[R^{3+}_2]_A[Mn^{3+}]_{A'}[Mn^{2+}]_{A''}[Mn^{3+}_2]_{B1}[Mn^{3+}Mn^{4+}]_{B2}O_{12}$ . Their structure has  $Mn^{2+}$  at a tetrahedral A'' site and a mixture of  $Mn^{3+}$  and  $Mn^{4+}$  cations at one of the B sites, while the average oxidation state of Mn is still 3+.  $Mn^{3+}$  at the A' site has a square-planar coordination environment similar to that of  $RMn_7O_{12}$ .

In this work, I report on the Mn self-doping of the 1:1  $RMnO_3$  perovskites, with the composition reaching  $(R_{0.667}Mn_{0.333})MnO_3$  or a 1:2 stoichiometric ratio. This level of doping was achieved through the HP and HT synthesis. The original idea was to keep the oxidation state of Mn at +3 at the B site, while increasing the degree of distortions in  $RMnO_3$ . Detailed structural and spectroscopic studies showed, however, that Mn enters the A site in the oxidation state of +2, creating the average oxidation state of +3.333 at the B site:  $[R^{3+}_{0.667}Mn^{2+}_{0.333}]_A[Mn^{3+}_{0.667}Mn^{4+}_{0.333}]_BO_3$ . Our present and recent results demonstrate the complexity of seemingly simple quasi-binary  $R_2O_3$ - $Mn_2O_3$  systems under HP and HT conditions.

## 5.2. Experimental details of Chapter 5

$(R_{0.667}Mn_{0.333})MnO_3$  ( $R = Tm, Yb, \text{ and } Lu$ ),  $(Er_{1-x}Mn_x)MnO_3$  ( $x = 0.2, 0.3, \text{ and } 1/3$ ), and  $(Lu_{0.6}Mn_{0.4})MnO_3$  samples were prepared from stoichiometric mixtures of  $Mn_2O_3$  and  $R_2O_3$  (99.9%). Single-phase  $Mn_2O_3$  was prepared from commercial  $MnO_2$  (99.99%) by heating in

air at 923 K for 24 h. The mixtures were placed in Pt capsules and treated at 6 GPa and about 1670 K for 2 h (the heating time to the synthesis temperature was 10 min) in a belt-type HP apparatus. After the heat treatments, the samples were quenched to room temperature (RT), and the pressure was slowly released. All of the samples obtained were black pellets (quite loose in some cases).  $\text{CaMnO}_3$  was synthesized from a stoichiometric mixture of  $\text{Mn}_2\text{O}_3$  and  $\text{CaCO}_3$  (99.99%); the mixture was first annealed at ambient pressure at 1423 K for 80 h with several intermediate grindings (to give a single-phase powder) and finally treated at 6 GPa and about 1670 K for 40 min in a Pt capsule to produce a single-phase dense pellet.  $\text{LuMnO}_3$  was synthesized from a stoichiometric mixture of  $\text{Mn}_2\text{O}_3$  and  $\text{Lu}_2\text{O}_3$  (99.9%); the mixture was first annealed at ambient pressure at 1423 K for 80 h with several intermediate grindings (to give a single-phase powder with hexagonal structure) and finally treated at 6 GPa and about 1470 K for 10 min in an Au capsule to produce a single-phase dense pellet with perovskite structure. Single-phase MnO was prepared from commercial  $\text{MnO}_2$  (99.997%, Alfa-Aesar) by annealing at 1273 K in a 10%  $\text{H}_2$  + 90% Ar flow for 18 h, and powder was pressed at 6 GPa (without heating) to prepare a dense pellet.

X-ray powder diffraction (XRPD) data were collected at RT on a Rigaku MiniFlex600 diffractometer using  $\text{CuK}\alpha$  radiation ( $2\theta$  range of 8-140°, a step width of 0.02°, and scan speed of 1°  $\text{min}^{-1}$ ). Synchrotron XRPD data were measured at RT on a large Debye-Scherrer camera at the undulator Beamline BL15XU of SPring-8 [18,19]. The intensity data were collected between 3° and 60.34° for  $(\text{Yb}_{0.667}\text{Mn}_{0.333})\text{MnO}_3$  and  $(\text{Lu}_{0.667}\text{Mn}_{0.333})\text{MnO}_3$  and between 3° and 71.40° for  $(\text{Tm}_{0.667}\text{Mn}_{0.333})\text{MnO}_3$  at 0.003° intervals in  $2\theta$ ; the incident beam was monochromatized at  $\lambda = 0.65298$  Å. The samples were packed into Lindemann glass capillaries (inner diameter: 0.1 mm), which were rotated during the measurement. The absorption coefficients were also measured. Rietveld analysis was performed using the RIETAN-2000 program [20].

Hard X-ray photoelectron spectroscopy (HAXPES) measurements were also performed at BL15XU of the SPring-8 [21,22]. The excitation photon energy was set to 5953.4 eV. The base pressure of the analysis chamber was better than  $1 \times 10^{-7}$  mbar. The HAXPES spectra were measured with a high-resolution hemispherical electron analyser (VG Scienta R400) with a pass energy of 200 eV. Samples were measured in a pellet form. The binding energy was referred to the Fermi level of an evaporated Au film. The total energy resolution was set to 240 meV at RT, which was verified by the Fermi cutoff of the Au film.  $(\text{Lu}_{0.6}\text{Mn}_{0.4})\text{MnO}_3$  and  $(\text{Er}_{0.667}\text{Mn}_{0.333})\text{MnO}_3$  samples and  $\text{MnO}$  ( $\text{Mn}^{2+}$ ),  $\text{LuMnO}_3$  ( $\text{Mn}^{3+}$ ), and  $\text{CaMnO}_3$  ( $\text{Mn}^{4+}$ ) as standards were measured. Sample charging was observed especially for the  $\text{MnO}$  reference. The photon flux was reduced and the experimental geometry slightly changed for this sample but despite this, a broadening of the  $\text{MnO}$  HAXPES spectra was observed. All spectra were additionally calibrated with the adventitious C 1s line by setting the C-C peak from 285.06 eV for  $(\text{Lu}_{0.6}\text{Mn}_{0.4})\text{MnO}_3$ , 285.37 eV for  $(\text{Er}_{0.667}\text{Mn}_{0.333})\text{MnO}_3$ , 290.95 eV for  $\text{MnO}$ , 285.42 eV for  $\text{LuMnO}_3$  and 285.20 eV for  $\text{CaMnO}_3$  to the literature value of 284.80 eV [23].

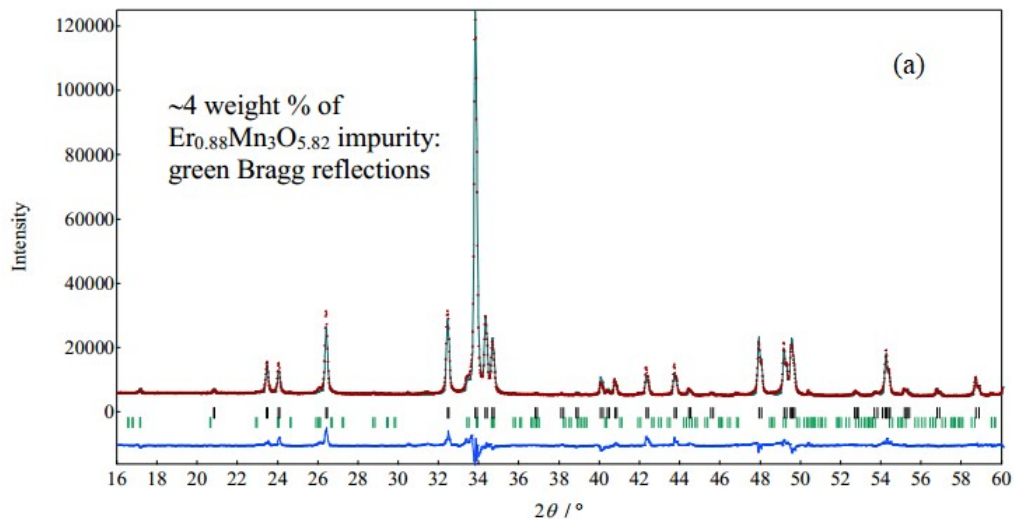
Magnetic measurements were performed on a SQUID magnetometer (Quantum Design, MPMS-XL-7T) between 2 and 400 K in different applied fields under both zero-field-cooled (ZFC) and field-cooled upon cooling (FCC) conditions. Isothermal magnetization measurements were performed between -70 and 70 kOe at different temperatures. Frequency-dependent alternating-current (ac) susceptibility measurements were performed with a Quantum Design MPMS-1T instrument at different frequencies ( $f$ ) and different applied oscillating magnetic fields ( $H_{ac}$ ). The specific heat ( $C_p$ ) values at magnetic fields of 0 and 90 kOe was recorded between 2 and 300 K upon cooling and heating by a pulse relaxation method using a commercial calorimeter (Quantum Design PPMS). The dielectric properties were measured using a NOVOCONTROL Alpha-A high-performance frequency analyzer between 5 and 300 K upon cooling and heating in the frequency range of 100 Hz

and 2 MHz and at 0 and 90 kOe.

### 5.3. Results and discussion

#### 5.3.1. Structural Properties of $(R_{0.667}Mn_{0.333})MnO_3$ and $(Er_{1-x}Mn_x)MnO_3$

$(Er_{0.667}Mn_{0.333})MnO_3$  contained about 4 weight % of  $Er_{0.88}Mn_3O_{5.82}$  impurity [16] (estimated RIETAN-2000 from the refined scale factors in the Rietveld fitting), as shown in **Figure 5.1**. This fact shows that the substitution limit at the A site is a little bit smaller than 33% in the case of  $R = Er$  (at the synthesis conditions used). For this reason, we prepared  $(Er_{1-x}Mn_x)MnO_3$  with  $x = 0.2$  and  $0.3$ , which were single-phase. Electronprobe microanalysis of a two-phase sample with a total chemical composition of  $TmMn_3O_6$  showed that one perovskite phase had a Tm/Mn ratio of  $0.643(11) : 1.357(13)$  [16]. This fact shows that the  $(Tm_{0.667}Mn_{0.333})MnO_3$  composition is very close to the boundary of the stability of  $(Tm_{1-x}Mn_x)MnO_3$  solid solutions (at the synthesis conditions used).



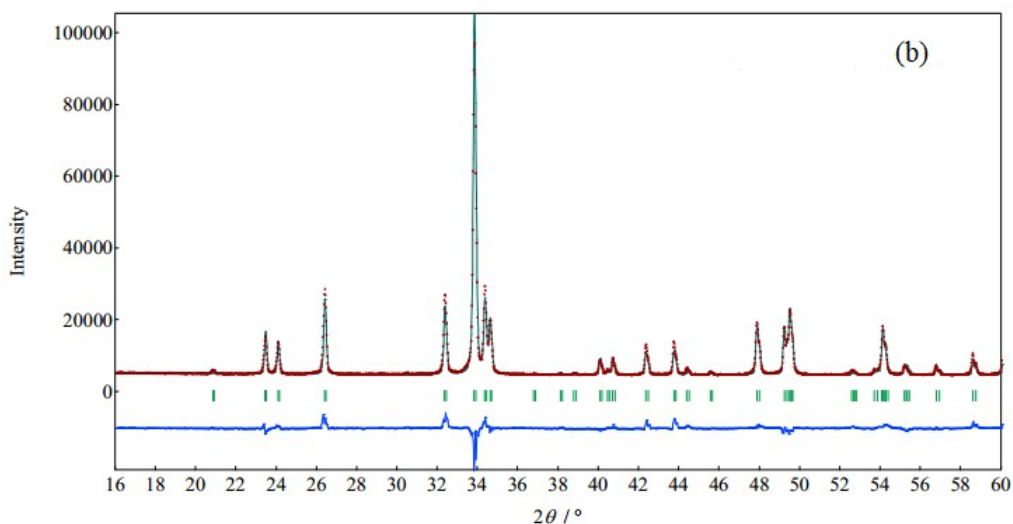


**Figure 5.1.** Laboratory X-ray powder diffraction patterns (brown crosses) at RT for  $(\text{Er}_{0.667}\text{Mn}_{0.333})\text{MnO}_3$  (a) and  $(\text{Er}_{0.7}\text{Mn}_{0.3})\text{MnO}_3$  (b) with fitting results.

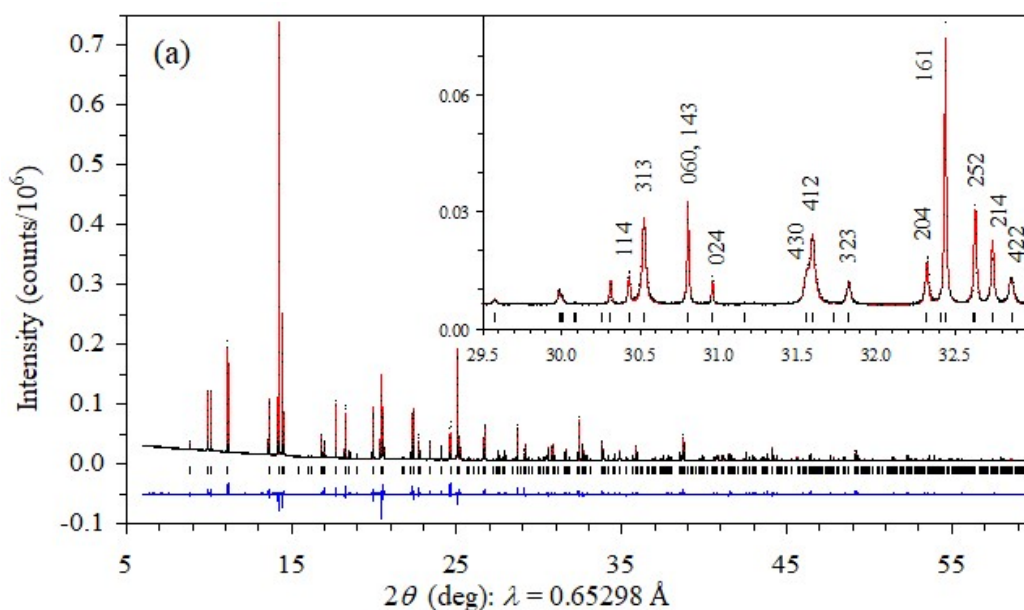
The refined lattice parameters are summarized in **Table 5.1**. The  $a$  lattice parameter of  $(\text{Lu}_{0.667}\text{Mn}_{0.333})\text{MnO}_3$  is significantly reduced in comparison with that of  $\text{LuMnO}_3$  ( $a = 5.50348$  vs  $5.7928$  Å), the  $c$  lattice parameter is slightly reduced ( $c = 5.18686$  vs  $5.2014$  Å), and the  $b$  lattice parameter is increased ( $b = 7.37564$  vs  $7.3023$  Å). Our own data were used for  $\text{LuMnO}_3$ ; but our lattice parameters are very close to the literature data [3]. The same behavior of the lattice parameters is observed in other compounds and can be more clearly seen in the case of  $(\text{Er}_{1-x}\text{Mn}_x)\text{MnO}_3$  solid solutions (**Table 5.1**).

**Table 5.1.** Lattice parameters ( $a$ ,  $b$ , and  $c$ ) of  $(R_{0.667}\text{Mn}_{0.333})\text{MnO}_3$  ( $R = \text{Tm}, \text{Yb},$  and  $\text{Lu}$ ) and  $(\text{Er}_{1-x}\text{Mn}_x)\text{MnO}_3$  solid solutions.

sample	$a$ (Å)	$b$ (Å)	$c$ (Å)
$\text{Lu}_{0.667}^a$	5.50348(2)	7.37564(1)	5.18686(1)
$\text{Yb}_{0.667}^a$	5.50811(3)	7.37534(1)	5.20430(1)
$\text{Tm}_{0.667}^a$	5.51410(1)	7.39113(1)	5.21583(1)
$\text{Er}_{0.667}^b$	5.5238(1)	7.4120(1)	5.2274(1)
$\text{Er}_{0.7}^b$	5.5374(1)	7.4040(1)	5.2253(1)
$\text{Er}_{0.8}^b$	5.6318(1)	7.3899(1)	5.2352(1)
$\text{Er}_{1.0}^b$	5.8304(1)	7.3396(2)	5.2431(1)

<sup>a</sup>From synchrotron XRPD. <sup>b</sup>From laboratory XRPD.

Experimental, calculated, and difference synchrotron XRPD patterns of  $(\text{Lu}_{0.667}\text{Mn}_{0.333})\text{MnO}_3$ ,  $(\text{Yb}_{0.667}\text{Mn}_{0.333})\text{MnO}_3$ , and  $(\text{Tm}_{0.667}\text{Mn}_{0.333})\text{MnO}_3$  are shown in **Figure 5.2**. All samples exhibited significant anisotropic broadening of some reflections, as shown in the insets of **Figure 5.2**. This broadening was modeled using an (100) anisotropic-broadening axis in RIETAN-2000 [with anisotropic strain broadening,  $U_e = 5.02(7)\times 10^{-6}$ ,  $6.88(9)\times 10^{-6}$ , and  $3.64(6)\times 10^{-6}$ , and anisotropic Scherrer broadening,  $P_e = 1.27(18)\times 10^{-8}$ ,  $2.4(2)\times 10^{-8}$ , and  $-0.05(1.40)\times 10^{-9}$ , for  $(\text{Lu}_{0.667}\text{Mn}_{0.333})\text{MnO}_3$ ,  $(\text{Yb}_{0.667}\text{Mn}_{0.333})\text{MnO}_3$ , and  $(\text{Tm}_{0.667}\text{Mn}_{0.333})\text{MnO}_3$ , respectively]. Because of the different sizes of  $\text{R}^{3+}$  and  $\text{Mn}^{2+}$  cations (see the discussion below), they are split at the A site: refinement with the split model resulted in  $R_{\text{wp}} = 4.74\%$ ,  $R_{\text{p}} = 2.87\%$ ,  $R_{\text{B}} = 5.30\%$ , and  $R_{\text{F}} = 3.08\%$ , while the one-site model gave  $R_{\text{wp}} = 4.85\%$ ,  $R_{\text{p}} = 2.92\%$ ,  $R_{\text{B}} = 5.57\%$ , and  $R_{\text{F}} = 3.36\%$  for  $(\text{Lu}_{0.667}\text{Mn}_{0.333})\text{MnO}_3$ .



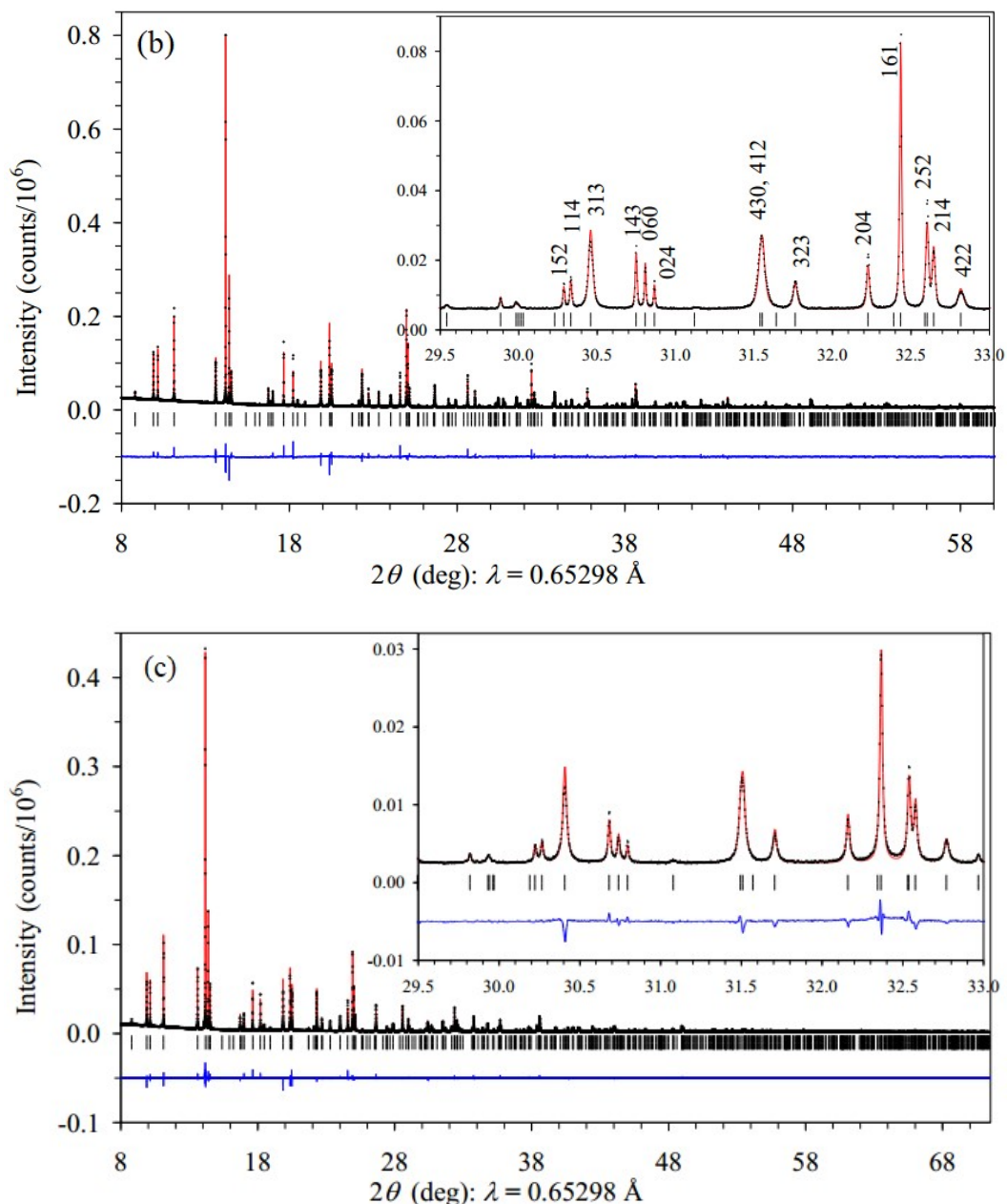


**Figure 5.2.** Experimental (black crosses), calculated (red lines), and difference (blue lines) synchrotron XRPD patterns of  $(\text{Lu}_{0.667}\text{Mn}_{0.333})\text{MnO}_3$  (a),  $(\text{Yb}_{0.667}\text{Mn}_{0.333})\text{MnO}_3$  (b), and  $(\text{Tm}_{0.667}\text{Mn}_{0.333})\text{MnO}_3$  (c) at 295 K. The insets show the enlarged fragments and emphasizes anisotropic broadening.

The refined structural parameters of  $(R_{0.667}\text{Mn}_{0.333})\text{MnO}_3$  with  $R = \text{Tm}, \text{Yb},$  and  $\text{Lu}$ , bond lengths, Mn-O-Mn bond angles, and bond-valence sums (BVSs) [24] are summarized in **Tables 5.2** and **Table 5.3**. The BVS values of the  $R$  atoms are close to the expected value of

+3, while the BVS values of Mn atoms at the A site support the oxidation state of +2. A typical A site (with 8-10 coordination numbers) of a perovskite is too large to accommodate small  $\text{Mn}^{3+}$  cations, and  $\text{Mn}^{3+}$  can be located at A sites only in a square-planar coordination realized in  $\text{RMn}_7\text{O}_{12}$  and  $\text{RMn}_3\text{O}_6$  [12,13,16]. The BVS values of Mn atoms at the B site (+3.32-3.39) are noticeably higher than +3. The  $\text{Mn}_2\text{O}_6$  octahedra have a noticeable elongated Jahn-Teller distortion, which is typical for  $\text{Mn}^{3+}$  cations. However, the octahedral distortion parameter,  $\Delta(\text{Mn})$ , of  $(11-15) \times 10^{-4}$  is significantly smaller than that for  $\text{Mn}^{3+}$  cations in  $\text{RMnO}_3$  ( $\Delta(\text{Mn}) = (30-50) \times 10^{-4}$ ) [3,7]. The survival of Jahn-Teller distortions can be explained by a large portion (67%) of  $\text{Mn}^{3+}$  cations at the B site. Relatively large distortions of  $\text{MnO}_6$  octahedra were also observed in  $(\text{R}_{0.5}\text{Ca}_{0.5})\text{MnO}_3$  ( $\text{R} = \text{Tm}$  and  $\text{Lu}$ ) in comparison with  $(\text{R}_{0.5}\text{Ca}_{0.5})\text{MnO}_3$  ( $\text{R} = \text{Nd}$ ,  $\text{Pr}$ , and  $\text{La}$ ) [25]. Therefore, additional contributions from small  $\text{R}^{3+}$  and  $\text{Mn}^{2+}$  cations at the A site could also play a role for large distortions of  $\text{MnO}_6$  octahedra in  $(\text{R}_{0.667}\text{Mn}_{0.333})\text{MnO}_3$ .

**Table 5.2.** Structure parameters of  $(\text{Lu}_{0.667}\text{Mn}_{0.333})\text{MnO}_3$ ,  $(\text{Yb}_{0.667}\text{Mn}_{0.333})\text{MnO}_3$ , and  $(\text{Tm}_{0.667}\text{Mn}_{0.333})\text{MnO}_3$  at RT<sup>a</sup>.

site	WP	<i>g</i>	<i>x</i>	<i>y</i>	<i>z</i>	B (Å <sup>2</sup> )
$(\text{Lu}_{0.667}\text{Mn}_{0.333})\text{MnO}_3$						
Lu	4c	2/3	0.07104(17)	0.25	0.98766(13)	0.166(9)
Mn1	4c	1/3	0.0834(13)	0.25	0.9422(8)	= <i>B</i> (Lu)
Mn2	4b	1	0	0	0.5	0.73(2)
O1	4c	1	0.4545(9)	0.25	0.1179(7)	0.53(9)
O2	8d	1	0.3221(6)	0.0563(4)	0.6914(6)	0.68(7)
$(\text{Yb}_{0.667}\text{Mn}_{0.333})\text{MnO}_3$						
Yb	4c	2/3	0.06820(17)	0.25	0.98763(15)	0.199(10)
Mn1	4c	1/3	0.0885(13)	0.25	0.9530(10)	= <i>B</i> (Yb)
Mn2	4b	1	0	0	0.5	0.492(18)
O1	4c	1	0.4598(9)	0.25	0.1118(7)	0.57(9)
O2	8d	1	0.3222(7)	0.0548(4)	0.6955(6)	0.62(7)

(Tm <sub>0.667</sub> Mn <sub>0.333</sub> )MnO <sub>3</sub>						
Tm	4c	2/3	0.06698(12)	0.25	0.98919(13)	0.542(7)
Mn1	4c	1/3	0.0909(9)	0.25	0.9534(8)	= <i>B</i> (Tm)
Mn2	4b	1	0	0	0.5	0.699(13)
O1	4c	1	0.4695(6)	0.25	0.1077(6)	0.82(7)
O2	8d	1	0.3198(5)	0.0518(3)	0.6929(5)	1.04(6)

<sup>a</sup> Crystal data: Space group *Pnma* (No. 62); *Z* = 4. *a* = 5.50348(2) Å, *b* = 7.37564(1) Å, *c* = 5.18686(1) Å, *V* = 210.544(1) Å<sup>3</sup>; *R*<sub>wp</sub> = 4.74%, *R*<sub>P</sub> = 2.87%, *R*<sub>B</sub> = 5.30%, *R*<sub>F</sub> = 3.08%, and  $\rho_{\text{cal}} = 7.505 \text{ g cm}^{-3}$  for (Lu<sub>0.667</sub>Mn<sub>0.333</sub>)MnO<sub>3</sub>. *a* = 5.50811(3) Å, *b* = 7.37534(1) Å, *c* = 5.20430(1) Å, *V* = 211.420(1) Å<sup>3</sup>; *R*<sub>wp</sub> = 5.47%, *R*<sub>P</sub> = 3.27%, *R*<sub>B</sub> = 4.82%, *R*<sub>F</sub> = 2.51%, and  $\rho_{\text{cal}} = 7.434 \text{ g cm}^{-3}$  for (Yb<sub>0.667</sub>Mn<sub>0.333</sub>)MnO<sub>3</sub>. *a* = 5.51410(1) Å, *b* = 7.39113(1) Å, *c* = 5.21583(1) Å, *V* = 212.574(1) Å<sup>3</sup>; *R*<sub>wp</sub> = 5.23%, *R*<sub>P</sub> = 3.48%, *R*<sub>B</sub> = 4.11%, *R*<sub>F</sub> = 2.71%, and  $\rho_{\text{cal}} = 7.308 \text{ g cm}^{-3}$  for (Tm<sub>0.667</sub>Mn<sub>0.333</sub>)MnO<sub>3</sub>. WP = Wyckoff position. *g* is the occupation factor.

**Table 5.3.** Selected bond lengths (*l* < 3.0 Å), bond angles (degree), BVSs, and distortion parameters of MnO<sub>6</sub> [ $\Delta(\text{Mn})$ ] in (Lu<sub>0.667</sub>Mn<sub>0.333</sub>)MnO<sub>3</sub>, (Yb<sub>0.667</sub>Mn<sub>0.333</sub>)MnO<sub>3</sub>, and (Tm<sub>0.667</sub>Mn<sub>0.333</sub>)MnO<sub>3</sub><sup>a</sup>.

	(Lu <sub>0.667</sub> Mn <sub>0.333</sub> )MnO <sub>3</sub>	(Yb <sub>0.667</sub> Mn <sub>0.333</sub> )MnO <sub>3</sub>	(Tm <sub>0.667</sub> Mn <sub>0.333</sub> )MnO <sub>3</sub>
R-O1	2.144(4)	2.169(4)	2.170(3)
R-O2 (×2)	2.186(3)	2.195(3)	2.215(3)
R-O1	2.216(5)	2.251(5)	2.304(4)
R-O2 (×2)	2.512(3)	2.518(3)	2.545(3)
R-O2 (×2)	2.563(3)	2.567(3)	2.549(3)
BVS (R <sup>3+</sup> )	3.13	3.12	3.10
Mn1-O1	2.237(8)	2.206(8)	2.238(6)
Mn1-O2 (×2)	2.142(6)	2.196(6)	2.227(4)
Mn1-O1	2.389(6)	2.374(9)	2.385(5)
Mn1-O2 (×2)	2.336(6)	2.350(6)	2.363(4)
Mn1-O2 (×2)	2.654(4)	2.625(4)	2.604(3)
BVS (Mn1 <sup>2+</sup> )	1.92	1.85	1.76
Mn2-O1 (×2)	1.959(1)	1.946(1)	1.939(1)

Mn2-O2 ( $\times 2$ )	1.922(3)	1.906(3)	1.923(3)
Mn2-O2 ( $\times 2$ )	2.074(3)	2.085(4)	2.066(3)
BVS ( $\text{Mn}^{2+}$ )	3.32	3.39	3.39
$\Delta(\text{Mn}2)$	$10.6 \times 10^{-4}$	$15.0 \times 10^{-4}$	$10.5 \times 10^{-4}$
Mn2-O1-Mn2 ( $\times 2$ )	140.6(1)	142.7(1)	144.8(1)
Mn2-O2-Mn2 ( $\times 2$ )	142.3(1)	143.3(1)	144.0(1)

<sup>a</sup> BVS =  $\sum_{i=1}^N v_i$ ,  $v_i = \exp[(R_0 - l_i)/B]$ ,  $N$  is the coordination number,  $B = 0.37$ ,  $R_0(\text{Lu}^{3+}) = 1.971$ ,  $R_0(\text{Yb}^{3+}) = 1.985$ ,  $R_0(\text{Tm}^{3+}) = 2.000$ ,  $R_0(\text{Mn}^{2+}) = 1.79$ , and  $R_0(\text{Mn}^{3+}) = 1.76$  [24].  $\Delta = (1/N)\sum_{i=1}^N [(l_i - l_{\text{av}})/l_{\text{av}}]^2$ , where  $l_{\text{av}} = (1/N)\sum_{i=1}^N l_i$  is the average Mn-O distance and  $N$  is the coordination number.

A partial charge disproportionation takes place during the synthesis from  $\text{R}_2\text{O}_3$  and  $\text{Mn}_2\text{O}_3$  in a closed environment of sealed capsules. A part of Mn that enters the A site is reduced to  $\text{Mn}^{2+}$ , and the same fraction is oxidized to  $\text{Mn}^{4+}$  (which is located at the B site).  $(\text{R}_{0.667}\text{Mn}_{0.333})\text{MnO}_3$  ( $R = \text{Tm}, \text{Yb}, \text{and Lu}$ ) and  $(\text{Er}_{1-x}\text{Mn}_x)\text{MnO}_3$  have  $Pnma$  symmetry in comparison with  $(\text{In}_{0.667}\text{Mn}_{0.333})\text{MnO}_3$ , where  $P2_1/n$  symmetry was observed due to ordering of Mn in different oxidation states at the B site while  $\text{In}^{3+}$  and  $\text{Mn}^{2+}$  cations are randomly distributed on one A site:  $[\text{In}^{3+}_{4/3}\text{Mn}^{2+}_{2/3}]_{\text{A}}[\text{Mn}^{3+}]_{\text{B1}}[\text{Mn}^{3.667+}]_{\text{B2}}\text{O}_6$  [26].  $Pnma$  symmetry has only one site for B-type cations, and this fact suggests random distribution of  $\text{Mn}^{3+}$  and  $\text{Mn}^{4+}$  at the B site of  $(\text{R}_{0.667}\text{Mn}_{0.333})\text{MnO}_3$ . The original idea to keep the oxidation state of +3 for manganese at all sites (especially at the B site) and to increase the degree of distortions of  $\text{RMnO}_3$  did not work. Aliovalent doping takes place at the A site in  $(\text{R}_{1-x}\text{Mn}_x)\text{MnO}_3$ . From this point of view,  $(\text{R}_{1-x}\text{Mn}_x)\text{MnO}_3$  compounds resemble  $(\text{R}_{1-x}\text{Ca}_x)\text{MnO}_3$  and  $(\text{R}_{1-x}\text{Sr}_x)\text{MnO}_3$  compounds [25,27,28]. However, the presence of a significant amount of magnetic  $\text{Mn}^{2+}$  cations at the A site produces differences in magnetic properties (see section 5.3.2). Moreover, magnetic  $\text{Mn}^{2+}$  cations could trigger magnetic ordering of the rare-earth cations.

Mn self-doping has recently been explored in cases of  $\text{TbMnO}_3$  and  $\text{EuMnO}_3$  by the ambient pressure synthesis [29-32]. However, the ambient-pressure synthesis can produce a

very limited range of solid solutions  $(R_{1-x}Mn_x)MnO_3$  up to about  $x \approx 0.126$  [32], and there is a problem with controlling and determination of the oxygen content in final products  $(R_{1-x}Mn_x)MnO_{3+\delta}$ . The HP, HT synthesis method can significantly increase the range of solid solutions up to  $x \approx 0.333$  ( $R = \text{Er-Lu}$ ) and allows control of the oxygen content during the synthesis. It was suggested from XPS results that all Mn cations have the oxidation state of +3 in  $(Eu_{1-x}Mn_x)MnO_3$  [32]. The failure to detect Mn cations in other oxidation states could be caused by small concentrations of  $Mn^{2+}$  and  $Mn^{4+}$ .

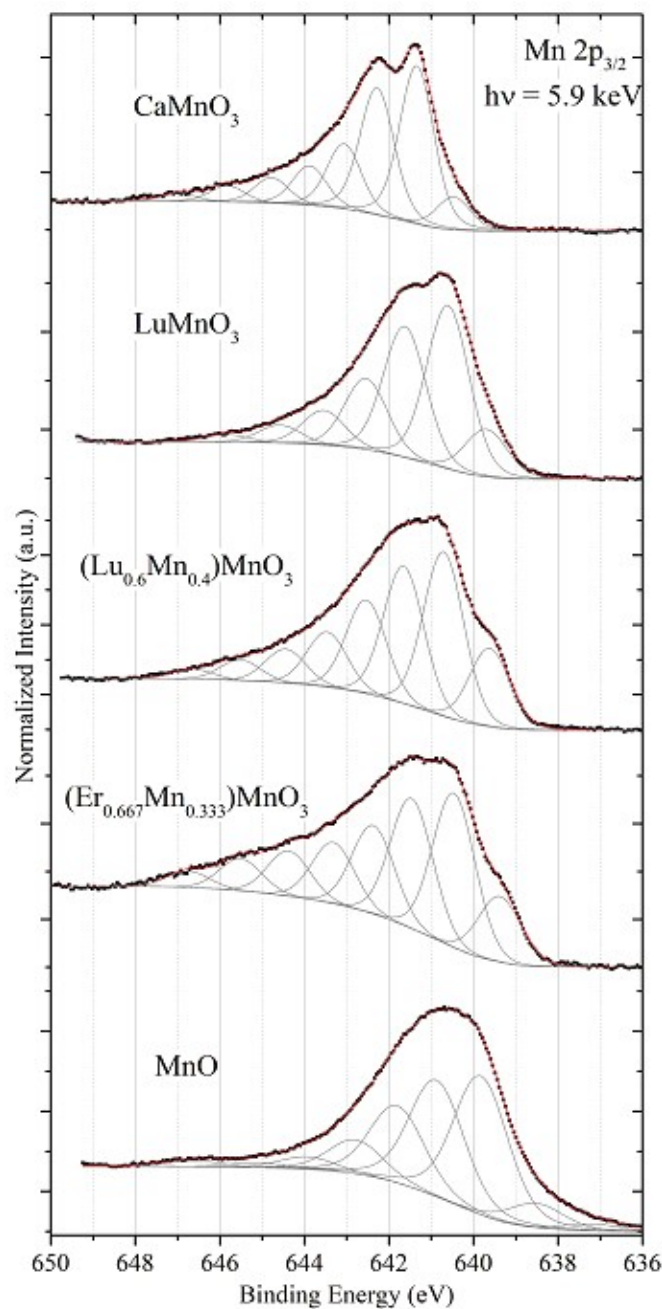


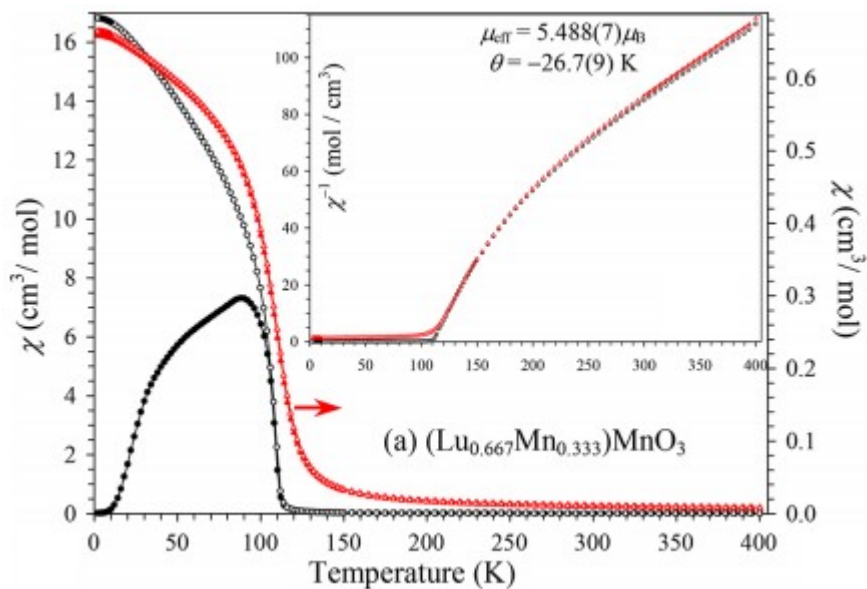
**Figure 5.3.** Mn  $2p_{3/2}$  HAXPES spectra of  $\text{CaMnO}_3$ ,  $\text{LuMnO}_3$ ,  $(\text{Lu}_{0.6}\text{Mn}_{0.4})\text{MnO}_3$ ,  $(\text{Er}_{0.667}\text{Mn}_{0.333})\text{MnO}_3$ , and  $\text{MnO}$  measured at 5.9 keV excitation energy. Shown are data (dots), fits (red line), and the individual Voigt components added to the Shirley background (gray lines). Spectra were normalized to the maximum energy calibrated to adventitious C 1s. I note a slight broadening of the spectrum for  $\text{MnO}$  due to charging.

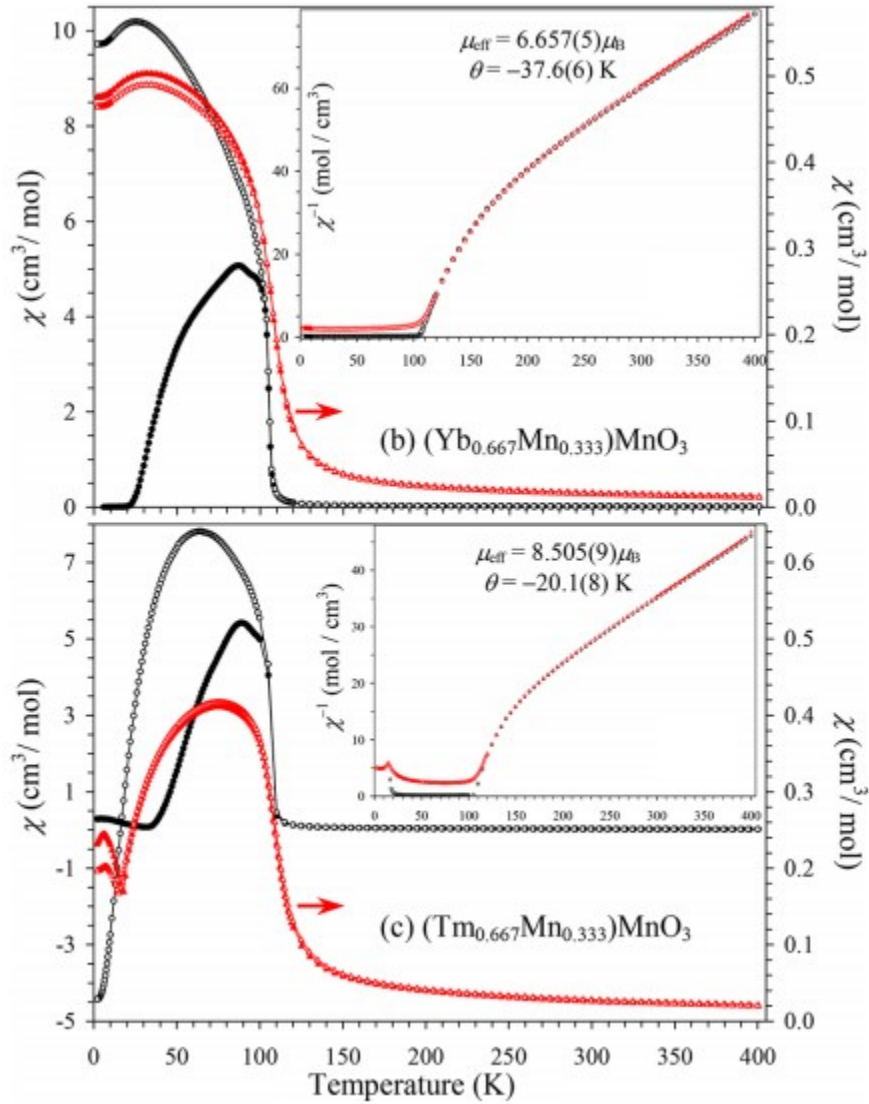
**Figure 5.3** shows the Mn  $2p_{3/2}$  HAXPES spectra of  $(\text{Lu}_{0.6}\text{Mn}_{0.4})\text{MnO}_3$  and  $(\text{Er}_{0.667}\text{Mn}_{0.333})\text{MnO}_3$  samples compared with the  $\text{MnO}$ ,  $\text{LuMnO}_3$ , and  $\text{CaMnO}_3$  references. Note that  $(\text{Lu}_{0.6}\text{Mn}_{0.4})\text{MnO}_3$  is used and shown here just as an additional supporting example; it was selected for the HAXPES studies because it should have the maximum amounts of  $\text{Mn}^{2+}$  and  $\text{Mn}^{4+}$  and because a pellet of  $(\text{Lu}_{0.6}\text{Mn}_{0.4})\text{MnO}_3$  was harder than that of  $(\text{Lu}_{0.667}\text{Mn}_{0.333})\text{MnO}_3$ . A comparison to previously reported XPS spectra of manganese (hydr)oxides gives us information on the Mn oxidization states [33]. The observed HAXPES spectra were fit with a Shirley background and multiple Voigt profiles with locked Gaussian and Lorentzian widths for simplicity. The spectra of  $(\text{Lu}_{0.6}\text{Mn}_{0.4})\text{MnO}_3$  and  $(\text{Er}_{0.667}\text{Mn}_{0.333})\text{MnO}_3$  show a more pronounced low-energy shoulder at 639.5 eV, a more intense tail towards higher binding energies and a broader double peak around 641 eV, in comparison with that of  $\text{LuMnO}_3$ . The low-energy shoulder and the broadening of the doublet peak suggest the presence of  $\text{Mn}^{2+}$  species because of the resemblance to the features found in the  $\text{MnO}$  spectrum. The high-energy tail might be due to an additional contribution of  $\text{Mn}^{4+}$  or multiplet interactions of the photoelectron final states.

### 5.3.2 Magnetic Properties of $(\text{R}_{0.667}\text{Mn}_{0.333})\text{MnO}_3$ and $(\text{Er}_{1-x}\text{Mn}_x)\text{MnO}_3$

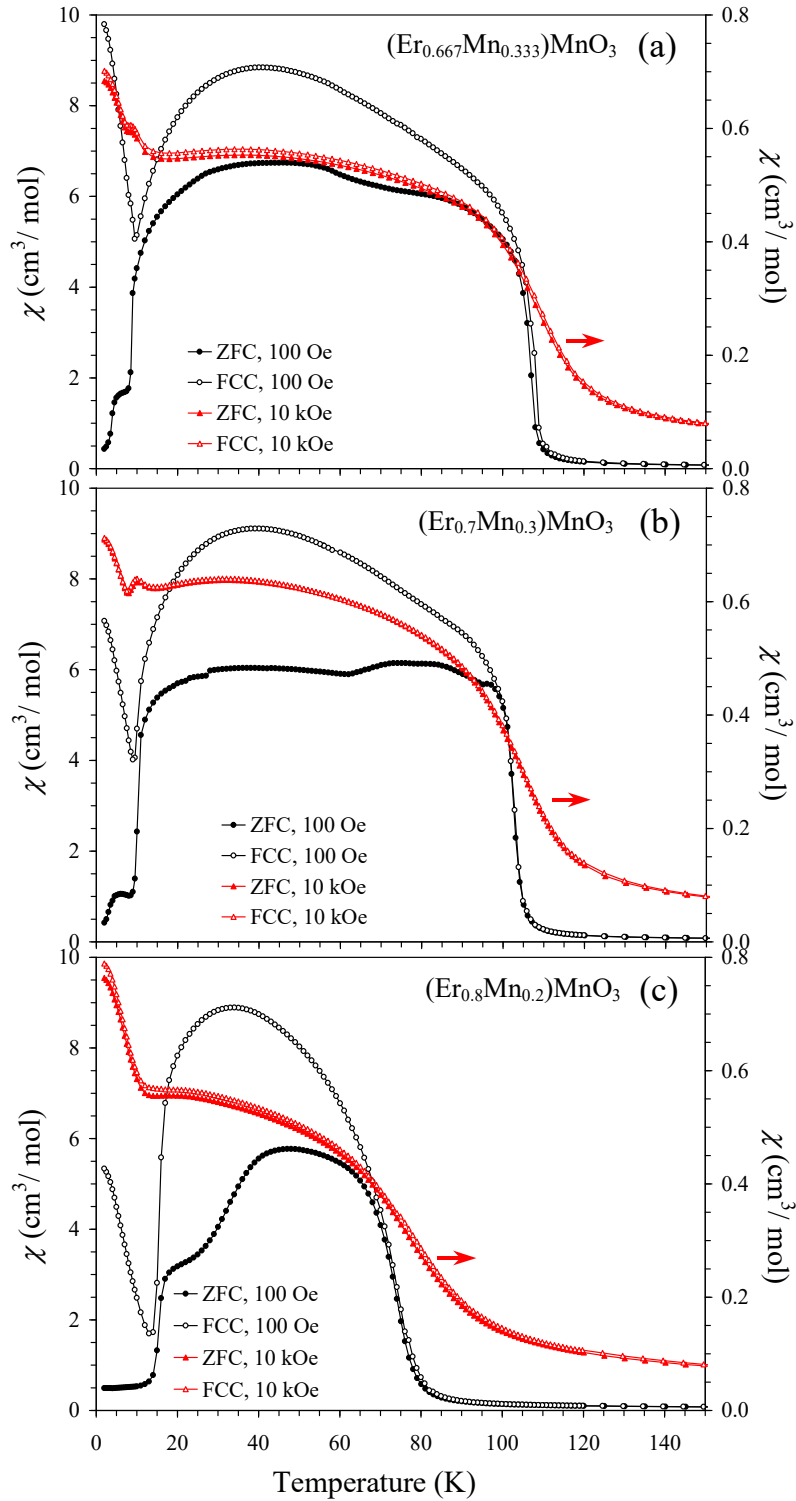
**Figures 5.4** and **Figure 5.5** show dc  $\chi$  vs  $T$  magnetic susceptibilities of  $(\text{R}_{0.667}\text{Mn}_{0.333})\text{MnO}_3$  ( $R = \text{Tm}, \text{Yb}, \text{and Lu}$ ) and  $(\text{Er}_{1-x}\text{Mn}_x)\text{MnO}_3$  with  $x = 0.333, 0.3, \text{ and } 0.2$ .  $(\text{R}_{0.667}\text{Mn}_{0.333})\text{MnO}_3$  compounds show the first magnetic transition  $T_{N1}$  at almost the same temperature of about 105-110 K (**Table 5.4**). The temperature dependence of magnetic

susceptibilities at low magnetic fields (e.g., 100 Oe) is typical for canted antiferromagnets or ferrimagnets with the characteristic divergence of the ZFC and FCC curves at  $T_{N1}$ . In **Figure 5.6**, Isothermal magnetization curves ( $M$  vs  $H$ ) of  $(\text{Lu}_{0.667}\text{Mn}_{0.333})\text{MnO}_3$  without magnetic  $R^{3+}$  cations show a saturation behavior with  $M_S = 1.91 \mu_B/\text{f.u.}$  at 5 K and 70 kOe that is typical for ferrimagnets. Samples containing magnetic  $R^{3+}$  cations demonstrate  $M$  vs  $H$  curves that are more typical for canted antiferromagnets with hysteresis near the origin and an almost linear increase of magnetization at higher magnetic fields. However, the linear increase could also be caused by contributions from magnetic  $R^{3+}$  cations. Neutron diffraction experiments are needed to determine magnetic structures of these compounds.  $M$  vs  $H$  curves of  $(\text{Tm}_{0.667}\text{Mn}_{0.333})\text{MnO}_3$  at 5 K demonstrate an upturn from about 60 kOe, suggesting a field-induced transition. On the other hand,  $M$  vs  $H$  curves of  $(\text{Er}_{1-x}\text{Mn}_x)\text{MnO}_3$  at 5 K exhibit a downturn from about 60 kOe, suggesting a saturation or plateau-like behavior at higher magnetic fields.

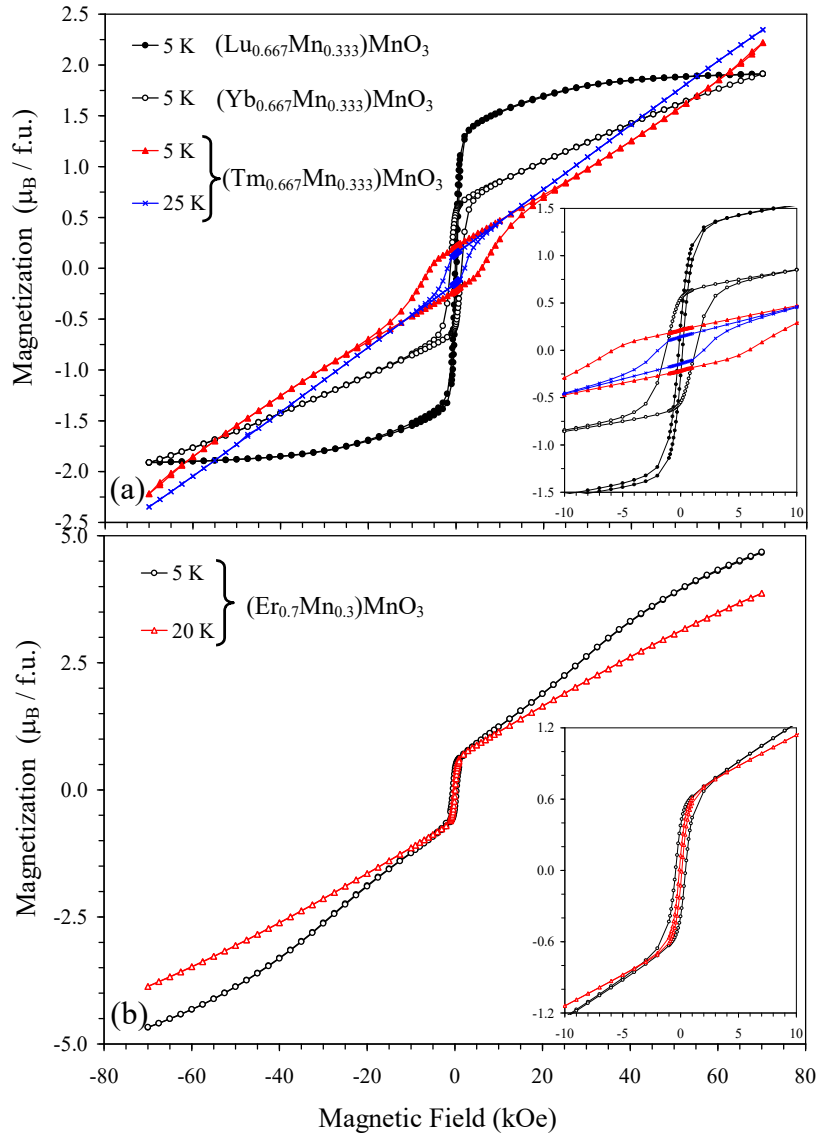




**Figure 5.4.** ZFC (filled symbols) and FCC (empty symbols) dc magnetic susceptibility ( $\chi = M/H$ ) curves of (a)  $(\text{Lu}_{0.667}\text{Mn}_{0.333})\text{MnO}_3$ , (b)  $(\text{Yb}_{0.667}\text{Mn}_{0.333})\text{MnO}_3$ , and (c)  $(\text{Tm}_{0.667}\text{Mn}_{0.333})\text{MnO}_3$ . Left-hand axes give the  $\chi$  vs  $T$  curves (black) at 100 Oe; right-hand axes give the  $\chi$  vs  $T$  curves (red) at 10 kOe. The insets show the FCC  $\chi^{-1}$  vs  $T$  curves at 100 Oe and 10 kOe with the Curie-Weiss fits (for the 10 kOe data).



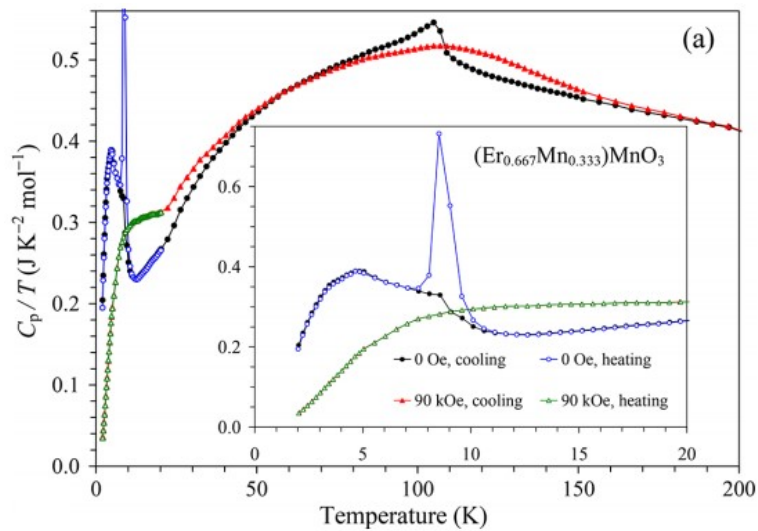
**Figure 5.5.** ZFC (filled symbols) and FCC (empty symbols) dc magnetic susceptibility ( $\chi = M/H$ ) curves of (a)  $(\text{Er}_{0.667}\text{Mn}_{0.333})\text{MnO}_3$ , (b)  $(\text{Er}_{0.7}\text{Mn}_{0.3})\text{MnO}_3$ , and (c)  $(\text{Er}_{0.8}\text{Mn}_{0.2})\text{MnO}_3$ . Left-hand axes give the  $\chi$  vs  $T$  curves (black) at 100 Oe; right-hand axes give the  $\chi$  vs  $T$  curves (red) at 10 kOe.



**Figure 5.6.** (a)  $M$  vs  $H$  curves of  $(\text{Lu}_{0.667}\text{Mn}_{0.333})\text{MnO}_3$  ( $T = 5$  K),  $(\text{Yb}_{0.667}\text{Mn}_{0.333})\text{MnO}_3$  ( $T = 5$  K), and  $(\text{Tm}_{0.667}\text{Mn}_{0.333})\text{MnO}_3$  ( $T = 5$  K and 25 K). (b)  $M$  vs  $H$  curves of  $(\text{Er}_{0.7}\text{Mn}_{0.3})\text{MnO}_3$  at  $T = 5$  K and 20 K. The insets show details near the origin.

$(\text{Er}_{1-x}\text{Mn}_x)\text{MnO}_3$  with  $x = 0.333, 0.3,$  and  $0.2$  shows additional sharp anomalies on the  $\chi$  vs  $T$  curves near  $T_{N2} = 9\text{-}16$  K suggesting the second magnetic transition, as shown in **Figure 5.5**. In **Figure 5.7**, specific heat measurements confirmed the existence of a transition at  $T_{N2}$  with very sharp anomalies. A very large difference between the cooling and heating curves was observed on specific heat at  $T_{N2}$ ; this fact shows that the transition is first order. [The

suppression of anomalies on cooling curves is actually an artifact of the pulse relaxation method, used to measure specific heat, because this method cannot sometimes give correct values for first-order transitions]. Below about 12 K, the  $C_p/T$  values increase with a broad peak near 5 K; these features could originate from Schottky-like or short-range contributions from  $\text{Er}^{3+}$  cations. A high magnetic field smeared specific heat anomalies near  $T_{N1}$  and suppressed anomalies near  $T_{N2}$  and contributions from  $\text{Er}^{3+}$  cations (shown in **Figure 5.7**). Neutron diffraction data are needed to understand the nature of the phase transition at  $T_{N2}$  in  $(\text{Er}_{1-x}\text{Mn}_x)\text{MnO}_3$ . I note that  $\text{ErMnO}_3$  shows two magnetic transitions at 28 K and 42 K originating from the Mn ordering [34], and these transitions are obviously different from the transitions at  $T_{N1}$  and  $T_{N2}$  in  $(\text{Er}_{1-x}\text{Mn}_x)\text{MnO}_3$  [for example, because no ferroelectricity appears at  $T_{N2}$  in  $(\text{Er}_{1-x}\text{Mn}_x)\text{MnO}_3$  (see below) in comparison with  $\text{ErMnO}_3$ ]. The upturn on the  $C_p/T$  vs  $T$  curves below 10 K with a maximum at 3 K was also observed in  $\text{ErMnO}_3$  originating from  $\text{Er}^{3+}$  contributions [3].



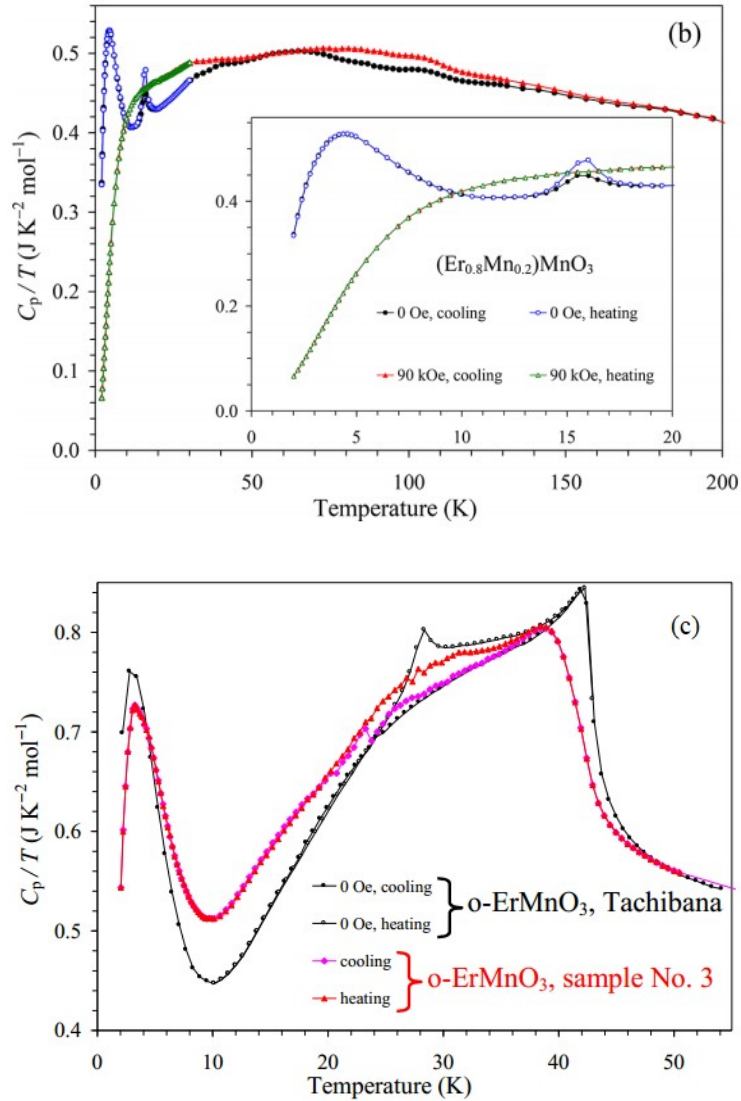


**Figure 5.7.** Specific heat data of (a)  $(Er_{0.667}Mn_{0.333})MnO_3$  and (b)  $(Er_{0.8}Mn_{0.2})MnO_3$  at a zero magnetic field (circles) and 90 kOe (triangles) plotted as  $C_p/T$  vs  $T$ . Measurements were performed upon cooling (filled symbols) and heating (empty symbols). The insets show details below 20 K. (c) Specific heat data of  $o-ErMnO_3$  at a zero magnetic field on cooling and heating plotted as  $C_p/T$  vs  $T$ . It shows the data for our sample [ $o-ErMnO_3$  (sample No.3)] and the one provided by Dr. M. Tachibana of NIMS (Japan) [3].

**Figure 5.8** shows the  $C_p/T$  vs  $T$  curves for  $(Lu_{0.667}Mn_{0.333})MnO_3$  and  $(Tm_{0.667}Mn_{0.333})MnO_3$  at 0 and 90 kOe. A broad additional anomaly was found in  $(Tm_{0.667}Mn_{0.333})MnO_3$  below about 20 K; a high magnetic field made the anomaly sharper with the maximum at about 9.5

K. No additional low-temperature anomalies (except for those at  $T_{N1}$ ) were found in  $(\text{Lu}_{0.667}\text{Mn}_{0.333})\text{MnO}_3$ . A high magnetic field smeared specific heat anomalies near  $T_{N1}$ . The  $C_p/T$  values were almost the same above about 115 K, while they were different below  $T_{N1}$ . This difference could be explained by contributions from  $\text{Tm}^{3+}$ . The contribution starts just below  $T_{N1}$ , indicating that  $\text{Tm}^{3+}$  could be (partially) involved in magnetic ordering already at this temperature. The similar behavior is observed in  $(\text{Er}_{0.667}\text{Mn}_{0.333})\text{MnO}_3$ , as shown in **Figure 5.8**. I note that the specific heat of  $(\text{Yb}_{0.667}\text{Mn}_{0.333})\text{MnO}_3$  is not reported because a pellet was too fragile to perform measurements.

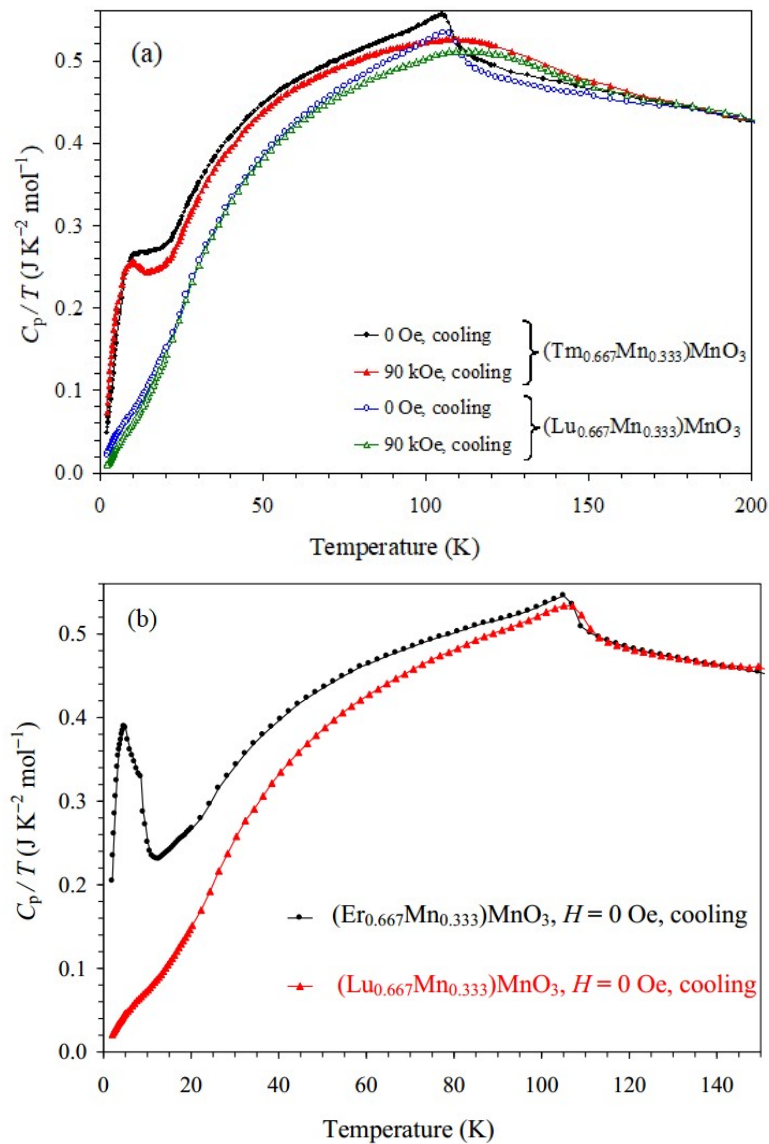


**Figure 5.8.** (a) Specific heat data of  $(\text{Lu}_{0.667}\text{Mn}_{0.333})\text{MnO}_3$  (empty symbols) and

(Tm<sub>0.667</sub>Mn<sub>0.333</sub>)MnO<sub>3</sub> (filled symbols) at a zero magnetic field and 90 kOe plotted as  $C_p/T$  vs  $T$ . (b) Specific heat data of (Er<sub>0.667</sub>Mn<sub>0.333</sub>)MnO<sub>3</sub> (black) and (Lu<sub>0.667</sub>Mn<sub>0.333</sub>)MnO<sub>3</sub> (red) at a zero magnetic field plotted as  $C_p/T$  vs  $T$ . Measurements were performed on cooling.

The inverse magnetic susceptibilities follow the Curie-Weiss law but only at high temperatures. Below about 200-250 K, which is much higher than  $T_{N1}$ , significant deviations from the Curie-Weiss behavior are observed (insets of **Figure 5.4** and **Figure 5.9**). This deviation is also observed in (Lu<sub>0.667</sub>Mn<sub>0.333</sub>)MnO<sub>3</sub> without magnetic R<sup>3+</sup> cations. This fact indicates that the deviation should originate from short-range magnetic interactions among Mn cations involving Mn<sup>2+</sup> at the A site. The same features were found in RMn<sub>3</sub>O<sub>6</sub>, which also has Mn (in different oxidization states) at the A site [16]. These features of  $\chi^{-1}$  vs  $T$  curves are also typical in ferrimagnets. Between 300 and 395 K, the inverse magnetic susceptibilities (measured at 10 kOe in the FCC mode) are fit by the Curie-Weiss equation

$$\chi(T) = \mu_{\text{eff}}^2 N [3k_B(T - \theta)]^{-1}$$

where  $\mu_{\text{eff}}$  is an effective magnetic moment,  $N$  is Avogadro's number,  $k_B$  is Boltzmann's constant, and  $\theta$  is the Curie-Weiss temperature. The fitting parameters are summarized in **Table 5.4**. The  $\mu_{\text{eff}}$  values are in good agreement with the theoretical values. The negative Curie-Weiss temperatures show that the strongest exchange interactions are antiferromagnetic in nature.

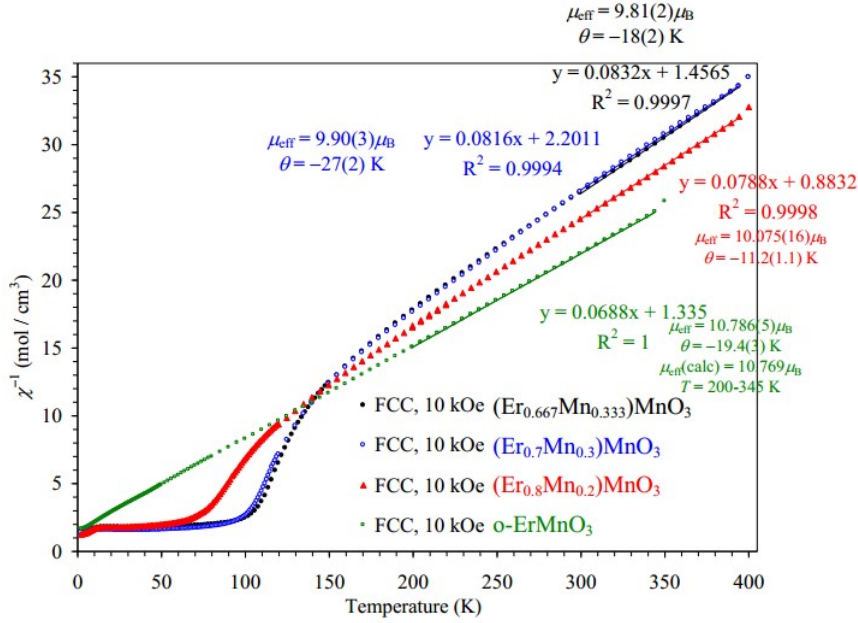


**Figure 5.9.** The field-cooled-on-cooling (FCC)  $\chi^{-1}$  vs  $T$  curves at 10 kOe with the Curie-Weiss fits (between 300 and 395 K) for  $(\text{Er}_{0.667}\text{Mn}_{0.333})\text{MnO}_3$ ,  $(\text{Er}_{0.7}\text{Mn}_{0.3})\text{MnO}_3$ , and  $(\text{Er}_{0.8}\text{Mn}_{0.2})\text{MnO}_3$ . The Curie-Weiss fit between 200 and 345 K for o- $\text{ErMnO}_3$  is shown for comparison.

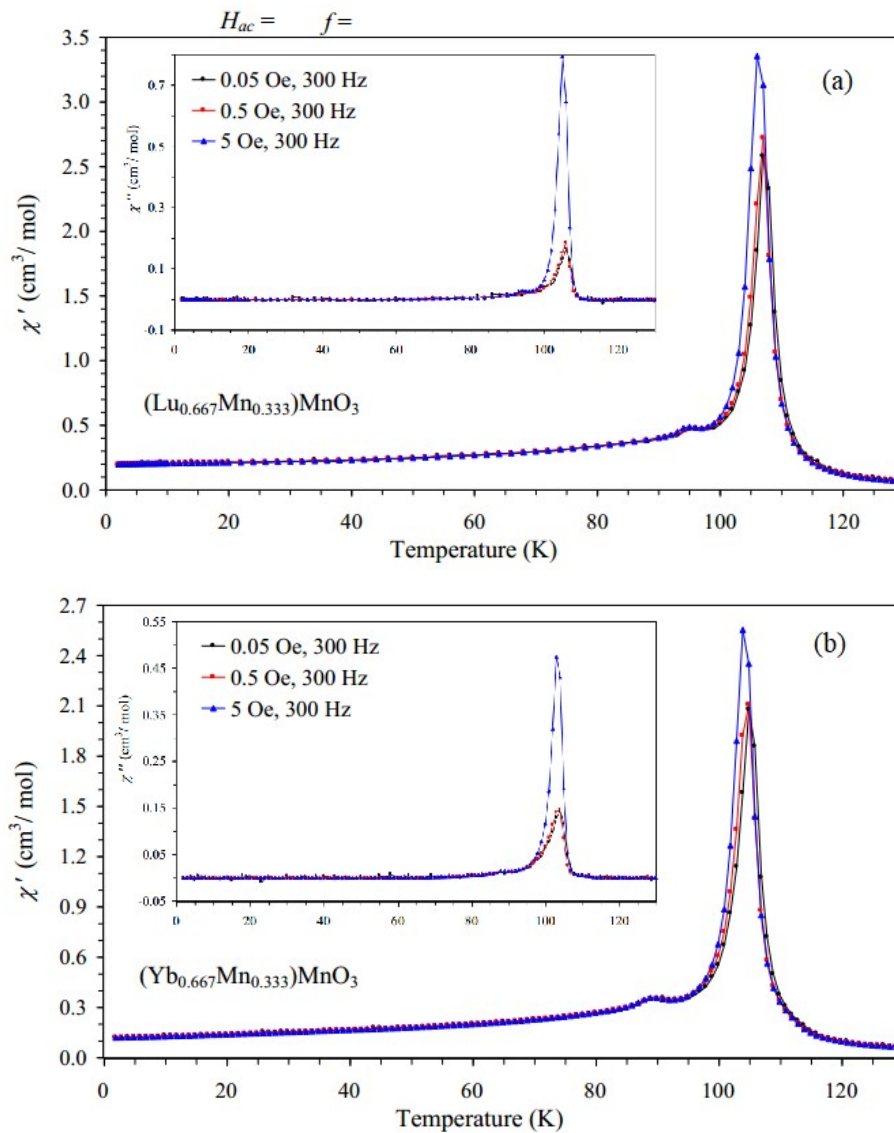
**Table 5.4.** Temperatures of magnetic anomalies and parameters of the Curie-Weiss fits of  $(\text{R}_{0.667}\text{Mn}_{0.333})\text{MnO}_3$  and  $(\text{Er}_{1-x}\text{Mn}_x)\text{MnO}_3^{\text{a}}$ .

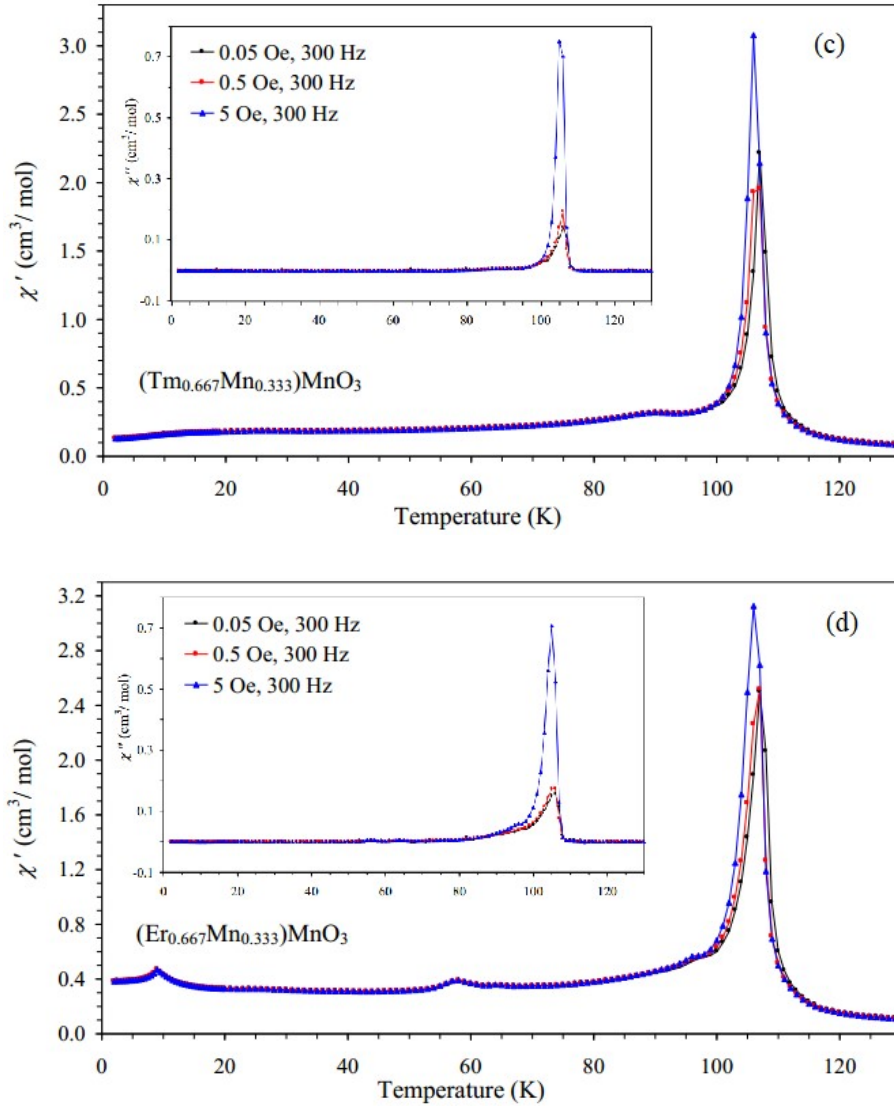
composition	$T_{\text{N}}$ (K)	$\mu_{\text{eff}}$ ( $\mu_{\text{B}}/\text{f.u.}$ )	$\mu_{\text{calc}}$ ( $\mu_{\text{B}}/\text{f.u.}$ )	$\theta$ (K)	$M_{\text{S}}$ ( $\mu_{\text{B}}/\text{f.u.}$ )
$\text{Lu}_{0.667}\text{Mn}_{0.333}$	110	5.488(7)	5.517	-26.7(9)	1.91
$\text{Yb}_{0.667}\text{Mn}_{0.333}$	106	6.667(5)	6.812	-37.6(6)	1.91
$\text{Tm}_{0.667}\text{Mn}_{0.333}$	15, 110	8.505(9)	8.419	-20.1(8)	2.22
$\text{Er}_{0.667}\text{Mn}_{0.333}$	9.5, 109	9.81(2)	9.695	-18(2)	4.36
$\text{Er}_{0.7}\text{Mn}_{0.3}$	10, 104	9.90(3)	9.807	-27(2)	4.68
$\text{Er}_{0.8}\text{Mn}_{0.2}$	16, 75	10.075(16)	10.138	-11.2(1.1)	4.93
ErMn	28, 42	10.786(5)	10.769	-19.4(3)	4.67

<sup>a</sup> The Curie-Weiss fits are performed between 300 and 395 K for the FCC data at 10 kOe (between 200 and 345 K for  $\text{ErMnO}_3$ ).  $M_{\text{S}}$  is the magnetization value at 5 K and 70 kOe.

The  $\chi'$  vs  $T$  and  $\chi''$  vs  $T$  ac susceptibility curves exhibit sharp peaks near  $T_{\text{N}1}$ , which are almost frequency-independent, but they depend on  $H_{\text{ac}}$  (**Figure 5.10**). This  $H_{\text{ac}}$  field

dependence is typical for ferromagnets, ferrimagnets, and canted antiferromagnets and caused by an interaction of the magnetic field with domain structures. All  $(R_{0.667}Mn_{0.333})MnO_3$  with  $R = Er, Tm, Yb,$  and  $Lu$  show some weak and broad additional anomalies near 90-95 K on both  $\chi'$  vs  $T$  and  $\chi''$  vs  $T$  curves.  $(Er_{0.667}Mn_{0.333})MnO_3$  has sharp anomalies on the  $\chi'$  vs  $T$  curves at  $T_{N2} = 9$  K (frequency and  $H_{ac}$  field independent) and no anomalies on the  $\chi''$  vs  $T$  curves. These features are typical for purely antiferromagnetic transitions. No hysteresis was found near 9 K in  $(Er_{0.667}Mn_{0.333})MnO_3$  on the ac susceptibility curves on heating and cooling in comparison with specific heat data.

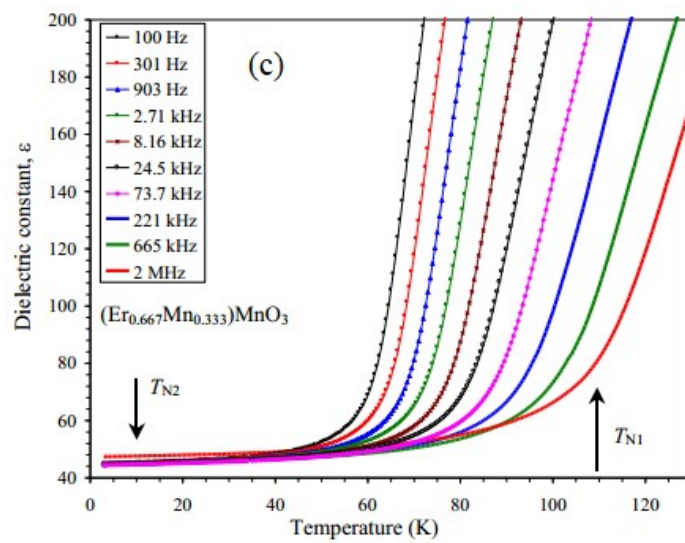
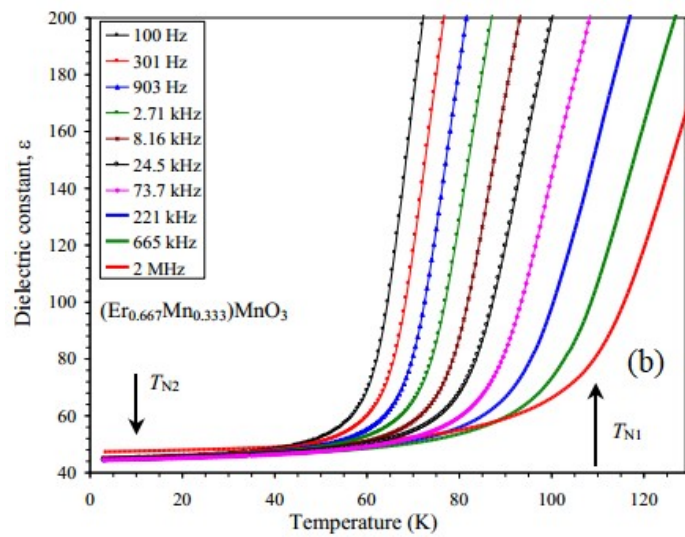
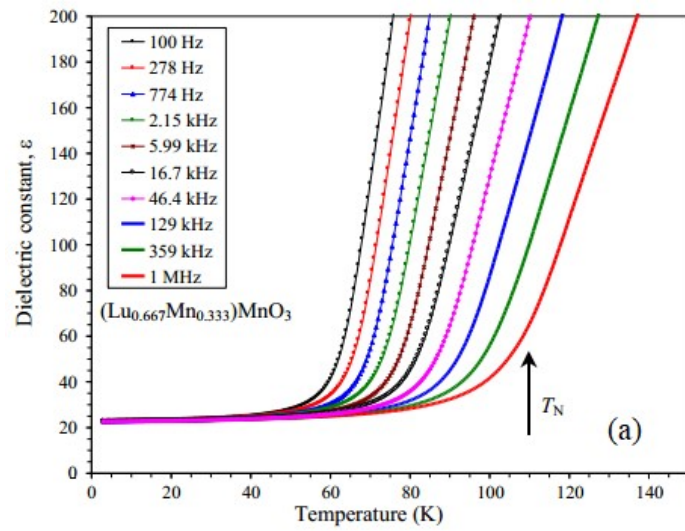


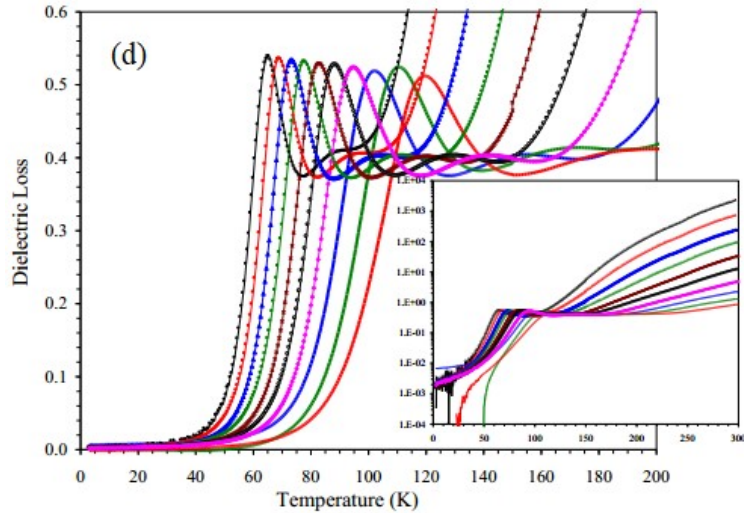


**Figure 5.10.** Real parts ( $\chi'$  vs  $T$ ) of the ac susceptibilities of  $(Lu_{0.667}Mn_{0.333})MnO_3$  (a),  $(Yb_{0.667}Mn_{0.333})MnO_3$  (b),  $(Tm_{0.667}Mn_{0.333})MnO_3$  (c), and  $(Er_{0.667}Mn_{0.333})MnO_3$  (d). The insets show the imaginary parts ( $\chi''$  vs  $T$ ) of the ac susceptibilities. Measurements were performed on cooling from 130 K to 2 K at a zero static magnetic field using ac fields with the amplitudes of  $H_{ac} = 0.05, 0.5,$  and 5 Oe and one frequency of  $f = 300$  Hz.

No dielectric anomalies are observed at the magnetic transition temperatures in  $(Lu_{0.667}Mn_{0.333})MnO_3$  (with one Néel temperature,  $T_{N1}$ ) and  $(Er_{0.667}Mn_{0.333})MnO_3$  (with two Néel temperatures,  $T_{N1}$  and  $T_{N2}$ ), and the magnetodielectric effect is negligible (**Figure 5.11**). These facts show that  $(R_{0.667}Mn_{0.333})MnO_3$  compounds are not (spin-driven) multiferroics in

comparison with the parent  $\text{RMnO}_3$  compounds [1-6].

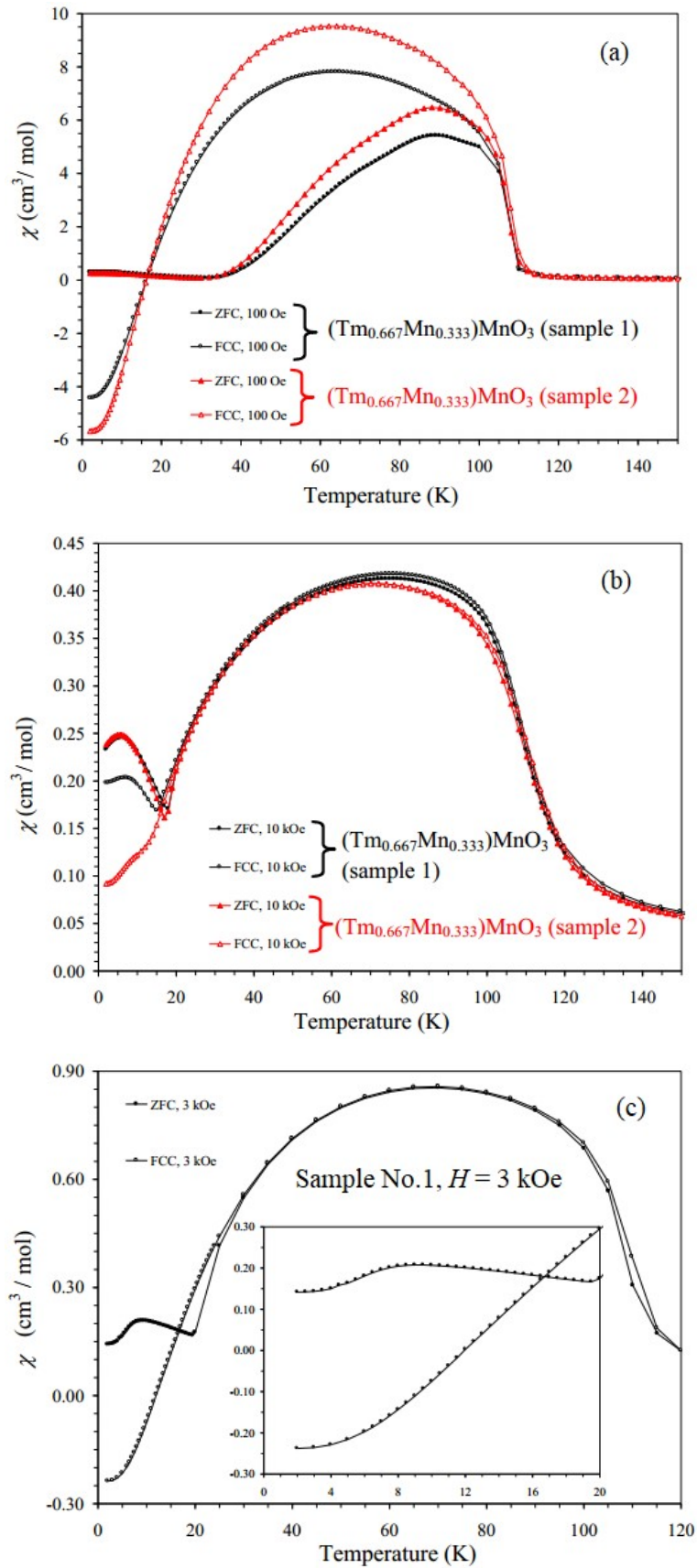




**Figure 5.11.** Temperature dependence of dielectric constant and loss tangent of  $(\text{Lu}_{0.667}\text{Mn}_{0.333})\text{MnO}_3$  (a, b) and  $(\text{Er}_{0.667}\text{Mn}_{0.333})\text{MnO}_3$  (c, d) at different frequencies measured on cooling at a zero magnetic field.

In this last paragraph, dc magnetic properties of  $(\text{Tm}_{0.667}\text{Mn}_{0.333})\text{MnO}_3$  were discussed in detail (**Figure 5.4c**). In comparison with  $(\text{Lu}_{0.667}\text{Mn}_{0.333})\text{MnO}_3$  with nonmagnetic R cations, the FCC curves (at both 0.1 and 10 kOe) pass through broad maxima near 60-70 K and decrease below these temperatures. At 100 Oe, this decrease continues to the lowest temperature, and the magnetic susceptibility becomes negative below about 16 K. At 10 kOe, a very sharp upturn behavior is observed below 15 K; this upturn looks like the data were reflected from a certain line parallel to the  $T$  axis. In **Figure 5.4c**, the sharp upturn was observed on both ZFC and FCC curves at 10 kOe. However, this behavior at 10 kOe was not reproducible; in some cases, the sharp upturn was observed, and in other cases, it was not observed (shown in **Figure 5.12**). I found that such behavior at 10 kOe is caused by slightly different coercive fields of different samples (shown in **Figure 5.13**). Actually, when measurements were performed at magnetic fields below coercive fields, FCC  $\chi$  vs  $T$  curves did not "feel" the transition at  $T_{N2}$ , and the curves decreased smoothly to the lowest temperatures. When measurements were performed above coercive fields, FCC  $\chi$  vs  $T$  curves demonstrated very sharp upturns near and  $T_{N2}$  looked like "reflected". All FCC curves

intersected in one point near  $T = 16.5$  K and  $\chi = 0.172$  cm<sup>3</sup> mol<sup>-1</sup>.



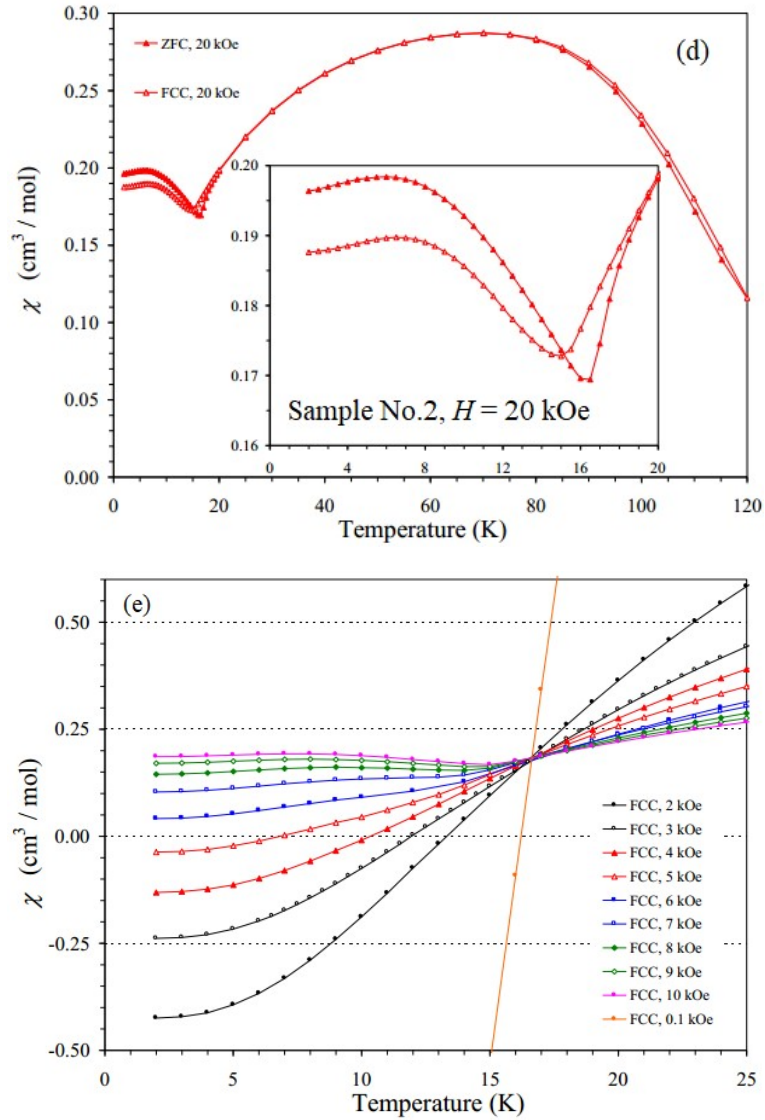


**Figure 5.12.** ZFC (filled symbols) and FCC (empty symbols) dc magnetic susceptibility ( $\chi = M/H$ ) curves of two different samples of  $(\text{Tm}_{0.667}\text{Mn}_{0.333})\text{MnO}_3$  (sample 1 and sample 2) at  $H = 100$  Oe (a) and 10 kOe (b). (c) ZFC (filled symbols) and FCC (empty symbols) dc magnetic susceptibility ( $\chi = M/H$ ) curves of  $(\text{Tm}_{0.667}\text{Mn}_{0.333})\text{MnO}_3$  (sample 1) at  $H = 3$  kOe. (d) ZFC (filled symbols) and FCC (empty symbols) dc magnetic susceptibility ( $\chi = M/H$ ) curves of  $(\text{Tm}_{0.667}\text{Mn}_{0.333})\text{MnO}_3$  (sample 2) at  $H = 20$  kOe.

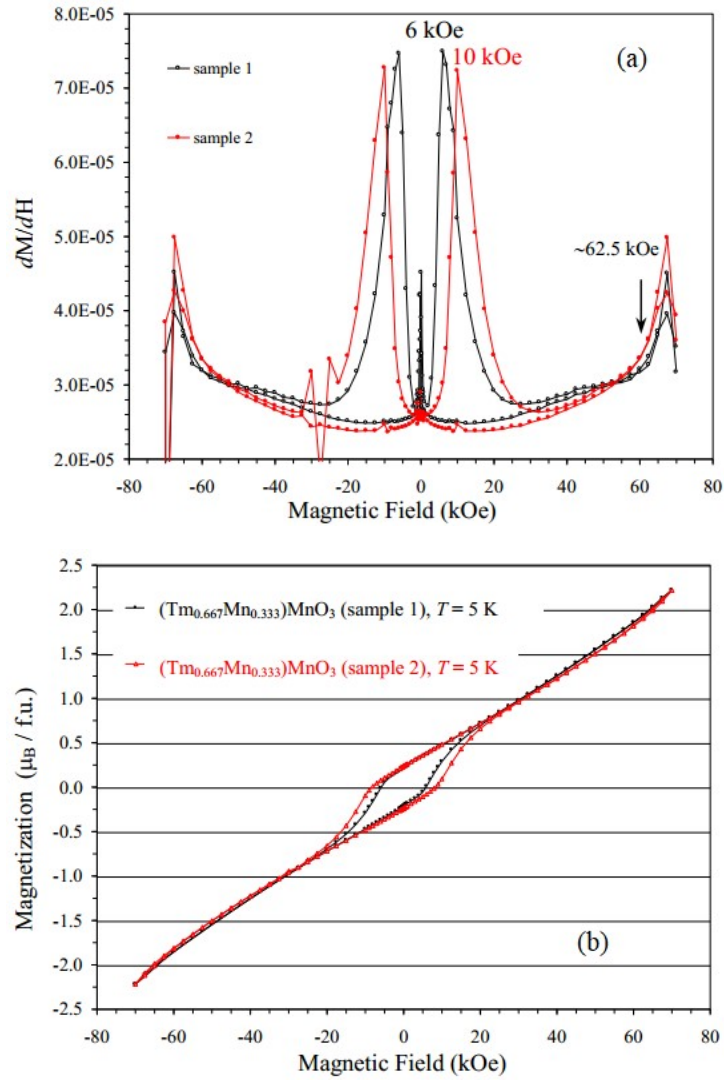


**Figure 5.13.** (a)  $dM/dH$  vs  $H$  curves and (b)  $M$  vs  $H$  curves of different samples of  $(\text{Tm}_{0.667}\text{Mn}_{0.333})\text{MnO}_3$  (sample 1 and sample 2) at  $T = 5$  K.

The FCC curves of  $(\text{Er}_{1-x}\text{Mn}_x)\text{MnO}_3$  at 100 Oe also pass through broad maxima and rather sharply decrease on decreasing temperature [especially, in  $(\text{Er}_{0.8}\text{Mn}_{0.2})\text{MnO}_3$  (**Figure 5.5c**)]. However, before reaching negative values, the magnetic susceptibility starts to increase sharply below  $T_{N2}$ . Changes of the magnetic or crystal structures (a new magnetic or structural phase) prevent the realization of negative susceptibility in  $(\text{Er}_{1-x}\text{Mn}_x)\text{MnO}_3$ . Negative magnetization (this term is widely used in the literature instead of negative susceptibility) has already been observed in a very large number of quite different materials [35].

In the case of perovskite materials, this behavior is usually explained by intrinsic ferrimagnetic or competing interactions between different sublattices (it would be  $\text{Tm}^{3+}/\text{Mn}^{2+}$  at the A site and  $\text{Mn}^{3+}/\text{Mn}^{4+}$  at the B site in our case). However, there are some results pointing toward extrinsic interfacial effects. For example, negative magnetization was observed in a two-phased  $\text{HoMn}_3\text{O}_6$  sample but not observed in single-phased  $\text{Ho}_{0.95}\text{Mn}_3\text{O}_{5.925}$  and  $\text{Ho}_{0.9}\text{Mn}_3\text{O}_{5.85}$ [16]. Negative magnetization was observed only in magnetized  $\text{BiFe}_{1-x}\text{Mn}_x\text{O}_3$  but not in fresh virgin samples [36]. Negative magnetization was observed or not observed in almost identical  $\text{YVO}_{3+\delta}$  samples [37]. To understand the behavior of  $(\text{Tm}_{0.667}\text{Mn}_{0.333})\text{MnO}_3$ , whether it is intrinsic and caused by a ferrimagnetic order or extrinsic, information about its magnetic structure is needed. **Figure 5.14** illustrates how  $M$  vs  $H$  curves measured in the FC mode behave in such cases.  $(\text{Tm}_{0.667}\text{Mn}_{0.333})\text{MnO}_3$  was cooled from 300 K to 5 K at a magnetic field of  $H$ , and measurements were performed from  $+H$  to  $-H$  and from  $-H$  to  $+H$ . At high enough magnetic fields (in this case,  $H = 50$  kOe),  $M$  vs  $H$  curves were almost symmetrical relative to the origin. However, at small fields,  $M$  vs  $H$  curves showed downshifts or the so-called positive exchange bias effect. In this case,  $M$  vs  $H$  curve shifts at 3 and 10 kOe look like minor-loop effects but on the lower part of  $M$  vs  $H$  curves.

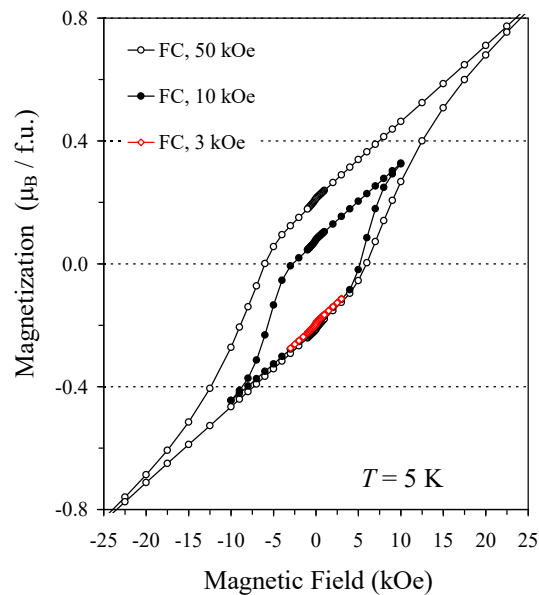


**Figure 5.14.**  $M$  vs  $H$  curves of  $(\text{Tm}_{0.667}\text{Mn}_{0.333})\text{MnO}_3$  at  $T = 5$  K measured in the field-cooled mode: a sample is cooled from 300 to 5 K at a magnetic field of  $H$ , and measurements were performed from  $+H$  to  $-H$  and from  $-H$  to  $+H$ . In this case,  $H = 50, 10, \text{ and } 3$  kOe.

## 5.4. Summary of Chapter 5

I found that solid solutions  $(R_{1-x}\text{Mn}_x)\text{MnO}_3$  exist up to  $x \approx 1/3$  on the basis of the 1:1  $\text{RMnO}_3$  perovskite structures. This level of Mn self-doping can be achieved through the HP and HT synthesis. The average oxidation state of Mn is +3 in  $(\text{R}_{0.667}\text{Mn}_{0.333})\text{MnO}_3$ . However, Mn enters the A-site in the oxidation state of +2, creating the average oxidation state of +3.333 at the B site.  $(\text{R}_{0.667}\text{Mn}_{0.333})\text{MnO}_3$  exhibits enhanced Néel temperatures of about  $T_{\text{N1}} = 106\text{-}110$  K and canted antiferromagnetic properties. Compounds with  $R = \text{Er}$  and  $\text{Tm}$  show additional magnetic transitions at about  $T_{\text{N2}} = 9\text{-}16$  K.

## References in Chapter 5

- [1] Kimura, T.; Goto, T.; Shintani, H.; Ishizaka, K.; Arima, T.; Tokura, Y. Magnetic Control of Ferroelectric Polarization. *Nature (London)* **2003**, *426*, 55-58.
- [2] Zhou, J.-S.; Goodenough, J. B. Unusual Evolution of the Magnetic Interactions versus Structural Distortions in  $\text{RMnO}_3$  Perovskites. *Phys. Rev. Lett.* **2006**, *96*, 247202.
- [3] Tachibana, M.; Shimoyama, T.; Kawaji, H.; Atake, T.; Takayama-Muromachi, E. Jahn-Teller Distortion and Magnetic Transitions in Perovskite  $\text{RMnO}_3$  ( $R = \text{Ho}, \text{Er}, \text{Tm}, \text{Yb}, \text{ and Lu}$ ). *Phys. Rev. B: Condens. Matter Mater. Phys.* **2007**, *75*, 144425.
- [4] Mochizuki, M.; Furukawa, N.; Nagaosa, N. Theory of Spin-Phonon Coupling in Multiferroic Manganese Perovskites  $\text{RMnO}_3$ . *Phys. Rev. B: Condens. Matter Mater. Phys.* **2011**, *84*, 144409.
- [5] Pomjakushin, V.Y.; Kenzelmann, M.; Dönni, A.; Harris, A.B.; Nakajima, T.; Mitsuda, S.;

Tachibana, M.; Keller L.; Mesot, J.; Kitazawa H.; Takayama-Muromachi, E. Evidence for large electric polarization from collinear magnetism in  $\text{TmMnO}_3$ . *New J. Phys.* **2009**, *11*, 04301911.

[6] Mukherjee, S.; Dönni, A.; Nakajima, T.; Mitsuda, S.; Tachibana, M.; Kitazawa, H.; Pomjakushin, V.; Keller, L.; Niedermayer, C.; Scaramucci, A.; Kenzelmann, M. E-type Noncollinear Magnetic Ordering in Multiferroic  $\text{o-LuMnO}_3$ . *Phys. Rev. B: Condens. Matter Mater. Phys.* **2017**, *95*, 104412.

[7] Alonso, J. A.; Martínez-Lope, M. J.; Casais, M. T.; Fernández-Díaz, M. T. Evolution of the Jahn-Teller Distortion of  $\text{MnO}_6$  Octahedra in  $\text{RMnO}_3$  Perovskites (R = Pr, Nd, Dy, Tb, Ho, Er, Y): A Neutron Diffraction Study. *Inorg. Chem.* **2000**, *39*, 917-923.

[8] Uusi-Esko, K.; Malm, J.; Imamura, N.; Yamauchi, H.; Karppinen, M. Characterization of  $\text{RMnO}_3$  (R = Sc, Y, Dy-Lu): High-Pressure Synthesized Metastable Perovskites and Their Hexagonal Precursor Phases. *Mater. Chem. Phys.* **2008**, *112*, 1029-1034.

[9] Bochu, B.; Chenavas, J.; Joubert, J. C.; Marezio, M. High Pressure Synthesis and Crystal Structure of a New Series of Perovskite-Like Compounds  $\text{CMn}_7\text{O}_{12}$  (C = Na; Ca; Cd; Sr; La; Nd). *J. Solid State Chem.* **1974**, *11*, 88-93.

[10] Prodi, A.; Allodi, G.; Gilioli, E.; Licci, F.; Marezio, M.; Bolzoni, F.; Gauzzi, A.; De Renzi, R.  $\mu\text{SR}$  Study of  $\text{AA}'_3\text{Mn}_4\text{O}_{12}$  Double Perovskites. *Phys. B* **2006**, *374-375*, 55-58.

[11] Mezzadri, F.; Calicchio, M.; Gilioli, E.; Cabassi, R.; Bolzoni, F.; Calestani, G.; Bissoli, F. High-Pressure Synthesis and Characterization of  $\text{PrMn}_7\text{O}_{12}$  Polymorphs. *Phys. Rev. B: Condens. Matter Mater. Phys.* **2009**, *79*, 014420.

[12] Prodi, A.; Gilioli, E.; Cabassi, R.; Bolzoni, F.; Licci, F.; Huang, Q.; Lynn, J. W.; Affronte,

M.; Gauzzi, A.; Marezio, M. Magnetic Structure of the High-Density Single-Valent  $e_g$  Jahn-Teller System  $\text{LaMn}_7\text{O}_{12}$ . *Phys. Rev. B: Condens. Matter Mater. Phys.* **2009**, *79*, 085105.

[13] Okamoto, H.; Karppinen, M.; Yamauchi, H.; Fjellvag, H. High-temperature Synchrotron X-ray Diffraction Study of  $\text{LaMn}_7\text{O}_{12}$ . *Solid State Sci.* **2009**, *11*, 1211-1215.

[14] Cabassi, R.; Bolzoni, F.; Gilioli, E.; Bissoli, F.; Prodi, A.; Gauzzi, A. Jahn-Teller-induced Crossover of the Paramagnetic Response in the Singly Valent  $e_g$  System  $\text{LaMn}_7\text{O}_{12}$ . *Phys. Rev. B: Condens. Matter Mater. Phys.* **2010**, *81*, 214412.

[15] Verseila, M.; Mezzadri, F.; Delmonte, D.; Baptiste, B.; Klein, Y.; Shcheka, S.; Chapon, L. C.; Hansen, T.; Gilioli, E.; Gauzzi, A. Effect of Chemical Pressure Induced by  $\text{La}^{3+}/\text{Y}^{3+}$  Substitution on the Magnetic Ordering of  $(\text{AMn}_3)\text{Mn}_4\text{O}_{12}$  Quadruple Perovskites. *Phys. Rev. Mater.* **2017**, *1*, 064407.

[16] Zhang, L.; Matsushita, Y.; Yamaura, K.; Belik, A. A. Five-Fold Ordering in High-Pressure Perovskites  $\text{RMn}_3\text{O}_6$  ( $\text{R} = \text{Gd-Tm}$  and  $\text{Y}$ ). *Inorg. Chem.* **2017**, *56*, 5210-5218.

[17] Belik, A. A. Rise of A-site Columnar-ordered  $\text{A}_2\text{A}'\text{A}''\text{B}_4\text{O}_{12}$  Quadruple Perovskites with Intrinsic Triple Order. *Dalton Trans.* **2018**, *47*, 3209-3217.

[18] Tanaka, M.; Katsuya, Y.; Yamamoto, A. A New Large Radius Imaging Plate Camera for High-Resolution and High-Throughput Synchrotron X-Ray Powder Diffraction by Multiexposure Method. *Rev. Sci. Instrum.* **2008**, *79*, 075106.

[19] Tanaka, M.; Katsuya, Y.; Matsushita, Y.; Sakata, O. Development of a Synchrotron Powder Diffractometer with a One-Dimensional X-Ray Detector for Analysis of Advanced Materials. *J. Ceram. Soc. Jpn.* **2013**, *121*, 287-290.

- [20] Izumi, F.; Ikeda, T. A Rietveld-Analysis Program RIETAN-98 and its Applications to Zeolites. *Mater. Sci. Forum* **2000**, 321-324, 198-205.
- [21] Ueda, S.; Katsuya, Y.; Tanaka, M.; Yoshikawa, H.; Yamashita, Y.; Ishimaru, S.; Matsushita, Y.; Kobayashi, K. Present Status of the NIMS Contract Beamline BL15XU at SPring-8. *AIP Conf. Proc.* **2010**, 1234, 403-406.
- [22] Ueda, S. Application of Hard X-Ray Photoelectron Spectroscopy to Electronic Structure Measurements for Various Functional Materials. *J. Electron Spectrosc. Relat. Phenom.* **2013**, 190, 235-241.
- [23] Barr, T. L.; Seal, S. Nature of the Use of Adventitious Carbon as a Binding Energy Standard. *J. Vac. Sci. Technol., A* **1995**, 13, 1239–1246.
- [24] Brese, N. E.; O’Keeffe, M. Bond-Valence Parameters for Solids. *Acta Crystallogr., Sect. B: Struct. Sci.* **1991**, 47, 192-197.
- [25] Martinelli, A.; Ferretti, M.; Cimberle, M. R.; Ritter, C. Neutron Powder Diffraction Analysis of  $(\text{Tm}_{0.50}\text{Ca}_{0.50})\text{MnO}_3$  and  $(\text{Lu}_{0.50}\text{Ca}_{0.50})\text{MnO}_3$ . *J. Solid State Chem.* **2012**, 196, 314-319.
- [26] Belik, A. A.; Matsushita, Y.; Tanaka, M.; Takayama-Muromachi, E.  $(\text{In}_{1-y}\text{Mn}_y)\text{MnO}_3$  ( $1/9 \leq y \leq 1/3$ ): Unusual Perovskites with Unusual Properties. *Angew. Chem. Inter. Ed.* **2010**, 49, 7723–7727.
- [27] Martinelli, A.; Ferretti, M.; Castellano, C.; Cimberle, M. R.; Masini, R.; Ritter, C. Neutron Powder Diffraction Investigation on the Crystal and Magnetic Structure of  $(\text{Ho}_{0.50+x}\text{Ca}_{0.50-x})(\text{Mn}_{1-x}\text{Cr}_x)\text{O}_3$ . *J. Phys.: Condens. Mat.* **2011**, 23, 416005.
- [28] Yoshii, K.; Abe, H.; Ikeda, N. Structure, Magnetism and Transport of the Perovskite

Manganites  $\text{Ln}_{0.5}\text{Ca}_{0.5}\text{MnO}_3$  (Ln = Ho, Er, Tm, Yb, and Lu). *J. Solid State Chem.* **2005**, *178*, 3615-3623.

[29] Zhang, H.; Flacau, R.; Sun, J.; Li, G.; Liao, F.; Lin, J. Synthesis, Structure, and Magnetic Properties of  $(\text{Tb}_{1-x}\text{Mn}_y)\text{MnO}_{3-\delta}$ . *Inorg. Chem.* **2014**, *53*, 4535–4540.

[30] Zhang, H.; Flacau, R.; Du, X.; Manuel, P.; Cong, J.; Sun, Y.; Sun, J.; Yang, S.; Li, G.; Liao, F.; Lin, J. Multiferroicity Broken by Commensurate Magnetic Ordering in Terbium Orthomanganite. *ChemPhysChem* **2016**, *17*, 1098–1103.

[31] Deng, J.; Farid, M. A.; Zhang, M.; Yang, A.; Zhang, H.; Zhang, H.; Tian, G.; Wu, M.; Liu, L.; Sun, J.; Li, G.; Liao, F. Lin, J. Enhancement of Ferroelectricity for Orthorhombic  $(\text{Tb}_{0.861}\text{Mn}_{0.121})\text{MnO}_{3-\delta}$  by Copper Doping. *Inorg. Chem.* **2017**, *56*, 3475-3482.

[32] Deng, J.; Yang, A.; Farid, M. A.; Zhang, H.; Li, J.; Zhang, H.; Li, G.; Liu, L.; Sun, J.; Lin, J. Synthesis, Structure and Magnetic Properties of  $(\text{Eu}_{1-x}\text{Mn}_x)\text{MnO}_{3-\delta}$ . *RSC Adv.* **2017**, *7*, 2019-2024.

[33] Ilton, S.; Post, E.; Heaney, J.; Ling, T.; Kerisit, N. XPS Determination of Mn Oxidation States in Mn (Hydr)Oxides. *Appl. Surf. Sci.* **2016**, *366*, 475-485.

[34] Ye, F.; Lorenz, B.; Huang, Q.; Wang, Y. Q.; Sun, Y. Y.; Chu, C. W.; Fernandez-Baca, J. A.; Dai, P. C.; Mook, H. A. Incommensurate Magnetic Structure in the Orthorhombic Perovskite  $\text{ErMnO}_3$ . *Phys. Rev. B: Condens. Matter Mater. Phys.* **2007**, *76*, 060402.

[35] Kumar, A.; Yusuf, S. M. The Phenomenon of Negative Magnetization and its Implications. *Phys. Rep.* **2015**, *556*, 1-34.

[36] Belik, A. A. Origin of Magnetization Reversal and Exchange Bias Phenomena in Solid Solutions of  $\text{BiFeO}_3$ - $\text{BiMnO}_3$ : Intrinsic or Extrinsic? *Inorg. Chem.* **2013**, *52*, 2015-2021.

[37] Belik, A. A. Fresh Look at the Mystery of Magnetization Reversal in  $\text{YVO}_3$ . *Inorg. Chem.* **2013**, 52, 8529-8539.



All of the samples exhibit complex magnetic properties.  $RMnO_3$  and  $(R_{1-x}Mn_x)MnO_3$  have canted antiferromagnetic performance. Especially in the series of  $RMn_3O_6$ , the radii of  $R^{3+}$  cations do not only play an important role in the composition, but also influence the transition temperatures of  $RMn_3O_6$  compounds, as shown in **Figure 6.1**. Besides that,  $CeCuMn_6O_{12}$  shows semiconducting behavior that resistivity sharply increases in the charge-ordered  $R-3$  phase below the charge ordering temperature.

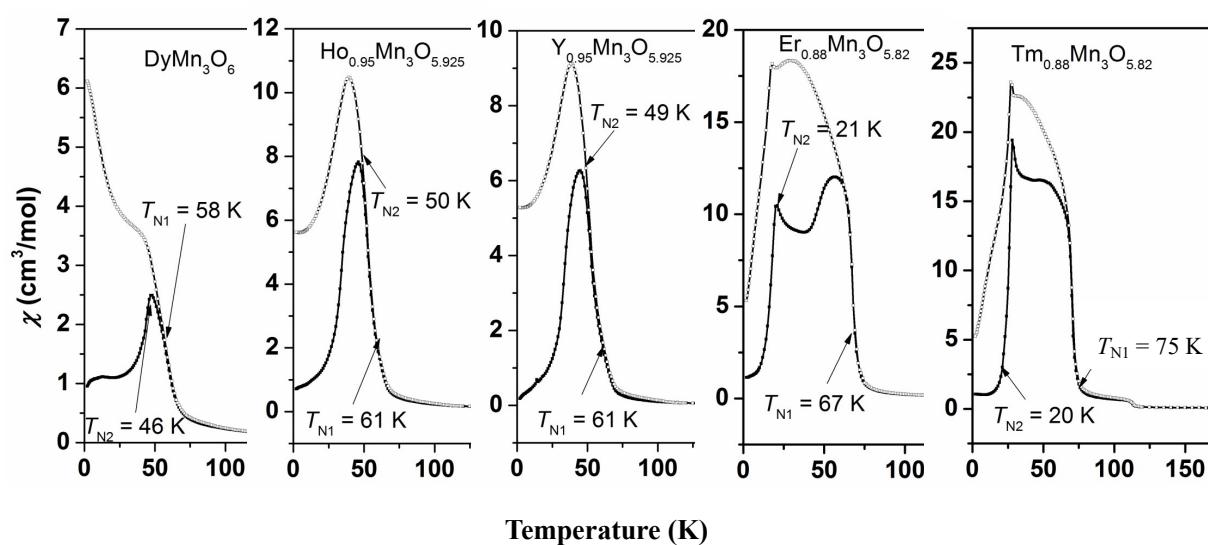


**Figure 6.1.** The dc susceptibility curves of  $DyMn_3O_6$ ,  $Ho_{0.95}Mn_3O_{5.925}$ ,  $Y_{0.95}Mn_3O_{5.925}$ ,  $Er_{0.88}Mn_3O_{5.82}$ , and  $Tm_{0.88}Mn_3O_{5.82}$ .

## 6.2. Future prospects

In the family of  $RMn_7O_{12}$ , the perovskites with the large size cations, such as  $LaMn_7O_{12}$  [3] and  $PrMn_7O_{12}$  [4], have been researched. For such compounds with the small size cations, it is difficult to obtain the single phase. I will try to prepare the  $RMn_7O_{12}$  by the method which is similar with the preparation of  $RMn_3O_6$  compounds, changing the ratio of the starting chemicals. Then the crystal structure and the magnetic properties will be researched.

Secondly, the rock salt ordering is the most favourable at the B-site, and the A-site cations

always favour the layered ordering [5]. Therefore, the columnar-ordered arrangements in A-site and B-sites are very rare. I will research new members of the  $A_2A'A''B_4O_{12}$  quadruple perovskite family:  $R_2CuMnMn_4O_{12}$  and  $R_2MnGaMn_4O_{12}$  (R = rare earth elements), which are derivatives of  $RMn_3O_6$  (or  $R_2MnMnMn_4O_{12}$ ) compounds, which was found in this thesis. And the A-site ordering of the two kinds of compounds will be investigated. A large group of other compounds is expected based on  $RMn_3O_6$  using different substitution schemes. Therefore, our findings of  $RMn_3O_6$  will contribute to the development of science of perovskite materials.

## References in chapter 6

- [1] Matsubara, M.; Manz, S.; Mochizuki, M.; Kubacka, T.; Iyama, A.; Aliouane, N.; Kimura, T.; Johnson, S. L.; Meier, D.; Fiebig, M. Magnetoelectric domain control in multiferroic  $TbMnO_3$ . *Science* **2015**, *348*, 1112-1115.
- [2] Prodi, A.; Gilioli, E.; Cabassi, R.; Bolzoni, F.; Licci, F.; Huang, Q.; Lynn, J. W.; Affronte, M.; Gauzzi, A.; Marezio, M. Magnetic structure of the high-density single-valent  $e_g$  Jahn-Teller system  $LaMn_7O_{12}$ . *Phys. Rev. B* **2009**, *79*, 085105.
- [3] Prodi, A.; Gilioli, E.; Cabassi, R.; Bolzoni, F.; Licci, F.; Huang, Q.; Lynn, J. W.; Affronte, M.; Gauzzi, A.; Marezio, M. Magnetic structure of the high-density single-valent  $e_g$  Jahn-Teller system  $LaMn_7O_{12}$ . *Phys. Rev. B* **2009**, *79*, 085105.
- [4] Mezzadri, F.; Calicchio, M.; Gilioli, E.; Cabassi, R.; Bolzoni, F.; Calestani, G.; Bissoli, F. High-pressure synthesis and characterization of  $PrMn_7O_{12}$  polymorphs. *Phys. Rev. B* **2009**, *79*, 014420.
- [5] King, G.; Woodward, P. M. Cation ordering in perovskites. *J. Mater. Chem.* **2010**, *20*, 5785-5796.

## List of appended publications

**This thesis is based on the following publications.**

### *1. Scientific papers*

[1] Zhang, L.; Matsushita, Y.; Yamaura, K.; Belik, A. A. Five-Fold Ordering in High-Pressure Perovskites  $\text{RMn}_3\text{O}_6$  (R = Gd-Tm and Y). *Inorg. Chem.* **2017**, *56*, 5210-5218.

[2] Zhang, L.; Matsushita, Y.; Katsuya, Y.; Tanaka, M.; Yamaura, K.; Belik, A. A. Charge and orbital orders and structural instability in high-pressure quadruple perovskite  $\text{CeCuMn}_6\text{O}_{12}$ . *J. Phys.: Condens. Matter* **2018**, *30*, 074003.

[3] Zhang, L.; Gerlach, D.; Dönni, A.; Chikyow, T.; Katsuya, Y.; Tanaka, M.; Ueda, S.; Yamaura, K.; Belik, A. A. Mn Self-Doping of Orthorhombic  $\text{RMnO}_3$  Perovskites:  $(\text{R}_{0.667}\text{Mn}_{0.333})\text{MnO}_3$  with R = Er-Lu. *Inorg. Chem.* **2018**, *57*, 2773-2781.

### *2. Verbal presentation*

[1] Lei ZHANG, et al., “High-pressure synthesis and properties of  $\text{RMn}_7\text{O}_{12}$  multiferroic perovskites”.

The 26th Annual Meeting of the Materials Research Society of Japan, Dec. 19<sup>th</sup>-22<sup>th</sup>, 2016, Yokohama, Japan.

[2] Lei ZHANG, et al., “High-Pressure Preparation and Properties of  $\text{RMn}_3\text{O}_6$  (R = Gd-Tm and Y)”.

The Tenth International Conference on the Science and Technology for Advanced Ceramics,

Aug. 1<sup>st</sup>, 2017, Yokohama, Japan.

[3] Lei ZHANG, et al., “High-Pressure Preparation and Properties of  $\text{RMn}_3\text{O}_6$  (R = Gd-Tm and Y)”.

The 15th International Conference on Advanced Materials, Aug. 31<sup>st</sup>, 2017, Kyoto, Japan.

[4] Lei ZHANG, et al., “High-Pressure Preparation and Properties of  $\text{RMn}_3\text{O}_6$  (R = Gd-Tm and Y)”.

The 27th Annual Meeting of the Materials Research Society of Japan, Dec. 6<sup>th</sup>, 2017, Yokohama, Japan.

## Acknowledgement

Here, I want to say thanks to all of the people who helped me complete this thesis. Firstly, I would like to express my heartfelt gratitude to my supervisors Prof. Kazunari Yamaura and Dr. Alexei Belik for give assistance in my research and work. When I encounter difficulties, their kindness and patience helped me solve the problems. During the three years, Prof. Yamaura not only supported my work but also was concerned about my living in Japan. Dr. Belik taught me how to be a scientist patiently. They are the exemplars for me because of their enthusiasm and diligence in work.

I would like to thank Dr. Yoshitaka Matsushita, Dr. Yoshio Katsuya, Dr. Masahiko Tanaka, and Dr. Yoshihiro Tsujimoto for their help in SXRD measurement and XRPD measurement. I would like to give my gratitude to Dr. Yahua Yuan, Dr. Jianfeng He, and Dr. Yu Su because they taught me how to use lab-facilities and gave me some advice. I would like to thank Dr. Shan Yu and Ms. Jie Chen for their help and supports. Furthermore, I would like to say thanks to my parents for their endless support.

I would like to express my gratitude to all of you again. Because of you I could get such achievements.